



Special Issue Reprint

Antenna Design and Optimization for 5G, 6G, and IoT

Edited by
Naser Ojaroudi Parchin

mdpi.com/journal/sensors



Antenna Design and Optimization for 5G, 6G, and IoT

Antenna Design and Optimization for 5G, 6G, and IoT

Guest Editor

Naser Ojaroudi Parchin



Basel • Beijing • Wuhan • Barcelona • Belgrade • Novi Sad • Cluj • Manchester

Guest Editor

Naser Ojaroudi Parchin
School of Computing,
Engineering & the Built
Environment
Edinburgh Napier University
Edinburgh
UK

Editorial Office

MDPI AG
Grosspeteranlage 5
4052 Basel, Switzerland

This is a reprint of the Special Issue, published open access by the journal *Sensors* (ISSN 1424-8220), freely accessible at: https://www.mdpi.com/journal/sensors/special_issues/antenna_design_5G_6G.

For citation purposes, cite each article independently as indicated on the article page online and as indicated below:

Lastname, A.A.; Lastname, B.B. Article Title. *Journal Name Year, Volume Number, Page Range.*

ISBN 978-3-7258-3641-3 (Hbk)

ISBN 978-3-7258-3642-0 (PDF)

<https://doi.org/10.3390/books978-3-7258-3642-0>

Contents

About the Editor	vii
Preface	ix
Haleh Jahanbakhsh Basherlou, Naser Ojaroudi Parchin and Chan Hwang See	
Antenna Design and Optimization for 5G, 6G, and IoT	
Reprinted from: <i>Sensors</i> 2025, 25, 1494, https://doi.org/10.3390/s25051494	1
Haleh Jahanbakhsh Basherlou, Naser Ojaroudi Parchin and Chan Hwang See	
A Dual-Polarized and Broadband Multiple-Antenna System for 5G Cellular Communications	
Reprinted from: <i>Sensors</i> 2025, 25, 1032, https://doi.org/10.3390/s25041032	7
Ha Hoang, Minh-Huy Nguyen and Vinh Pham-Xuan	
Analysis of Near-Field Characteristics on Improved Structures of Double-Slot Antipodal Vivaldi Antenna	
Reprinted from: <i>Sensors</i> 2024, 24, 4986, https://doi.org/10.3390/s24154986	29
Xianjing Lin, Jielin Mai, Hongjun He and Yao Zhang	
Dual-Polarized Dipole Antenna with Wideband Stable Radiation Patterns Using Artificial Magnetic Conductor Reflector	
Reprinted from: <i>Sensors</i> 2024, 24, 3911, https://doi.org/10.3390/s24123911	46
Xinxin Huang, Sai Zhu and Guanhui Liang	
Reliability Evaluation Method for Array Antenna Considering Performance Changes	
Reprinted from: <i>Sensors</i> 2024, 24, 1914, https://doi.org/10.3390/s24061914	57
Manoj Prabhakar Mohan, Hong Cai, Arokiaswami Alphones and Muhammad Faeyz Karim	
mmWave Zero Order Resonant Antenna with Patch-like Radiation Fed by a Butler Matrix for Passive Beamforming	
Reprinted from: <i>Sensors</i> 2023, 23, 7973, https://doi.org/10.3390/s23187973	70
Victor Dmitriev, Rodrigo M. S. de Oliveira, Rodrigo R. Paiva and Nilton R. N. M. Rodrigues	
Multifunctional THz Graphene Antenna with 360° Continuous ϕ -Steering and θ -Control of Beam	
Reprinted from: <i>Sensors</i> 2023, 23, 6900, https://doi.org/10.3390/s23156900	85
Madiha Farasat, Dushantha Thalakotuna, Yang Yang, Zhonghao Hu and Karu Esselle	
Suppression of Common-Mode Resonance in Multiband Base Station Antennas	
Reprinted from: <i>Sensors</i> 2023, 23, 2905, https://doi.org/10.3390/s23062905	109
Esraa Mousa Ali, Wahaj Abbas Awan, Mohammed S. Alzaidi, Abdullah Alzahrani, Dalia H. Elkamchouchi, Francisco Falcone and Sherif S. M. Ghoneim	
A Shorted Stub Loaded UWB Flexible Antenna for Small IoT Devices	
Reprinted from: <i>Sensors</i> 2023, 23, 748, https://doi.org/10.3390/s23020748	119
Daniel R. Prado	
Near Field Models of Spatially-Fed Planar Arrays and Their Application to Multi-Frequency Direct Layout Optimization for mm-Wave 5G New Radio Indoor Network Coverage	
Reprinted from: <i>Sensors</i> 2022, 22, 8925, https://doi.org/10.3390/s22228925	134
Changhyeon Im, Tae Heung Lim and Hosung Choo	
Design of a mmWave Antenna Printed on a Thick Vehicle-Glass Substrate Using a Linearly Arrayed Patch Director and a Grid-Slotted Patch Reflector for High-Gain Characteristics	
Reprinted from: <i>Sensors</i> 2022, 22, 6187, https://doi.org/10.3390/s22166187	156

**Martins Odiamenhi, Haleh Jahanbakhsh Basherlou, Chan Hwang See, Naser Ojaroudi
Parchin, Keng Goh and Hongnian Yu**

Advancements and Challenges in Antenna Design and Rectifying Circuits for Radio Frequency
Energy Harvesting

Reprinted from: *Sensors* 2024, 24, 6804, <https://doi.org/10.3390/s24216804> 171

About the Editor

Naser Ojaroudi Parchin

Naser Ojaroudi Parchin (SMIEEE) is an assistant professor at Edinburgh Napier University, UK. He holds a Ph.D. in Electrical Engineering from the University of Bradford, UK, where he also worked as a postdoctoral research assistant and contributed to the European Space Agency's SATNEX V project. His research spans over 15 years, focusing on Antennas and Microwave Engineering. From 2018 to 2020, he served as a Marie Curie Research Fellow for the H2020-ITN-SECRET project, which targeted 5G mobile small cells. His expertise extends to phased arrays, MIMO systems, smartphone antennas, full-duplex diversity, 5G antennas, biomedical sensors, and millimeter-wave/terahertz components.

He has designed and tested numerous antenna systems, focusing on next-generation wireless communication, especially 5G and beyond. His interests also include fractal structures, metamaterials, metasurfaces, PCB realization, microwave filters, and wireless propagation. He has published over 400 technical journal articles and conference papers, contributing significantly to antenna research. He has been an active participant in international IEEE conferences, presenting his work globally. He has co-authored several books and chapters on antenna design and optimization.

In recognition of his contributions, he has received multiple awards, including best paper accolades at prominent conferences such as the URSI Symposium, IMDC, and IMS. He has been listed in the World's Top Scientists list in 2016, 2020, 2021, 2022, 2023, and 2024. He is also a reviewer for several prestigious journals and grants, including those for the IEEE and the Dutch Science Council. His current research focuses on advanced wireless technologies and biomedical applications. He is an active member of the IEEE, EurAAP, and MCAA and has been recognized by the Royal Academy of Engineering as a UK Talent.

Preface

This Special Issue focuses on the latest advancements in antenna design and optimization for 5G, 6G, and IoT applications. It delves into cutting-edge methodologies, novel architectures, and emerging trends, addressing the growing demand for efficient, adaptive, and multifunctional antennas in next-generation wireless communication systems. From MIMO configurations to AI-driven optimization, this Special Issue provides valuable insights into the future of antenna technologies. We express our gratitude to all the authors and reviewers for their valuable contributions to this comprehensive collection.

Naser Ojaroudi Parchin

Guest Editor



Editorial

Antenna Design and Optimization for 5G, 6G, and IoT

Haleh Jahanbakhsh Basherlou *, Naser Ojaroudi Parchin * and Chan Hwang See

School of Computing, Engineering and the Built Environment, Edinburgh Napier University, Edinburgh EH10 5DT, UK; c.see@napier.ac.uk

* Correspondence: haleh.jahanbakhshbasherlou@napier.ac.uk (H.J.B.); n.ojaroudiparchin@napier.ac.uk (N.O.P.)

1. Introduction

In the ever-expanding domain of wireless communication, the continuous evolution of network technologies has underscored the critical role of antenna design and optimization. As we transition from 5G to the emerging era of 6G and the Internet of Things (IoT), the need for highly efficient, adaptive, and multifunctional antennas has become paramount [1,2]. The increasing demand for seamless connectivity, ultra-reliable low-latency communication (URLLC), massive machine-type communication (mMTC), and enhanced mobile broadband (eMBB) necessitate innovative antenna solutions that can cater to diverse and stringent performance requirements. Antennas are no longer mere transmission and reception devices; they serve as fundamental enablers of advanced wireless systems, dictating the efficiency, reliability, and scalability of next-generation networks [3,4]. With the advent of reconfigurable intelligent surfaces (RIS) and metamaterials, antenna technology is poised to revolutionize wireless communication by enabling dynamic beamforming, energy efficiency, and spectrum utilization enhancements [5,6].

The integration of advanced antenna technologies is central to addressing the challenges associated with higher frequency bands, increased data rates, and network densification [7]. In 5G and beyond, Multiple-Input Multiple-Output (MIMO) systems, beamforming techniques, and reconfigurable intelligent surfaces (RIS) have emerged as key solutions to optimize spectral and energy efficiency. Furthermore, the move towards sub-terahertz (THz) and millimeter-wave (mmWave) frequency bands has introduced new complexities in antenna design, including the need for compact, high-gain, and low-loss structures [8]. The convergence of artificial intelligence (AI) and machine learning (ML) in antenna design and optimization is also paving the way for smart, self-adaptive antennas capable of dynamic performance enhancement. The rapid proliferation of IoT applications has further fueled research in miniaturized, energy-efficient, and cost-effective antennas. From smart cities and autonomous vehicles to healthcare monitoring and industrial automation, IoT-driven ecosystems demand antennas that can seamlessly operate across multiple frequency bands while ensuring reliability in highly dynamic environments. The integration of flexible and conformal antennas, alongside novel materials such as graphene and metamaterials, is redefining the landscape of IoT connectivity [9].

This Special Issue focuses on the latest advancements in antenna design and optimization for 5G, 6G, and IoT applications. The contributions presented in this collection explore cutting-edge methodologies, novel architecture, and emerging trends that are shaping the future of wireless communication. Topics range from innovative MIMO and phased-array configurations to the development of highly efficient THz and mmWave antennas, as well as AI-driven optimization techniques. By providing a comprehensive overview of state-of-the-art research, this Special Issue aims to foster new insights and inspire further exploration into next-generation antenna technologies. The research featured here not only

Received: 12 February 2025

Accepted: 25 February 2025

Published: 28 February 2025

Citation: Jahanbakhsh Basherlou, H.;

Ojaroudi Parchin, N.; See, C.H.

Antenna Design and Optimization for 5G, 6G, and IoT. *Sensors* **2025**, *25*, 1494.

<https://doi.org/10.3390/s25051494>

Copyright: © 2025 by the authors.

Licensee MDPI, Basel, Switzerland.

This article is an open access article distributed under the terms and conditions of the Creative Commons Attribution (CC BY) license

(<https://creativecommons.org/licenses/by/4.0/>).

highlights significant theoretical and experimental advancements but also underscores the transformative potential of antennas in shaping the future of connectivity.

2. Overview of Published Papers

Jahankhani Basherlou et al. (Contribution 1) present a newly designed MIMO antenna array tailored for sub-6 GHz 5G applications incorporating eight compact trapezoidal slot elements with L-shaped CPW feedlines, ensuring wide bandwidth and polarization diversity. The antennas, placed at the smartphone's peripheral corners, cover 3.2–6 GHz with a compact 75 mm × 150 mm footprint. The array achieves high isolation without decoupling structures and provides a bandwidth of 2800 MHz. It demonstrates excellent radiation efficiency, low ECC (<0.005), and low TARC (<−20 dB). The design is implemented on a single-layer FR4 substrate, optimizing cost and performance. Experimental results closely match simulations, confirming reliability. A compact mmWave phased array is introduced for future 5G/6G applications. The design supports high data rates, efficient connectivity, and future smartphone integration.

Hoang et al. (Contribution 2) present a characterization of near-field impulse responses in a double-slot Vivaldi antenna using electromagnetic (EM) near-field data. Their analysis explores EM energy flow, reorientation, and scattering across different antenna segments. Geometric features of near-field wavefront surfaces aid in evaluating antenna directivity and optimizing structural details. The study introduces partitional far-field response characteristics in frequency and time domains. By simplifying the near-field propagation model, the approach enhances insight into EM propagation in Vivaldi antennas. The proposed methodology identifies dominant EM flow regions and structural impacts on radiation performance. Partitional gain and impulse response characteristics guide structural optimization. The study highlights how localized EM characteristics improve antenna design efficiency. The optimization process is validated through near-field, far-field, and conventional characteristics. This framework is also applicable to other traveling wave antennas for better propagation understanding and design improvements.

Lin et al. (Contribution 3) propose a wideband dual-polarized dipole antenna operating from 1.7 to 3.8 GHz. Traditional 4G dipole antennas struggle with impedance matching and stable radiation patterns in the 5G sub-6 GHz band. To address this, a connected-ring-shaped metasurface structure functions as an artificial magnetic conductor (AMC). The AMC stabilizes radiation patterns without increasing antenna height. The measured results confirm an 80.7% impedance bandwidth (1.7–4.0 GHz). The antenna maintains a stable realized gain of 7.0 ± 1.0 dBi. It also achieves a consistent half-power beamwidth (HPBW) of $70^\circ \pm 5^\circ$. The simple structure enhances practicality for base station applications. The design ensures compatibility with both 4G and 5G networks. These attributes make it a strong candidate for next-generation base stations.

Huang et al. (Contribution 4) analyze the limitations of traditional array antenna reliability evaluation methods based on the n/k system. Existing approaches overestimate reliability by ignoring the impact of failed T/R modules on performance. To enhance accuracy, a new evaluation method accounts for performance variations caused by T/R failures in different locations. The method calculates reliability by analyzing all available states of the antenna system. For large-scale array antennas, the system is divided into subarrays, each evaluated separately. The minimum failure threshold for each subarray is determined to refine the overall reliability assessment. The proposed model incorporates fault position and quantity, reducing overestimation errors. Simulation results validate improved accuracy over conventional methods. The approach ensures a more precise reliability assessment for array antennas. This methodology is beneficial for large-scale antenna systems requiring high reliability.

Mohan et al. (Contribution 5) design a zero-order resonant antenna using the composite right-left-handed (CRLH) principle at 30 GHz. The antenna is fabricated without metallic vias, utilizing mirror-image CRLH structures for patch-like radiation. Its characteristics are analyzed through equivalent circuit modeling, parameter extraction, and dispersion diagrams. The measured realized gain is 5.35 dBi, with a radiation efficiency of 87%. The antenna operates without spurious resonance over a 10 GHz bandwidth. A passive beamforming array is implemented using a Butler matrix and CRLH antennas. The CRLH antennas are connected to the 4×4 Butler matrix output ports. Beam-scanning angles of 12° , -68° , 64° , and -11° are achieved. Experimental results confirm the antenna's effectiveness for 5G, wireless power transfer, and IoT sensing. The design offers a compact, high-efficiency solution for next-generation wireless applications.

Dmitriev et al. (Contribution 6) propose a novel graphene antenna with a dipole and four graphene sheet reflectors. The antenna achieves dynamic beam control through electric field-tuning of the chemical potentials of its graphene elements. It supports quasi-omnidirectional, one- or two-directional beam configurations and 360° azimuthal beam steering. An additional graphene layer allows control of the radiation pattern in the elevation plane. The operating frequency range is 1.75–2.03 THz, with a gain varying between 0.86 and 1.63, depending on the active regime. Group-theoretical analysis predicts radiation properties, reducing computational complexity. The proposed antenna offers seamless and continuous beam steering, enhancing adaptability for THz communication. Applications include tracking moving transmitters, medical imaging, and security screening. Numerical simulations validate the theoretical model and performance. Future work will focus on optimizing radiation efficiency and expanding its potential applications.

Farasat et al. (Contribution 7) address pattern distortion in multiband base-station antennas caused by common-mode (CM) currents. The study focuses on mitigating CM interference between low-band (690–960 MHz) and high-band (1810–2690 MHz) antenna elements. A novel common-mode suppression circuit is integrated into the high-band impedance matching network. This circuit shifts the CM resonance frequency outside the low-band range, reducing unwanted distortions. Experimental results confirm significant improvement in low-band radiation patterns. The suppression technique minimizes inter-cell interference and improves network performance. A quarter-wavelength short line with a capacitor effectively suppresses CM currents. High-band performance remains unaffected, maintaining proper impedance matching. The proposed approach ensures stable low-band beamwidth variation within $65^\circ \pm 5^\circ$. This solution enhances multiband antenna efficiency for 5G base stations.

Ali et al. (Contribution 8) presents a compact ultra-wideband (UWB) antenna with simple geometry. The antenna is designed using the flexible ROGERS 5880 substrate, which has a low dielectric loss and a thickness of 0.254 mm. By modifying a conventional rectangular monopole with triangular slots and a semi-circular stub, the impedance bandwidth is significantly extended. The optimized design covers a wide frequency range of 2.73–9.68 GHz. It features a compact 15×20 mm² size, making it ideal for integration into flexible electronics. The antenna maintains stable performance when bent along the x and y axes. Simulated and measured results confirm its robustness in both rigid and flexible conditions. It exhibits an omnidirectional radiation pattern with a minimum gain of >2.5 dBi. The CPW feeding technique ensures easy integration with electronic circuits. The proposed UWB antenna is a strong candidate for flexible and compact wireless applications.

Prado (Contribution 9) presents two near-field models for analyzing spatially fed planar array antennas. The first model is based on radiation equations derived from the A and F vector potentials, while the second model employs the superposition of far-field contributions from individual array elements. Despite different assumptions, both models

show a high degree of agreement, with a relative error below 3.2% at 13λ . The faster model is then used for near-field beam-shaping optimization in a 5G mmWave indoor network. A phase-only synthesis (POS) is applied first to optimize reflectarray layout at 28 GHz. Multi-frequency optimization follows using a method of moments based on local periodicity (MoM-LP). The optimization approach ensures compliance across the 5G NR n257 band. The final optimized antenna achieves a magnitude ripple lower than 1.5 dB. This demonstrates the effectiveness of the proposed method for wideband near-field beam shaping in spatially fed arrays.

Im et al. (Contribution 10) propose a 5G mmWave glass antenna that can be printed on thick vehicle windows. The proposed design features a coplanar waveguide (CPW), a printed monopole, parasitic elements, a linearly arrayed patch director, and a grid-slotted patch reflector. The director and reflector improve bore-sight gain, enhancing the antenna's high-gain performance. Fabrication and measurements validate broadband operation from 24.1 GHz to 31.0 GHz, with a measured reflection coefficient of -33.1 dB and a peak gain of 6.2 dBi at 28 GHz. Simulation and experimental results exhibit strong correlation. The antenna maintains a 4.5 dBi bore-sight gain even with increasing glass window size. It does not require structural remodeling of the vehicle. The results confirm its suitability for 5G wireless communication.

Odiamenhi et al. (Contribution 11) explore the role of RF energy harvesting in powering IoT and 5G systems for Industry 4.0, highlighting the need for energy-efficient, maintenance-free technologies. The review focuses on challenges in miniaturization, circular polarization, and efficiency, with an emphasis on improving rectifier nonlinearity. It evaluates components like rectifiers, impedance-matching networks, and antennas, particularly in biomedical and IoT applications. Key challenges include rectifier performance, miniaturization trade-offs, and impedance matching. Recommendations include developing versatile rectifiers, advancing miniaturization techniques, optimizing impedance matching, and integrating machine learning for real-time design adjustments. The study concludes that addressing these challenges will enhance the sustainability and efficiency of future IoT and 5G systems.

Collectively, these contributions offer a comprehensive perspective on the latest advancements in antenna design and optimization, specifically for 5G, 6G, and IoT applications. They delve into the multifaceted challenges and opportunities in developing antennas that cater to the ever-expanding demands of modern wireless communication. From the innovative use of graphene in dynamic beam-steering antennas to the integration of RF energy harvesting technologies for sustainable IoT networks, the research highlights both novel solutions and critical considerations in antenna performance, efficiency, and miniaturization. These findings not only push the boundaries of current antenna capabilities but also pave the way for next-generation systems that will support increasingly complex communication networks. The methodologies presented play a pivotal role in shaping the future of wireless communication and sensing, contributing significantly to the evolution of smarter, more efficient, and versatile antenna systems for 5G, 6G, and beyond.

3. Conclusions

The journey through the diverse and impactful contributions in this collection has highlighted the breadth and depth of contemporary research in antenna design and optimization for 5G, 6G, and IoT applications. Each contribution, whether focused on novel antenna architectures, innovative optimization methods, or materials advancements, underscores the remarkable progress made in wireless communication and sensing systems. The research presented here not only addresses existing challenges but also pushes the boundaries of what is possible, laying the groundwork for future developments in the

field. Collectively, the contributions presented in this issue serve as a powerful testament to the ingenuity and dedication of researchers, each striving to advance antenna technologies in novel directions. From flexible and compact antennas for mobile applications to energy-efficient RF harvesting solutions for IoT devices, the solutions proposed here are shaping the trajectory of future wireless networks and communications. The fusion of advanced materials, miniaturization techniques, and cutting-edge computational methods signifies the vibrant and dynamic nature of antenna research, which will undoubtedly play an even more pivotal role as we move towards an interconnected world driven by 5G and beyond. As we look to the future, new opportunities emerge in enhancing antenna adaptability, improving energy efficiency, and expanding operational bandwidth to meet the demands of emerging technologies. Advancements in machine learning and AI for antenna optimization, alongside the development of sustainable materials, will continue to be at the forefront of this rapidly evolving field. The integration of these technologies will likely revolutionize how antennas function, both in terms of performance and application scope. The future promises exciting challenges and opportunities to further enhance the capabilities of antennas to meet the growing demands of global connectivity, smart cities, and autonomous systems.

A sincere acknowledgment goes to the dedicated editorial board and the supportive editorial office of MDPI's *Sensors* journal. Their consistent guidance, expertise, and tireless assistance throughout the entire publication process have been indispensable in bringing this collection to fruition. Their unwavering support has significantly contributed to the quality and success of this Special Issue, ensuring that it meets the highest standards of academic excellence. We deeply appreciate their dedication to facilitating the progress and dissemination of cutting-edge research in the field of antenna design and optimization. We are confident that readers will find these contributions both informative and thought-provoking, offering valuable insights into the rapidly advancing world of antenna technologies. As the field continues to evolve, we look forward to further collaborations and future contributions from researchers working to push the boundaries of antenna science. Together, we will continue to advance this field, shaping the future of wireless communications.

Conflicts of Interest: The author declares no conflicts of interest.

List of Contributions:

1. Jahanbakhsh Basherlou, H.; Ojaroudi Parchin, N.; See, C.H. A Dual-Polarized and Broadband Multiple-Antenna System for 5G Cellular Communications. *Sensors* **2025**, *25*, 1032. <https://doi.org/10.3390/s25041032>.
2. Hoang, H.; Nguyen, M.-H.; Pham-Xuan, V. Analysis of Near-Field Characteristics on Improved Structures of Double-Slot Antipodal Vivaldi Antenna. *Sensors* **2024**, *24*, 4986. <https://doi.org/10.3390/s24154986>.
3. Lin, X.; Mai, J.; He, H.; Zhang, Y. Dual-Polarized Dipole Antenna with Wideband Stable Radiation Patterns Using Artificial Magnetic Conductor Reflector. *Sensors* **2024**, *24*, 3911. <https://doi.org/10.3390/s24123911>.
4. Huang, X.; Zhu, S.; Liang, G. Reliability Evaluation Method for Array Antenna Considering Performance Changes. *Sensors* **2024**, *24*, 1914. <https://doi.org/10.3390/s24061914>.
5. Mohan, M.P.; Cai, H.; Alphones, A.; Karim, M.F. mmWave Zero Order Resonant Antenna with Patch-Like Radiation Fed by a Butler Matrix for Passive Beamforming. *Sensors* **2023**, *23*, 7973. <https://doi.org/10.3390/s23187973>.
6. Dmitriev, V.; de Oliveira, R.M.S.; Paiva, R.R.; Rodrigues, N.R.N.M. Multifunctional THz Graphene Antenna with 360° Continuous ϕ -Steering and θ -Control of Beam. *Sensors* **2023**, *23*, 6900. <https://doi.org/10.3390/s23156900>.

7. Farasat, M.; Thalakotuna, D.; Yang, Y.; Hu, Z.; Esselle, K. Suppression of Common-Mode Resonance in Multiband Base Station Antennas. *Sensors* **2023**, *23*, 2905. <https://doi.org/10.3390/s23062905>.
8. Ali, E.M.; Awan, W.A.; Alzaidi, M.S.; Alzahrani, A.; Elkamchouchi, D.H.; Falcone, F.; Ghoneim, S.S.M. A Shorted Stub Loaded UWB Flexible Antenna for Small IoT Devices. *Sensors* **2023**, *23*, 748. <https://doi.org/10.3390/s23020748>.
9. Prado, D.R. Near Field Models of Spatially-Fed Planar Arrays and Their Application to Multi-Frequency Direct Layout Optimization for mm-Wave 5G New Radio Indoor Network Coverage. *Sensors* **2022**, *22*, 8925. <https://doi.org/10.3390/s22228925>.
10. Im, C.; Lim, T.H.; Choo, H. Design of a mmWave Antenna Printed on a Thick Vehicle-Glass Substrate Using a Linearly Arrayed Patch Director and a Grid-Slotted Patch Reflector for High-Gain Characteristics. *Sensors* **2022**, *22*, 6187. <https://doi.org/10.3390/s22166187>.
11. Odiamenhi, M.; Jahanbakhsh Basherlou, H.; Hwang See, C.; Ojaroudi Parchin, N.; Goh, K.; Yu, H. Advancements and Challenges in Antenna Design and Rectifying Circuits for Radio Frequency Energy Harvesting. *Sensors* **2024**, *24*, 6804. <https://doi.org/10.3390/s24216804>.

References

1. Kulkarni, P. *Antennas for IoT*; Artech House: Norwood, MA, USA, 2023.
2. Ojaroudi Parchin, N. *Antenna Design for 5G and Beyond*; MDPI-Multidisciplinary Digital Publishing Institute: Basel, Switzerland, 2022.
3. Ziolkowski, R.W. Electrically Small Antenna Advances for Current 5G and Evolving 6G and Beyond Wireless Systems. In *Antenna and Array Technologies for Future Wireless Ecosystems*; IEEE: New York, NY, USA, 2022; pp. 335–391.
4. Parchin, N.O. Editorial on “Design, Analysis, and Measurement of Antennas”. *Appl. Sci.* **2023**, *13*, 10069. [CrossRef]
5. Wu, Q.; Wang, H.; Hong, W. Machine Learning-Assisted Optimization and Its Application to Antenna and Array Designs. In *Advances in Electromagnetics Empowered by Artificial Intelligence and Deep Learning*; IEEE: New York, NY, USA, 2023; pp. 371–383.
6. Hong, W.; Jiang, Z.H.; Yu, C.; Hou, D.; Wang, H.; Guo, C.; Hu, Y.; Kuai, L.; Yu, Y.; Jiang, Z.; et al. The Role of Millimeter-Wave Technologies in 5G/6G Wireless Communications. *IEEE J. Microw.* **2021**, *1*, 101–122. [CrossRef]
7. Sharawi, M.S. *Printed MIMO Antenna Engineering*; Artech House: Norwood, MA, USA, 2014.
8. Shi, D. An Intelligent Antenna Synthesis Method Based on Machine Learning. *IEEE Trans. Antennas Propag.* **2022**, *70*, 4965–4976. [CrossRef]
9. Zheng, T.-X.; Wang, H.M.; Ng, D.W.K.; Yuan, J. Multi-Antenna Covert Communications in Random Wireless Networks. *IEEE Trans. Wirel. Commun.* **2019**, *18*, 1974–1987. [CrossRef]

Disclaimer/Publisher’s Note: The statements, opinions and data contained in all publications are solely those of the individual author(s) and contributor(s) and not of MDPI and/or the editor(s). MDPI and/or the editor(s) disclaim responsibility for any injury to people or property resulting from any ideas, methods, instructions or products referred to in the content.



Article

A Dual-Polarized and Broadband Multiple-Antenna System for 5G Cellular Communications

Haleh Jahanbakhsh Basherlou ^{*}, Naser Ojaroudi Parchin ^{*} and Chan Hwang See

School of Computing, Engineering and the Built Environment, Edinburgh Napier University, Edinburgh EH10 5DT, UK; c.see@napier.ac.uk

* Correspondence: haleh.jahanbakhshbasherlou@napier.ac.uk (H.J.B.); n.ojaroudiparchin@napier.ac.uk (N.O.P.)

Abstract: This study presents a new multiple-input multiple-output (MIMO) antenna array system designed for sub-6 GHz fifth generation (5G) cellular applications. The design features eight compact trapezoid slot elements with L-shaped CPW (Coplanar Waveguide) feedlines, providing broad bandwidth and radiation/polarization diversity. The antenna elements are compact in size and function within the frequency spectrum spanning from 3.2 to 6 GHz. They have been strategically positioned at the peripheral corners of the smartphone mainboard, resulting in a compact overall footprint of 75 mm × 150 mm FR4. Within this design framework, there are four pairs of antennas, each aligned to offer both horizontal and vertical polarization options. In addition, despite the absence of decoupling structures, the adjacent elements in the array exhibit high isolation. The array demonstrates a good bandwidth of 2800 MHz, essential for 5G applications requiring high data rates and reliable connectivity, high radiation efficiency, and dual-polarized/full-coverage radiation. Furthermore, it achieves low ECC (Envelope Correlation Coefficient) and TARC (Total Active Reflection Coefficient) values, measuring better than 0.005 and –20 dB, respectively. With its compact and planar configuration, quite broad bandwidth, acceptable SAR (Specific Absorption Rate) and excellent radiation characteristics, this suggested MIMO antenna array design shows good promise for integration into 5G hand-portable devices. Furthermore, a compact phased-array millimeter-wave (mmWave) antenna with broad bandwidth is introduced as a proof of concept for higher frequency antenna integration. This design underscores the potential to support future 5G and 6G applications, enabling advanced connectivity in smartphones.

Academic Editor: Yingjie Jay Guo

Received: 31 December 2024

Revised: 21 January 2025

Accepted: 4 February 2025

Published: 9 February 2025

Citation: Jahanbakhsh Basherlou, H.; Ojaroudi Parchin, N.; See, C.H. A Dual-Polarized and Broadband Multiple-Antenna System for 5G Cellular Communications. *Sensors* **2025**, *25*, 1032. <https://doi.org/10.3390/s25041032>

Copyright: © 2025 by the authors. Licensee MDPI, Basel, Switzerland. This article is an open access article distributed under the terms and conditions of the Creative Commons Attribution (CC BY) license (<https://creativecommons.org/licenses/by/4.0/>).

1. Introduction

The continuous evolution of wireless systems has driven demand for higher data rates and improved services. As a result, 5G wireless communication has emerged to tackle the challenges posed by the limitations of the current generation's (4G) cellular networks [1,2]. It is poised that 5G technology can transform wireless connectivity by delivering a wide array of services, including enabling the IoT, enhancing mobile broadband, and offering ultra-reliable communication systems. Its ability to integrate these capabilities positions 5G a critical enabler for the next generation of connected devices and services [3]. One of the key technologies driving the advancements in 5G networks is MIMO systems. MIMO technology utilizes multiple antennas at both the transmitting and receiving ends, enhancing communication reliability and significantly increasing channel capacity. By

leveraging multiple signal paths, MIMO improves data throughput and efficiency in wireless communication systems, making it a key component in modern wireless networks. While MIMO technology has been extensively utilized in 4G LTE systems, it plays an even more pivotal role in 5G and 6G networks. By increasing the number of radiation elements, MIMO systems in 5G can achieve even higher performance levels. This makes it a highly efficient and promising solution for meeting the increasing demands of data-heavy applications [4]. In addition to its reliability and capacity benefits, MIMO technology also employs diversity schemes in antenna configurations. This involves sending the same signals with uncorrelated antennas, which helps combat fading and significantly improves the reliability of wireless links. By leveraging the benefits of MIMO technology and diversity schemes, 5G networks are poised to deliver seamless connectivity and cater to a wide array of emerging applications.

Multiple antennas in the system enable advanced techniques like MIMO, beamforming, and spatial diversity, paving the way for efficient data transmission, improved link reliability, and overall performance enhancements in 5G smartphones [5,6]. The focus on broadband capabilities is another key attribute enabling seamless connectivity across a wide frequency range [7]. In addition, by incorporating dual polarization, this antenna system allows the simultaneous transmission and reception of signals with both horizontal and vertical polarizations, significantly enhancing data throughput and mitigating potential interference issues. This capability is especially crucial in dense urban environments and areas with high network congestion, ensuring a stable and reliable connection for smartphone users [8]. As a result, 5G smartphones equipped with this technology can efficiently adapt to diverse network deployments, regulatory environments, and varying user requirements, ensuring a consistent and high-quality user experience. Moreover, printed antennas are becoming increasingly popular in cellular communications. Their compact size and simple design contribute to efficiency and ease of integration into mobile devices. Among various printed antennas, omnidirectional antennas such as monopole, slot, loop, and PIFA are predominantly employed in MIMO smartphone systems, as they offer superior omnidirectional coverage and wider bandwidth. These characteristics ensure comprehensive performance across different sides of the mainboard. In contrast, directional antennas like patch antennas are less commonly used due to their larger size and limited radiation coverage [9].

In recent years, various smartphone MIMO antenna designs have been reported to cater to the needs of sub-6 GHz cellular networks [10–35]. However, many existing smartphone antennas face challenges, such as narrow operational bandwidths, single-polarized radiators, or uniplanar designs that occupy substantial PCB space and increase system complexity. To address these challenges, we introduce a new 5G MIMO antenna featuring four-element/eight-port radiators with a CPW feeding technique, ensuring a quite broad impedance bandwidth and facilitating polarization/pattern diversity functionality. CPW-fed antennas and microwave components have gained significant popularity in wireless applications due to their appealing characteristics, including compact size, conformal shape, lightweight composition, ease of fabrication, and seamless integration. In comparison to probe/microstrip-fed antennas, CPW-fed antennas offer the advantage of achieving wide-band impedance matching effortlessly [36,37]. Moreover, the suggested design comprises four pairs of compact antennas positioned at the four edges of the smartphone's board featuring dual-polarization characteristics. Realized on an inexpensive FR-4 substrate, each element incorporates a trapezoid slot antenna complemented by an L-shaped microstrip stub. To enhance the isolation between adjacent slot antennas, the arrow-shaped strip between antennas serves as a decoupling structure. The compact antenna elements efficiently operate within the frequency range of 3.2–6 GHz, exhibiting dual-polarization functionality.

and providing full radiation coverage, ensuring comprehensive connectivity. The novelty of the proposed MIMO smartphone antenna lies in its development as a compact, wide-band, and dual-polarized antenna array designed to overcome key limitations of existing designs. Unlike most of the reported antennas with limited bandwidth, this array offers an extended frequency range of over 2800 MHz, effectively covering a broad spectrum of sub-6 GHz frequencies. In addition, its planar and compact design allows for seamless integration into a single-layer PCB, reducing system complexity. Furthermore, the array features dual-polarized radiation, enhancing coverage and performance across various device orientations. These innovations provide superior functionality, distinguishing the proposed antenna from other sub-6 GHz MIMO smartphone antenna designs.

In addition to the sub-6 GHz spectrum, future smartphones are expected to support high frequencies like mmWave (the 24–100 GHz range) [38]. Compact antennas arranged as arrays on the PCB can form linear phased arrays with high gain and directional radiation beams [39]. A new, compact phased array mmWave antenna with broad bandwidth and end-fire radiation is introduced, and its fundamental characteristics are investigated. It consists of eight loop-dipole antennas arranged linearly, enabling easy integration into smartphone systems. The properties and performance of the element, as well as the entire MIMO smartphone design and the mmWave array, are meticulously evaluated using CST software 2022 [40]. Through rigorous investigations, the capabilities and efficacy of the proposed antenna system are thoroughly examined, establishing a foundation for an advanced and efficient wireless communication solution for future smartphones.

2. Characteristics of the Dual-Polarized CPW-Fed Antenna

This section discusses the critical characteristics of the single-element antenna. The antenna schematic is depicted in Figure 1, featuring two closely positioned trapezoidal slot antennas equipped with L-shaped radiating stubs. The antenna is designed on a substrate made of 1.6 mm FR4 material. This substrate has a permittivity (also known as relative permittivity or ϵ_r) of 4.3 and a loss tangent ($\tan \delta$) of 0.023. These material properties are crucial in determining the electrical properties and overall performance of the antenna. The choice of the dielectric material influences the antenna's impedance, radiation efficiency, and bandwidth, among other factors. FR4 is a popular low-cost material commonly used in designing RF and microwave circuits and antennas. The specific dimensions and parameter values of the single and the MIMO antenna designs are outlined in Table 1.

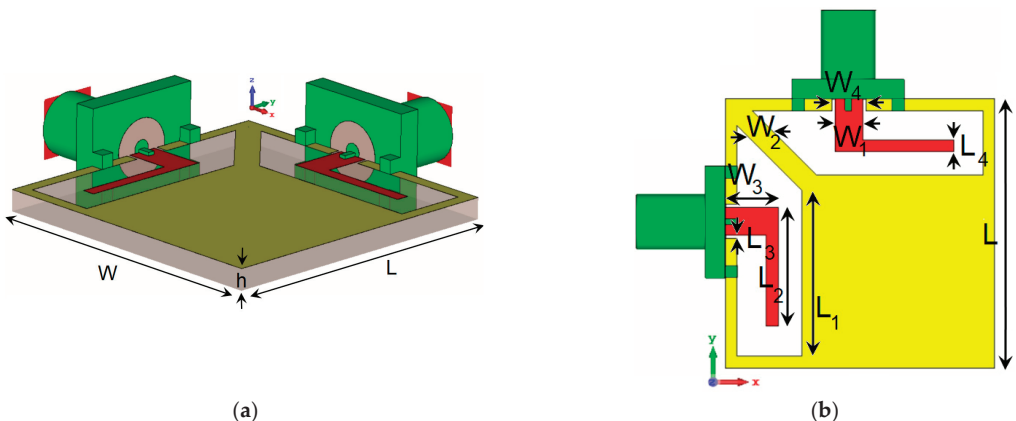
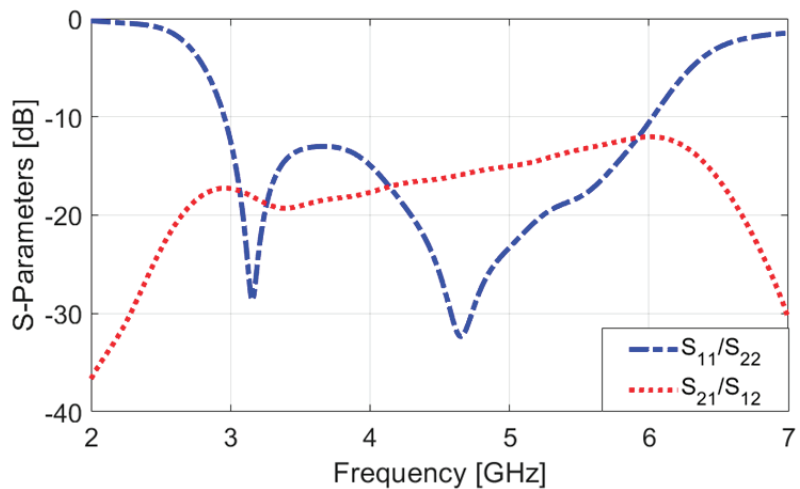


Figure 1. (a) Side and (b) front views of the introduced antenna design.

Table 1. Design values of the antenna parameters.

Param.	mm	Param.	mm
W	23	W ₂	1.8
L	23	L ₂	10.2
W _S	150	W ₃	4.5
L _S	75	L ₃	0.25
W ₁	2.4	W ₄	2.9
L ₁	14.25	L ₄	1

The S-parameters of the antenna are shown in Figure 2. Notably, the dual-polarized single antenna pair exhibits a wide operational bandwidth from 3.2 GHz to 6 GHz, with an $S_{nn} -10$ dB. Moreover, the designed CPW-fed antenna demonstrates high isolation, particularly at the center frequency. Figure 3 showcases the antenna's S-parameters (S_{11}/S_{21}) with varying L_1 , a specific parameter in the antenna design. During the simulation, L_1 is adjusted while all other parameters remain constant, as listed in Table 1. The plot demonstrates that different values of L_1 have a substantial effect on the matching and mutual coupling characteristics between the feeding ports. Notably, for $L_1 = 14.25$ mm, the antenna achieves its optimal performance, indicating the best impedance matching and mutual coupling properties among the investigated values of L_1 . As illustrated in Figure 3a, adjusting the value of L_1 has improved the antenna's impedance bandwidth, particularly at higher frequencies. Additionally, as shown in Figure 3a, when L_1 is set to 11.75, the mutual coupling between the elements at the lower frequency (3 GHz) and higher frequency (6 GHz) is approximately -16 dB and -11 dB, respectively. Increasing L_1 to 14.25 further improves the mutual coupling, reducing it to about -20 dB at 3 GHz and -13 dB at 6 GHz. These demonstrate that adjustments to the L_1 parameter can influence and reduce mutual coupling within the desired operating band.

**Figure 2.** S-parameters of the suggested antenna design.

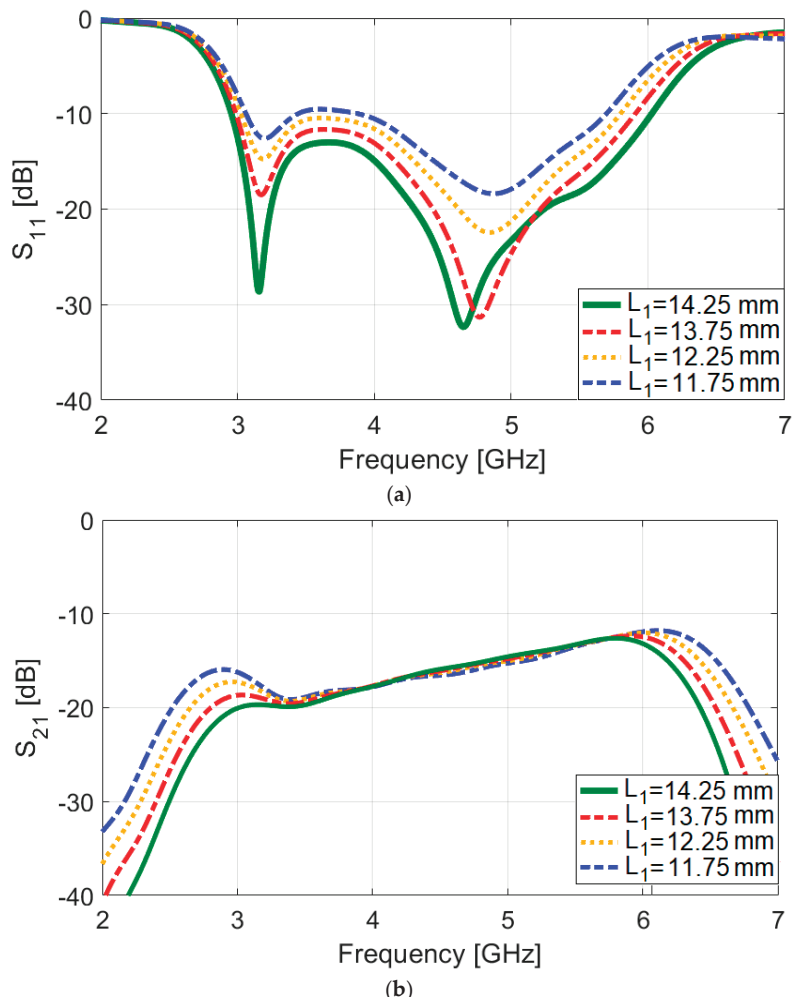


Figure 3. (a) S_{nn} and (b) S_{mn} results for different values of L_1 .

To better understand the broadband and multi-resonant behavior of the proposed antenna design, Figure 4 presents the surface current densities at 3.2 GHz, 4.7 GHz, and 5.5 GHz. The same maximum scale is applied across all plots for consistency. A detailed examination reveals that significant resonance activity occurs in several key areas as follows: the L-shaped radiation stub, as well as both the inner and outer regions of the trapezoidal slot antenna. These combined contributions from multiple components of the antenna are crucial in achieving the wide bandwidth performance observed. This synergy between the design elements highlights the antenna's effectiveness in generating broad-spectrum resonances [41,42]. Figure 5 presents the efficiency characteristics of the dual-polarized antenna, including both the radiation efficiency (R.E.) and total efficiency (T.E.). The antenna demonstrates impressive efficiency, achieving over 80% efficiencies across a frequency range from 3 to 6 GHz. This high efficiency indicates that a substantial fraction of the input power is emitted as electromagnetic radiation, making the antenna an effective and capable performer within the specified frequency band. Such efficiency levels reflect the antenna's strong potential for practical applications in modern systems.

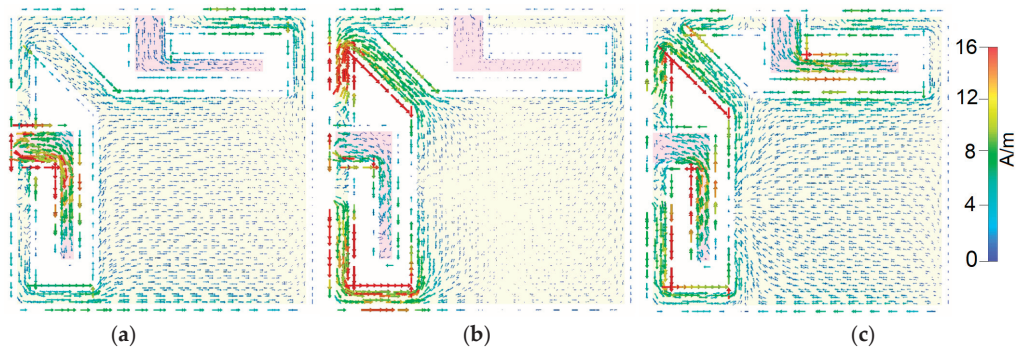


Figure 4. Current densities at (a) 3.2, (b) 4.7, and (c) 5.5 GHz.

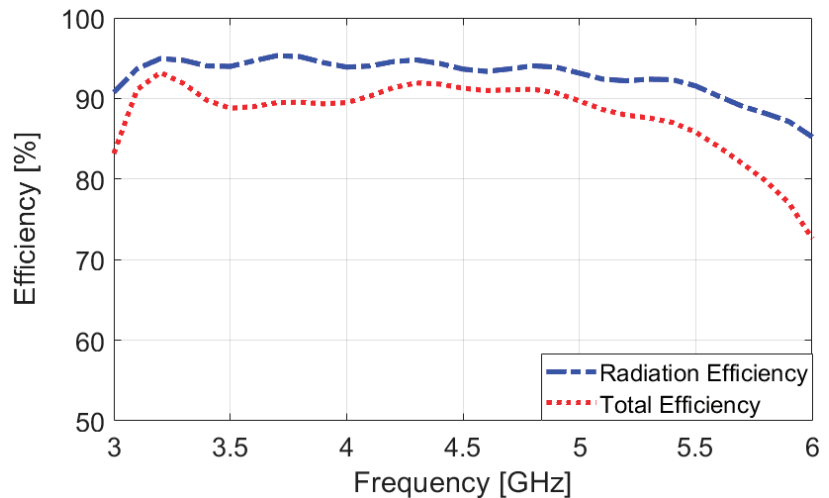


Figure 5. Efficiency results across the antenna's broad bandwidth.

In Figure 6a, the linear-scaled radiation patterns (Φ) for the various antenna ports are depicted. The figure reveals that the dual-polarized antenna exhibits identical radiation patterns from these ports. In Figure 6b, similar 2D radiation performances are clearly observed, with a 90° phase difference and polarization diversity resulting from the different arrangements of the ports. The antenna's design allows it to maintain consistent radiation characteristics across its dual-polarized nature, providing reliable and balanced performance regardless of the feeding port arrangement. Figure 7 demonstrates the 3D radiation patterns of the antenna at 3.5 and 5.5 GHz. It is evident that the antenna exhibits similar radiation patterns with distinct orthogonal polarizations. Additionally, the antenna gain, which refers to the actual power gain realized by the antenna in a specific direction, exceeds 3 dB. This indicates that the antenna achieves good directional performance and efficiently radiates electromagnetic waves when fed from both Port 1 and Port 2, offering a balanced and effective radiation pattern for diverse applications [43,44]. It is worth noting that the antenna's 3–4 dBi gain meets the typical smartphone requirements, prioritizing omnidirectional coverage over high gain. For sub-6 GHz applications requiring higher gain, directional antennas such as patch or end-fire designs (e.g., Yagi or Vivaldi) are potential options. However, their larger size and limited coverage make them less suitable for compact smartphone designs. Array antennas can also enhance gain but are more commonly

employed in higher frequency mmWave smartphone systems, where smaller element sizes are practical. This is discussed further in Section 6.

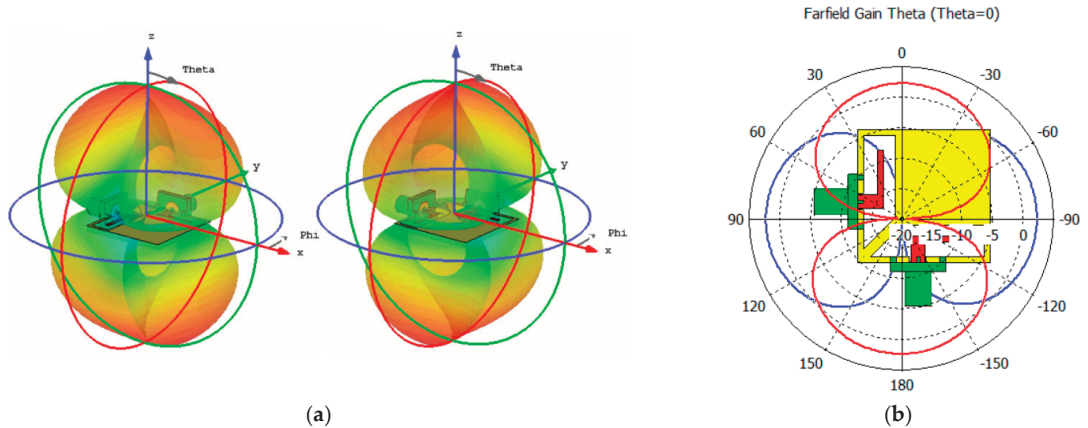


Figure 6. Linear-scaled (a) 3D and (b) 2D dual-polarized radiation patterns at 4.5 GHz.

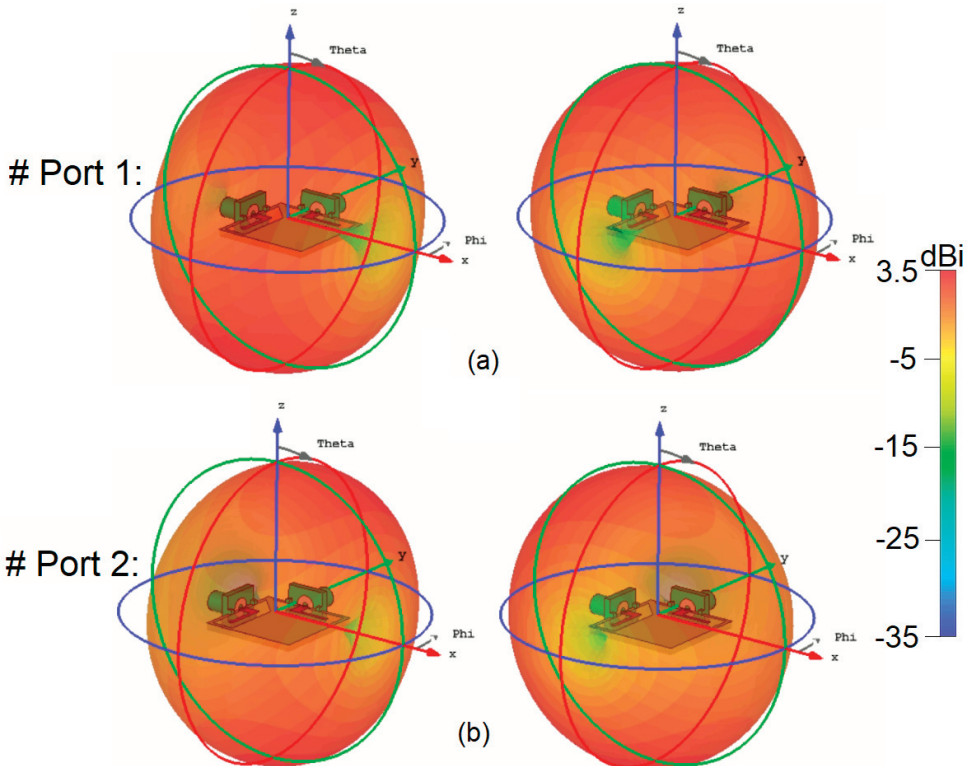


Figure 7. 3D radiation patterns of the dual-polarized antenna at (a) 3.5 and (b) 5.5 GHz.

3. Fundamental Characteristics of the Suggested MIMO Antenna

Figure 8 depicts the schematic of the investigated MIMO antenna design. The structural layout of this multi-feed antenna system is relatively simple and straightforward. The antenna's overall dimension is $75 \times 150 \text{ mm}^2$, and it includes an array of 8×8 trapezoidal

slot antennas, each paired with L-shaped stubs and CPW feeds, all positioned in close proximity to one another. It is worth mentioning that multiple similar antenna elements are positioned at PCB's edges. The utilization of the suggested antennas has several advantages. Firstly, it enhances the frequency response and matching characteristics of the antenna. Secondly, it results in symmetrical radiation patterns that cover both/bottom areas of the board. This symmetrical radiation pattern is desirable as it provides better overall coverage and performance for the MIMO system. Overall, the design aims to achieve efficient and reliable performance for smartphone applications, considering the compact size and appropriate radiation characteristics [45,46]. Figure 9 presents the S-parameters for the designed antenna array, demonstrating that the antenna elements exhibit consistent performance across the frequency range. The reflection coefficients (S_{nn}) are notably low, with values better than -15 dB within the broad operational frequency band from 3.2 to 6 GHz, indicating excellent matching. Additionally, as depicted in Figure 9b, the mutual coupling between the elements is effectively minimized, with isolation levels (S_{nm}) exceeding -13 dB. This indicates that the antenna elements maintain strong isolation from each other, contributing to improved overall performance and reduced interference. Typically, values as low as -10 dB, and in some cases even -6 dB, are considered standard and acceptable isolation levels in smartphone MIMO antenna designs. However, it is worth mentioning that to further enhance isolation between the antenna elements, various decoupling techniques such as applying additional parasitic elements, using metamaterials, introducing neutralization networks, or implementing electromagnetic bandgap (EBG) can be employed [47]. They might, however, increase the complexity and size of the antenna, which is important considering the limited space occupied by antennas in smartphone boards.

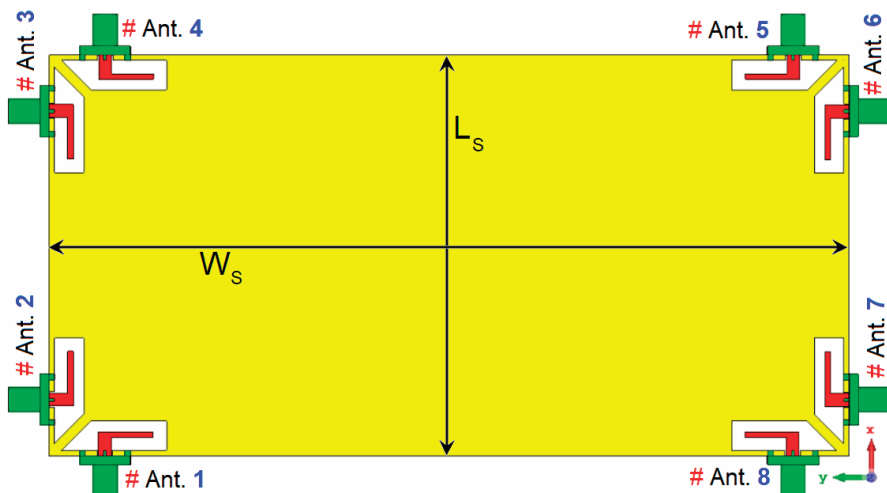


Figure 8. Schematic of the introduced MIMO antenna.

In Figure 10, the 3D radiation patterns of the multiple elements, along with their corresponding gain values at different frequencies, including 3.5 and 5.5 GHz, are displayed. The figure reveals that the 8-antenna system provides radiation with various polarizations. It is important to note that the observation of polarization diversity stems from the placement and orientation of the antenna elements, as clarified in Figure 6a. In the smartphone MIMO antenna layout, adjacent elements are positioned at 90-degree angles to each other. This polarization diversity applies to all antenna pairs in the array, enabling the system to support multiple polarization states, which is reflected in the overall radiation performance

illustrated in Figure 10. Moreover, the gain levels are sufficient to cover the different regions of the smartphone board effectively. This observation suggests that the investigated array design is robust concerning the holding positions of 5G handheld devices. Regardless of how users hold their smartphones, the antenna array maintains reliable and strong signal reception and transmission due to its multi-antenna configuration and diverse radiation patterns. This characteristic is essential in 5G smartphones to ensure consistent and stable connectivity in various usage scenarios and positions [48–50].

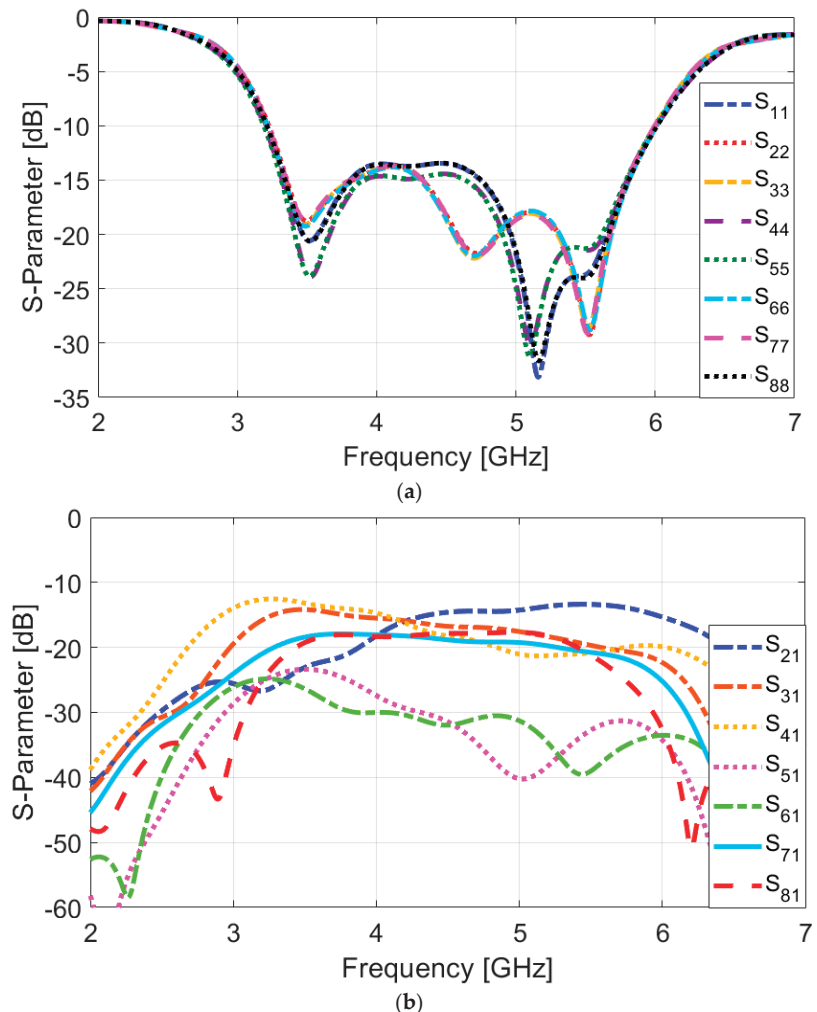


Figure 9. (a) S_{nn} and (b) S_{mn} results of the antenna elements.

In Figure 11, the efficiency characteristics of the MIMO design are represented. Figure 11a illustrates the high radiation efficiency of each antenna element, surpassing 80%. Additionally, it can be observed that these elements exhibit total efficiencies exceeding 70% over most of the operational frequency range. The achieved efficiencies are deemed quite satisfactory for smartphone operation, indicating that the introduced MIMO antenna design performs efficiently in practical scenarios. High radiation efficiency ensures that a significant portion of the input power is converted into electromagnetic waves, leading to effective signal transmission and reception. Moreover, the total efficiency considers

all losses and mismatches in the system, reflecting the effectiveness of the antenna in real-world usage [51,52].

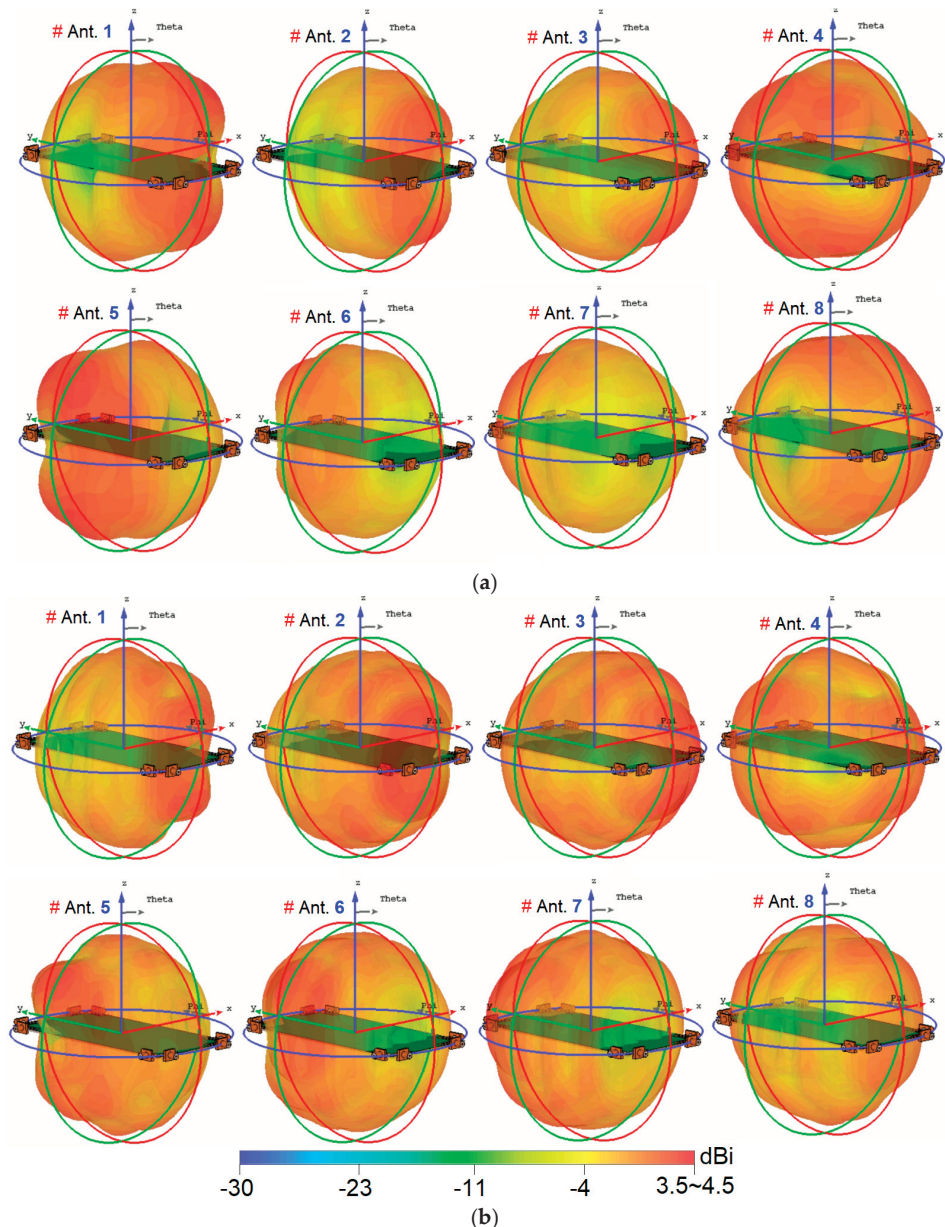


Figure 10. Three-dimensional radiation patterns at (a) 3.5 GHz and (b) 5.5 GHz.

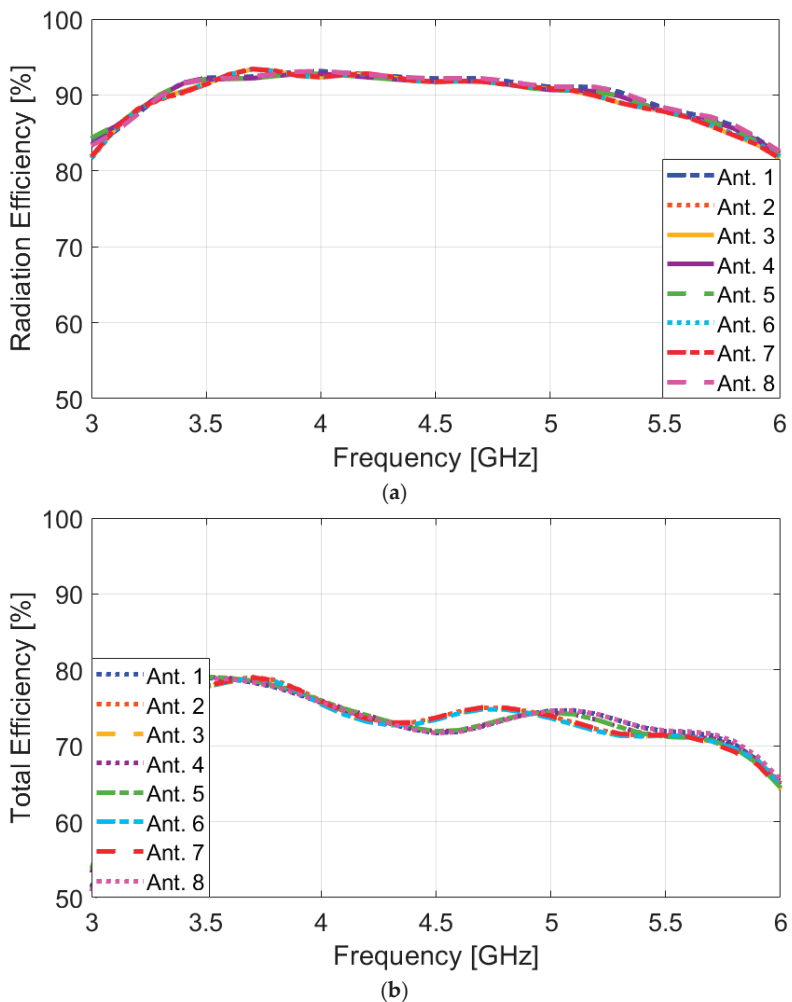


Figure 11. (a) Radiation and (b) total efficiency results of the elements over 3–6 GHz.

4. Prototyping and Measurements of the Suggested Design

In this section, the fabricated prototype sample of the MIMO antenna design is presented, along with measurement results and comparisons. Figure 12a displays a photograph of the prototype sample. The antenna is implemented on a single side of a low-cost FR4 substrate and features an 8×8 MIMO configuration. Figure 12b illustrates the feeding method used for the antenna pair. The SMA connectors' inner conductors are soldered to the CPW antennas, while the outer connectors are attached to the ground plane. This configuration ensures effective signal transmission and reception between the antenna elements and the measurement equipment, optimizing performance and reliability in the testing process.

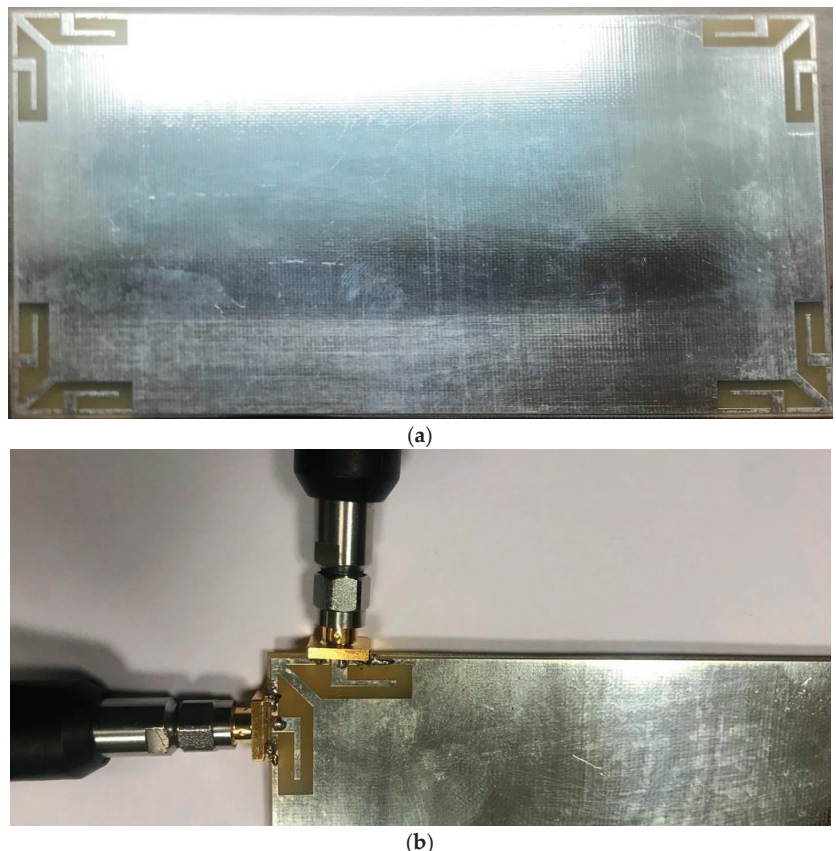


Figure 12. (a) Prototyped sample and (b) feeding method.

In the following analysis, the performance characteristics of the smartphone array design for Ports 1 and 2 are assessed and compared, due to their similar placements and the overall characteristics of the antenna pairs. Figure 13 displays the measured and simulated S-parameter results. It is evident from the figure that the measured and simulated S_{11}/S_{22} values align well, particularly in covering the necessary multi-operation bands. The antenna design demonstrates an impressive impedance bandwidth, with S_{11} values below -10 dB, spanning from 3.2 GHz to over 6 GHz. This broad bandwidth indicates that the antenna is well-suited for a variety of frequency applications. Moreover, the mutual couplings (S_{21}) between the adjacent antenna elements are measured to be less than -14 dB at the desired frequency band. This indicates that the interference between the elements is effectively minimized, ensuring the proper isolation and individual performance of each antenna in the MIMO array [53]. Figure 14 presents the 2D radiation patterns (H-plane and E-plane) of the antenna elements, both from measurements and simulations, at frequencies of 3.5 GHz and 5.5 GHz. During the measurement process, one port of the antenna was excited while the other was terminated with a $50\ \Omega$ load to ensure precise characterization. The resulting radiation patterns reveal that the prototype of the sample handset antenna demonstrates effective quasi-omnidirectional radiation performance across these resonance frequencies, indicating its suitability for applications requiring broad coverage. This means that the radiation of the antenna has been distributed relatively evenly in various directions around

the element, making it ideal for practical mobile communication scenarios where users may hold their devices in different orientations [54–56].

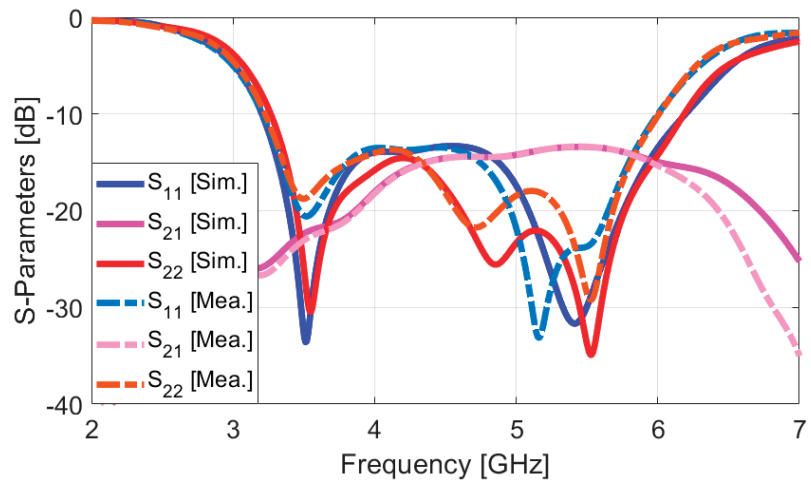


Figure 13. Measured/simulated S-parameters.

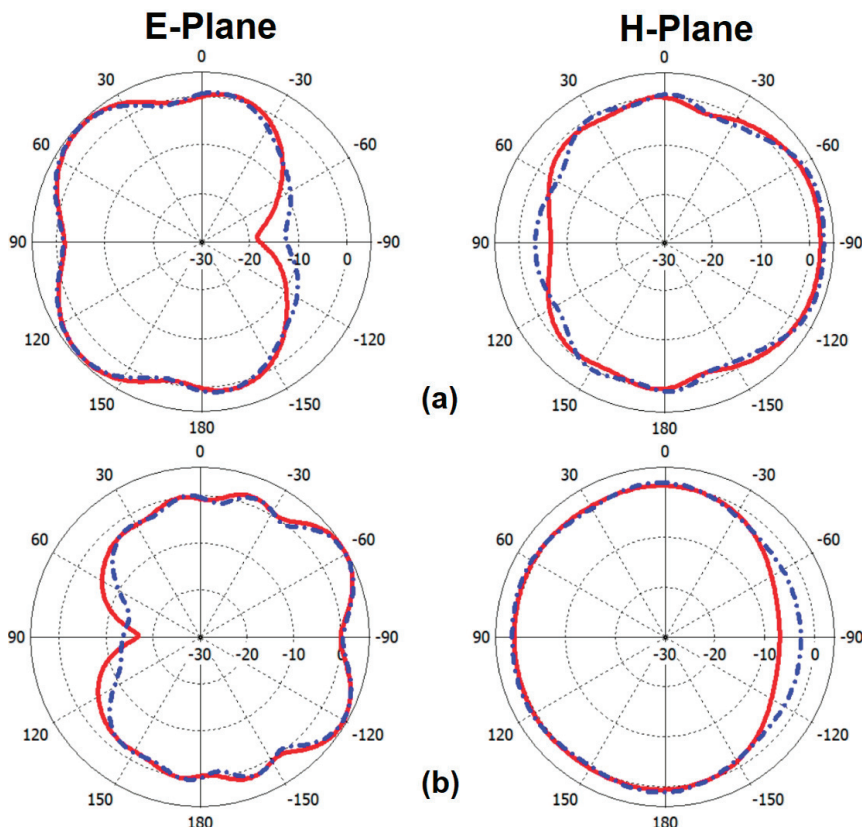


Figure 14. Measured/simulated 2D radiation patterns of the pair at (a) 3.5 GHz and (b) 5.5 GHz.

To evaluate the MIMO capability of the presented array, two important parameters, the ECC and the TARC properties, are examined to ensure that the antenna array provides optimal performance in terms of signal diversity and efficiency, which are critical for effective MIMO operation [57]. These parameters are determined using the following formula:

$$\text{ECC} = \frac{|S_{mm}^* S_{mn} + S_{nm}^* S_{nn}|^2}{\left(1 - |S_{mm}|^2 - |S_{mn}|^2\right) \left(1 - |S_{nm}|^2 - |S_{nn}|^2\right)^*} \quad (1)$$

$$\text{TARC} = -\sqrt{\frac{(S_{mm} + S_{mn})^2 + (S_{nm} + S_{nn})^2}{2}} \quad (2)$$

Figure 15a,b depicts the calculated ECC/TARC characteristics, respectively. The results show that the ECC is quite low, measuring less than 0.005, and the TARC is below -20 dB, both taken from within the target frequency band. A low ECC value indicates that the signals received or transmitted by the different elements exhibit minimal correlation. This is desirable in MIMO systems as it reduces interference and enhances the antenna array's ability to provide independent and diverse communication paths. Similarly, a low TARC value implies that the antenna array efficiently radiates the input power, resulting in little to no reflection back to the input ports. The presented ECC and TARC demonstrate that the antenna array is highly compatible with MIMO functionality, as it maintains low correlation and optimal radiation efficiency across the target band, providing reliable and effective performance for multi-antenna scenarios.

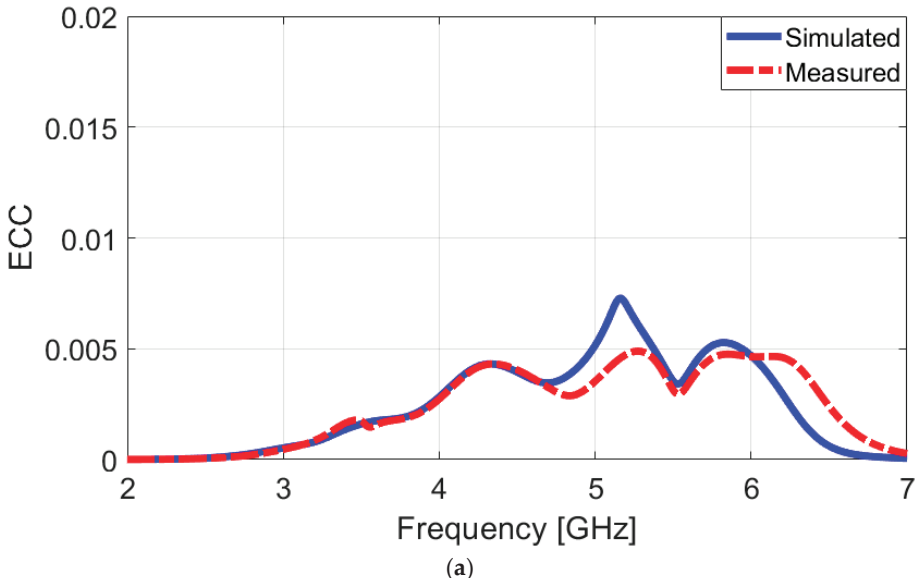


Figure 15. Cont.

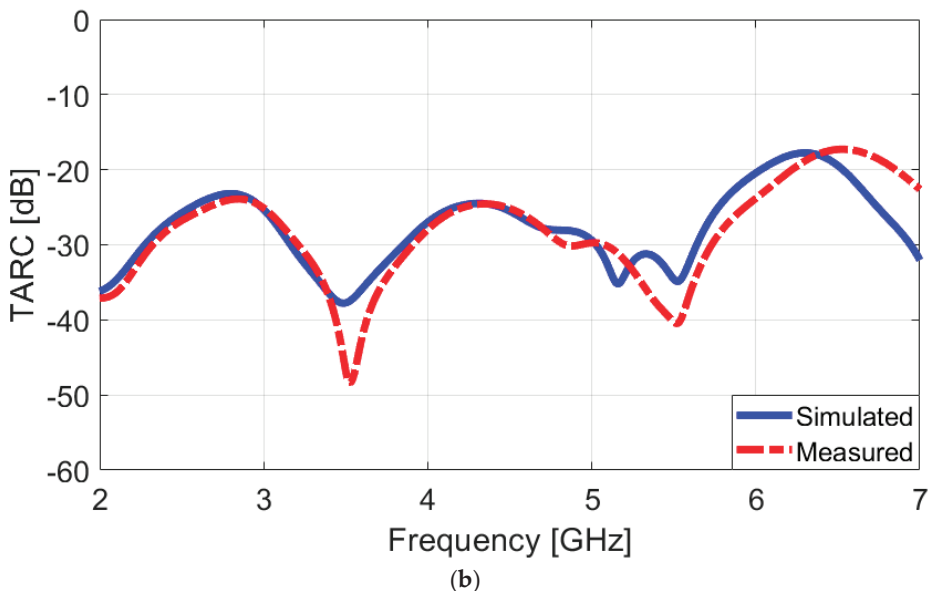


Figure 15. Measured/simulated comparison for (a) ECC and (b) TARC.

5. SAR Evaluation

The Specific Absorption Rate (SAR) measures the energy absorbed by the human body upon exposure to radio frequency (RF) electromagnetic fields. It is presented in watts per kilogram (W/kg), and it indicates the rate at which energy is absorbed by tissue. It is a critical metric for ensuring that electronic devices, particularly mobile phones, comply with safety standards to minimize potential health risks [58]. SAR values are influenced by device design, usage scenarios, and environmental conditions. Regulatory bodies like the FCC and ICNIRP have established SAR limits to protect public health, typically set at 2 W/kg, to prevent excessive energy absorption that can lead to tissue heating [59]. The SAR distribution for the selected antenna elements in talk-mode scenarios has been analyzed and is illustrated in Figure 16. This figure highlights the antenna elements with both the highest and lowest SAR levels observed in the scenarios. Specifically, Figure 16 reveals that, during talk mode, Antenna 2 exhibits the highest SAR level, whereas Antenna 7 shows the lowest SAR value. This variation is linked to the arrangement of the antenna array as follows: Antenna 2 is positioned closer to the hand phantom compared to Antenna 7. Consequently, it can be inferred that a shorter distance between the antennas and the phantom results in an elevated SAR level, while a greater distance corresponds to a lower SAR level.

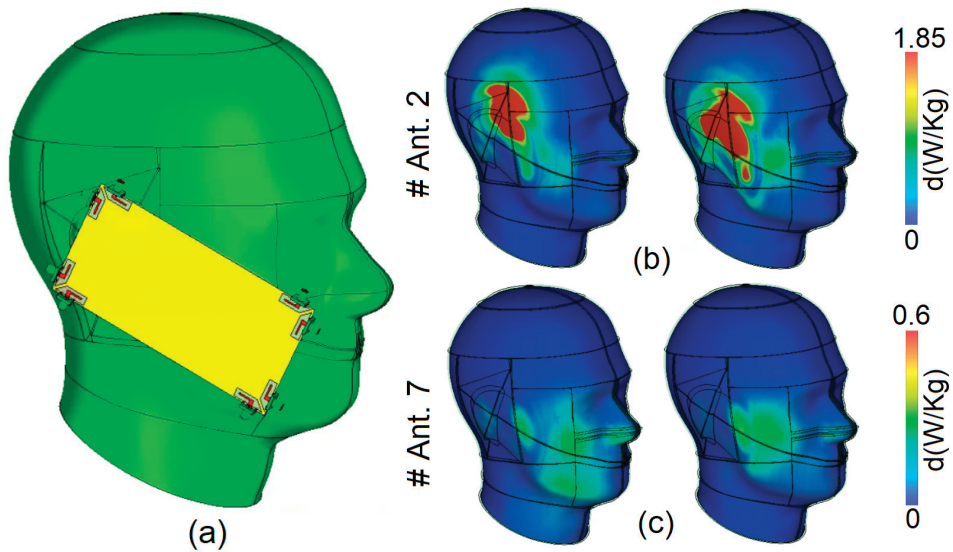


Figure 16. (a) Talk-mode and SAR analysis at (b) 3.5 GHz and (c) 5.5 GHz.

6. Comparison

Table 2 provides a performance comparison among the newly introduced MIMO array and various other designs discussed in the existing literature. Various fundamental properties, such as the employed antennas, efficiency, Envelope Correlation Coefficient (ECC), among others, are discussed for each design. The results of the comparison reveal that the developed array exhibits improved functionalities and offers several advantageous characteristics, particularly in terms of the operational frequency band. The designed array offers an impressive frequency bandwidth of more than 2800 MHz, making it capable of covering a wide range of sub-6 GHz frequencies. This broad bandwidth is crucial for supporting various 5G applications that require high data rates and reliable connectivity. An additional advantage of the presented antenna array is its planar schematic and ease of integration on a single-layer substrate. Furthermore, the presented antenna provides a diversity function in terms of both pattern and polarization characteristics, offering full coverage while supporting various sides of the board. These significant advantages position the proposed antenna as a competitive and practical solution for enabling advanced 5G communication technologies.

Table 2. Comparison table of the suggested broadband MIMO antenna.

Ref.	Antenna Type	Bandwidth (GHz)	Efficiency (%)	Size (mm ²)	Isolation (dB)	ECC	Diversity
[10]	Monopole-slot	2.55–2.65 (0.1)	50–70	136 × 68	12	<0.15	Yes
[11]	L-shaped monopole	3.4–3.6 (0.2)	50–5	136 × 68	15	<0.10	No
[12]	Self-isolated monopole	3.4–3.6 (0.2)	60–70	150 × 75	19	<0.02	No
[13]	Balanced open-slot	3.4–3.6 (0.2)	60–75	150 × 80	17	<0.05	No
[14]	Inverted-F antenna	3.4–3.6 (0.2)	-	110 × 60	19	-	Yes (Limited)
[15]	Decoupled open-slot	3.4–3.6 (0.2)	40–60	150 × 75	12	<0.40	No
[16]	Rectangular Slot	3.4–3.6 (0.2)	50–60	136 × 68	11	c < 0.05	No
[17]	H-shaped monopole	3.4–3.6 (0.2)	60–70	150 × 75	11	<0.15	No
[18]	Gap-Coupled Loop	3.4–3.6 (0.2)	40–60	150 × 75	12	<0.20	No
[19]	S-shaped monopole	3.45–3.55 (0.1)	50–68	130 × 50	15	<0.30	No
[20]	Shorted loop	3.4–3.6 (0.2)	50–78	150 × 77	10	<0.1	No
[21]	L-shaped monopole	3.4–3.6 (0.2)	40–70	145 × 75	15	<0.15	No

Table 2. Cont.

Ref.	Antenna Trype	Bandwidth (GHz)	Efficiency (%)	Size (mm ²)	Isolation (dB)	ECC	Diversity
[22]	L-shaped strip monopole	3.4–3.6 (0.2)	40–70	150 × 63	10	<0.1	No
[23]	Folded dipole	3.45–3.55 (0.1)	50–70	154 × 74	15	<0.1	No
[24]	Inverted-F antenna	3.3–3.8 (0.5)	40–75	150 × 75	13	<0.06	No
[25]	Corner-cut patch	4.4–5 (0.6)	40–80	150 × 75	10	<0.1	No
[26]	Square-loop with slot	3.4–3.8 (0.4)	55–70	150 × 75	17	<0.03	Yes
[27]	E-shaped slot	3.4–3.6 (0.2)	40–75	150 × 75	19	<0.1	No
[28]	L-shaped slot	3.6–4.7 (1.1)	85–95	150 × 75	10	<0.08	No
[29]	SCS Patch-Slot	3.5–3.7 (0.2)	50–80	150 × 75	16	<0.03	Yes
[30]	Coupled-loop monopole	3.3–5 (1.7)	40–70	150 × 75	13	<0.1	No
[31]	E-shaped slot with F-probe	3.5/4.7 (0.2/0.2)	65–70	150 × 80	18	<0.1	Yes (Limited)
[32]	PIFA	3.8/5.4 (0.1/0.1)	40–85	150 × 74	13	<0.01	No
[33]	Monopole with T-slot	3.5/5.5(0.4/1)	30–80	150 × 75	14	<0.02	No
[34]	Open-loop monopole	3.5/4.9 (0.2/0.2)	60–80	150 × 75	10	<0.1	No
[35]	Paired Slot	3.4–3.6 (0.2)	40–65	150 × 75	18	<0.1	No
This Work	Trapezoid slot with L-monopole feeding	3.2–6 (2.8)	65–80	150 × 75	13	<0.005	Yes

7. Possible Integration of a High-Frequency Antenna

Beyond the sub-6 GHz spectrum, integrating high-frequency antennas, such as mmWave phased arrays, is crucial for advancing 5G and paving the way for future 6G networks [60]. As proof of concept, a new mmWave phased array antenna has been developed for integration into shared smartphone PCBs. The configuration and design details are shown in Figure 17, featuring eight end-fire loop-dipole antenna elements that are linearly arranged on a compact board with overall dimension $W_X = 36$, L_X . The parameter values in millimeters are as follows: $W_X = 36$, $L_X = 5$, $W_{X1} = 0.4$, $L_{X1} = 3.25$, $W_{X2} = 0.15$, $L_{X2} = 1.35$, $W_{X3} = 1.5$, and $L_{X3} = 0.15$. Figure 18a shows the S-parameters of the array, demonstrating a broad impedance bandwidth of 27–44 GHz, supporting key mmWave frequencies (such as 28, 36, 38, and 45 GHz) with adequate mutual coupling (<−13 dB) between elements. Figure 18b compares the maximum gains of a single antenna element and the phased array over the operating frequency band. The individual element achieves gains of 4–5 dBi, while the phased array significantly outperforms this, with gains exceeding 12 dBi.

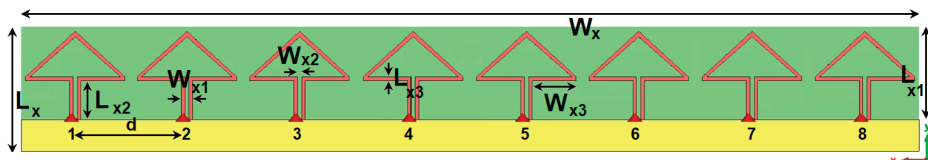


Figure 17. Schematic of the phased array.

Figure 19 further illustrates the 3D beam-steering functionality of the phased array at 30 GHz, showing robust beam-steering capabilities with end-fire radiation patterns and high gain levels. These results underscore the array's potential for enhanced directional communication and connectivity in mmWave 5G and future 6G applications. Figure 20 illustrates the potential placements of the proposed mmWave phased array within the smartphone PCB configuration. Its compact design allows for seamless integration into small areas of the board, demonstrating versatility and adaptability. Further investigation could be considered in future research to fully unlock the potential of high frequency antennas for 5G and 6G technologies.

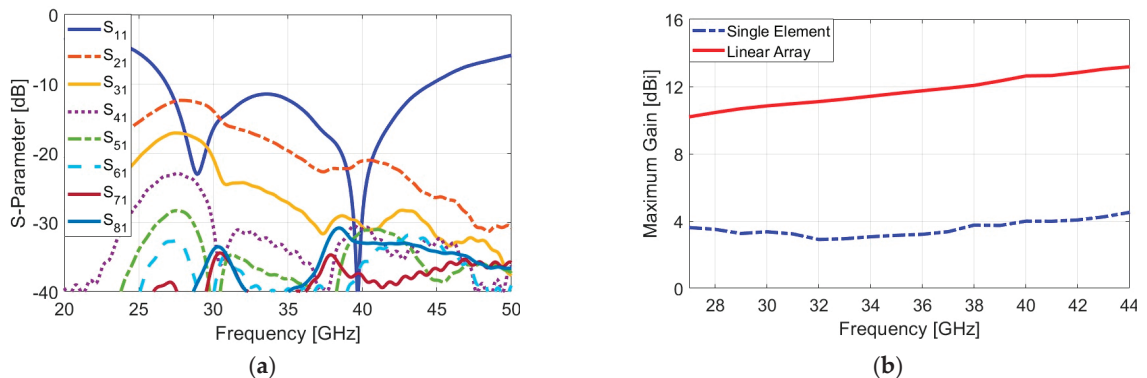


Figure 18. (a) S-parameters and (b) gain comparison of the designed phased array.

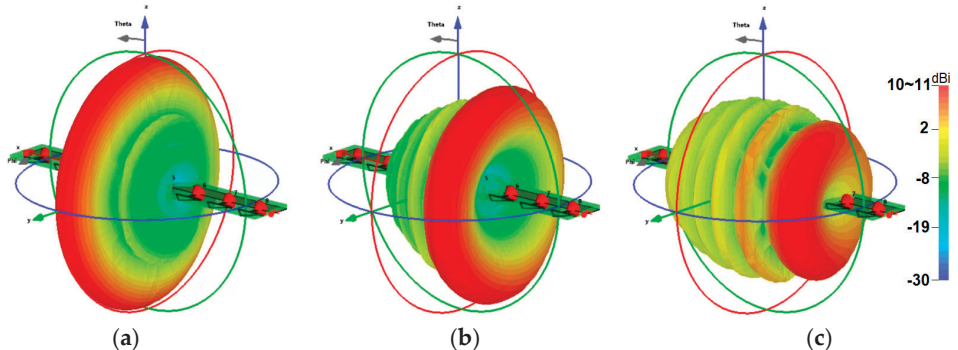


Figure 19. Beam-steering of the phased array at (a) 0, (b) 30, and (c) 60 degrees.

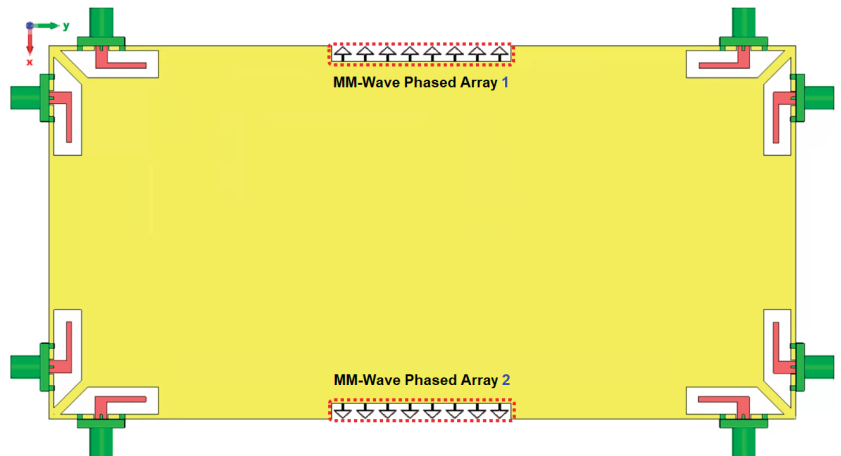


Figure 20. Possible placements of the mmWave phased array.

8. Conclusions

This paper introduces a new dual-polarized eight-antenna array design that employs CPW-fed trapezoid slot antennas with L-shaped feedings. The primary goal of this design was to achieve a wide/broad bandwidth from 3.2 to 6 GHz to accommodate the 5G spectra. The presented MIMO design is implemented on a single layer of a smartphone board,

utilizing the cost-effective and widely used FR4 substrate material, without compromising its overall performance. The results demonstrate that the proposed smartphone antenna design outperforms recently reported designs in several key aspects. It exhibits superior efficiency results, improved coverage, minimal ECC/TARC parameters, and a notably wider impedance bandwidth. Furthermore, due to its single-layer planar structure without ohmic losses, the design proves to be highly promising for future handheld platforms. The experimental results of the suggested design align well with the simulation data, affirming its reliability and validity. These compelling features make the proposed design an ideal candidate for high data-rate mobile networks in future smartphones. Overall, this dual-polarized/eight-antenna model presents a significant advancement in MIMO smartphone antenna technology, offering enhanced performance and broader applications in the rapidly evolving world of mobile communications. Moreover, a compact mmWave phased array antenna with broad bandwidth is presented, and its properties are discussed, highlighting its potential for future smartphone connectivity.

Author Contributions: Conceptualization, H.J.B., N.O.P. and C.H.S.; Methodology, H.J.B.; Software, H.J.B. and C.H.S.; Validation, H.J.B., N.O.P. and C.H.S.; Investigation, H.J.B. and N.O.P.; Writing—original draft, H.J.B.; Writing—review & editing, N.O.P. and C.H.S.; Supervision, N.O.P. and C.H.S.; Project administration, N.O.P. All authors have read and agreed to the published version of the manuscript.

Funding: This research received no external funding.

Institutional Review Board Statement: Not applicable.

Informed Consent Statement: Not applicable.

Data Availability Statement: The original contributions presented in this study are included in the article. Further inquiries can be directed to the corresponding authors.

Conflicts of Interest: The authors declare no conflicts of interest.

References

1. Osseiran, A.; Boccardi, F.; Braun, V.; Kusume, K.; Marsch, P.; Maternia, M.; Queseth, O.; Schellmann, M.; Schotten, H.; Taoka, H.; et al. Scenarios for 5G mobile and wireless communications: The vision of the METIS project. *IEEE Commun. Mag.* **2014**, *52*, 26–35. [[CrossRef](#)]
2. Yarali, A. Fifth Generation (5G) Cellular Technology. In *Public Safety Networks from LTE to 5G*; Wiley: Hoboken, NJ, USA, 2020; pp. 171–188.
3. Wang, Y.; Li, J.; Huang, L.; Jing, Y.; Georgakopoulos, A.; Demestichas, P. 5G mobile: Spectrum broadening to higher-frequency bands to support high data rates. *IEEE Veh. Technol. Mag.* **2014**, *9*, 39–46. [[CrossRef](#)]
4. Al-Yasir, Y.; Abdulkhaleq, A.M.; Parchin, N.O.; Elfergani, I.T.; Rodriguez, J.; Noras, J.M.; Abd-Alhameed, R.A.; Rayit, A.; Qahwaji, R. Green and Highly Efficient MIMO Transceiver System for 5G Heterogenous Networks. *IEEE Trans. Green Commun. Netw.* **2022**, *6*, 500–511. [[CrossRef](#)]
5. Jensen, M.; Wallace, J. A review of antennas and propagation for MIMO wireless communications. *IEEE Trans. Antennas Propag.* **2004**, *52*, 2810–2824. [[CrossRef](#)]
6. Luo, F.-L.; Zhang, C. Massive MIMO for 5G: Theory, Implementation and Prototyping. In *Signal Processing for 5G: Algorithms and Implementations*; Wiley: Hoboken, NJ, USA, 2016; pp. 189–230.
7. Sharawi, M.S. *Printed MIMO Antenna Engineering*; Artech House: Norwood, MA, USA, 2014.
8. Zhang, K.; Wang, Y.; Burokur, S.N. Generating Dual-Polarized Vortex Beam by Detour Phase: From Phase Gradient Metasurfaces to Metagratings. *IEEE Trans. Microw. Theory Tech.* **2022**, *70*, 200–209. [[CrossRef](#)]
9. Jabbar, A.; Jamshed, M.A.; Rehman, M.U. Antennas for Wireless Sensors. in Multimodal Intelligent Sensing in Modern Applications, IEEE, 2025, pp. 29–54.
10. Li, M.; Ban, Y.-L.; Xu, Z.-Q.; Wu, G.; Sim, C.-Y.-D.; Kang, K.; Yu, Z.-F. Eight-Port Orthogonally Dual-Polarized Antenna Array for 5G Smartphone Applications. *IEEE Trans. Antennas Propag.* **2016**, *64*, 3820–3830. [[CrossRef](#)]
11. Abdullah, M.; Altaf, A.; Anjum, M.R.; Arain, Z.A.; Jamali, A.A.; Alibakhshikenari, M.; Falcone, F.; Limiti, E. Future Smartphone: MIMO Antenna System for 5G Mobile Terminals. *IEEE Access* **2021**, *9*, 91593–91603. [[CrossRef](#)]

12. Zhao, A.; Ren, Z. Size Reduction of Self-Isolated MIMO Antenna System for 5G Mobile Phone Applications. *IEEE Antennas Wirel. Propag. Lett.* **2019**, *8*, 152–156. [CrossRef]
13. Li, Y.; Sim, C.; Luo, Y.; Yang, G. High-Isolation 3.5 GHz Eight-Antenna MIMO Array Using Balanced Open-Slot Antenna Element for 5G Smartphones. *IEEE Trans. Antennas Propag.* **2019**, *67*, 3820–3830. [CrossRef]
14. Zhao, X.; Yeo, S.P.; Ong, L.C. Decoupling of Inverted-F Antennas With High-Order Modes of Ground Plane for 5G Mobile MIMO Platform. *IEEE Trans. Antennas Propag.* **2018**, *66*, 4485–4495. [CrossRef]
15. Wong, K.-L.; Lu, J.Y.; Chen, L.Y.; Li, W.Y.; Ban, Y.L. 8-antenna and 16-antenna arrays using the quad-antenna linear array as a building block for the 3.5-GHz LTE MIMO operation in the smartphone. *Microw. Opt. Technol. Lett.* **2016**, *58*, 174–181. [CrossRef]
16. Abdullah, M.; Kiani, S.H.; Abdulrazak, L.F.; Iqbal, A.; Bashir, M.A.; Khan, S.; Kim, S. High-performance multiple-input multiple-output antenna system for 5G mobile terminals. *Electronics* **2016**, *8*, 1090. [CrossRef]
17. Kiani, H.S.; Altaf, A.; Anjum, M.R.; Afzidi, S.; Arain, Z.A.; Anwar, S.; Khan, S.; Alibakhshikenari, M.; Lalbakhsh, A.; Khan, M.A.; et al. MIMO Antenna System for Modern 5G Handheld Devices with Healthcare and High Rate Delivery. *Sensors* **2021**, *21*, 7415. [CrossRef]
18. Wong, K.; Tsai, C.; Lu, J. Two Asymmetrically Mirrored Gap-Coupled Loop Antennas as a Compact Building Block for Eight-Antenna MIMO Array in the Future Smartphone. *IEEE Trans. Antennas Propag.* **2017**, *65*, 1765–1778. [CrossRef]
19. Kiani, S.H.; Iqbal, A.; Wong, S.-W.; Savci, H.S.; Alibakhshikenari, M.; Dalarsson, M. Multiple Elements MIMO Antenna System With Broadband Operation for 5th Generation Smart Phones. *IEEE Access* **2022**, *10*, 38446–38457. [CrossRef]
20. Alja’afreh, S.S.; Altarawneh, B.; Alshamaileh, M.H.; E’qab, R.A.; Hussain, R.; Sharawi, M.S.; Xing, L.; Xu, Q. Ten Antenna Array Using a Small Footprint Capacitive-Coupled-Shorted Loop Antenna for 3.5 GHz 5G Smartphone Applications. *IEEE Access* **2021**, *9*, 33796–33810. [CrossRef]
21. Liu, Y.; Ren, A.; Liu, H.; Wang, H.; Sim, C.-Y.-D. Eight-Port MIMO Array Using Characteristic Mode Theory for 5G Smartphone Applications. *IEEE Access* **2019**, *7*, 45679–45692. [CrossRef]
22. Ye, Y.; Zhao, X.; Wang, J. Compact High-Isolated MIMO Antenna Module With Chip Capacitive Decoupler for 5G Mobile Terminals. *IEEE Antennas Wirel. Propag. Lett.* **2022**, *21*, 928–932. [CrossRef]
23. Zhang, H.H.; Yu, G.G.; Liu, X.Z.; Cheng, G.S.; Xu, Y.X.; Liu, Y.; Shi, G.M. Low-SAR MIMO Antenna Array Design Using Characteristic Modes for 5G Mobile Phones. *IEEE Trans. Antennas Propag.* **2022**, *70*, 3052–3057. [CrossRef]
24. Zeng, W.-F.; Chen, F.-C.; Chu, Q.-X. Bandwidth-Enhanced 5G Mobile Phone Antenna Pair With Tunable Electric Field Null. *IEEE Trans. Antennas Propag.* **2023**, *71*, 1960–1964. [CrossRef]
25. Tian, X.; Du, Z. Wideband Shared-Radiator Four-Element MIMO Antenna Module for 5G Mobile Terminals. *IEEE Trans. Antennas Propag.* **2023**, *71*, 4799–4811. [CrossRef]
26. Parchin, N.O.; Amar, A.S.I.; Darwish, M.; Moussa, K.H.; See, C.H.; Abd-Alhameed, R.A.; Alwadai, N.M.; Mohamed, H.G. Four-Element/Eight-Port MIMO Antenna System With Diversity and Desirable Radiation for Sub 6 GHz Modern 5G Smartphones. *IEEE Access* **2022**, *10*, 133037–133051. [CrossRef]
27. Abubakar, H.S.; Zhao, Z.; Wang, B.; Kiani, S.H.; Parchin, N.O.; Hakim, B. Eight-Port Modified E-Slot MIMO Antenna Array with Enhanced Isolation for 5G Mobile Phone. *Electronics* **2023**, *12*, 316. [CrossRef]
28. Wang, Z.; You, W.; Yang, M.; Nie, W.; Mu, W. Design of MIMO Antenna with Double L-Shaped Structure for 5G NR. *Symmetry* **2023**, *15*, 579. [CrossRef]
29. Parchin, N.O.; Mohamed, H.G.; Moussa, K.H.; See, C.H.; Abd-Alhameed, R.A.; Alwadai, N.M.; Amar, A.S. An efficient antenna system with improved radiation for multi-standard/multi-mode 5G cellular communications. *Sci. Rep.* **2023**, *13*, 4179.
30. Zhao, A.; Ren, Z. Wideband MIMO antenna systems based on coupled-loop antenna for 5G N77/N78/N79 applications in mobile terminals. *IEEE Access* **2019**, *7*, 93761–93771. [CrossRef]
31. Sufyan, A.; Khan, K.B.; Zhang, X.; Siddiqui, T.A.; Aziz, A. Dual-band independently tunable 8-element MIMO antenna for 5G smartphones. *Heliyon* **2024**, *10*, e25712. [CrossRef] [PubMed]
32. Kazmi, A.; Zada, M.; Islam, S.; Yoo, H. Dual-Band MIMO Prototype in the Sub-6 GHz Integrated With mm-Wave Arrays: Ensuring Beamforming and Safety Measures. *IEEE Access* **2024**, *12*, 38957–38971. [CrossRef]
33. Wei, X.; Lu, J.; Miao, Y.; Huang, J.; Chen, Z.; Liu, G. High Isolation MIMO Antenna System for 5G N77/N78/N79 Bands. *Micromachines* **2024**, *15*, 721. [CrossRef] [PubMed]
34. Huang, J.; Dong, G.; Cai, Q.; Chen, Z.; Li, L.; Liu, G. Dual-Band MIMO Antenna for 5G/WLAN Mobile Terminals. *Micromachines* **2021**, *12*, 489. [CrossRef]
35. Fang, Y.; Jia, Y.; Zhu, J.-Q.; Liu, Y.; An, J. Self-Decoupling, Shared-Aperture, Eight-Antenna MIMO Array With MIMO-SAR Reduction. *IEEE Trans. Antennas Propag.* **2024**, *72*, 1905–1910. [CrossRef]
36. Valizade, A.; Ojaroudi, M.; Ojaroudi, N. CPW-fed small slot antenna with reconfigurable circular polarization and impedance bandwidth characteristics for DCS/WiMAX applications. *Prog. Electromagn. Res. C* **2015**, *56*, 65–72.

37. Ojaroudi, N.; Ghadimi, N. Design of CPW-Fed slot antenna for MIMO system applications. *Microw. Opt. Technol. Lett.* **2014**, *56*, 1278–1281. [CrossRef]
38. Naqvi, A.H.; Lim, S. Review of Recent Phased Arrays for Millimeter-Wave Wireless Communication. *Sensors* **2018**, *18*, 3194. [CrossRef] [PubMed]
39. Parchin, N.O.; Zhang, J.; Abd-Alhameed, R.A.; Pedersen, G.F.; Zhang, S. A Planar Dual-Polarized Phased Array with Broad Bandwidth and Quasi-Endfire Radiation for 5G Mobile Handsets. *IEEE Trans. Antennas Propag.* **2021**, *69*, 6410–6419. [CrossRef]
40. CST Microwave Studio, version 2022; CST: Danvers, MA, USA, 2022.
41. Parchin, N.O.; Al-Yasir, Y.I.A.; Noras, J.M.; Abd-Alhameed, R.A. Dual-Polarized MIMO Antenna Array Design Using Miniaturized Self-Complementary Structures for 5G Smartphone Applications. In Proceedings of the 2019 13th European Conference on Antennas and Propagation (EuCAP), Krakow, Poland, 31 March–5 April 2019.
42. Parchin, N.O.; Al-Yasir, Y.; Alabdullah, A.; Basherlou, H.; Abdulkhaleq, A.; Abd-Alhameed, R.; Noras, J. 8×8 MIMO antenna system with coupled-fed elements for 5G handsets. In Proceedings of the The IET Conference on Antennas and Propagation (APC), Birmingham, UK, 11–12 November 2019.
43. Muhsin, M.Y.; Salim, A.J.; Ali, J.K. An Eight-Element MIMO Antenna system for 5G Mobile Handsets. In Proceedings of the 2021 International Symposium on Networks, Computers and Communications (ISNCC), Dubai, United Arab Emirates, 30 October–2 November 2021; pp. 1–4.
44. Shi, C.; Sun, Y. Wideband Six-Port 5G MIMO Mobile Phone Antenna. In Proceedings of the International Conference on Microwave and Millimeter Wave Technology (ICMWT), Nanjing, China, 23–26 May 2021; pp. 1–3.
45. Rao, L.; Tsai, C. 8-Loop Antenna Array in the 5 Inches Size Smartphone for 5G Communication the 3.4 GHz–3.6 GHz Band MIMO Operation. In Proceedings of the 2018 Progress in Electromagnetics Research Symposium (PIERS-Toyama), Toyama, Japan, 1–4 August 2018; pp. 1995–1999.
46. Ullah, A.; Parchin, N.O.; Abdul-Al, M.; Santos, H.M.D.; See, C.H.; Hu, Y.F.; Abd-Alhameed, R.A. Internal MIMO Antenna Design for Multi-Band Mobile Handset Applications. In Proceedings of the 2021 29th Telecommunications Forum (TELFOR), Belgrade, Serbia, 23–24 November 2021; pp. 1–4.
47. Chen, X.; Zhang, S.; Li, Q. A Review of Mutual Coupling in MIMO Systems. *IEEE Access* **2018**, *6*, 24706–24719. [CrossRef]
48. Faouri, Y.S.; Ahmad, S.; Parchin, N.O.; See, C.H.; Abd-Alhameed, R. A Novel Meander Bowtie-Shaped Antenna with Multi-Resonant and Rejection Bands for Modern 5G Communications. *Electronics* **2022**, *11*, 821. [CrossRef]
49. Ahmad, S.; Ijaz, U.; Naseer, S.; Ghaffar, A.; Qasim, M.A.; Abrar, F.; Parchin, N.O.; See, C.H.; Abd-Alhameed, R. A Jug-Shaped CPW-Fed Ultra-Wideband Printed Monopole Antenna for Wireless Communications Networks. *Appl. Sci.* **2022**, *12*, 821. [CrossRef]
50. Zhang, H.H.; Liu, X.Z.; Cheng, G.S.; Liu, Y.; Shi, G.M.; Li, K. Low-SAR Four-Antenna MIMO Array for 5G Mobile Phones Based on the Theory of Characteristic Modes of Composite PEC-Lossy Dielectric Structures. *IEEE Trans. Antennas Propag.* **2022**, *70*, 1623–1631. [CrossRef]
51. Khaleel, S.A.; Hamad, E.K.I.; Parchin, N.O.; Saleh, M.B. MTM-Inspired Graphene-Based THz MIMO Antenna Configurations Using Characteristic Mode Analysis for 6G/IoT Applications. *Electronics* **2022**, *11*, 2152. [CrossRef]
52. Abdelghany, M.A.; Ibrahim, A.A.; Mohamed, H.A.; Tammam, E. Compact Sub-6 GHz Four-Element Flexible Antenna for 5G Applications. *Electronics* **2024**, *13*, 537. [CrossRef]
53. Elabd, R.H. Low mutual coupling miniaturized dual-band quad-port MIMO antenna array using decoupling structure for 5G smartphones. *Discov. Appl. Sci.* **2024**, *6*, 189. [CrossRef]
54. Munir, M.E.; Al Harbi, A.G.; Kiani, S.H.; Marey, M.; Parchin, N.O.; Khan, J.; Mostafa, H.; Iqbal, J.; Khan, M.A.; See, C.H.; et al. A New mm-Wave Antenna Array with Wideband Characteristics for Next Generation Communication Systems. *Electronics* **2022**, *11*, 1560. [CrossRef]
55. Al-Yasir, Y.I.A.; Parchin, N.O.; Alabdullah, A.; Mshwat, W.; Ullah, A.; Abd-Alhameed, R. New Pattern Reconfigurable Circular Disk Antenna Using Two PIN Diodes for WiMax/WiFi (IEEE 802.11a) Applications. In Proceedings of the 2019 16th International Conference on Synthesis, Modeling, Analysis and Simulation Methods and Applications to Circuit Design (SMACD), Lausanne, Switzerland, 15–18 July 2019.
56. Ji, Z.; Guo, Y.; He, Y.; Zhao, L.; Huang, G.L.; Zhou, C.; Zhang, Q.; Lin, W. Low Mutual Coupling Design for 5G MIMO Antennas Using Multi-Feed Technology and Its Application on Metal-Rimmed Mobile Phones. *IEEE Access* **2021**, *9*, 151023–151036. [CrossRef]
57. Vaughan, R.G.; Andersen, J.B. Antenna diversity in mobile communication. *IEEE Trans. Veh. Technol.* **1987**, *VT-36*, 149–172.
58. Repacholi, M.H.; Grandolfo, M.; Ahlbom, A. Health issues related to the use of hand-held radiotelephones and base transmitters. *Health Phys.* **1996**, *70*, 587–593.

59. Zhang, H.H.; Yu, G.G.; Liu, Y.; Fang, Y.X.; Shi, G.; Wang, S. Design of low-SAR mobile phone antenna: Theory and applications. *IEEE Trans. Antennas Propag.* **2021**, *69*, 698–707. [CrossRef]
60. Hong, W.; Jiang, Z.H.; Yu, C.; Hou, D.; Wang, H.; Guo, C.; Hu, Y.; Kuai, L.; Yu, Y.; Jiang, Z.; et al. The Role of Millimeter-Wave Technologies in 5G/6G Wireless Communications. *IEEE J. Microw.* **2021**, *1*, 101–122. [CrossRef]

Disclaimer/Publisher’s Note: The statements, opinions and data contained in all publications are solely those of the individual author(s) and contributor(s) and not of MDPI and/or the editor(s). MDPI and/or the editor(s) disclaim responsibility for any injury to people or property resulting from any ideas, methods, instructions or products referred to in the content.



Article

Analysis of Near-Field Characteristics on Improved Structures of Double-Slot Antipodal Vivaldi Antenna

Ha Hoang ^{1,*}, Minh-Huy Nguyen ¹ and Vinh Pham-Xuan ²

¹ Department of Telecommunications Engineering, Ho Chi Minh City University of Technology—Vietnam National University, Ho Chi Minh City 700000, Vietnam

² Dassault Systèmes Deutschland GmbH, 64289 Darmstadt, Germany

* Correspondence: hahoang@hcmut.edu.vn or hmanhha@gmail.com

Abstract: A characterization of near-field impulse responses based on electromagnetic (EM) near-field data from an EM solver to explore features of the propagation process on a well-known wideband traveling wave antenna—double-slot Vivaldi antenna—is presented in this article. The intensity, propagating time and partitional response characteristics facilitate interpretation of the propagation process and impacts of the antenna partitions on the process. The EM energy flows guided, reoriented and scattered along a sequence of antennas transmitting and radiating segments were recognized. The geometric features of near-field waveform surfaces supported evaluation of the EM flow proportions and antenna directivity. Impact of the structural section on radiation was also assessed by the partitional far-field response characteristic in frequency and time domains. Supported by many complementary characteristics in the analyses, inherent features of the propagation process were emphasized and false flags were minimized. By this approach, the simplification for the near-field propagation model contributed to enhancing the insight of near-field propagation processes on the double-slot antipodal Vivaldi antennas and enabled optimizing the antenna structure details.

Keywords: electromagnetic propagation; near-field analysis; near-field characteristic; near-field to far-field transformation; impulse response; structural effect; Vivaldi antenna

Citation: Hoang, H.; Nguyen, M.-H.; Pham-Xuan, V. Analysis of Near-Field Characteristics on Improved Structures of Double-Slot Antipodal Vivaldi Antenna. *Sensors* **2024**, *24*, 4986. <https://doi.org/10.3390/s24154986>

Academic Editors: Shah Nawaz
Burokur and Naser Ojaroudi Parchin

Received: 3 June 2024

Revised: 9 July 2024

Accepted: 26 July 2024

Published: 1 August 2024



Copyright: © 2024 by the authors. Licensee MDPI, Basel, Switzerland. This article is an open access article distributed under the terms and conditions of the Creative Commons Attribution (CC BY) license (<https://creativecommons.org/licenses/by/4.0/>).

1. Introduction

The first Gibson's Vivaldi planar antenna [1] introduced in 1979 is a directional antenna with its main EM radiation beam following the antenna's guiding structure. This results in a high gain over a wide bandwidth. In 1988, Gazit proposed an antipodal Vivaldi structure based on a direct parallel excitation strip line [2] instead of a stub slot-based excitation structure to expand in lower frequency band for the antipodal kind of Vivaldis. Later research has proposed a variety of improved structures to enhance antenna performances [3–7], such as changing the shape of the antennas, adding slots or etched shapes on the wings. Such modifications may aid in enhancing the directivity of the main beam and/or to broaden the radiation bandwidth. These improvements can be achieved by leveraging the resonance phenomenon or higher-order scattering of EM propagation flows. Moreover, integrating dielectric or metal structured parts/components along the Vivaldi slot or at the radiating aperture can effectively trap or couple EM energy from the Vivaldi wings [8–11]. This strategy enables the redirection of EM flows at the radiating aperture into free space, enhancing the overall performance of the antenna system. The double-slot Vivaldi structures were proposed in [12–15], where the distribution of the two slots forms a core section between the two lateral Vivaldi wings. The parallelism of the two slots and the EM field guiding of the core facilitate the radiation of EM flows, resulting in flattening wavefronts and consequently better directivity.

Based on conventional characteristics, the impacts of an improved structure on antenna performances can be explored through a simple comparison between overall antenna

characteristics with and without the improved structure. The characteristics can be estimated or computed using simulation or measurement. However, creating or optimizing an improved structure needs many deep factors, such as diversity and depth of knowledge about relevant structures and materials; the operating mechanisms; characteristics and equivalent models, in the phase of creation, selection or synthesis of a design process, and sensitivity and effectiveness of optimization algorithms in optimization phase. Each overall antenna characteristic is a superposition of the contributions from all parts of the antenna. It is difficult to interpret the correspondence between a structural detail and a response detail to satisfy requirements for the above deep factors by solely inspecting overall characteristics.

Near-field propagation characteristics analysis can be instrumental in strengthening conventional analysis methods [16,17] as it interprets the impact of locally modified structures such as added slots to near-field responses at their local spaces. Evaluation of antennas can be performed using simulation where an EM solver solves Maxwell's equations applied to a given geometry. There are different types of EM solver such as time-domain solvers (e.g., Finite-Difference Time-Domain or Finite-Integration Technique) and frequency-domain solvers (e.g., Finite Element Method, Method of Moment). Once an EM solver is provided with a proper model and an appropriate setup, the result of the simulation will accurately describe the response of a given geometry. A wide range of structural sizes and customizability of structure modeling demonstrates generality in applications of EM solvers. Informational wealth in near-field data from EM solvers can resolve the shortages mentioned above. However, the bulk of raw near-field data has been challenging for observations and analyses of near-field features.

This work is a development from previous research in [16,17]. Based on the commercial SIMULIA CST Studio Suite® EM solver [18], the double-slot antipodal Vivaldis with or without improved structures were simulated in the time domain with an impulse excitation to generate near-field data for the next post-processes. Characterization was based on the first-cluster propagation analysis, focusing on the magnitude and time of arrival (ToA) of EM field and Poynting vectors. This facilitated both observations and quantitative analyses of the near-field propagation features from both overall and detail perspectives. The analyses unveiled the concentrations and directions of the EM energy flows in different regions of the antennas. Qualitative and quantitative analyses were conducted on characteristics such as intensity, energy flux, wavefront shape and wavefront flatness in specific regions of interest. The propagation features of the improved structures were measured by comparing the characteristics of the different geometries in the improvement process. These impacts were evaluated, serving as the targets for design optimization. Furthermore, the near-field responses within the partitions of antenna structures were characterized into partitional far-field gains in the frequency domain and partitional far-field impulse responses in the time domain. These near-field and locally reflected characteristics were employed as criteria for the analyses, evaluations and optimizations of three improved versions of double-slot antipodal Vivaldi antennas. These improvements included adjustments such as offsetting the excitation strip line, lengthening the core between Vivaldi double-slots and etching comb slots on lateral wings.

The contributions of this work can be summarized as follows:

- Characterization of near-field propagation using impulse response analysis. New characteristics are proposed, including the first-cluster magnitude and ToA of the Poynting vector, and the flatness of the wavefronts.
- Proposal of the partitional near-field to far-field transformation in time and frequency domains. The transformation is applied to sub-structures of the geometry to analyze the impact of individual sub-structures and local near-field propagation features on the overall performance of the entire geometry.
- Application of all these proposed characteristics and the conventional characteristics to the design of three improved versions of double-slot Vivaldis, including Vivaldi with strip line offset, Vivaldi with adjusted core length and Vivaldi with lateral comb slots.

Diversity, complementarity and granularity in the analyzability of the characteristics emphasize the intrinsic nature of the near-field propagation process and reduce false possibilities in the analysis. These contribute to enhance the insight of near-field propagation processes on this kind of traveling wave antenna.

The Section 2 presents definitions of near-field propagation characteristics and partitional near-field to far-field characteristics and a comparison with conventional overall characteristics. Section 3 presents the analyses of near-field characteristics on a structure with excitation strip line offset. The analyses of core length impacts on near-field propagation are presented in Section 4. In Section 5, the effectiveness of the comb slots on the lateral wings is demonstrated. Finally, Section 6 concludes the article.

2. Near-Field Propagation Characteristics vs. Conventional Overall Characteristics

The near-field propagation features and local impacts on far-field features were characterized using simulated near-field data extracted from the EM solver. These characteristics can be divided into three groups, including characteristics of EM intensity and energy flow distribution, ToA characteristics and partitional near-field to far-field characteristics.

In this section, the characterization was implemented on a double-slot antipodal Vivaldi antenna modified from [14], as shown in Figure 1. This structure was used as a reference, and its analysis results were compared to those obtained from subsequent analyses of the improved structures. A Gaussian signal with a 0–20 GHz bandwidth was applied simultaneously to two waveguide ports located at the two strip lines' ends. The signal spectrum of the excitation source signal is shown in Figure 2a,b.

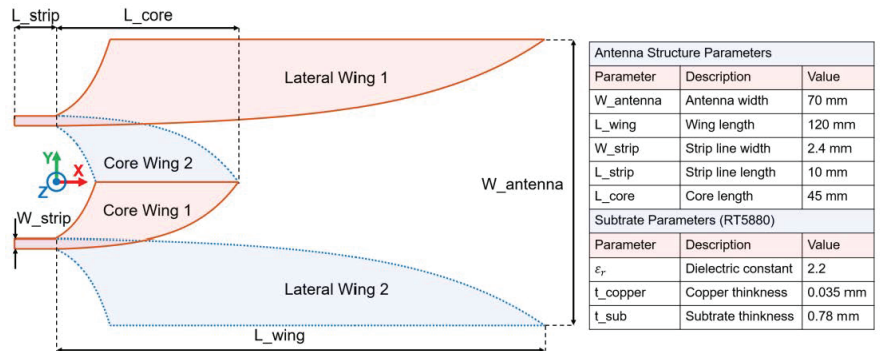


Figure 1. Reference structure and parameters.

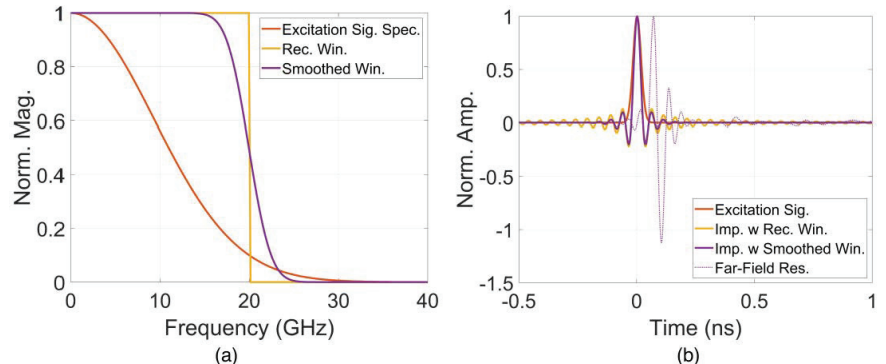


Figure 2. (a) Spectrum and (b) time signal of excitation, impulses and far-field response.

Although the excitation signal exhibits a Gaussian distribution in the frequency spectrum, conventional characteristics such as S11 or gain were assessed using uniform distribution within the 0–20 GHz band. Therefore, to facilitate a comparative analysis of these characteristics, impulse response analyses were also applied within this frequency range. The impulses and responses were processed by the method mentioned in [16,17] using the rectangular and smoothing windows as shown in Figure 2a. The corresponding time impulses and a time response example in far-field are presented in Figure 2b. Due to the prolonged time impulse associated with the rectangular window in the time domain, which complicates observations, the impulse response corresponding to a smooth window was employed instead.

2.1. Electromagnetic Intensity and Energy Flow Distribution

The first near-field characteristic, representing the intensity distribution of E and H fields on a selected region of the antenna, was calculated based on the maximum magnitude of E and H field vectors within the analysis space over time during impulse response analysis. The magnitudes of E and H fields were normalized relative to their respective maximum value at the excitation ports. Figure 3 illustrates the maximum magnitude distribution of the E and H field vectors in the middle substrate layer of the reference antenna. As shown in the figure, this characteristic highlights critical regions within the antenna structure where high intensity field flows occur.

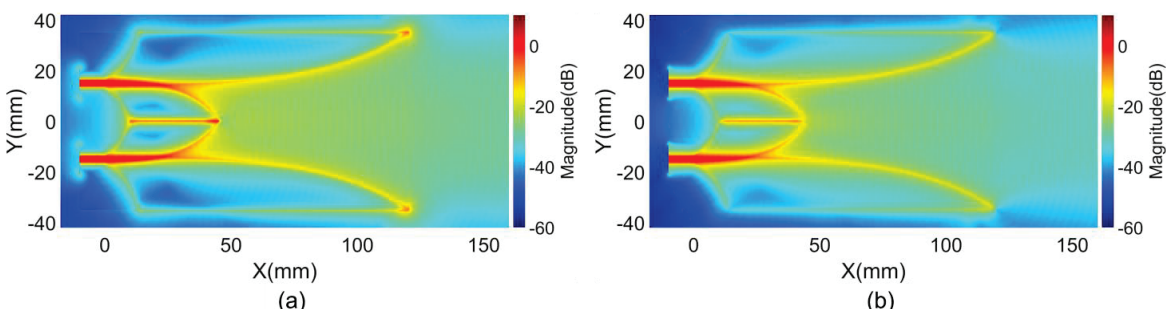


Figure 3. Maximum magnitudes of (a) E field and (b) H field vectors on reference structure.

The characteristics of the first clusters magnitudes of the E and H field vectors indicate the distribution of these magnitudes within antenna space. These characteristics, presented in Figure 4, show the distribution in the middle substrate layer. Since first clusters typically propagate along the shortest paths, they carry the maximum energy. Consequently, the distribution of the first clusters magnitudes in Figure 4 closely resembles the maximum magnitude distribution shown in Figure 3, except in regions where light-of-sight paths or shortest paths do not support efficient EM transmission. In these areas, the energy of the arriving EM flows from different directions becomes more dominant.

To supplement the E and H field magnitude characteristics, the magnitude and direction characteristics of the first clusters of Poynting vectors were evaluated and are illustrated in Figure 5. These characteristics demonstrate the distributions of both the strength and direction of energy flows within various regions of the antenna.

The distribution of the magnitude and direction of the E, H fields and Poynting vectors reveals crucial areas within antenna structures that play significant roles in the transmission of EM energy. By observing and conducting enhanced analyses based on these characteristics, it is possible to discern not only EM propagation features such as direction, intensity and the concentration level of EM energy on guiding and orienting structures, but also the impacts of sub-structures of the antenna on EM propagation and scattering.

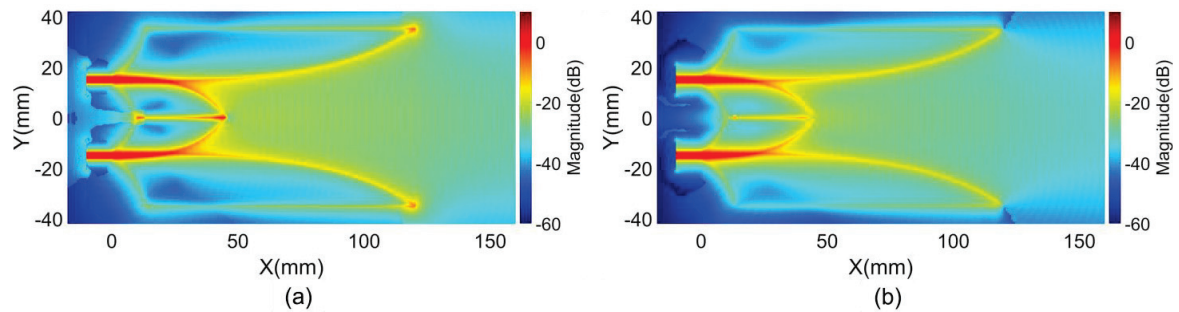


Figure 4. First clusters magnitudes of (a) E field and (b) H field vectors on reference structure.

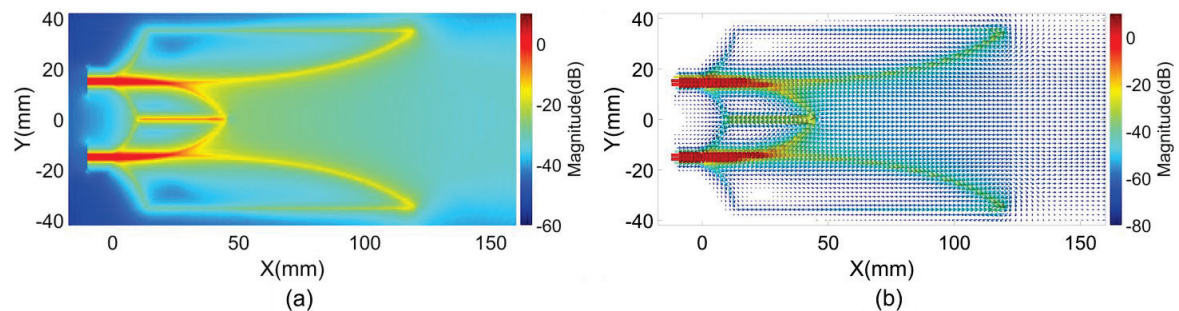


Figure 5. First clusters (a) magnitudes and (b) directions and magnitudes of Poynting vectors on reference structure.

2.2. Time of Arrivals

In impulse response analysis, the ToA of the first clusters is a crucial characteristic for qualitatively analyzing the features of a propagation process. When ToAs at adjacent positions are represented as a contour curve or surface, this delineates a wavefront. Observing contour curves of adjacent ToAs from or around a source allow the identification of energy spreading properties. The impact of objects within the propagation environment, which cause aberrations in energy flows, can also be detected. Characterizing the geometries of these contour curves or surfaces enables the measurement of local or overall propagation features.

In this work, ToAs were characterized based on the first clusters of E and H field vectors and Poynting vectors. The results at the middle substrate layer of the reference structure are presented in Figure 6. The figure reveals the properties of the energy spreading from the excitation sources and the impacts of the Vivaldi wings and core on the orientation of energy flows. The flatness of the wavefronts can be quantified by the radius of a circle fitted to a wavefront at the radiating antenna aperture, as illustrated in Figure 6. This flatness serves as a near-field characteristic to measure the directivity of the radiating field from the antenna.

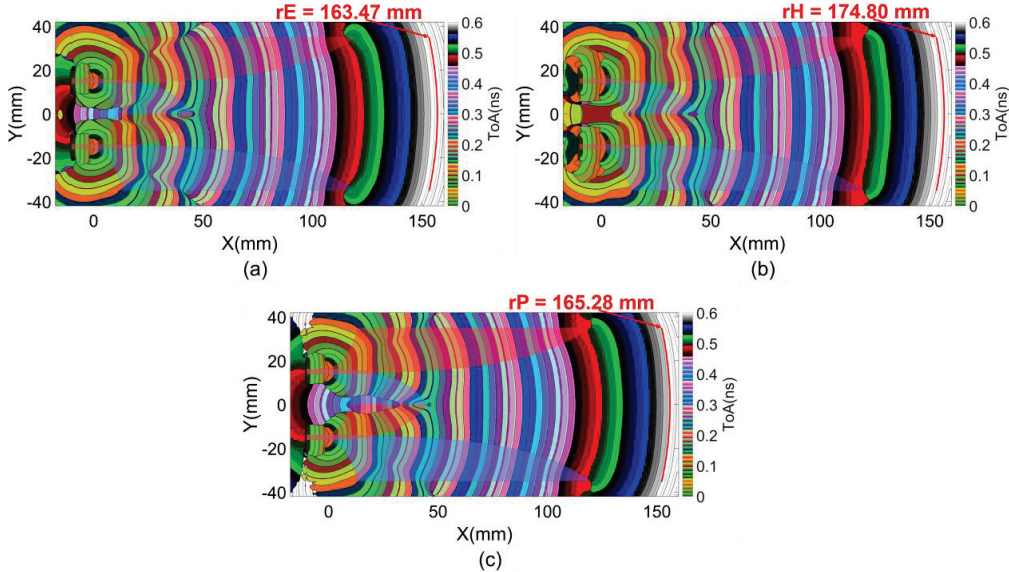


Figure 6. ToAs of first clusters of (a) E field, (b) H field and (c) Poynting vectors on referent structure.

2.3. Structural Partition for Near-Field to Far-Field Transformation

According to Huygen's equivalence surface principle, the scattered EM field outside an actual source is equal to an EM field produced by equivalent electric and magnetic current sources on an imaginary surface surrounding the sources [19,20]. It is important to notice that this volume is imaginary and contains only equivalent current sources on its surface, with no fields inside, meaning $\mathbf{E}_I = \mathbf{0}$ and $\mathbf{H}_I = \mathbf{0}$. This principle was applied to transform near-field to far-field based on simulated near-field data extracted on an equivalent surface, denoted as \mathbf{E}_S and \mathbf{H}_S . The equivalent electric and magnetic currents, \mathbf{J}_S and \mathbf{M}_S , are required to fulfil the boundary conditions

$$\mathbf{J}_S = \hat{\mathbf{n}} \times (\mathbf{H}_S - \mathbf{H}_I) = \hat{\mathbf{n}} \times \mathbf{H}_S, \quad (1)$$

$$\mathbf{M}_S = -\hat{\mathbf{n}} \times (\mathbf{E}_S - \mathbf{E}_I) = -\hat{\mathbf{n}} \times \mathbf{E}_S. \quad (2)$$

The magnetic potential vector is related to the equivalent electric currents as

$$\mathbf{A} = \frac{\mu}{4\pi} \iint_S \mathbf{J}_S(\mathbf{r}') \frac{e^{-jkR}}{R} dS', \quad (3)$$

while the electric potential vector is given in terms of the equivalent magnetic current

$$\mathbf{F} = \frac{\varepsilon}{4\pi} \iint_S \mathbf{M}_S(\mathbf{r}') \frac{e^{-jkR}}{R} dS', \quad (4)$$

where R is the distance from point \mathbf{r}' on the integral surface to the far-field observation point.

Based on the equations representing the relationships between electric, magnetic fields and potentials, and approximations in the far-field region [20], the total electric far-field \mathbf{E} and the total magnetic far-field \mathbf{H} can be written as

$$\mathbf{E} = \mathbf{E}_A + \mathbf{E}_F \quad (5)$$

$$\mathbf{H} = \mathbf{H}_A + \mathbf{H}_F, \quad (6)$$

where the subscripts A and F indicate the component fields due to the \mathbf{A} and \mathbf{F} potentials, respectively. These component fields are expressed by

$$\mathbf{E}_A \approx -j\omega\mathbf{A}, \quad \mathbf{E}_F \approx j\omega\eta\hat{\mathbf{r}} \times \mathbf{F} \quad (7)$$

$$\mathbf{H}_A \approx j\frac{\omega}{\eta}\hat{\mathbf{r}} \times \mathbf{A}, \quad \mathbf{H}_F \approx -j\omega\mathbf{F}. \quad (8)$$

Partitioning the simulated volume into sub-volumes allows the calculation of the far-field response on a surface that covers each corresponding sub-volume. By selecting a sub-volume to exclusively cover the analyzed structural object, the far-field characteristic calculated based on its surface can represent the partitioned response of the object.

In this study, specific sub-volumes of the reference antenna were chosen, comprising the core section, the lateral wings section, the combination of core and wings sections and the entire structure, as illustrated in the Figure 7. Additionally, the boundaries of these sub-volumes were also defined based on subsections of the wings, as detailed in Section 5. The boundary of each section was selected to encompass and enclose the two copper planar layers of the structure.

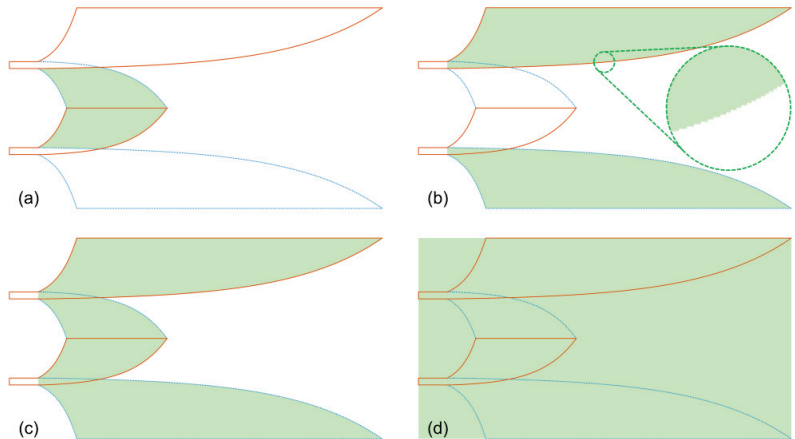


Figure 7. Structural sub-volumes for near-field to far-field transformation: (a) core section, (b) wings section, (c) wings & core and (d) whole structure.

The electric field at a point located 10 m from the antenna origin in the main radiating direction was derived from the near-field response using an impulse bandwidth ranging from 0 to 20 GHz. This transformation was conducted across different structural sections. Additionally, realized gain was characterized for these structural sections within the same frequency band. The characteristics of gains in the frequency domain and electric far-field impulse responses in the time domain are shown in Figure 8. Moreover, the simulated gain of the entire simulation space, as characterized by CST, was included in the figure to validate the calculated characteristics. This validation was achieved by comparing CST gain with the gain calculated in the case of the entire structure.

The contribution of each structural partition to the antenna gain in the main radiating direction and the far-field response at a point in this direction is expressed by these characteristics. The contribution to energy transmission can be evaluated through derivatives such as average gain and total energy of the time response. ToAs of far-field propagation can be also determined from the time responses. For convenience in comparison with the time of the impulse at the excitation ports, the propagation time in free space corresponding to the 10 m distance from the antenna origin to the far-field sampling point was subtracted from the far-field time response.

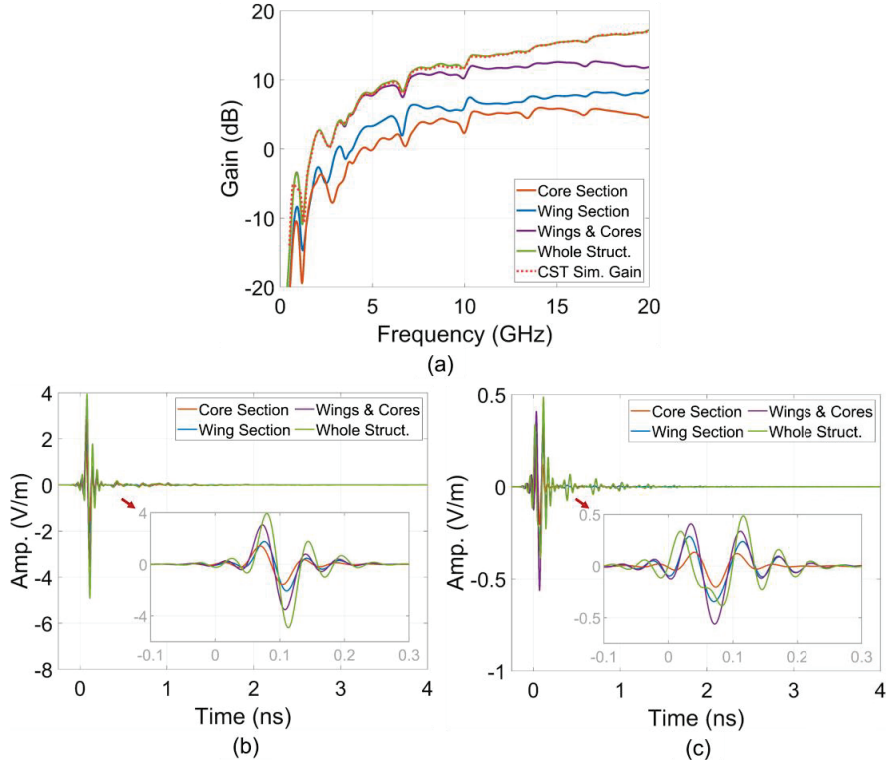


Figure 8. Structural partition (a) gains, (b) E-phi and (c) E-theta far-field impulse responses.

2.4. Conventional Overall Characteristics

Typical overall antenna characteristics include S11, gain and far-field vectors. These characteristics provide insights into the overall responses of the entire analyzed structure. S11 represents the reflections from all regions within the structure back to the source. However, S11 only provides magnitude and phase information, and lacks spatial information, making it insufficient for analyzing propagation in 2D and 3D practical structures. Gain and far-field vectors of an antenna are the comprehensive far-field characteristics that describe the magnitude, intensity, phase and vector direction of the entire antenna's radiation field in various directions. These characteristics are derived from near-field data through simulation. To conduct near-field analyses from a set of far-field vectors data in different directions, an inverse transform from far-field to near-field is required. However, losses of precisely spatial information in the transformation; and effects of obstacles and/or predominance of higher-order scattering in the analyzed structures significantly impact accuracy and reliability of this solution.

3. Analysis of Near-Field Characteristics on Structure With Strip Line Offset

The first improvement on the reference structure was introduced within the excitation strip line, where the EM field reaches its peak intensity and concentration. The propagation is directed along the flux of the EM flows originating from the waveguide excitation ports and is guided by the strip line. Particularly at the start of the Vivaldi structure, as illustrated in the magnified Figure 9a, there is asymmetric expansion and shrinking of the width between the top and bottom wings relative to the width of the parallel strips. In the reference structure, along the main Vivaldi curve, only a small width shrinking occurs at the first segment of the main Vivaldi edge. To amplify this effect, an offset d_0 in wing width

was introduced immediately after the strip, as shown in Figure 9b [21], to achieve a more substantial narrowing. This modification significantly changes the near-field EM flows and their responses in the far-field region. The outcomes of the near-field wavefront analyses conduct on the structure, and their structural effects on the far-field region, are presented in this section.

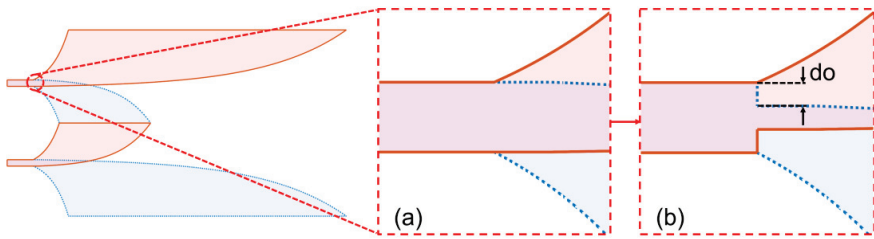


Figure 9. Zoom in structure (a) without and (b) with strip line offset.

3.1. Near-Field Intensity and Wavefront Analysis

The magnitude of the first clusters and their ToA characteristics of Poynting vectors on the copper bottom layer inside the substrate of the reference structures are depicted in Figure 10a,b. These figures illustrate the concentration of parallel EM flows in the $+x$ direction within the region guided by the strip. The expansion of the copper wing in the $-y$ direction reorients a portion of EM flows spreading laterally to the wing. The small narrowing of the edge at $X > 2$ mm, $Y \approx 16$ mm is also evidenced by an increase in the magnitude along the edge.

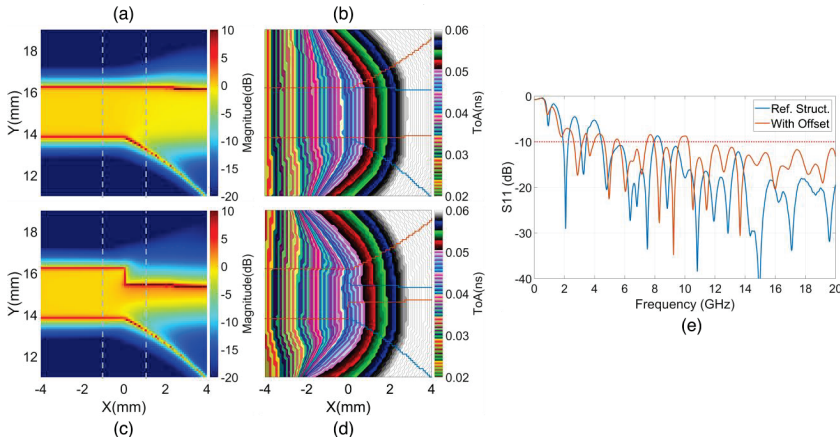


Figure 10. Zoomed-in image of Poynting magnitudes and ToAs of the first clusters on the structures (a,b) without, (c,d) with strip line offset and (e) S11 characteristics.

The magnitude and ToAs on the structure with the strip line offset do are characterized in Figure 10c,d. These figures demonstrate that the reduction in the width at the offset reoriented EM flows from the strip line into higher density EM flows along the Vivaldi edges of the radiating slot. Despite the abrupt transition at the offset, the reflection back to the source is insignificant, as shown in the S11 characteristic in Figure 10e.

To compare EM fluxes ahead and beyond the offset position, the characteristics at the faces with $X = \pm 1$ mm were examined. The face nearer to the source, at $X = -1$ mm, lies within the strip line regions, while the face at $X = 1$ mm is beyond the starting of Vivaldi curves or the offset position and is within the wing region. Figure 11a presents

the magnitudes of Poynting vectors at the face $X = 1$ mm and on the middle substrate layer, normalized by the maximum magnitude at the nearer source face at $X = -1$ mm, with strip line offsets do ranging from 0 to 1.2 mm. Figure 11b characterizes the normalized values of the maximum magnitude of Poynting vectors and the normalized flux values of Poynting vectors through the face $X = 1$ mm over the same offset range as in Figure 11a.

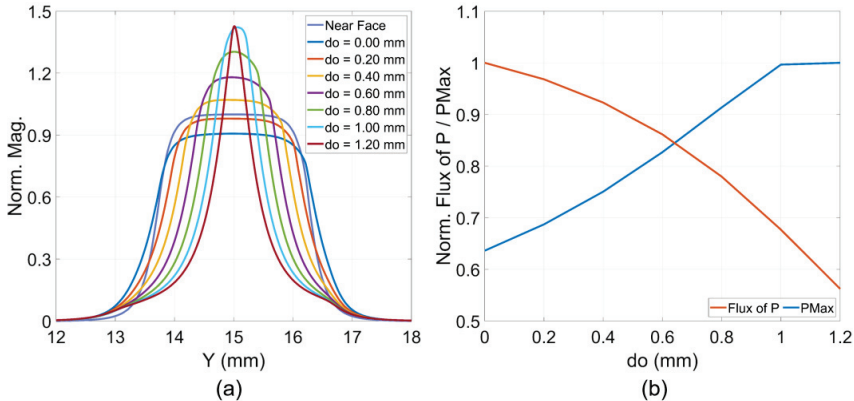


Figure 11. (a) Plot of normalized Poynting magnitudes on the cut lines $X = \pm 1$ mm and (b) normalized maximum magnitude and flux of Poynting vectors.

The characteristics in Figure 11a simplify the features observed in Figure 10a,c. The results, parameterized by the do offset, demonstrate that increasing do leads to a concentration of EM energy density in the Vivaldi edge region, as clarified by the PMax characteristic in Figure 11b. Although there is an enhancement in the magnitude of the Poynting vectors at the edge, the flux of the Poynting vectors through the face at $X = 1$ mm decreases with an increase in the do offset, as shown in Figure 11b.

These observations reveal two opposing trends. The first trend facilitates radiation at the Vivaldi edges due to increased intensity in this region. The second trend resists radiation because of the reduction in the area within the guiding or intersection part of the strips, which is necessary for transmitting EM energy to the radiating wings. These two trends suggest that an optimal do offset value likely falls in the middle of the analyzed do range 0–1.2 mm. This prediction is demonstrated in the subsequent analysis based on the near-field to far-field characteristics for gain and impulse responses.

3.2. Near-Field Effects to Far-Field Analysis

Analysis based on the near-field to far-field transform for the entire structure was conducted. The results, shown in Figure 12, indicate that the do offset significantly influences the gain and impulse responses intensity in the far-field. Figure 12b demonstrates that the average gain and energy of the far-field impulse responses, corresponding to different do offsets, suggest that $do = 0.8$ mm is the optimal value for maximizing the average gain and time response energy in the far-field.

The ToA characteristics in Figure 10b,d show that the offset reorients the dominant EM flow from the edge of the strip to the Vivaldi edge, as depicted in Figure 10d. The ToAs of the clusters on the Vivaldi edge of the structure with the offset are a bit later than those on the reference structure. However, an opposite trend is observed in the ToAs of far-field time response, as shown in Figure 12c,d. With an increase in the do offset, the ToAs of far-field responses become earlier. This indicates that the do offset facilitates the EM flow propagating along the Vivaldi edges, enabling EM radiation to free space sooner than in the case without the offset. The faster propagation velocity in free space compared to the propagation velocity in the strip substrate contributes to the earlier ToAs at the far-field sampling point in the $+x$ direction. This effect can be recognized by comparing

the structures in Figure 9a,b. With the do offset, the area for guiding the EM field in the structure, similar to the strip line ahead the offset position, is reduced, and the radiating area of the Vivaldi edge is moved closer to the offset position. While the total distance from source plane to the far-field sampling point remains unchanged, the increased distance of propagation in free space leads to earlier ToAs. Additionally, the extension of the radiating length proportion of the Vivaldi edge caused by the do offset also contributes to the increased gain of the improved structure.

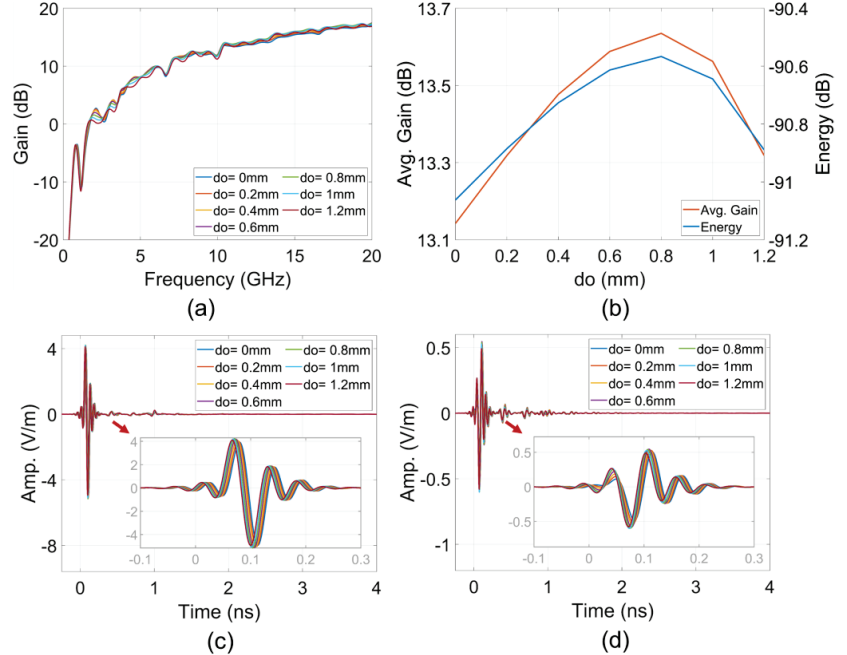


Figure 12. (a) Total gains, (b) far-field average gain, time response energy, (c) E- ϕ and (d) E- θ time response.

4. Analysis of Core Length Effects to Near-Field Characteristics

In this section, based on the optimized structure of the previous section, the analyses on the effects of the length geometry feature of the core formed by the two center wings [14] on the antenna responses in near-field and far-field were implemented. Figure 13a illustrates the core length parameterization over a range of 40 to 120 mm with 20 mm step increments.

4.1. Near-Field Wavefront Analysis

The ToA characteristics of the first clusters of Poynting vectors analyzed on the middle layer of the substrate are illustrated in Figure 13b–d, corresponding to core lengths of 40, 80 and 120 mm, respectively. In regions along segments from the offset position to the middle of the Vivaldi edges, EM flows from the source propagate along and are guided or constrained by the metal Vivaldi edge strip of the wings. These source flows also generate first-order scattering EM flows along these metal strips. In these regions, the source flows and the first-order scattering flows are more dominant than higher-order scattering flows. These first clusters are not significantly affected by other first-order scattering flows, such as reflecting flows from the end of the Vivaldi wing.

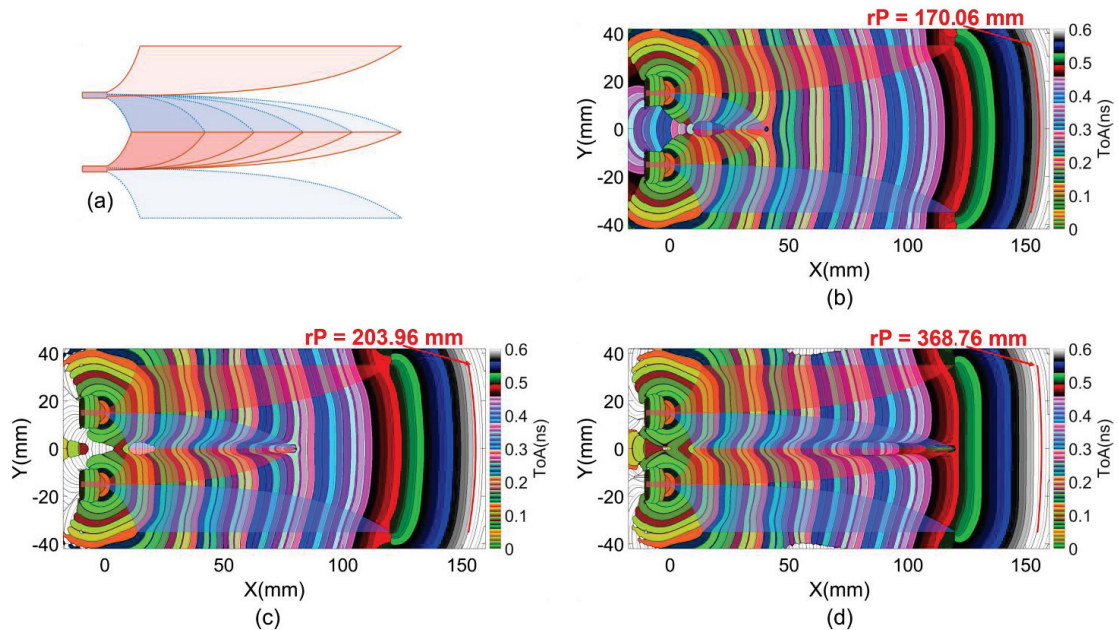


Figure 13. (a) Structure with different core lengths and first cluster ToAs with (b) 40 mm, (c) 80 mm, and (d) 120 mm core lengths.

Additionally, with the extension of the Vivaldi curves in the $\pm y$ directions, the length of the propagation path along the metal edge strip is longer than that in the $+x$ direction in the slot. Consequently, the ToAs of the constrained flows along the metal strip are later than those of flows scattered at lower x coordinates and propagating in the $+x$ direction within the dielectric of the slot. This is expressed in the curvature of the wavefronts at the Vivaldi slots. The balanced excitation of the two Vivaldi slots facilitates the serial connection of two parts of the wavefronts from the lower and upper Vivaldi slots, propagating into the common radiating aperture.

Lengthening the core not only enhances geometric balance for the two slots but also extends the propagation path length of the constrained flows on the core wing strips, facilitating more first-order scattering flows from these parts of the structure. These effects are evident in the enhanced flatness and the later ToAs at the radiating aperture as the core length increases, as shown in Figure 13b–d. The curvature of the wavefronts was approximated by a fitted circle at the radiating antenna aperture. The trend of wavefront flatness enhancement over all analyzed core lengths is presented in Table 1.

Table 1. Radius of wavefronts over core lengths.

Core Length (mm)	Radius of Wavefront (mm)
40	170.05
45	170.34
60	173.91
80	202.96
100	245.23
120	368.76

4.2. Partitional Near-Field Effects to Far-Field Analysis

In this section, the core section as described in Figure 7a of the structures, with a core length ranging from 40 to 120 mm, was analyzed as the sub-volume for near-field

to far-field transformation. This analysis examined the effects of this part on the far-field region at the point 10 m away from the origin in the +x direction.

The result in Figure 14a shows the increasing trend in core partition gains across almost the entire frequency band as the core length increases. This trend is further clarified by the results shown in Figure 14b, which clearly indicate that the average gains and energies of far-field time responses increase with the elongation of the core. The effectiveness of increasing the core length from 40 mm to 120 mm results in an approximate 3 dB improvement in the partitional average gain and response energy.

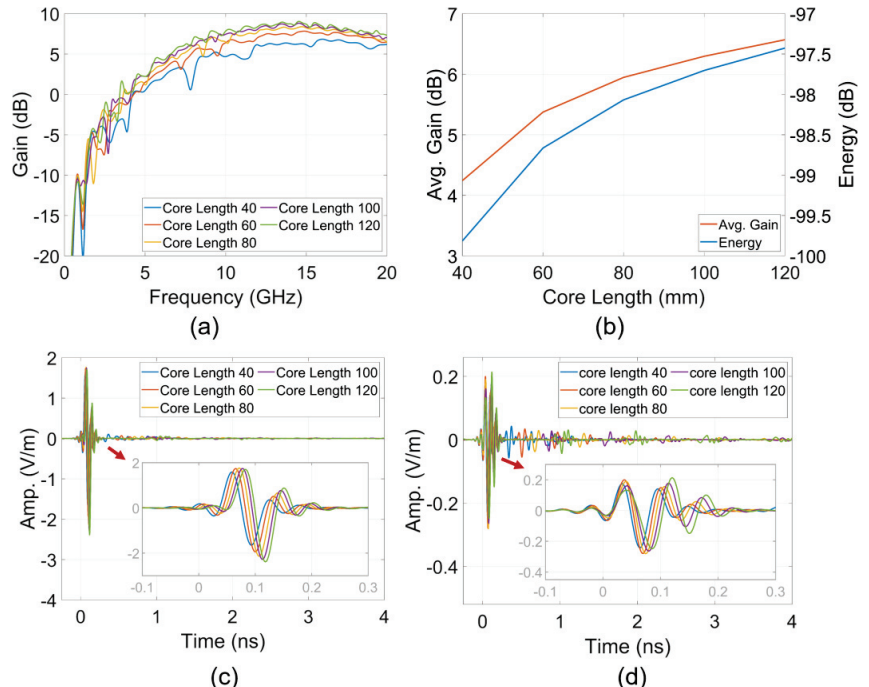


Figure 14. (a) Partitional gains, (b) average partitional gains and time impulse response energy, (c) E-phi and (d) E-theta.

The detailed results in Figure 14c,d for the core partition far-field responses reveal not only an increase in amplitude with longer core lengths but also an increase in ToAs. These findings validate the near-field wavefront analyses, emphasizing the contributions of the core, particularly the core edge strips. The core edge strips facilitate first-order scattering flows or radiating flows and also extend the ToAs of the wavefronts, as discussed in the previous section.

5. Analysis of Near-Field Characteristics on Structure With Lateral Comb Slots

In continuation of the optimization process outlined in the previous two sections, another improvement was added to the existing structure. This enhancement involves an addition of 29 parallel slots etched into each of the two lateral copper wings at an angle of 45 or -45 degree in the +x direction [14]. The lengths of these slots were adapted to the Vivaldi curve to maintain a consistent 4 mm width strip along the Vivaldi edge of the lateral wing as illustrated in Figure 15a. The impacts on near-field and far-field regions of these lateral comb slots are analyzed in this section.

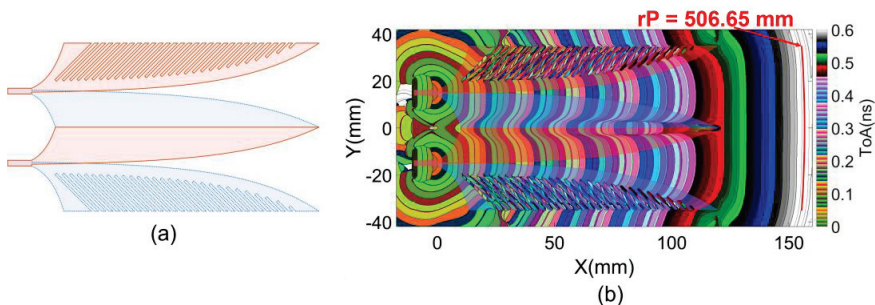


Figure 15. (a) Structure with lateral comb-slots and (b) first cluster ToAs of Poynting vectors.

5.1. Near-Field Wavefront Analysis

The ToAs wavefront result in Figure 15b indicates that, within the regions of the Vivaldi edge strip and dielectric slot, the wavefronts produced by the source EM flow and the first-order scattering EM flows are quite similar to those in the previous structure shown in Figure 13d. However, the lateral comb slots introduce complex scattering EM flows within their regions. This complexity also affects the curvature of the wavefront part stretching across the boundary line between the Vivaldi main strip and the Vivaldi slot, specifically increasing the curvature.

The increase in the wavefront curvature evidences an increase in density of scattering flows in the Vivaldi slot, resulting in earlier ToAs compared to the constrained flow on the Vivaldi strip, which exhibits later ToAs. The scattering in the comb slots regions contributes to this increased density of scattering flows in the Vivaldi slot. This results in a significant improvement of wavefront flatness at the radiating aperture, with a wavefront radius reaching up to 506.65 mm.

Additionally, parallel lines formed by the comb slots with varying lengths facilitate higher-order scattering or resonance on individual lines and/or groups of lines. This extends the response time and also improves antenna performances at low frequencies. These impacts of the comb slots on response improvements of the antenna are more clearly observed in the partitional far-field analysis.

5.2. Partitional Near-Field Effects to Far-Field Analysis

Volumes containing the main Vivaldi strip with a 4 mm width and the comb slots in the lateral wings were selected as sub-volumes for analysis of the antenna with the comb slots, as illustrated in Figure 16. To facilitate a comparison with the antenna without the comb slots, the two lateral wings without the comb slots were divided into the same two sections: the main Vivaldi strip section and the remaining section of the lateral wings.

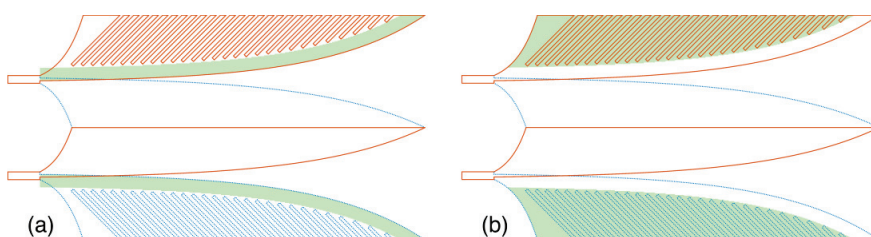


Figure 16. Structural sub-volumes for near-field to far-field transformation: (a) main Vivaldi strip section and (b) remaining or comb slots section.

The results of partitional gains for these sections, shown in Figure 17a, indicate that the 4 mm main strip sections of both antennas—those with and without the comb

slots—contribute similarly to the gains feature across the entire frequency band. However, the remaining section of the wings with the comb slots contributes significantly higher partitional gains compared to the same section of the antenna without the comb slots. The gains contributed by the partition comb slots are also high at lower frequencies such as around 2 GHz. This supports the earlier discussion about the impact of the comb slots on scattering flows.

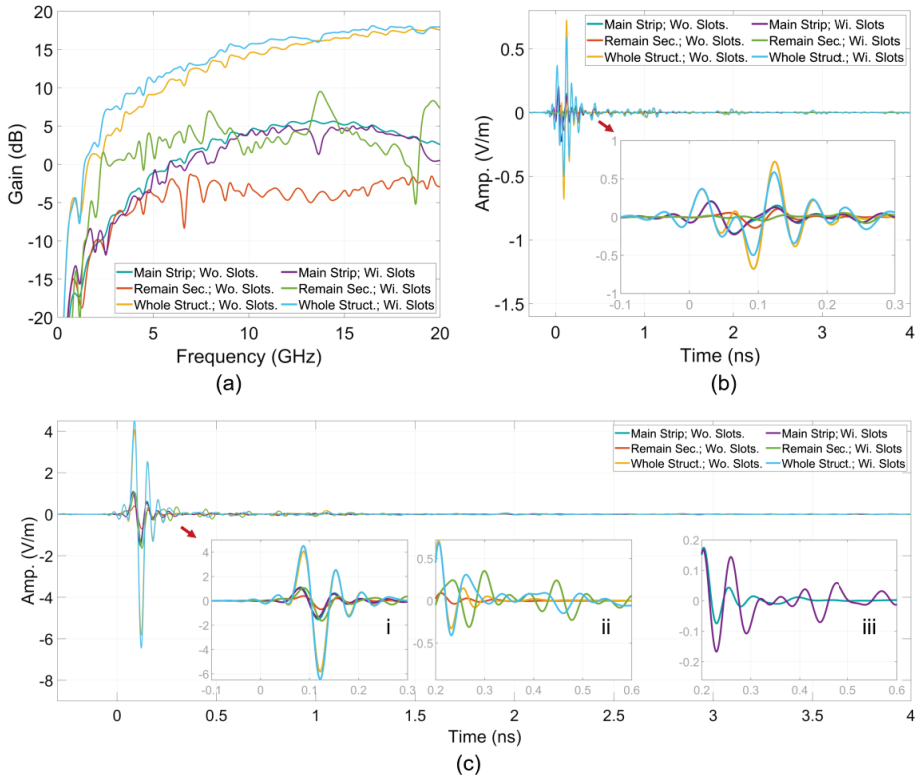


Figure 17. (a) Partitional and total gains, (b) E-theta and (c) E-phi time impulse responses.

The gain of the entire structure further highlights the contribution of the comb slots to improving the antenna's performance. The amplitudes of the far-field impulse responses, shown in Figure 17b,c, also present as the feature in the partitional gains. Analysis of the lengthening in response time of these signals, as depicted in Figure 17c(i–iii), demonstrates that the comb slots facilitate higher-order scattering or resonance within the lines of these regions, resulting in a longer response time for these signals.

During the research Sections 3–5, the near-field wavefront, far-field response and gain characteristics of the antennas were improved step by step. For a complete presentation of near-field response features of the antennas, the S11 characteristic was evaluated on the reference structure and the improved structures of each step as in Figure 18. This shows that the offset in the excitation line does not cause a significant adverse effect on S11, and the increase in core length and adding the lateral comb slots on the structure significantly enhance S11 performance, especially in the lower frequency band.

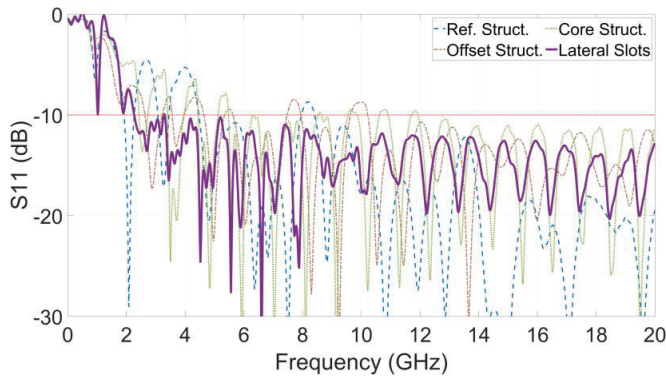


Figure 18. S11 Characteristic on structures.

6. Conclusions

The near-field characteristics of intensity, ToA of EM cluster, partitional gain in frequency domain, partitional far-field impulse response in time domain and their derivatives are proposed. The approach allows the interpretation of the EM propagation process within the structure as features such as the dominant regions, dominant flows, ToAs/velocities/wavefronts of the flows and far-field impulse responses of the localized structural regions. This consequentially allows a simplification of the propagation process into a simpler and more manageable model, which elucidates the role and impact of the structural geometries or the structural details on the EM response features or the near-field characteristics. The detail or locality in spatial distribution of the characteristics facilitates the analysis of the effects of sub-structures of the geometry. The geometry, correlation and extrema feature of the near-field and partition characteristics along with their derivatives are used as criteria for optimizing structural parameters during the design process. The optimization of these parameters and the effectiveness of the improved structures are demonstrated using both these characteristics and the conventional overall characteristics.

The analyses based on near-field and partitional near-field to far-field characteristics simplifies near-field propagation models, thereby enhancing the understanding of near-field propagation processes in the double-slot antipodal Vivaldi antennas and contributing to their improvement. This methodology is also promising for exploring EM propagation processes in various other traveling wave antennas.

Author Contributions: Conceptualization, H.H.; methodology, H.H. and V.P.-X.; software, H.H. and M.-H.N.; validation, H.H., M.-H.N. and V.P.-X.; formal analysis, H.H., M.-H.N. and V.P.-X.; investigation, H.H., M.-H.N. and V.P.-X.; resources, H.H. and V.P.-X.; data curation, H.H., M.-H.N. and V.P.-X.; writing—original draft preparation, H.H.; writing—review and editing, H.H., M.-H.N. and V.P.-X.; visualization, H.H. and M.-H.N.; supervision, H.H.; project administration, H.H.; funding acquisition, H.H. All authors have read and agreed to the published version of the manuscript.

Funding: This research is funded by Vietnam National University Ho Chi Minh (VNU—HCM) under grant number DS2022-20-06.

Data Availability Statement: Data are contained within the article.

Conflicts of Interest: Author Vinh Pham-Xuan was employed by the company Dassault Systèmes Deutschland GmbH. The remaining authors declare that the research was conducted in the absence of any commercial or financial relationships that could be construed as a potential conflict of interest.

References

1. Gibson, P.J. The Vivaldi Aerial. In Proceedings of the 1979 9th European Microwave Conference, Brighton, UK, 17–20 September 1979; pp. 101–105.
2. Gazit, E. Improved design of the Vivaldi antenna. *IEE Proc. H Microwaves Antennas Propag.* **1988**, *135*, 89–92. [CrossRef]

3. Nurhayati, N.; Setijadi, E.; de Oliveira, A.M.; Kurniawan, D.; Yasin, M.N.M. Design of 1×2 MIMO Palm Tree Coplanar Vivaldi Antenna in the E-Plane with Different Patch Structure. *Electronics* **2023**, *12*, 177. [CrossRef]
4. Dixit, A.S.; Kumar, S. A Survey of Performance Enhancement Techniques of Antipodal Vivaldi Antenna. *IEEE Access* **2020**, *8*, 45774–45796. [CrossRef]
5. Liu, Y.; Zhou, W.; Yang, S.; Li, W.; Li, P.; Yang, S. A novel miniaturized Vivaldi antenna using tapered slot edge with resonant cavity structure for ultrawideband applications. *IEEE Antennas Wirel. Propag. Lett.* **2016**, *15*, 1881–1884. [CrossRef]
6. Hossain, A.; Pham, A.-V. A novel Gain-Enhanced miniaturized and lightweight Vivaldi antenna. *IEEE Trans. Antennas Propag.* **2023**, *71*, 9431–9439. [CrossRef]
7. Fei, P.; Jiao, Y.-C.; Hu, W.; Zhang, F.-S. A Miniaturized Antipodal Vivaldi Antenna with Improved Radiation Characteristics. *IEEE Antennas Wirel. Propag. Lett.* **2011**, *10*, 127–130.
8. Ding, M.; Wang, X.; Wang, Y.; Hu, Z.; Liu, G.; Liu, Z.; Wang, B. A High Gain Vivaldi Antenna with Multiple Near-Field Dielectric Lenses and Grooved Edges. *Int. J. RF Microw. Comput. Eng.* **2023**, *2023*, 1–11. [CrossRef]
9. Samsuzzaman, M.; Islam, M.T.; Islam, M.T.; Shovon, A.A.; Faruque, R.I.; Misran, N. A 16-modified antipodal Vivaldi antenna array for microwave-based breast tumor imaging applications. *Microw. Opt. Technol. Lett.* **2019**, *61*, 2110–2118. [CrossRef]
10. Faeghi, P.; Ghobadi, C.; Nourinia, J.; Virdee, B. Nanoparticle-coated Vivaldi antenna array for gain enhancement. *Appl. Physics. A Mater. Sci. Process.* **2023**, *129*, 3. [CrossRef]
11. Portosi, V.; Loconsole, A.M.; Campana, A.; Anelli, F.; Prudenzano, F. A novel L-Shaped Metalens for Ultra-Wide Band (UWB) antenna gain improvement. *Appl. Sci.* **2023**, *13*, 4802. [CrossRef]
12. Wang, Y.-W.; Wang, G.-M.; Zong, B.-F. Directivity Improvement of Vivaldi Antenna Using Double-Slot Structure. *IEEE Antennas Wirel. Propag. Lett.* **2013**, *12*, 1380–1383. [CrossRef]
13. Hoang, M.; Yang, K.; John, M.; McEvoy, P.; Ammann, M. Ka-band Vivaldi Antenna with Novel Core Element for High-Gain. In Proceedings of the Loughborough Antennas & Propagation Conference (LAPC 2017), Loughborough, UK, 13–14 November 2017.
14. Hoang, M.; Yang, K.; John, M.; McEvoy, P.; Ammann, M.J. Ka-band Planar Vivaldi antenna with a core for high gain. *IET Microw. Antennas Propag.* **2019**, *13*, 732–735. [CrossRef]
15. Yang, G.; Ye, S.; Zhang, F.; Ji, Y.; Zhang, X.; Fang, G. Dual-Polarized Dual-Loop Double-Slot antipodal tapered slot antenna for Ultra-Wideband radar applications. *Electronics* **2021**, *10*, 1377. [CrossRef]
16. Hoang, H.; John, M.; McEvoy, P.; Ammann, M.J. Near-Field Propagation Analysis for Vivaldi Antenna Design: Insight into the propagation process for optimizing the directivity, integrity of signal transmission, and efficiency. *IEEE Antennas Propag. Mag.* **2021**, *63*, 46–60. [CrossRef]
17. Hoang, H. Near-Field Propagation Analysis for Traveling-Wave Antennas. *Antenna Syst.* **2022**, *217*.
18. CST Studio Suite. Available online: <https://www.3ds.com/products-services/simulia/products/cst-studio-suite/> (accessed on 1 January 2024).
19. Balanis, C.A. *Advanced Engineering Electromagnetics*, 2nd ed.; Wiley Global Education: Hoboken, NJ, USA, 2012.
20. Balanis, C.A. *Antenna Theory: Analysis and Design*, 4th ed.; John Wiley & Sons: Hoboken, NJ, USA, 2016.
21. Bui, M.-T.; Nguyen, M.-H.; Le-Nguyen, T.-T.; Pham-Xuan, V.; Hoang, H. Analysis of Improved Structures Impact on Features of Antipodal Vivaldi Antenna. In Proceedings of the 2023 International Conference on Advanced Technologies for Communications (ATC23), Da Nang, Vietnam, 19–21 October 2023; pp. 254–258.

Disclaimer/Publisher’s Note: The statements, opinions and data contained in all publications are solely those of the individual author(s) and contributor(s) and not of MDPI and/or the editor(s). MDPI and/or the editor(s) disclaim responsibility for any injury to people or property resulting from any ideas, methods, instructions or products referred to in the content.

Communication

Dual-Polarized Dipole Antenna with Wideband Stable Radiation Patterns Using Artificial Magnetic Conductor Reflector

Xianjing Lin ¹, Jielin Mai ¹, Hongjun He ¹ and Yao Zhang ^{2,*}

¹ School of Electronic Engineering and Intelligence, Dongguan University of Technology, Dongguan 523808, China; linxj@dgut.edu.cn (X.L.); 13413325001@163.com (J.M.); hongjun_he77@163.com (H.H.)

² Institute of Electromagnetics and Acoustics, Xiamen University, Xiamen 361005, China

* Correspondence: zhangsantu@xmu.edu.cn

Abstract: This paper presents a wideband dual-polarized dipole antenna structure operating at 1.7–3.8 GHz (76.4%). For a traditional 4G dipole antenna that covers the band 1.71–2.69 GHz, it is difficult to maintain the satisfactory impedance matching and normal stable radiation patterns within the 5G sub-6 GHz band 3.3–3.8 GHz, mainly due to the fixed antenna height no longer being a quarter-wavelength. To solve this, a connected-ring-shaped metasurface structure is proposed and deployed to operate as an artificial magnetic conductor (AMC). As a result, stable antenna radiation patterns are obtained within the whole band 1.7–3.8 GHz. For verification, this wideband dipole antenna using AMC is implemented and tested. The measured results show that the proposed antenna has an impedance bandwidth of 80.7% (1.7–4.0 GHz). It has an average measured in-band realized gain of 7.0 ± 1.0 dBi and a stable 70 ± 5 half power beam width (HPBW) within the 4G/5G-sub 6GHz bands 1.71–2.69 GHz and 3.3–3.8 GHz.

Keywords: wideband antenna; dual-polarized antenna; dipole antenna; radiation pattern restoration

1. Introduction

The dual-polarized dipole antenna has been widely used in the base-station antenna array scenario as the basic antenna array element [1–5]. The antennas, which operate at 1.71–2.69 GHz [1,6–10] and 3.3–3.8 GHz [11] bands, are widely used in sub-6 GHz base-station applications. The antenna designers are devoted to developing wideband antennas that simultaneously cover the above two frequency bands.

However, it is challenging to maintain stable antenna radiation patterns with a fixed antenna height in such a wide frequency band of 1.71–3.8 GHz. Two mainstream approaches are used to solve this problem. One is to design dual-band or notched-band antennas that operate at the two target frequency bands 1.71–2.69 GHz and 3.3–3.8 GHz [12,13]. The other method is to use parasitic components to increase the impedance bandwidth [14–18]. In [14], an extra pair of shorted dipoles were added, and the impedance bandwidth was increased to 74.5% (1.69–3.7 GHz). In [15], parasitic elements such as metal cylinders and triangle metal palates were involved, and the antenna realized a 78.6% bandwidth (1.59–3.65 GHz). However, for the above two designs, the antenna gains at upper-band frequencies (>3 GHz) decreased/increased a lot, indicating unstable radiation patterns. To improve the radiation performance in upper-band frequencies, the design in [16] printed a circular patch and four pairs of dipole strips on an extra substrate layer. Stable radiation patterns over the entire frequency band were realized. However, since this layer substrate is installed above the antenna structure, it inevitably increases the overall antenna profile, which is undesirable for base station applications. Other components such as parasitic posts [17] and partially coupled stubs [18] have also been applied to stabilize the antenna radiation patterns recently. AMC reflectors have been extensively studied for low-profile antenna designs [19–21], but they have not been used for the wideband stable radiation performance. With regard to this

Citation: Lin, X.; Mai, J.; He, H.; Zhang, Y. Dual-Polarized Dipole Antenna with Wideband Stable Radiation Patterns Using Artificial Magnetic Conductor Reflector. *Sensors* **2024**, *24*, 3911. <https://doi.org/10.3390/s24123911>

Academic Editor: Simone Genovesi

Received: 18 May 2024

Revised: 11 June 2024

Accepted: 12 June 2024

Published: 17 June 2024



Copyright: © 2024 by the authors. Licensee MDPI, Basel, Switzerland. This article is an open access article distributed under the terms and conditions of the Creative Commons Attribution (CC BY) license (<https://creativecommons.org/licenses/by/4.0/>).

problem, this work utilized a connected-ring-shaped metasurface structure as an artificial magnetic conductor (AMC). As a result, a dual-polarized cross-dipole antenna achieved an average in-band realized gain of 7.0 ± 1.0 dBi and a stable $70^\circ \pm 5^\circ$ half power beam width (HPBW) within the band 1.7–3.8 GHz.

2. Wideband Antenna Design

2.1. Problem of Traditional Wideband Antenna

Figure 1a displays a traditional directional dipole antenna using a reflector. Suppose this antenna operates at 1.7–3.8 GHz and the antenna height h is set to be a quarter wavelength of 2.2 GHz ($\lambda_{2.2}$ GHz), which is the center operating frequency of the band 1.71–2.69 GHz. As is known, the antenna radiation patterns at upper-band frequencies are distorted since the fixed antenna height is no longer quarter-wavelength at these frequencies. Figure 1b illustrates the antenna radiation patterns at 2.2 GHz, 3.0 GHz, and 3.8 GHz. As can be seen, the radiation patterns at 3.0 and 3.8 GHz are not stable or even distorted. This is because the 3 dB beamwidth increases as the frequency enhances from 1.7 GHz to 2.8 GHz. However, it decreases drastically when the frequency is larger than 3.6 GHz.

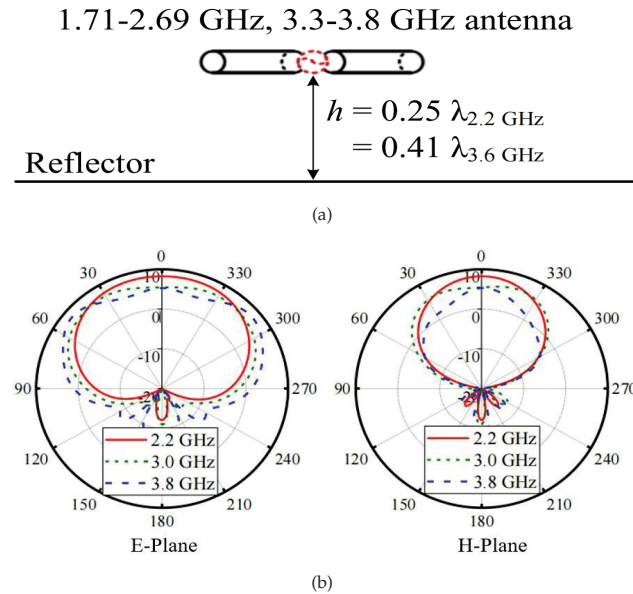


Figure 1. (a) Diagram and (b) E-/H-plane radiation patterns of a 1.7–3.8 GHz antenna.

To solve this problem, this letter proposed a wideband dual-polarized dipole antenna with normal stable radiation patterns within the band 1.7–3.8 GHz, as shown in Figure 2. It consists of three parts: a dipole antenna radiator, a connected-ring-shaped metasurface structure as the AMC, and a ground as the reflector. An air layer exists between the AMC reflector and the ground plane. The AMC structure is inserted between the antenna radiator and the reflector, and therefore it does not increase the overall antenna height. The antenna radiators are excited by a pair of Y-shaped feedlines that are directly connected to two coaxial cables. The AMC structure is realized by a 7×7 connected ring array. This AMC is deliberately designed to operate at upper-band frequencies (3.3–3.8 GHz) for phase shift compensation. Detailed parameter values are also included in Figure 2. The design procedure and working principle are investigated and revealed in the following part.

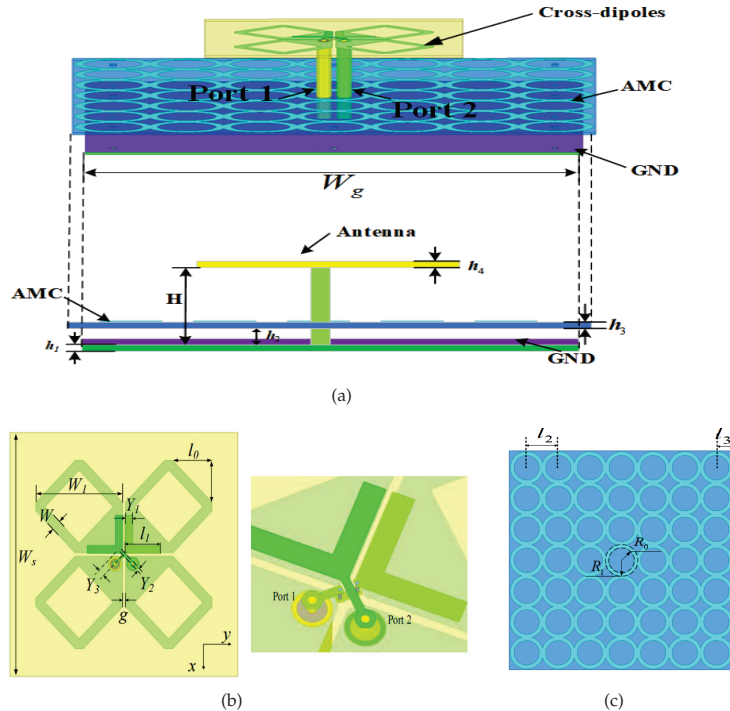


Figure 2. Geometry of the proposed wideband antenna: (a) total view, (b) dipole antenna, and (c) AMC ($H = 30$, $h_1 = 1$, $h_2 = 2.5$, $h_3 = 0.8$, $h_4 = 0.8$, $l_0 = 12$, $l_1 = 10.9$, $l_2 = 20$, $l_3 = 11$, $W = 1.7$, $W_s = 70$, $W_g = 135$, $W_1 = 26.5$, $Y_1 = 2.3$, $Y_2 = 0.8$, $Y_3 = 2.0$, $g = 1$, $R_0 = 8.1$, and $R_1 = 10.6$, all in mm).

2.2. Design Procedure

Figure 3 depicts the structures of four reference antennas, denoted as Antenna I, II, III, IV. The original Antenna I is a dipole antenna with rectangular radiators and Y-shaped coupled feedlines [7]. To enhance the antenna impedance bandwidth and maintain stable radiation patterns, this structure is then modified to Antennas II, III, and IV. The simulation results of the four antennas, including the reflection coefficient S_{11} , isolation parameter S_{12} , realized gain, and HWPB, are plotted and compared in Figure 4. As observed, Antenna I has limited impedance bandwidth (41.2%, 1.64–2.49 GHz).

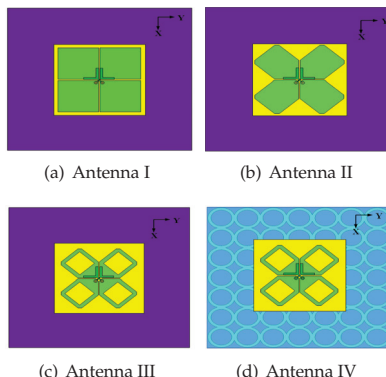


Figure 3. Structures of Antennas (a) I, (b) II, (c) III, and (d) IV.

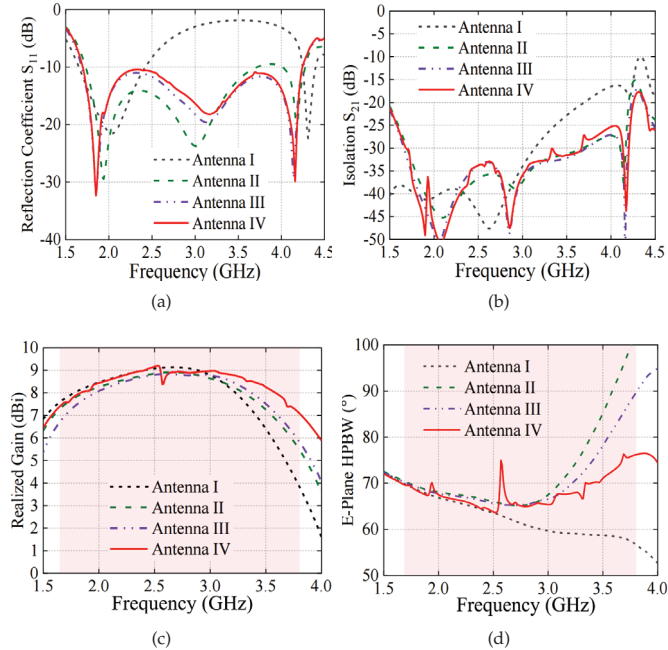


Figure 4. Antenna results including (a) reflection coefficient S_{11} , (b) isolation parameter S_{12} , (c) realized gain, and (d) HPBW.

However, Antennas II, III, and IV are well matched within the band 1.7–3.8 GHz, and the port-to-port isolation $|S_{12}|$ is better than 25 dB. It is noted that the realized gains and HPBW of the four antennas differ a lot, especially at upper-band frequencies (3.0–3.8 GHz). Within the band 1.7–3.8 GHz, the Antenna IV has a stable realized gain ranging from 7.0 dBi to 9.1 dBi. The HPBW is also stable within the range $70^\circ \pm 5^\circ$.

2.3. AMC Working Principle

For an antenna, the reflector is an important factor affecting its radiation performance, and analyzing the formation principle of its reflection phase characteristics is the key to studying the reflector. Assuming there is an electromagnetic wave that is vertically incident on the reflector, a coordinate system is established based on the material surface, as shown in Figure 5a. The corresponding equivalent model is shown in Figure 5b. The transmission line network can be used to calculate the reflection coefficient:

$$\Gamma = \frac{Z_S - Z_0}{Z_S + Z_0} = |\Gamma| e^{\pm i\phi} \quad (1)$$

$$\phi = im \left\{ In \left(\frac{Z_S - Z_0}{Z_S + Z_0} \right) \right\} = im \left\{ In \left(\frac{Z_S - \eta}{Z_S + \eta} \right) \right\} \quad (2)$$

where Z_S is regarded as the impedance of the material surface, Z_0 is the impedance of the dipole antenna, and ϕ is the phase difference between the incident and the reflected wave of the electromagnetic wave. When $Z_S = 0$, then $\Gamma = 1$, $\phi = \pi$. It can be seen that when the surface impedance is an ideal electrical conductor, the reflection phase of the reflector is 180° . Only when the distance between the radiator and the reflector is $\lambda/4$ can the phase difference with a spatial phase delay of 180° be offset with the 180° phase difference generated by the reflector, so that the reflected wave is in the same direction as the main radiation beam. Thus, enhanced radiation is obtained.

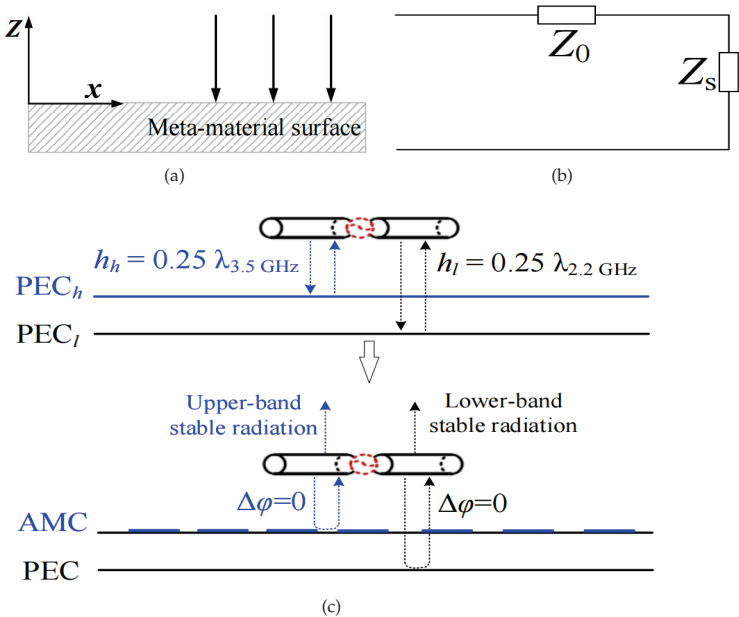


Figure 5. Diagram of Antenna IV's working principle: (a) electromagnetic waves incident on the surface of the material, (b) equivalent single port model, and (c) constructive interference of the antenna.

According to the above analysis, when the antenna height is set around $\lambda/4$ (λ denotes the wavelength of center frequency 2.2 GHz), the impedance bandwidth for normal stable radiation patterns of a traditional dipole antenna is about 45.4% (1.7–2.7 GHz). To maintain normal stable radiation patterns at 2.7–3.8 GHz, another perfect electric conductor (PEC_h) is required. This PEC_h can be realized by using an AMC, as diagramed in Figure 5c. The surface impedance of an AMC is very high over a certain frequency region, so it is also known as a high-impedance surface, which is a type of frequency-selective surface or meta-material surface.

The schematic diagram and equivalent circuit of the AMC is shown in Figure 6. The AMC reflector consists of a group of AMC units (metal ring patch) arranged periodically. The capacitor is generated between the metal ring patches, and the inductance is generated between the ground plane and the patches, so the AMC structure can be denoted as a series of LC circuits in parallel. According to the circuit principle, the resonant frequency of the AMC can be obtained as:

$$f = \frac{1}{2\pi\sqrt{\frac{C_1 C_2}{C_1 + C_2} L_1}} \quad (3)$$

To search for the frequency band in which the periodic structure behaves as an AMC, a finite element method (FEM) model is established based on the Bloch–Floquet theory [22]. A single unit cell of the structure, with periodic boundary conditions (PBC) along its four sides, is simulated as seen in Figure 7a to model an infinite periodic surface. It is worth mentioning that the circular ring is chosen as the AMC unit as an example, and other structures, such as square rings, have the same effect. The reflected phase from the periodic surface is normalized to the one from the PEC by

$$\theta = \theta_{FSS} - \theta_{PEC} + \pi \quad (4)$$

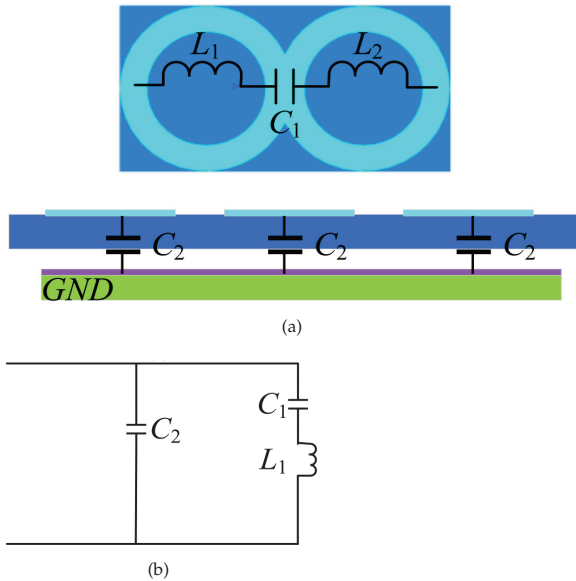


Figure 6. (a) Schematic diagram and (b) equivalent circuit of the AMC.

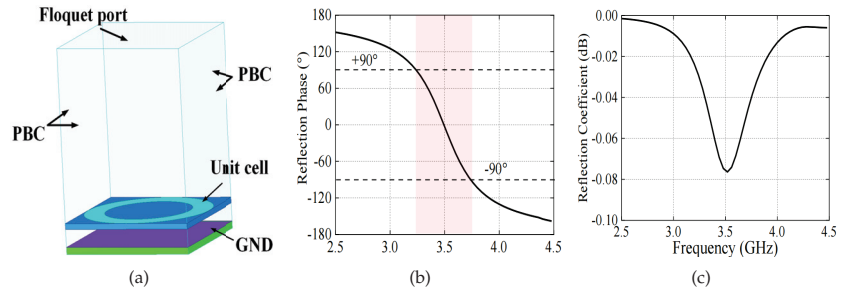


Figure 7. (a) Simulation model and (b) results including the reflection phase and (c) coefficient for determining the reflection properties of the AMC.

The characteristics of the AMC behavior can be verified by calculating the reflection coefficient for a uniform incident plane wave. The phase of the reflection coefficient of an AMC should exhibit a difference of 180° compared to that of a PEC plane. The reflection phase and magnitude of a normally incident plane are shown in Figure 7b. As observed, the reflection phase on the AMC plane varies continuously from -180° to 180° against frequency and is zero at the resonance frequency. The reflection coefficient is larger than -0.1 dB, indicating that almost all the incident waves are reflected. The useful bandwidth of AMC performance is, in general, defined as $+90^\circ$ to -90° on either side of the resonance frequency. The AMC bandwidth can be obtained as

$$BW_{AMC} = [(f_{up} - f_{lo}/f_c)] \times 100\% \quad (5)$$

where f_{up} and f_{lo} are the frequencies at which the reflection phase equals -90° and 90° , respectively. f_c is the center frequency where the reflection phase equals 0° . The AMC frequency bandwidth of the proposed structure is about 16.6% (3.2–3.78 GHz).

In addition, the operating frequency of the AMC can be shifted to desired values. Figure 8 illustrates the reflection phase of the AMC against the unit cell size AMC_L , the

unit cell height AMC_H , and the ring dimensions. As seen, the center operating frequency as well as the bandwidth can be easily controlled and optimized. Based on such a structure, the radiation patterns of a dipole antenna within the upper frequency band 2.7–3.8 GHz can be restored without increasing the overall antenna height.

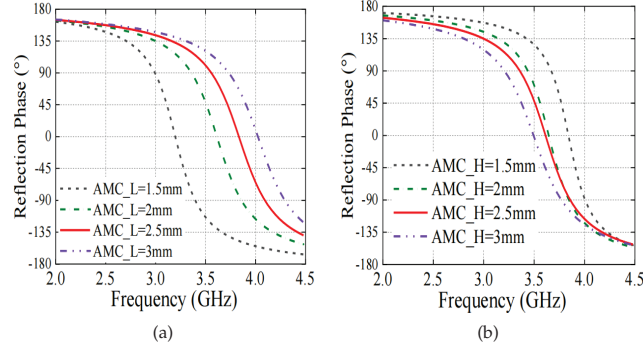


Figure 8. Reflection phase related to different (a) unit cell size AMC_L and (b) unit cell height AMC_H .

3. Dual-Polarized Antenna Implementation

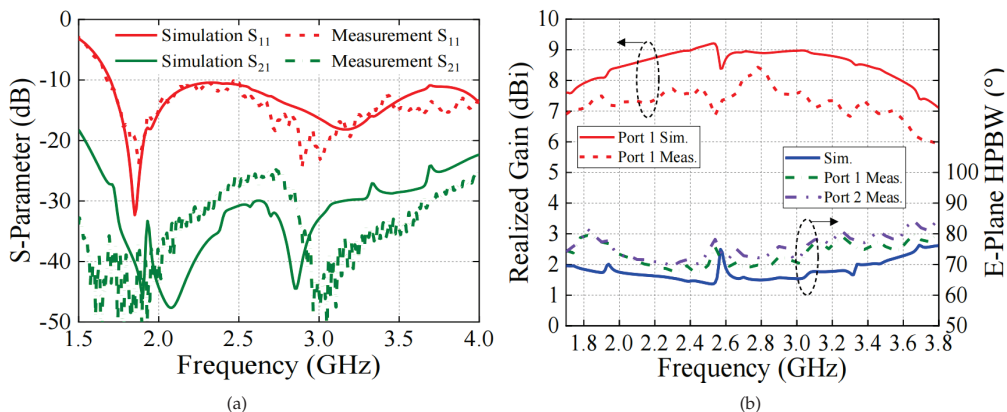
The proposed dual-polarized antenna was designed, fabricated, and measured, as shown in Figure 9. The optimization was performed using the high-frequency structural simulator (HFSS), and the measurement was accomplished via the Agilent N5227A network analyzer and Satimo system. Figure 10 shows the results including the S-parameters and radiation response. The simulation results agree well with the measurement ones. As seen, the measured bandwidth ($|s_{11}| < -10$ dB) is 76.4% (1.7–3.8 GHz). The measured isolation between two ports within this band is lower than -25 dB, and the average measured in-band gain is about 7.5 dBi. It is 1.5 dBi lower than the simulated gain because of the measured error. A stable $70^\circ \pm 5^\circ$ half power beam width (HPBW) within the band 1.7–3.8 GHz is obtained. There are some abrupt changes in the gain and HPBW curves because of the diffraction effect of the electromagnetic waves at certain frequencies. However, this phenomenon has little impact on the antenna performance.

The antenna radiation patterns at 1.7 GHz, 2.7 GHz, 3.3 GHz, and 3.8 GHz are plotted in Figure 11 when Port1 is excited. As expected, normal stable radiation patterns with low cross-polarization levels are observed. To address the advantages of the proposed work, the comparison results with other related designs are tabulated in Table 1. The dual-band or notched-band antenna concept was adopted in [12,13], and stable radiation patterns were obtained within the target bands 1.71–2.69 GHz and 3.3–3.8 GHz. In [16], an extra superstrate was deployed to print parasitic elements, and thus the antenna overall height was increased. Also, parasitic strips and posts were applied in [18] to achieve a stable realized gain curve. The AMC reflector is used in [19–21] to reduce the profile height of the dual-polarized antenna but is not used to achieve wideband (1.7–3.8 GHz) stable radiation performance. Different from the abovementioned methods, by inserting an AMC structure between the antenna radiator and ground, wideband operation and normal stable radiation patterns were realized in the proposed work.

Table 1. Comparison of the wideband dual-polarized antennas.

	Size (λ_0^3)	FBW% (BW/GHz)	Implementation	HBPW (°)	Realized Gain (dBi)
[12]	$0.8 \times 0.8 \times 0.26$	(47.8%) 1.67–2.72 (16.7%) 3.3–3.9	Parasitic director + baffle	67.5 ± 8.5 64 ± 5	8.1 ± 0.5 8.35 ± 0.25
[13]	$0.8 \times 0.8 \times 0.24$	(44%) 1.71–2.69 (7.2%) 3.35–3.6	Notch band antenna	69.5 ± 4 90 ± 10	8.1 ± 0.4 6.6 ± 0.5
[16]	$0.8 \times 0.8 \times 0.22$	(100%) 1.7–5.1	Parasitic elements on superstrate	65 ± 5	8.2 ± 0.7
[18]	$0.8 \times 0.8 \times 0.2$	(77.7%) 1.7–3.86	Parasitic strips + baffle	72 ± 5	8 ± 0.6
[19]	$1.1 \times 1.1 \times 0.17$	(45.4%) 1.7–2.7	AMC	N.A.	4 ± 0.5
[20]	$0.9 \times 0.9 \times 0.13$	(19.8%) 3.14–3.83 (23.2%) 4.4–5.02	AMC	N.A.	6 ± 0.8 7 ± 0.5
[21]	$3.2 \times 3.2 \times 0.14$	(58.8%) 2.16–3.99	AMC	N.A.	8.8 ± 0.7
This work	$0.8 \times 0.8 \times 0.17$	(76%) 1.7–3.8	AMC	70 ± 5	7.0 ± 1.0

λ_0 is the free-space wavelength at the the lowest frequency of the operating bands.

**Figure 9.** Antenna fabrication prototype. (a) side view and (b) top view.**Figure 10.** Simulation and measurement results including (a) S-parameters and (b) realized gains, HPBW.

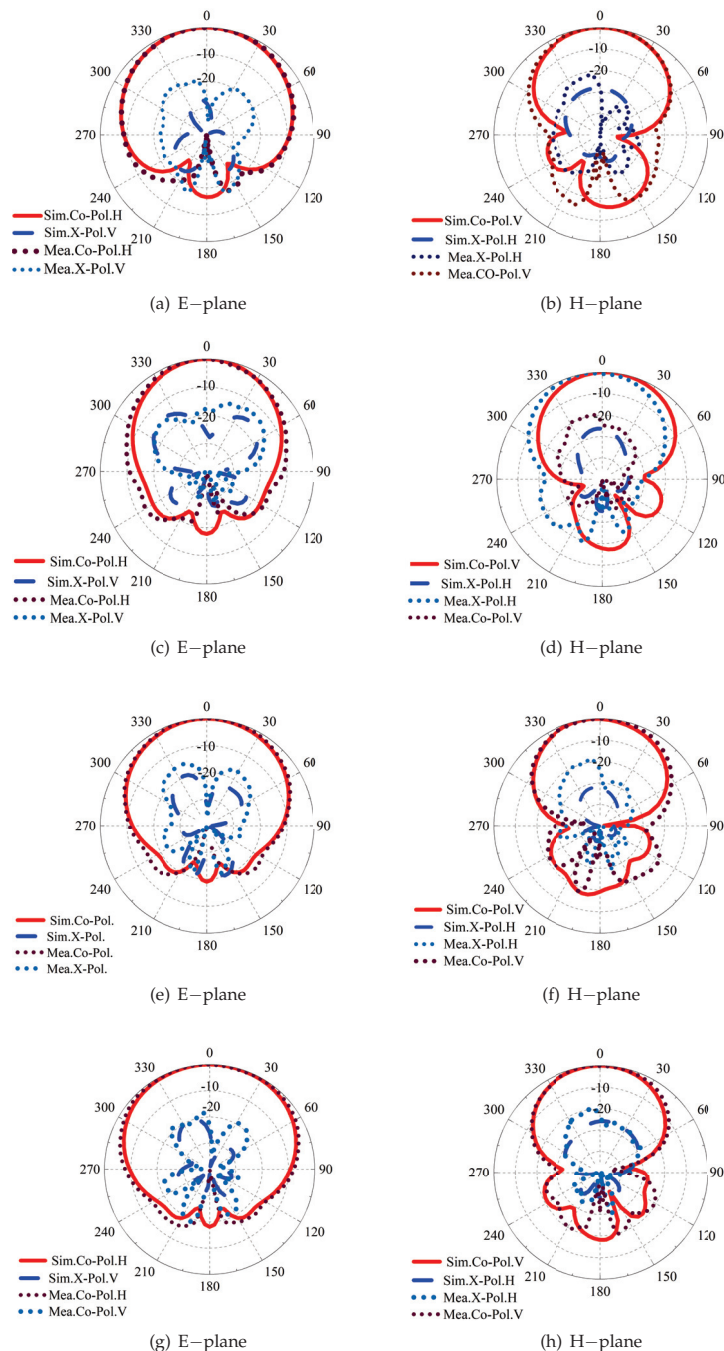


Figure 11. Simulated and measured normalized radiation patterns at (a,b) 1.7 GHz, (c,d) 2.7 GHz, (e,f) 3.3 GHz, and (g,h) 3.6 GHz.

4. Conclusions

In this paper, a wideband dual-polarized dipole antenna operating at 1.7–3.8 GHz has been proposed. To restore the distorted antenna radiation patterns within 3.3–3.8 GHz, an AMC has been presented by developing a connected-ring-shaped metasurface or frequency-selective surface structure. This AMC structure was inserted between the antenna radiator and ground, and therefore it did not increase the overall antenna height. The measured results revealed that the proposed antenna simultaneously obtained the wide impedance bandwidth of 76.4%, 7.0 ± 1.0 stable realized gain, normal radiation patterns with $70^\circ \pm 5^\circ$ HPBW, and a simple structure. These merits make the proposed antenna a good candidate for the base station antenna applications.

Author Contributions: Conceptualization, X.L.; validation, J.M.; software, H.H.; project administration, X.L.; funding acquisition, Y.Z.; and supervision, Y.Z. All authors have read and agreed to the published version of the manuscript.

Funding: This work was supported in part by the National Natural Science Foundation of China under Grant 62001407 and Grant U2241222, in part by the College Student Innovation and Entrepreneurship Training Program Project under Grant 202311819005 (Corresponding author: Yao Zhang).

Institutional Review Board Statement: Not applicable.

Informed Consent Statement: Not applicable.

Data Availability Statement: Data are contained within the article.

Conflicts of Interest: The authors declare no conflicts of interest.

Abbreviations

The following abbreviations are used in this manuscript:

AMC	Artificial magnetic conductor
HPBW	Half-Power Beamwidth
CD	Crossed Dipole
BSA	Base station antenna

References

- Ye, L.H.; Zhang, X.Y.; Gao, Y.; Xue, Q. Wideband Dual-Polarized Four-Folded-Dipole Antenna Array with Stable Radiation Pattern for Base-Station Applications. *IEEE Trans. Antennas Propag.* **2020**, *68*, 4428–4436. [CrossRef]
- Wu, R.; Wen, G.H.; Liu, Y.; Chen, F.C. A Broadband Filtering Antenna Array for Sub-6 GHz Base Station Applications. *IEEE Antennas Wirel. Propag. Lett.* **2024**, *23*, 394–398. [CrossRef]
- Wu, R.; Xue, Q.; Chu, Q.X.; Chen, F.C. Ultrawideband Dual-Polarized Antenna for LTE600/LTE700/GSM850/GSM900 Application. *IEEE Antennas Wirel. Propag. Lett.* **2021**, *20*, 1135–1139. [CrossRef]
- Dai, X.; Luk, K.M. A Wideband Dual-Polarized Antenna for Millimeter-Wave Applications. *IEEE Trans. Antennas Propag.* **2021**, *69*, 2380–2385. [CrossRef]
- Jiang, W.; Liao, S.; Che, W.; Xue, Q. Millimeter-Wave Wideband $\pm 45^\circ$ Dual-Polarized Phased Array Antenna Based on Compact Wideband Widebeam Dipole Element Antenna. *IEEE Antennas Wirel. Propag. Lett.* **2023**, *22*, 1813–1817. [CrossRef]
- Li, B.; Yin, Y.Z.; Hu, W.; Ding, Y.; Zhao, Y. Wideband Dual-Polarized Patch Antenna with Low Cross Polarization and High Isolation. *IEEE Antennas Wirel. Propag. Lett.* **2012**, *11*, 427–430. [CrossRef]
- Chu, Q.X.; Wen, D.L.; Luo, Y. A Broadband $\pm 45^\circ$ Dual-Polarized Antenna with Y-Shaped Feeding Lines. *IEEE Trans. Antennas Propag.* **2015**, *63*, 483–490. [CrossRef]
- Huang, H.; Liu, Y.; Gong, S. A Broadband Dual-Polarized Base Station Antenna with Sturdy Construction. *IEEE Antennas Wirel. Propag. Lett.* **2017**, *16*, 665–668. [CrossRef]
- Wen, L.H.; Gao, S.; Luo, Q.; Mao, C.X.; Hu, W.; Yin, Y.; Zhou, Y.; Wang, Q. Compact Dual-Polarized Shared-Dipole Antennas for Base Station Applications. *IEEE Trans. Antennas Propag.* **2018**, *66*, 6826–6834. [CrossRef]
- Zhou, Z.; Wei, Z.; Tang, Z.; Yin, Y. Design and Analysis of a Wideband Multiple-Microstrip Dipole Antenna with High Isolation. *IEEE Antennas Wirel. Propag. Lett.* **2019**, *18*, 722–726. [CrossRef]
- Li, Y.; Zhao, Z.; Tang, Z.; Yin, Y. Differentially-Fed, Wideband Dual-Polarized Filtering Antenna with Novel Feeding Structure for 5G Sub-6 GHz Base Station Applications. *IEEE Access* **2019**, *7*, 184718–184725. . [CrossRef]

12. Ye, L.H.; Li, Y.J.; Wu, D.L. Dual-Wideband Dual-Polarized Dipole Antenna with T-Shaped Slots and Stable Radiation Pattern. *IEEE Antennas Wirel. Propag. Lett.* **2022**, *21*, 610–614. [CrossRef]
13. Fu, S.; Cao, Z.; Quan, X.; Xu, C. A Broadband Dual-Polarized Notched-Band Antenna for 2/3/4/5G Base Station. *IEEE Antennas Wirel. Propag. Lett.* **2020**, *19*, 69–73. [CrossRef]
14. Wen, L.H.; Gao, S.; Mao, C.X.; Luo, Q.; Hu, W.; Yin, Y.; Yang, X. A Wideband Dual-Polarized Antenna Using Shorted Dipoles. *IEEE Access* **2018**, *6*, 39725–39733. [CrossRef]
15. Zhao, L.; Zhu, H.; Zhao, H.; Liu, G.; Wang, K.; Mou, J.; Zhang, W.; Li, J. Design of Wideband Dual-Polarized ME Dipole Antenna with Parasitic Elements and Improved Feed Structure. *IEEE Antennas Wirel. Propag. Lett.* **2023**, *22*, 174–178. [CrossRef]
16. Ye, L.H.; Ye, D.G.; Chen, Z.; Li, J.F. Ultra-Wideband Dual-Polarized Base-Station Antenna with Stable Radiation Pattern. *IEEE Trans. Antennas Propag.* **2023**, *71*, 1919–1924. . [CrossRef]
17. Peng, J.D.; Li, X.L.; Ye, L.H.; Li, J.F.; Wu, D.L.; Zhang, X.Y. Low-Profile Wideband Dual-Polarized Dipole Antenna with Parasitic Strips and Posts. *IEEE Antennas Wirel. Propag. Lett.* **2023**, *22*, 844–848. [CrossRef]
18. Yang, J.Y.; Ding, X.H.; Yang, W.W.; Chen, J.X. Compact Wideband Dual-Polarized Antenna Using Shared Dipoles Loaded with Partially Coupled Stubs. *IEEE Antennas Wirel. Propag. Lett.* **2023**, *22*, 2886–2890. [CrossRef]
19. Wu, J.; Yang, S.; Chen, Y.; Qu, S.; Nie, Z. A Low Profile Dual-Polarized Wideband Omnidirectional Antenna Based on AMC Reflector. *IEEE Trans. Antennas Propag.* **2017**, *65*, 368–374. [CrossRef]
20. Liu, Q.; Liu, H.; He, W.; He, S. A Low-Profile Dual-Band Dual-Polarized Antenna with an AMC Reflector for 5G Communications. *IEEE Access* **2020**, *8*, 24072–24080. [CrossRef]
21. Yang, S.; Liang, L.; Wang, W.; Fang, Z.; Zheng, Y. Wideband Gain Enhancement of an AMC Cavity-Backed Dual-Polarized Antenna. *IEEE Trans. Veh. Technol.* **2021**, *70*, 12703–12712. [CrossRef]
22. de Cos, M.E.; Heras, F.L.; Franco, M. Design of Planar Artificial Magnetic Conductor Ground Plane Using Frequency-Selective Surfaces for Frequencies Below 1 GHz. *IEEE Antennas Wirel. Propag. Lett.* **2009**, *8*, 951–954. [CrossRef]

Disclaimer/Publisher’s Note: The statements, opinions and data contained in all publications are solely those of the individual author(s) and contributor(s) and not of MDPI and/or the editor(s). MDPI and/or the editor(s) disclaim responsibility for any injury to people or property resulting from any ideas, methods, instructions or products referred to in the content.



Article

Reliability Evaluation Method for Array Antenna Considering Performance Changes

Xinxin Huang, Sai Zhu * and Guanhui Liang

Department of Electronic and Optical Engineering, Shijiazhuang Campus, Army Engineering University of PLA, Shijiazhuang 050003, China; sjzhxx2023@aeu.edu.cn (X.H.); lianggh@aeu.edu.cn (G.L.)
* Correspondence: zhuz@aeu.edu.cn

Abstract: The existing array antenna reliability evaluation method based on the n/k system is analyzed. As the failed T/R module's influence on the array antenna's performance is not considered, the reliability of the array antenna is overestimated. To improve the accuracy of the array antenna reliability evaluation, the performance changes caused by T/R failures in different locations are considered. The reliability evaluation method considering the performance changes is established. The performance and probability of the array antenna's state are calculated, and accurate reliability is obtained by calculating all the available state's probabilities. The complexity of the reliability evaluation method is analyzed, and the reliability evaluation method for large-scale array antennae is established. The large-scale array antenna is divided into several subarrays. The performance and reliability of each subarray are analyzed, and the array antenna's reliability is calculated through subarrays. The array antenna's performance changes are considered with the proposed method, the overestimation problem of the existing reliability evaluation method is solved, and the accuracy of the array antenna reliability evaluation is improved.

Keywords: array antenna; reliability evaluation; performance; subarray

1. Introduction

An array antenna has characteristics such as high power, high gain, and fast beam scanning, and it is widely used in communication systems [1–3], radar equipment [4,5] and other applications [6–8]. A phased array antenna is composed of a large number of transceiver channels, which consist of a transmitter and receiver module (T/R module) and element. The T/R module mainly completes the amplitude and phase adjustment of the transmitted and received signals. The fault of transmitting and receiving channels and the coupling [9] between different channels are important problems in the application of array antennas. When a fault occurs in the transceiver channel, such as the T/R module being faulty, the array antenna's performance will be changed. The array antenna's performance could decline with a large number of transceiver channel faults [10,11], and the expected function of the array antenna could be affected seriously. Lots of array antennas with high reliability have been designed [12–15].

Reliability is an important factor for the array antenna [16–18], and many reliability models have been proposed. The basic reliability model used for array antenna is the “K-out-of-N” model [19,20]. If the single T/R module in the array antenna is a failure, only the signal radiation of the connected element is affected. The performance of the other transceiver channel is unchanged. When a small number of transceiver channels fail, the array antenna's performance will be slightly reduced. Therefore, the array antenna is a typical “K-out-of-N” system; that is, the array antenna's total transceiver channels are noted as n . When k transceivers are working properly, the array antenna's expected

Citation: Huang, X.; Zhu, S.; Liang, G. Reliability Evaluation Method for Array Antenna Considering Performance Changes. *Sensors* **2024**, *24*, 1914. <https://doi.org/10.3390/s24061914>

Academic Editor: Antonio Lázaro

Received: 7 December 2023

Revised: 6 March 2024

Accepted: 9 March 2024

Published: 16 March 2024



Copyright: © 2024 by the authors. Licensee MDPI, Basel, Switzerland. This article is an open access article distributed under the terms and conditions of the Creative Commons Attribution (CC BY) license (<https://creativecommons.org/licenses/by/4.0/>).

function can be completed. The transceiver's reliability function is noted as $r(t)$, and the array antenna's reliability function is [19]

$$R(t) = \sum_{i=k}^n C_n^i r(t)^i (1 - r(t))^{n-i}. \quad (1)$$

The array antenna's mean time to failure (MTTF) is noted as θ , and the array antenna's average lifetime is [21]

$$\theta = \int_0^\infty R(t) dt. \quad (2)$$

In practical applications, when the number of failed transceiver channels is less than 10% of the system's total transceiver channel number, the array antenna's performance is considered to have no significant change, and the array antenna can be used normally. That is, $k = 90\% \times n$, and the maximum number of failed transceiver channels is $f_{\max} = 10\% \times n$.

In this reliability model, only the number of failed transceiver channels is analyzed, and the location of the failed transceiver channel is not considered. When the location of the failed transceiver channel is changed, its influence on the array antenna's performance is different. Therefore, even with the faulty transceiver channel number $f < f_{\max}$, if the faulty transceiver channels are concentrated in a certain area, the array antenna's performance could degenerate seriously, and the requirement would not be met. Therefore, there is a reliability overestimation problem during the array antenna's reliability evaluation using this reliability model.

The reliability model of an AESA subsystem is formed using the "K-out-of-N" reliability configuration [22]. The reliability model [23] based on the performance margin is developed for satellite-based phased array antennas, considering the performance degradation and multiple sources of uncertainties. The distribution of the uplink sum-rate is asymptotically analyzed for an LIS system, and the reliability of large intelligent surfaces has been analyzed in [24]. The reliability of the array antenna with k/n redundant structure is analyzed in [25]. The reliability of irregular subarrayed phased array antenna is analyzed in [26]. A new method that efficiently and effectively analyses the statistical performance of phased-array antenna systems using a spherical harmonics expansion approach is presented in [27].

In this paper, a reliability evaluation method of array antenna considering performance changes is proposed. The performance degeneration process caused by the transceiver channel faults is considered, and a more accurate reliability is calculated. The rest of this paper is organized as follows. In Section 2, the Reliability evaluation method considering performance changes is presented, and the reliability calculation flow considering performance changes is presented and analyzed in Section 3. The reliability calculation flow considering performance changes for larger-scale array antenna is proposed in Section 4. The proposed Reliability evaluation method of array antenna considering performance changes is simulated and verified in Section 5. Finally, conclusions are reached in Section 6. Furthermore, more suggestions are put forward for future research.

2. Reliability Analysis Flow Considering Performance Changes

To improve the accuracy of the array antenna's reliability analysis, the performance of the array antenna in each state is calculated first. The available state and unavailable state are determined according to the performance threshold. Then the probability function of the available state is analyzed, and the reliability of the array antenna and its average life can be calculated. The steps of the reliability analysis flow are shown in Figure 1.

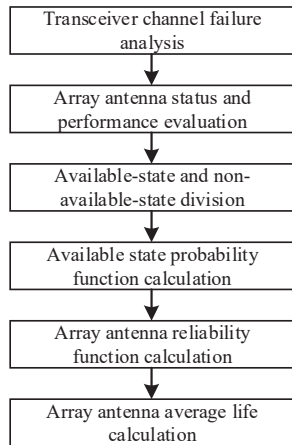


Figure 1. Array antenna reliability evaluation process.

Six steps are included in the array antenna reliability evaluation process, as shown in Figure 1. The transceiver channel's failure will be analyzed first. Then the array antenna's status and performance would be evaluated. Based on the array antenna's performance analysis, the array antenna's state could be divided into available-state and non-available-state. Then the probability of all available states could be calculated, and the array antenna's reliability function could be established. At last, the array antenna's average life could be calculated.

- (1) Transceiver channel failure analysis. According to the structure and composition of the array antenna, the failure characteristic of the transceiver channel is analyzed. The basis for the array antenna's state-changing analysis is provided.
- (2) Array antenna's status and performance evaluation. According to the array antenna's scale and structure, all possible states of the array antenna are defined. The array antenna's performance in different states is calculated.
- (3) Available-state and non-available-state divisions. According to the array antenna's performance in each state and the performance requirements during the application process, all possible states of the array antenna are divided into available states and non-available states. In the available state, the array antenna's performance could meet the application requirements and the array antenna can be used normally. In non-available states, the application requirement cannot be satisfied by the array antenna's performance, and the array antenna cannot be used normally.
- (4) Available state probability function calculation. According to the fault law of the array antenna's transceiver channel, considering the transition between different states, the probability function of each available state is calculated, and the probability of the array antenna being in the available state at different times is determined.
- (5) Array antenna reliability function calculation. Based on the array antenna available state probability function calculation, the array antenna availability probability is obtained by adding all the available state probabilities together. And the array antenna's reliability function can be obtained.
- (6) Array antenna's average life calculation. Based on the calculation of the array antenna's reliability function, the array antenna's average life can be calculated with Formula (2).

The array antenna reliability evaluation process shown in Figure 1, evaluates each working state of the array antenna is evaluated. Each state's performance is analyzed, and the available state is determined according to the state performance and required performance threshold. Then the probability function of each available state is calculated according to the state changing and the transition probability between different

states. Based on the available state's probability, the array antenna's reliability function and average life can be calculated. The impact of the failure on performance is considered in the reliability evaluation process, and the array antenna's reliability can be calculated accurately.

3. Reliability Calculation Flow Considering Performance Changes

3.1. Reliability Calculation Flow

To improve the analysis accuracy of array antenna reliability, it is necessary to accurately calculate the performance of the array antenna in each state, and determine whether the state is available according to the performance threshold. Then the available states and unavailable states can be determined, the probability of each available state is analyzed, and the array antenna's reliability can be calculated. The steps of the reliability calculation flow are shown as follows.

(1) Failure analysis of transceiver channels

The array antenna is composed of a large number of transceiver channels, and the structure and function of all transceiver channels are the same. The transceiver channel is composed of a transceiver module (T/R module) and radiation antenna, as shown in Figure 2.

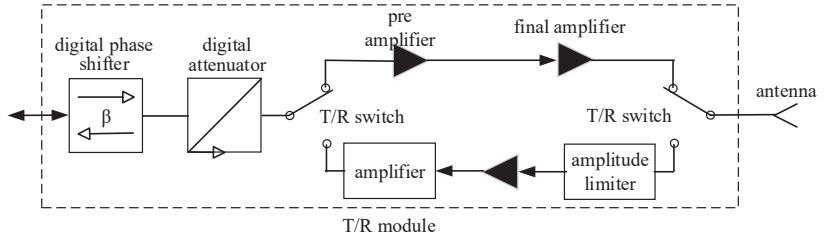


Figure 2. Array antenna's transceiver channel structure.

In the transceiver channel structure shown in Figure 2, the probability of the antenna's failure is small. The T/R module is an electronic module composed of a variety of RF devices. The probability of the T/R module's failure conforms to the exponential distribution law, that is, its fault probability function is [21]

$$F(t) = 1 - e^{-\lambda t}, \quad (3)$$

where λ is the failure rate.

For the transceiver channel composed of the T/R module and radiant antenna, since the probability of the antenna's failure is very small, the failure probability of the transceiver channel is equal to the T/R module's failure probability. So the failure probability function of the transceiver channel is the same as Formula (3).

(2) Array status and performance evaluation

In the working process of the array antenna, the array antenna would be in different states, with the continuous failure of the different transceiver channels. When the array antenna is working in a different state, its performance changes too. Array antenna performance is usually represented by the antenna pattern and the parameters such as the maximum secondary lobe level, the half-power beam width, and the antenna direction coefficient.

For the array antenna to be analyzed, the total number of transceiver channels is recorded as N , and the signal normalization amplitude of each transceiver channel is $A = [A_i], i = 0, 1, \dots, N - 1$. All the array antenna's possible states with different failure transceiver channels are traversed, and the array antenna's parameters such as maximum

secondary lobe level, half-power beam width, and antenna direction coefficient are calculated in each state. The performance of the array antenna in a certain state is evaluated with its key parameters. The calculation process is shown in Figure 3.

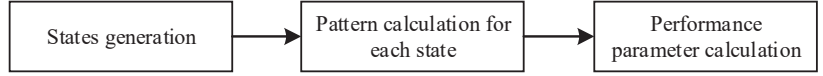


Figure 3. Array antenna status and performance evaluation process.

There are three steps in the evaluation process shown in Figure 3, state generation, direction map calculation, and performance parameter calculation:

- (a) States generation. All possible states of the array antenna are generated. For the array antenna with N transceiver channels, the number of faults $n = 0, 1, \dots, N - 1$. Under each fault number, the corresponding total number of states is C_N^n . Then the total number of the array antenna in all possible states is $C_N^0 + C_N^1 + \dots + C_N^N = 2^N$. The set of array antenna's states is denoted as $S = \{S_i\}$, where S_i is the i th state of the array antenna, which contains 0, 1 values with the number of N , when $S_i(j) = 1$, it means that the array antenna's j th transceiver channel is normal; When $S_i(j) = 0$, it means that the array antenna's j th transceiver channel is faulty.
- (b) Pattern calculation for each state. For each state S_i , the channel signal amplitude of $A \cdot S_i$ is regenerated according to its state. The antenna pattern in that state is calculated according to the pattern formula.
- (c) Performance parameter calculation. Based on the calculation results of the antenna pattern, the array antenna's performance parameters are calculated according to the definition of each performance parameter.
- (3) Available state and non-available state division

Based on the performance evaluation of the array antenna in each state, every state is marked as an available state or non-available state, according to the application requirements of performance.

The application requirements of performance parameters are denoted as maximum secondary lobe level maxSLL_L , average secondary lobe level avSLL_L , half-power beam width HPBW_L , first null beam width FNBW_L and direction coefficient D_L . For the array antenna under the status S_i , its maximum secondary lobe level, average secondary lobe level, half-power beam width, first null beam width and direction coefficient are denoted as maxSLL_{S_i} , avSLL_{S_i} , HPBW_{S_i} , FNBW_{S_i} and D_{S_i} . When its performance parameters meet $\text{maxSLL}_{S_i} > \text{maxSLL}_L$, $\text{avSLL}_{S_i} > \text{avSLL}_L$, $\text{HPBW}_{S_i} < \text{HPBW}_L$, $\text{FNBW}_{S_i} < \text{FNBW}_L$, $D_{S_i} > D_L$, the state S_i is an available state. If any of the parameters cannot meet the application requirements, the state is a non-available state.

The performance parameters and their thresholds are set according to the application scenarios of the array antenna.

- (4) Available state probability calculation

For the available state of the array antenna, the occurrence probability of the state is calculated based on the number of faulty transceiver channels.

For the available status S_i , the number of normal transceiver channels in the array antenna is N_n

$$N_n = \sum_{j=1}^N S_i(j), \quad (4)$$

In this state, the number of faulty transceiver channels in the array antenna is $N_f = N - N_n$.

At time t , the probability of a transceiver channel failure is shown in Equation (3), and then the occurring probability of the available state S_i is

$$p_{s_i}(t) = \left(1 - e^{-\lambda t}\right)^{N_f} \left(e^{-\lambda t}\right)^{N_n}. \quad (5)$$

(5) Array antenna's reliability function calculation

Based on the analysis of all available state's probability, the array antenna's reliability function is calculated. The array antenna's reliability function is the sum of all the available state's probability. Note that the array antenna reliability function as $R(t)$, then

$$R(t) = \sum p_{s_i}(t). \quad (6)$$

In Equation (6), S_i is all available states.

By substituting Formula (6) into Formula (2), the average life of the array antenna can be obtained.

3.2. Suitable Size Analysis of Array Antenna

For array antennas with size N , the total number of array antenna states that need to be analyzed is 2^N . It can be seen that the calculation amount in the reliability evaluation process is increased exponentially with the array antenna's size. For array antennas with different sizes, the number of states that need to be calculated is shown in Table 1.

Table 1. State number for array antenna with different sizes.

Array Antenna Scale N	State Number
10	1024
20	1.05×10^6
30	1.07×10^9
40	1.10×10^{12}
50	1.13×10^{15}
60	1.15×10^{18}
70	1.18×10^{21}
80	1.21×10^{24}
90	1.24×10^{27}
100	1.27×10^{30}

As can be seen from Table 1, when the array antenna's size is greater than 50, the total number of states calculated is bigger than 1.13×10^{15} . The reliability evaluation process would be seriously time-consuming, so the method in this paper only targets small-scale array antennas with a scale of less than 50.

Because every possible state needs to be analyzed during the calculation process shown in Figure 1, the calculation amount of the array state and its performance evaluation is rapidly increased with the array antenna's size. For small-scale array antennas, the reliability and average life can be accurately obtained by this method. For large-scale array antennae, the total number of available states is increased dramatically, the computing amount increases significantly, and the cost of computing time will be unbearable.

4. Reliability Calculation Flow Considering Performance Changes for Larger Scale Array Antenna

To improve the accuracy of reliability calculation, reduce the reliability calculation amount of large-scale array antenna, and improve the calculation speed, the reliability calculation flow considering performance changes for larger-scale array antenna is proposed. Based on the "K-out-of-N" reliability model shown in Equation (1), the more accurate reliability function is obtained by eliminating the fault state probability. The specific steps are shown in Figure 4.

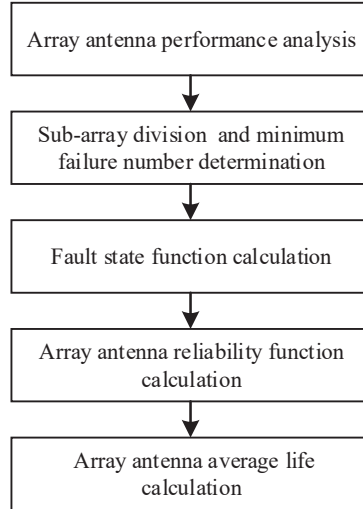


Figure 4. The reliability calculates flow for large-scale array antenna.

There are five steps in the reliability calculation flow for large-scale array antennas shown in Figure 2. That is array antenna performance analysis, subarray division and determination of the minimum number of faults, fault state function calculation, array antenna reliability function and average life calculation.

- (1) Array antenna's performance analysis. The array antenna's performance is analyzed with different faults occurring in different scale subarrays. The subarray is a small array composed of some transceiver channels in the array antenna. The basis for subarray division and determination of T/R modules' minimum failure number is provided with the analysis result.

During the array antenna's performance analysis, the analysis range is determined as a circle. And the center of the array antenna is taken as the center of the circle, and the fixed length r is taken as the radius. Within the analysis range, the fault number is set as $f \in [1, f_{\max}]$, and the fault position is assigned randomly. Then the array antenna's performance is calculated. In the process of performance analysis, the changes of gain and maximum sidelobe level are analyzed emphatically. In the performance calculation process of each analysis range, for the fixed failures number f , the performance calculation under multiple random failures can be performed, and the mean of the calculation results is taken as the performance of the analysis range r under the n failure number f .

- (2) The subarray division and the determination of the minimum failure number. According to the performance of the array antenna under different analysis ranges and different fault numbers, the array antenna is divided into multiple subarrays concerning the working performance requirements. And the minimum failure number is determined. If the number of failures that occurred in the subarray is bigger than the minimum failure number, the array antenna's performance would not satisfy the working requirement. If the array antenna can be divided into m subarrays, for the i th subarray, $i \in [0, m - 1]$, its radius, T/R module number and minimum fault number are recorded as r_i , n_i , and f_i , respectively, as shown in Table 2.

Table 2. Subarray division.

Subarray Sequence Number	Radius r	TR Number in Subarray	Minimal Failure Number
0	r_0	n_0	f_0
1	r_1	n_1	f_1
2	r_2	n_2	f_2
...
$m - 1$	r_{m-1}	n_{m-1}	f_{m-1}

In the array antenna, the transceiver channel that is closer to center of the array antenna has a greater impact on the array antenna's performance. For the two subarrays with the sequence numbers i and j , if the radius $r_i < r_j$, there will usually be $n_i \leq n_j, f_i \leq f_j$.

- (3) Array antenna's fault state function $F(t)$ calculation. When the number of faulty transceiver channels f is less than f_{\max} , it means $f < f_{\max}$, the probability function that the array antenna is unavailable is denoted as $F(t)$. $F(t)$ is the sum of the failure probability of each subarray causing the array to be unavailable. Taking subarray i as an example, the minimum failure number that causes the array to be unavailable is f_i , and then the probability function $F_i(t)$ that the array would be unavailable is

$$F_i(t) = r(t)^{n-n_i} \cdot \sum_{j=f_i}^{f_{\max}} C_{n_i}^j r(t)^{n_i-j} (1-r(t))^j - r(t)^{n-n_{i-1}} \cdot \sum_{j=f_i}^{f_{\max}} C_{n_{i-1}}^j r(t)^{n_{i-1}-j} (1-r(t))^j. \quad (7)$$

Array antenna's fault state function is

$$\begin{aligned} F(t) &= \sum_{i=0}^{m-1} F_i(t) \\ &= \sum_{i=0}^{m-1} \left[r(t)^{n-n_i} \cdot \sum_{j=f_i}^{f_{i+1}-1, f_{\max}} C_{n_i}^j r(t)^{n_i-j} (1-r(t))^j \right]. \end{aligned} \quad (8)$$

- (4) Array antenna's reliability function and average life calculation. Based on the k out of n reliability model of Equation (1), subtract the array antenna's fault state function, and the array antenna's reliability function $R(t)$ can be obtained

$$\begin{aligned} R(t) &= \sum_{i=k}^n C_n^i r(t)^i (1-r(t))^{n-i} - F(t) \\ &= \sum_{i=k}^n C_n^i r(t)^i (1-r(t))^{n-i} - \sum_{i=0}^{m-1} \left[r(t)^{n-n_i} \cdot \sum_{j=f_i}^{f_{i+1}-1, f_{\max}} C_{n_i}^j r(t)^{n_i-j} (1-r(t))^j \right], \end{aligned} \quad (9)$$

where $k = 0.9n$ and $f_{\max} = 0.1n$.

Bring Formula (9) into Formula (2), and the average life of the array antenna can be calculated.

5. Simulation and Analysis

5.1. Reliability Analysis for Small-Scale Array Antenna

Taking the Chebyshev linear array as an example, the reliability calculation is carried out by using the existing method and the proposed method in this paper. The linear array scale N is set to 20, the array spacing $d = 0.5\lambda$, λ is the wavelength of the radiated electromagnetic wave. And the maximum secondary lobe level $SLL = -30$ dB. After the array antenna's pattern synthesis, the maximum secondary lobe level (maxSLL), mean secondary lobe level (avSLL), half-power beam width (HPBW), first null beam width (FNBW) and direction coefficient D of the array antenna under different faults are calculated.

The failure rate of the transceiver channel is set as $\lambda = 4.5 \times 10^{-6}/h$. The maximum number of faults tolerated is 2 when the existing method is used for array antenna reliability

analysis. And the number of normal transceiver channels k is 18~20, and the array antenna's reliability function is

$$R(t) = \sum_{i=18}^{20} C_{20}^i \left(e^{-4.5 \times 10^{-6} t} \right)^i \left(1 - e^{-4.5 \times 10^{-6} t} \right)^{20-i} \quad (10)$$

The array antenna's reliability is analyzed with the proposed method. When the array antenna is working normally, the maximum secondary lobe level threshold is set as $SLL_L = -21$ dB. Then the $2^{32} = 1,048,576$ states of the array antenna are analyzed, and the maximum secondary lobe level of each state is analyzed. All the available states are determined according to the threshold, and finally, the total number of available states is 120. The probability function of each available state is calculated using Equation (5), and the array antenna's reliability is calculated with Equation (6). The array antenna's reliability is evaluated with the proposed method and the existing method [19], as shown in Figure 5. When calculated using existing methods, the average life of the array antenna is 35,203 h. When calculated using the proposed method in this paper, the average life of the array antenna is 18,937 h.

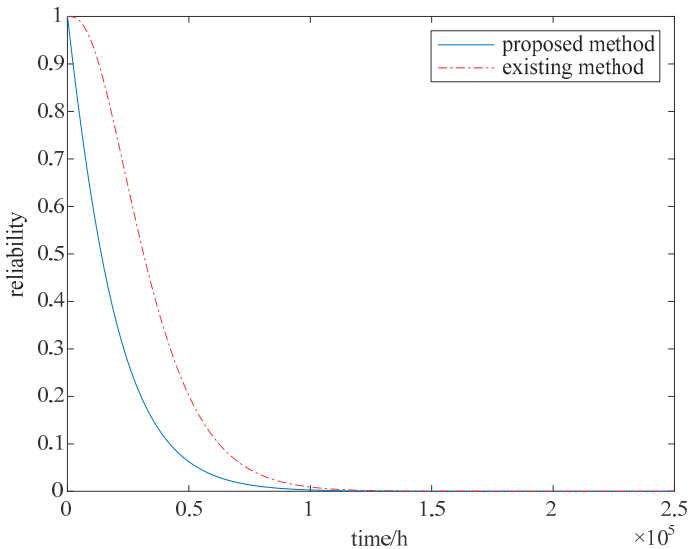


Figure 5. Reliability of array antenna with small-scale.

As can be seen from Figure 5 and Table 3, the number of faulty transceiver channels was only considered in the evaluation of existing methods, and the impact of faults in different locations was not considered. For the array antenna with a scale of 20 in this paper, when the number of fault transceiver channels is 1, if the fault location is in the center of the array, the array antenna's performance cannot meet the requirements. Although the number of failures meets the requirements, its performance does not meet the requirements, and the array antenna in this state is unavailable. In the existing reliability evaluation methods, the array antenna status is treated as non-available states only based on the number of fault transceiver channels, resulting in an overestimation of the reliability evaluation results. The available state and unavailable state are determined according to the array antenna's performance in the proposed method, and the reliability evaluation results are more accurate.

Table 3. Array antenna's average life of small-scale array antenna with different methods.

Method	Array Antenna Scale	Average Life/h
existing method [19]	20	35,203
proposed method	20	18,937

5.2. Reliability Analysis for Larger-Scale Array Antenna

Taking the linear array containing 64 elements as an example, the array antenna's reliability is analyzed with the proposed method and the existing method. The linear array is synthesized with the Chebyshev method, and the maximum secondary lobe level $SLL = -45$ dB. Based on the subarray's influence on the array antenna's performance, the array antenna is divided into four subarrays, and the minimum failure number is determined based on the influence of faulty cells on the array antenna.

When the primary–secondary lobe ratio (SLR) is considered to meet $SLR < 0.5 \cdot iniSLR$, that is, the primary–secondary lobe ratio drops to half of the initial primary–secondary lobe ratio, the array antenna is considered as faulty, and the minimum failure number in each subarray is shown in Table 4.

Table 4. Subarray division for experimented array antenna.

Subarray Sequence Number	Radius r	TR Number in Subarray	Minimal Failure Number
0	12	24	3
1	21	42	4
2	28	56	5
3	32	64	5

The failure rate of the transceiver channel is set as $\lambda = 4.5 \times 10^{-6}/h$, and the ideal reliability of the array antenna, the probability of the array antenna's fault state, and the array antenna's reliability considering the fault impact are analyzed by using Formulas (1), (4) and (5), respectively. And the results are shown in Figure 6 and Table 5.

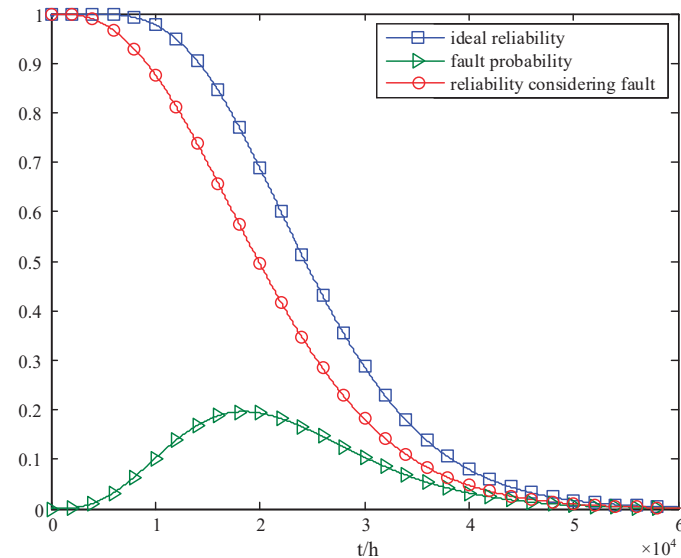
**Figure 6.** Reliability changes considering performance changes.

Table 5. Array antenna's average life of large-scale array antenna with different methods.

Method	Array Antenna Scale	Average Life/h
existing method [19]	64	25,531
proposed method	64	21,158

As can be seen from Figure 6 and Table 5, due to the faults at different locations having different effects on the array antenna's performance, even if the number of faults in the array antenna is less than 10%, the array antenna still has a large probability of failure. And the array antenna's reliability calculated with the existing method is overestimated. When the array antenna's reliability is analyzed with Equation (1), the average life of the array antenna is 25,531 h, and the average life of the array antenna is 21,158 h when considering the impact of faults on different subarrays.

Through the reliability analysis experimental results of large-scale array antenna and small-scale array antenna, it can be seen that the influence of performance changes on the array antenna's reliability is considered in the proposed method. Each available state of the array antenna is determined accurately by analyzing the performance of all possible states, the array antenna's reliability function is calculated based on all available states, and accurate reliability evaluation for the array antenna is achieved. For the large-scale array antenna, based on the proposed calculation process, the sub-array is further divided. The performance of each sub-array is analyzed, and the sub-array's reliability is calculated. Then the accurate reliability evaluation for the large-scale array antenna is completed. Not only the influence of different fault locations and fault numbers on the array antenna's performance is considered, but also the influence of the array antenna's size on the reliability evaluation speed is considered in the proposed method. The accurate and rapid reliability evaluation for the array antenna is realized, and a novel method for the large-scale array antenna's high-precision reliability evaluation is provided.

6. Conclusions

To improve the accuracy of the array antenna's reliability analysis, a reliability evaluation process considering performance changes is established. The array antenna's reliability is calculated through all the possible available state analyses. Through the analysis of the array antenna's performance in every state, each non-available state is determined, the reliability overestimation problem is solved, and the accuracy of the array antenna's reliability evaluation is improved. For the large-scale array antenna, based on the "K-out-of-N" model, the array antenna is divided into multiple subarrays, and the minimum failure number for each subarray is determined. The array antenna's fault function is determined by each subarray. The array antenna's reliability model considering the performance changes is obtained. The simulation results show that the influence of fault position and number on the array antenna's performance is considered in the proposed method, the overestimation problem of existing evaluation methods is reduced and the accuracy of array antenna reliability evaluation is improved.

Author Contributions: Conceptualization, S.Z.; methodology, X.H.; validation, G.L. All authors have read and agreed to the published version of the manuscript.

Funding: The APC was funded by National Natural Science Foundation of China under Grant No. 61601495, and Youth Talent Promotion Project of China under Grant No. 18-JCJQ-QT-001.

Institutional Review Board Statement: Not applicable.

Informed Consent Statement: Not applicable.

Data Availability Statement: Data are contained within the article.

Conflicts of Interest: The authors declare no conflict of interest.

Abbreviations

T/R	Transmitter and Receiver
MTTF	Mean Time To Failure
maxSLL	maximum Secondary Lobe Level
avSLL	average Secondary Lobe Level
HPBW	Half-Power Beam Width
FNBW	First Null Beam width

References

- Hamid, S.; Chopra, S.R.; Gupta, A.; Tanwar, S.; Florea, B.C.; Taralunga, D.D.; Alfarraj, O.; Shehata, A.M. Hybrid beamforming in massive MIMO for next-generation communication technology. *Sensors* **2023**, *16*, 7294. [CrossRef]
- Fan, F.F.; Chen, Q.L.; Xu, Y.X.; Zhao, X.F. A wideband compact printed dipole antenna array with SICL feeding network for 5G application. *IEEE Antennas Wirel. Propag. Lett.* **2022**, *22*, 283–287. [CrossRef]
- Sim, C.Y.D.; Lo, J.J.; Chen, Z.N. Design of a broadband millimeter-wave array antenna for 5G applications. *IEEE Antennas Wirel. Propag. Lett.* **2023**, *22*, 1030–1034. [CrossRef]
- Tan, Q.; Fan, K.; Yu, W.; Wang, W.; Liu, L.; Luo, G.Q. A circularly polarized magneto-electric dipole antenna array with wide AR and impedance bandwidth for millimeter-wave applications. *IEEE Antennas Wirel. Propag. Lett.* **2023**, *22*, 2250–2254. [CrossRef]
- El-Hameed, A.S.; Ouf, E.G.; Elboushi, A.E.; Seliem, A.G.; Izumi, Y. An improved performance radar sensor for K-band automotive radars. *Sensors* **2023**, *16*, 7070. [CrossRef]
- Yamauchi, Y.; Shimoi, N. Posture classification with a bed-monitoring system using radio frequency identification. *Sensors* **2023**, *16*, 7304. [CrossRef] [PubMed]
- Sekehravani, E.A.; Leone, G. Evaluation of the resolution in inverse scattering of dielectric cylinders for medical applications. *Sensors* **2023**, *16*, 7250. [CrossRef] [PubMed]
- Cho, H.; Jo, H.W.; Kim, J.W.; Kim, K.S.; Oh, J. Shorted trapezoidal SIW antenna with quasi-hemispherical pattern for 2D wide scanning planar phased array antenna. *IEEE Trans. Antennas Propag.* **2022**, *70*, 7211–7216. [CrossRef]
- Roshani, S.; Koziel, S.; Yahya, S.I.; Chaudhary, M.A.; Ghadi, Y.Y.; Roshani, S.; Golunski, L. Mutual coupling reduction in antenna arrays using artificial intelligence approach and inverse neural network surrogates. *Sensors* **2023**, *16*, 7089. [CrossRef]
- He, T.; Zhu, G.F.; Wang, L. Possible fault types and impact analysis of phased array antennas. In Proceedings of the 2019 IEEE 4th Advanced Information Technology, Electronic and Automation Control Conference (IAEAC 2019), Chengdu, China, 20–22 December 2019.
- Vakalis, S.; Nanzer, J.A. Analysis of element failures in active incoherent microwave imaging arrays using noise signals. *IEEE Microw. Wirel. Compon. Lett.* **2019**, *29*, 161–163. [CrossRef]
- Zhu, S.; Han, C.H.; Meng, Y.F.; Xu, J.W.; An, T. Embryonics based phased array antenna structure with self-repair ability. *IEEE Access* **2020**, *8*, 209660–209673. [CrossRef]
- Agrawal, A.K.; Holzman, E.L. Active phased array design for high reliability. *IEEE Trans. Aerosp. Electron. Syst.* **1999**, *35*, 1204–1211. [CrossRef]
- Costantine, J.; Tawk, Y.; Barbin, S.E. Reconfigurable antennas: Design and applications. *Proc. IEEE* **2015**, *103*, 424–437. [CrossRef]
- Koziel, S.; Dabrowska, A.P.; Hasan, M.A. Frequency based regularization for improved reliability optimization of antenna structures. *IEEE Trans. Antennas Propag.* **2021**, *69*, 4246–4251. [CrossRef]
- Kouassi, A.; Nguyen-Trong, N.; Kaufmann, T. Reliability-aware optimization of a wideband antenna. *IEEE Trans. Antennas Propag.* **2016**, *64*, 450–460. [CrossRef]
- Kumar, B.P.; Kumar, C.; Kumar, V.S. Reliability considerations of spherical phased array antenna for satellites. *IEEE Trans. Aerosp. Electron. Syst.* **2018**, *54*, 1381–1391. [CrossRef]
- Marchiori, G.; Formentin, F.; Rampini, F. Reliability-centered maintenance for ground-based large optical telescopes and radio antenna arrays. In Proceedings of the SPIE, Montréal, QC, Canada, 22 July 2014.
- Tymoteusz, B. VTS ZATOKA radar system reliability and availability analysis. *Int. J. Reliab. Qual. Saf. Eng.* **2007**, *14*, 537–545.
- Hongan, L.; Huairui, G.; Monteforte, A.; Mettas, A. Reliability analysis for phased array radar system. In Proceedings of the 2009 8th International Conference on Reliability, Maintainability and Safety, Chengdu, China, 20–24 July 2009; pp. 20–23.
- Serkan, E. Mean time to failure of weighted k-out-of-n: G systems. *Commun. Stat.-Simul. Comput.* **2015**, *44*, 2705–2713.
- Serkan, S.T.; Bakir, C. Reliability modeling & analysis for active phased array antenna design. In Proceedings of the 2017 Annual Reliability and Maintainability Symposium (RAMS), Orlando, FL, USA, 23–26 January 2017; pp. 1–5.
- Zhao, Z.C.; Chen, W.B.; Li, X.Y. Reliability modeling and analysis of satellite-based phased array antenna. In Proceedings of the 2022 13th International Conference on Reliability, Maintainability, and Safety (ICRMS), Kowloon, Hong Kong, 21–24 August 2022; pp. 238–242.
- Jung, M.; Saad, W.; Jang, Y. Reliability analysis of large intelligent surfaces (LISs): Rate distribution and outage probability. *IEEE Wirel. Commun. Lett.* **2019**, *8*, 1662–1666. [CrossRef]
- Yang, J.; Zhang, H.; Luo, H. Application of flexible degradation technology to phased-array antenna. In Proceedings of the 2021 2nd China International SAR Symposium (CISS), Shanghai, China, 3–5 November 2021; pp. 1–3.

26. Dong, W.; Xu, Z.H.; Wang, L.S.B. Array reliability analysis for irregular subarrayed phased array antenna. In Proceedings of the 2020 IEEE International Symposium on Antennas and Propagation and North American Radio Science Meeting, Montreal, QC, Canada, 5–10 July 2020; pp. 283–284.
27. Famoriji, O.J.; Akingbade, K.; Ogunti, E. Analysis of phased array antenna system via spherical harmonics decomposition. *IET Commun.* **2019**, *18*, 3097–3104. [CrossRef]

Disclaimer/Publisher’s Note: The statements, opinions and data contained in all publications are solely those of the individual author(s) and contributor(s) and not of MDPI and/or the editor(s). MDPI and/or the editor(s) disclaim responsibility for any injury to people or property resulting from any ideas, methods, instructions or products referred to in the content.



Article

mmWave Zero Order Resonant Antenna with Patch-like Radiation Fed by a Butler Matrix for Passive Beamforming

Manoj Prabhakar Mohan ¹, Hong Cai ², Arokiaswami Alphones ¹ and Muhammad Faeyz Karim ^{1,3,*}

- ¹ School of Electrical & Electronic Engineering, Nanyang Technological University, Singapore 639798, Singapore
² Institute for Microelectronic, IME, A*STAR, Singapore 117685, Singapore
³ ETID Department, Texas A&M University, College Station, TX 77843, USA
* Correspondence: faeyz@ntu.edu.sg

Abstract: A small zero-order resonant antenna based on the composite right-left-handed (CRLH) principle is designed and fabricated without metallic vias at 30 GHz to have patch-like radiation. The mirror images of two CRLH structures are connected to design the antenna without via holes. The equivalent circuit, parameter extraction, and dispersion diagram are studied to analyze the characteristics of the CRLH antenna. The antenna was fabricated and experimentally verified. The measured realized gain of the antenna is 5.35 dBi at 30 GHz. The designed antenna is free of spurious resonance over a band width of 10 GHz. A passive beamforming array is designed using the proposed CRLH antenna and the Butler matrix. A substrate integrated waveguide is used to implement the Butler matrix. The CRLH antennas are connected to four outputs of a 4×4 Butler matrix. The scanning angles are 12° , -68° , 64° , and -11° for excitations from port 1 to port 4 of the 4×4 Butler matrix feeding the CRLH antenna.

Keywords: CRLH antenna; mmWave antenna; resonant mode; radiation; patch antenna

1. Introduction

Recently, the millimeter wave (mmWave) spectrum has become popular due to its applications in wireless power transfer, synthetic aperture radar imaging, satellite systems, and non-destructive testing [1–3]. So, the design of the antennas and beam-forming circuits at mmWave frequencies has also gained much interest.

Techniques to miniaturize antennas have been used for a long time [4]. Most of the techniques fall into two categories: topology-based techniques and material-based miniaturization techniques. Techniques to minimize the size of the wide-band antenna were also reported in [4]. The antenna structures with large dimensions can be miniaturized by bending to form meander lines or broken into small segments using fractals. Even though engineering the ground planes helps reduce the size of the antenna, it also results in an increase in radiation on the back side. Periodic loading, which results in slow wave structures, can also be used to reduce the size of the antenna. Using high-dielectric substrates and superstrates and lowering the dielectric constant using perforation fall under material-based miniaturization. Using magnetodielectric substrates and using piezo electric materials also fall under this category [4]. CRLH concepts have been used in the design of leaky wave antennas and small resonant antennas [5]. The CRLH resonator has resonances in the left-handed region, the right-handed region, and the zero-order resonance. At zero-order resonance, the resonant frequency depends on the parameters of the CRLH resonator and not on the physical dimension of the CRLH resonator. So, a zero-order resonator (ZOR) can be designed at a frequency independent of its physical dimensions [5]. It is an important advantage compared to other miniaturization techniques. The miniaturization using metamaterial also comes under material-based miniaturization of the antennas [4].

Citation: Mohan, M.P.; Cai, H.; Alphones, A.; Karim, M.F. mmWave Zero Order Resonant Antenna with Patch-like Radiation Fed by a Butler Matrix for Passive Beamforming. *Sensors* **2023**, *23*, 7973. <https://doi.org/10.3390/s23187973>

Academic Editor: Antonio Lázaro

Received: 7 August 2023

Revised: 13 September 2023

Accepted: 13 September 2023

Published: 19 September 2023



Copyright: © 2023 by the authors. Licensee MDPI, Basel, Switzerland. This article is an open access article distributed under the terms and conditions of the Creative Commons Attribution (CC BY) license (<https://creativecommons.org/licenses/by/4.0/>).

The general structure of the CRLH resonator has a metallic via for achieving the left-handed inductance. The shape of the radiation pattern is mainly influenced by the position of the metallic via. So, even though CRLH resonators are smaller in size, the design of the antenna with patch-like radiation is difficult. Several techniques were used in the literature to obtain broad-side radiation using CRLH resonators at zero-order resonance, but monopole like radiation is more common. In [6], monopole-like radiation was achieved using a mushroom-like CRLH resonator and an inductor-loaded resonator. The metallic vias were at the center of the rectangular patch for the CRLH resonator and along the central axis for the inductor-loaded resonator. A patch-like radiation using the CRLH resonator at 4.88 GHz was reported in [7], where metallic-via were replaced by large patches. An eight-cell CRLH resonator arranged in a ring-like fashion with stubs connected at the center was used to design a dual-band antenna [8]. Since the stubs are connected at the center, metallic vias were avoided. Two semicircle patches with shorting pins at one corner formed a two-cell CRLH resonator in [9]. The radiation pattern achieved was patch-like, but if the position of the shorting pin was moved to the center of the semi-circle, monopole-like radiation could be obtained. Broadside radiation was achieved in [10] using a hybrid antenna consisting of a mushroom-type CRLH resonator imbedded inside a rectangular hole of a rectangular patch antenna. The antenna in [10] was fed using a circular patch with a coaxial probe. Via holes were connected to the patch antenna edges through switchable stubs [11] to obtain two types of radiation patterns. If the vias are connected to the patch antenna, negative permittivity is added, and a monopole-like radiation pattern is obtained at zero-order resonance. If the vias were not connected, the antenna in [11] would operate like a patch antenna. A monopolar radiation was obtained for the metamaterial antennas proposed in [12]. To avoid the metallic vias, a few papers designed the resonant antenna based on coplanar waveguide (CPW) [13,14], but CPW configuration increased the back lobes. An artificial magnetic conductor (AMC) screen has been used to minimize the back lobes [14], and it also acts as a separation layer between the human body and the antenna. In the mmWave frequency range, a small change in the dimensions will affect the performance to a greater extent. Therefore, for an antenna at mmWave, it is desirable to design it without metallic vias. A broad-band balun [15] and filter [16] where the CRLH is designed without metallic-via were reported. Only a few works have reported patch-like radiation at zero-order resonance, and that too at the lower frequency range. In this paper, ZOR with patch-like radiation at 30 GHz is designed.

The Butler matrix [17] is one of the methods to realize passive-beam-forming circuits. Since the operating frequency is 30 GHz, the substrate integrated waveguide (SIW) configuration is chosen to design the Butler matrix. The analysis of properties of SIW like dispersion characteristics, propagation constant, modeling, cutoff frequency, and relation between the width of the rectangular waveguide and SIW was reported in [18–20]. A review of different microwave circuits implemented on SIW was reported in [21]. The SIW discontinuities were analyzed in [22]. The taper was used in the integration of the microstrip and SIW [23,24] on a single substrate. The different transitions between SIW and other transmission lines were discussed in [25].

There are many beam-forming networks reported, like the Rotman lens [26], Blass matrix [27], Nolan matrix [28], and Butler matrix. The Blass matrix is a lossy network since it requires a direction coupler with a coupling coefficient of one to achieve a lossless Blass matrix [27]. The Nolan matrix is also a type of Blass matrix with losses suppressed, and it also has directional couplers and phase shifters [28]. Among the beam-forming networks, the Butler matrix is chosen because of its simple and modular design. A wide-band Butler matrix in SIW was proposed without crossover in [29]. The comparison between losses in microstrip bends and SIW bends at 77 GHz was also discussed [29]. A compact two-layer SIW Butler matrix was reported in [30] with reduced errors in magnitude and phase. Another two-layer 4 × 8 Butler matrix in SIW at 38 GHz was proposed in [31] with an antenna array in the third layer, and the crossover was avoided in this reported work also. A 4 × 8 Butler matrix with a reduced number of crossovers was presented in [32] with

amplitude tapering. The number of crossovers was reduced in the two-layer SIW Butler matrix reported in [33] by changing the -3 dB hybrid couplers near the input ports to E-plane hybrid couplers and by reversing the -3 dB hybrid couplers near the output ports. A 7×8 Butler matrix with an antenna array was implanted in three SIW layers in [34] where the boresight beam was created by merging two inputs at the center. The Butler matrix with a modified hybrid coupler was reported in [35]. A mmWave SIW Butler matrix designed at 60 GHz was systematically explained in [36]. The detailed design of the 30 GHz Butler matrix used in this paper is explained in [37]. Metamaterial properties were used to enhance the performance of the antenna implemented in SIW [38]. A power splitter was designed to support an array with two dipole antennas. An epsilon-negative lattice with 3×2 unit cells was used to increase the broadside gain and reduce the cross-section radiation in [38]. Here, the newly designed ZOR antenna is added to the Butler matrix implemented in SIW.

In this paper, a new CRLH resonant antenna at 30 GHz is designed without metallic vias to obtain patch-like radiation. The open-circuited CRLH transmission line is used to design the resonant structure, which is different from the balanced structures reported in [15,16]. The parameter extraction and analysis of CRLH structure using a dispersion diagram are provided along with the simulated and measured results in Section 2. The SIW Butler matrix is used as the feeding structure of the CRLH antenna for beam forming, and the results are discussed in Section 3.

2. Design of the CRLH Resonant Antenna

The CRLH resonant antenna is designed as shown in Figure 1. Usually, the CRLH structure is designed using an interdigital capacitor and a short-circuited stub. But the metallic vias in the short-circuited stub prevent the radiation in the broadside direction. To obtain patch-like radiation in the broadside direction, the CRLH resonator is formed without metallic vias. The interdigital capacitor with three fingers followed by a stub with length $l_1/2$ forms the first part of the resonator, and this is concatenated with its mirror image to form the CRLH structure. The interdigital capacitor and stub and their x -axis mirror image are concatenated to form the CRLH resonator, as shown in Figure 1. This creates a virtual zero at the center of the stub of the resonant antenna. So, the metallic vias needed for the short-circuit stub are removed. The electric field pattern of the CRLH resonant antenna, along with the equivalent circuit, is shown in Figure 2. From the electric field pattern, it can be found that the antenna has an electric zero approximately around the center of the antenna and at that point a virtual ground is formed. The interdigital capacitor with its three fingers is represented by L_{R1} and C_{L1} in the equivalent circuit shown in Figure 2b. The stub is represented by L_{L1} and C_{R1} . The mirror image of the interdigital capacitor and short-circuited stubs are also represented as L_{R1} and C_{L1} and L_{L1} and C_{R1} , respectively. The electric zero point between the interdigital capacitor and stub and their mirror image is represented as ground in Figure 2b.

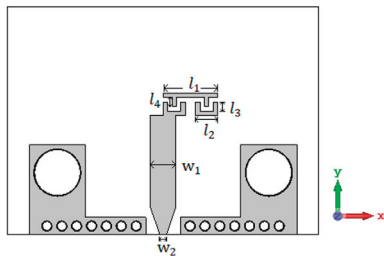


Figure 1. Structure of the CRLH antenna with dimensions $l_1 = 2.46$ mm; $l_2 = 1$ mm; $l_3 = l_4 = 0.4$ mm; $w_1 = 1.16$ mm; $w_2 = 0.3$ mm. The width and gap of the interdigital capacitor are 0.2 mm. The two L-shaped structures with two big metallic vias at the sides are for placing the connector.

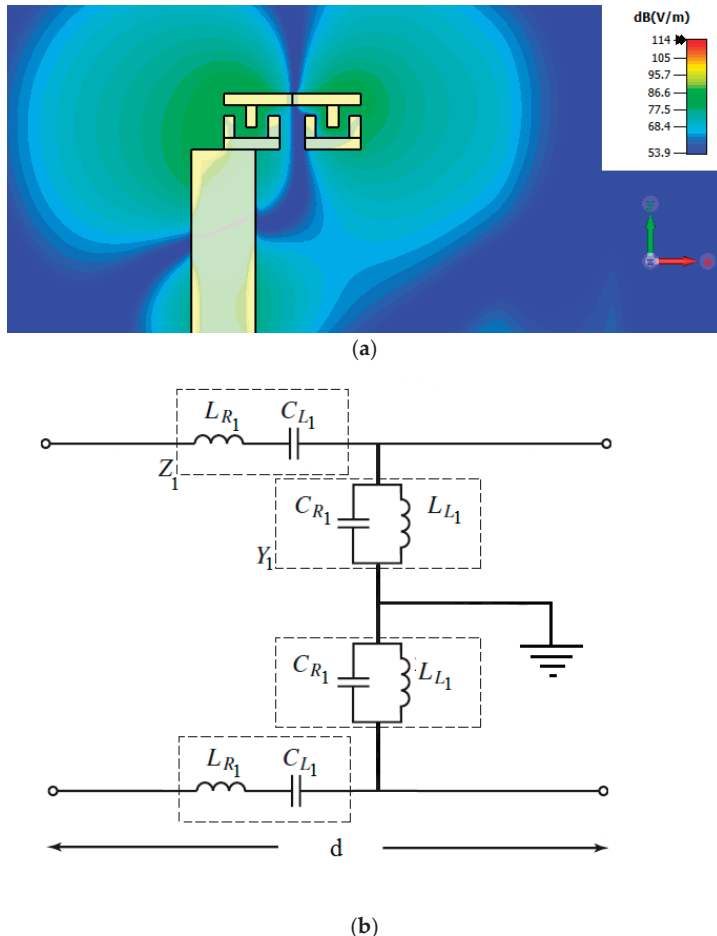


Figure 2. (a) Electric field distribution of the antenna; (b) equivalent circuit of the CRLH antenna.

The dispersion diagram is obtained by simulating the CRLH unit cell, as shown in Figure 3. The feed lines are de-embedded to obtain the S-parameter response of the CRLH unit cell, and from the S-parameters, the ABCD parameters are found out. The propagation constant is given as $\cosh\gamma d = (A + D)/2$ [39]. The dispersion diagram of the CRLH unit cell is shown in Figure 3. The dispersion diagram shows the CRLH unit cell is unbalanced. The left-handed response is below 30 GHz, and the right-handed response is above 40 GHz. The attenuation gap is between 30 GHz and 40 GHz. The shunt resonance is around 30 GHz, and the series resonance is around 40 GHz. So, the open-circuited resonator formed from this unit cell is resonating at around 30 GHz. The antenna is formed from the open-circuit CRLH resonator.

The antenna is fabricated on Rogers substrate RO4003c with a dielectric constant of 3.55, a loss tangent of 0.0027, and a thickness of 0.508 mm. The photograph of the fabricated structure is shown in Figure 4. The simulated and measured reflection coefficient (S_{11}) responses of the antenna are compared in Figure 5. The simulated and measured S parameter responses match well. There is a slight frequency shift, which is due to the fabrication errors. From the measured response, it can be found that the antenna resonates with a central frequency of around 30.77 GHz, and the measured 10 dB fractional bandwidth is 4.2%. The antenna is free of spurious resonant frequencies over the entire band width of

10 GHz. The normalized simulated and measured radiation patterns of the antenna in the YZ ($\varphi = 90^\circ$) plane are shown in Figure 6. The simulated radiated efficiency of the antenna at the central frequency is approximately 87%. The simulated total gain of the antenna is 5.82 dBi. The measured gain of the antenna is 5.35 dBi. Since the connector is of comparable size to the antenna, during the measurements some of the waves from the transmitting antenna were reflected by the connector, which also contributed to the difference between the simulated and measured radiation patterns in Figure 6 in addition to the fabrication errors.

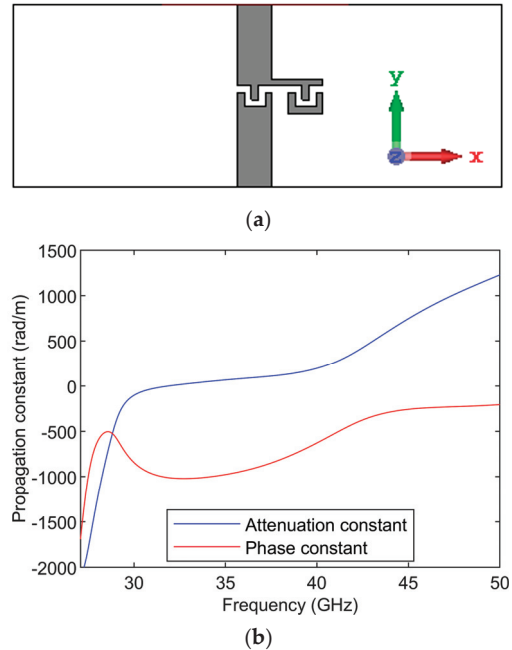


Figure 3. (a) Structure of CRLH unit cell used to find the dispersion diagram (b) dispersion diagram of the CRLH unit cell used for the antenna.



Figure 4. Photograph of the fabricated CRLH antenna.

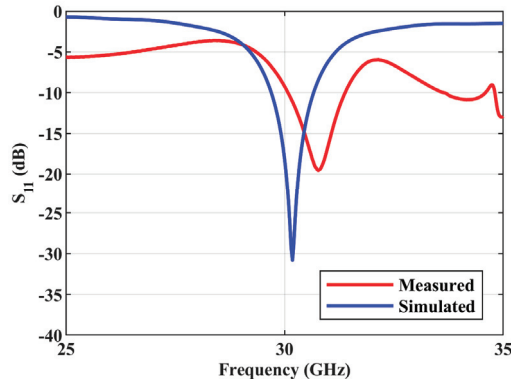


Figure 5. Simulated and measured S parameter response of the antenna.

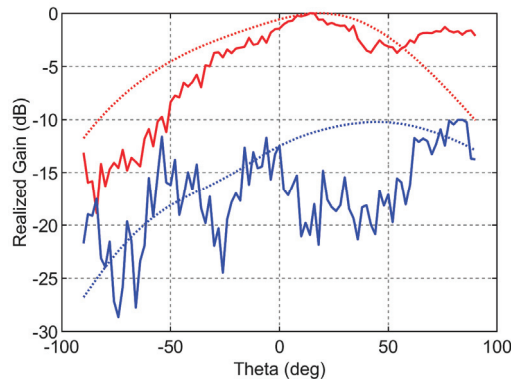


Figure 6. Radiation pattern in the YZ plane. The solid lines denote the measured patterns, and the dotted lines denote the simulated patterns. The red color denotes the co-pol patterns, and the blue color denotes the cross-pol patterns.

For the size comparison, the designed antenna is compared with the patch antenna at 30 GHz in Figure 7. The area of the patch antenna is $3.38 \text{ mm} \times 2.545 \text{ mm}$, and the area of the designed CRLH resonant antenna is $2.46 \text{ mm} \times 0.8 \text{ mm}$, which becomes $0.25 \lambda_0 \times 0.08 \lambda_0$ in terms of free space wavelength λ_0 . Thus, a reduction of 22.8% is achieved. The comparison of the designed CRLH antenna with the previously reported CRLH resonant antennas is given in Table 1. Patch-like radiation is achieved at the 30 GHz band in this work.



Figure 7. Size comparison. (a) Patch antenna at 30 GHz with $l_p = 3.38 \text{ mm}$ and $w_p = 2.545 \text{ mm}$; (b) CRLH resonant antenna with $l = 2.46 \text{ mm}$ and $w = 0.8 \text{ mm}$.

Table 1. Comparison of the designed antenna with already published works.

	Frequency of Operation	Antenna Footprint	Radiation Pattern	Gain	Bandwidth %
This work	30 GHz	2.46 mm × 0.8 mm	Patch like	5.35 dBi	4.2%
[6]	3.38 GHz (CRLH) 3.37 GHz (inductor loaded)	$\frac{\lambda_0}{6} \times \frac{\lambda_0}{6} \times \frac{\lambda_0}{53}$	Monopole like	0.87 dBi (CRLH) 0.7 dBi (inductor loaded)	Not mentioned
[7]	4.88 GHz	75% reduction to patch	Patch like	Not mentioned	Not mentioned
[8]	1.93 GHz and 4.16 GHz	Not mentioned	Patch like	−3.21 dBi (lower band), 7.45 dBi (higher band)	Not mentioned
[9]	5.83 GHz	Not mentioned	Patch like	5.06 dBi	Not mentioned
[10]	5.76 GHz	0.28 λ_0 × 0.191 λ_0 and ground plane size 0.861 λ_0 × 0.766 λ_0	Broadside	4.7 dBi	3.3%
[11]	2.445 GHz	0.32 λ_0 × 0.38 λ_0	Monopole like	3.9 dBi	4.87%

3. CRLH Antenna with Butler Matrix

The detailed description of the design of the substrate integrated waveguide (SIW) Butler matrix at 30 GHz is given in [36,37]. Figure 8 shows the block diagram of a 4×4 Butler matrix with four 90° hybrid couplers, two crossovers, two 45° phase shifters, and two 0° phase shifters that are required. Short-slot couplers are used to implement hybrid couplers and crossovers [36].

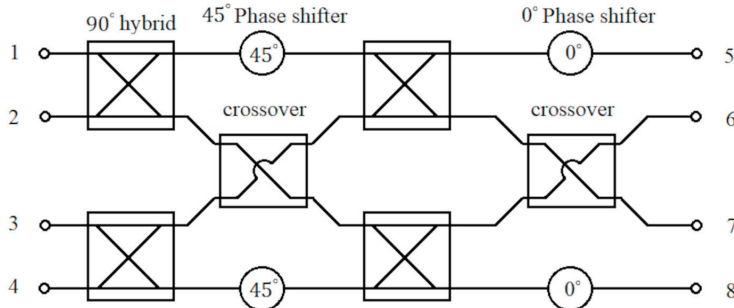


Figure 8. Block diagram of the 4×4 Butler matrix with input ports from 1 to 4 and the output ports from 5 to 8.

The short slot coupler is formed by combining two SIWs sideways and removing the central via hole wall to form the slot region. The short slot coupler along with the coupling region are shown in Figure 9. By adjusting the dimensions of the coupling region of the short slot coupler, the ratio of power transmitted to the output ports can be varied. The even and odd-mode analyses are used to analyze the short slot coupler. The ports of the coupler in Figure 9 are denoted as 1 to 4. The ports at the extremes of the coupling regions are denoted by 1' to 4' and the reference planes are denoted by dotted lines in Figure 9. Consider an input at port 1. The incident waves for this condition are given as $a = [a_1, 0, 0, 0]$. For even- and odd-mode cases, the incident waves are represented as $a_e = [a_1/2, 0, 0, a_1/2]$ and $a_o = [a_1/2, 0, 0, -a_1/2]$ respectively and odd and even mode cases are added to obtain the total incident wave, which is $a = a_e + a_o$. The even- and odd-mode excitations introduce modes TE_{10} and TE_{20} , respectively, in the coupling region. The incident waves from ports 1' to 4' are given as $a'_e = [a'_1/2, 0, 0, a'_1/2]$ and $a'_o = [a'_1/2, 0, 0, -a'_1/2]$ for the even- and odd-mode excitations. Since ports 1' to 4' have a few electrical lengths from ports 1 to 4, the waves a'_e and a'_o are obtained by phase shifting the waves a_e and a_o , respectively. In the odd-mode case, there is an electric wall at

the center parallel to the electric walls at the sides in the coupling region. So, the reflected waves from ports 1' to 4' are given as $b'_o = [0, \left(\frac{a'_1}{2}\right)e^{-j\beta_{20}l}, -\left(\frac{a'_1}{2}\right)e^{-j\beta_{20}l}, 0]$, where β_{20} is the phase constant of the TE_{20} mode. In contrast to the odd-mode case, for the even-mode excitation, there is a magnetic wall at the center of the coupling region parallel to electric walls at the sides. Because of this, there are small reflections of the incident waves that are cancelled by imposing conditions on the length of the coupling or slot region. The reflected waves from ports 1' to 4' are given as $b'_e = [0, \left(\frac{a'_1}{2}\right)e^{-j\beta_{10}l}, \left(\frac{a'_1}{2}\right)e^{-j\beta_{10}l}, 0]$ with β_{10} as the phase constant of the TE_{10} mode. The total reflected waves from ports 1' to 4' can be found out as $b' = [0, \left(\frac{a'_1}{2}\right)(e^{-j\beta_{10}l} + e^{-j\beta_{20}l}), \left(\frac{a'_1}{2}\right)(e^{-j\beta_{10}l} - e^{-j\beta_{20}l}), 0]$. Since the slot or the coupling region considered is symmetric, the S parameters at port 1 are sufficient to fully characterize the region. The S parameters are given as $S_{1'1'} = 0$, $S_{2'1'} = \cos((\beta_{10} - \beta_{20})\frac{l}{2})e^{-j(\beta_{10} - \beta_{20})\frac{l}{2}}$, $S_{3'1'} = -j\sin((\beta_{10} - \beta_{20})\frac{l}{2})e^{-j(\beta_{10} - \beta_{20})\frac{l}{2}}$, and $S_{4'1'} = 0$.

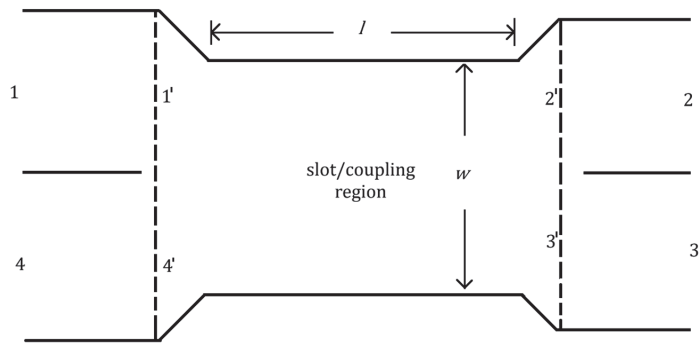


Figure 9. Short slot coupler with the ports 1 to 4 and the ports at the extremes of the coupling region are from 1' to 4'.

From $S_{3'1'}$, it can be written as

$$(\beta_{10} - \beta_{20})\frac{l}{2} = \sin^{-1}|S_{3'1'}| \quad (1)$$

The values of the phase constants β_{10} and β_{20} are given as

$$\beta_{10}^2 = k^2 - \left(\frac{\pi}{w}\right)^2 \quad (2)$$

and

$$\beta_{20}^2 = k^2 - \left(\frac{2\pi}{w}\right)^2 \quad (3)$$

Substituting (2) and (3) in (1), the equation obtained is

$$\left(\sqrt{\left(k^2 - \left(\frac{\pi}{w}\right)^2\right)} - \sqrt{\left(k^2 - \left(\frac{2\pi}{w}\right)^2\right)} \right) = \sin^{-1}|S_{3'1'}| \quad (4)$$

where k is the wavenumber and w is the width of the slot or the coupling region.

As previously mentioned in the even mode or TE_{10} , there are reflections and these reflections can be cancelled out if the following approximate condition is satisfied [40]:

$$1 + e^{-j2\beta_{10}l} = 0 \quad (5)$$

where l is the length of the slot or the coupling region.

From (5), l can be found out as

$$l = \frac{(2n+1)\pi}{2\beta_{10}} \quad (6)$$

where n can be zero or a positive integer. Substituting (6) in (4) and substituting the value of β_{10} , the design equations of the short slot coupler can be found out. A detailed analysis of the short slot coupler can be found in [36,40]. The width and length of the slot region of the short slot coupler are given by

$$w = \frac{\pi}{k} \sqrt{\frac{[\pi(2n+1) + 4\sin^{-1}|S_{3'1'}|][3\pi(2n+1) - 4\sin^{-1}|S_{3'1'}|]}{8\sin^{-1}|S_{3'1'}|[3\pi(2n+1) - 2\sin^{-1}|S_{3'1'}|]}} \quad (7)$$

$$l = \frac{(2n+1)\pi}{2\sqrt{k^2 - (\frac{\pi}{w})^2}} \quad (8)$$

where k is the wavenumber, n can be zero or a positive integer, and $S_{3'1'}$ is the S parameter response in the slot region between ports 3' and 1'.

For 90° hybrid couplers, the S parameter response $|S_{3'1'}|$ is $1/\sqrt{2}$. Substituting this in (7) and (8) gives the width and length of the slot region to the 90° hybrid coupler. They are given as [36]

$$w_1 = \frac{\pi}{k} \sqrt{\frac{4(3n+1)(n+1)}{4n+1}} \quad (9)$$

$$l_1 = \frac{\pi}{k} \sqrt{\frac{(3n+1)(n+1)}{3}} \quad (10)$$

The S parameter responses for the case of crossover are given as $|S_{3'1'}| = 1$ and $|S_{2'1'}| = 0$. These values are again substituted in (7) and (8) to find width and length of the slot region of the crossover. They are given as [36]

$$w_2 = \frac{\pi}{k} \sqrt{\frac{(6n+1)(2n+3)}{8n}} \quad (11)$$

$$l_2 = \frac{\pi}{k} \sqrt{\frac{(6n+1)(2n+3)}{12}} \quad (12)$$

For the implementation of 90° hybrid couplers and crossovers in the Butler matrix, n is chosen as 2 in this work. The 90° hybrid coupler and its dimensions are shown in Figure 10a. The simulated S parameter responses for the port 1 excitation is shown in Figure 10b, along with the phase difference between the S parameter responses S_{31} and S_{21} . The simulated magnitude responses of S_{21} and S_{31} are approximately -2.89 dB and -3.53 dB, respectively, at 30 GHz, and the simulated phase difference between them is $S_{31} - S_{21}$ is 90° at 30 GHz. The crossover and its simulated S parameter responses for the input at port 1 are shown in Figure 11. The dimensions of the crossover are also mentioned in Figure 11. As can be found in Figure 11b, only S_{31} is above -3 dB at 30 GHz and all the other S parameter responses are less than -10 dB, so the power is transferred from port 1 to port 3. The simulated insertion loss of S_{31} is approximately 0.53 dB at 30 GHz.

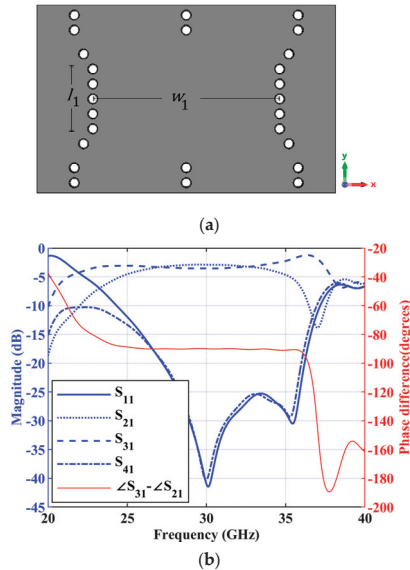


Figure 10. A 90° hybrid coupler (a) structure with dimensions $w_1 = 7.51$ mm and $l_1 = 2.4$ mm; (b) simulated S parameter responses of the hybrid coupler for input at port 1 and a phase difference between S_{31} and S_{21} .

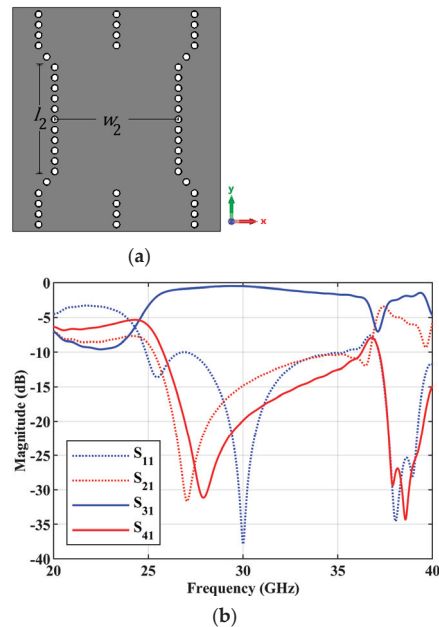


Figure 11. Crossover (a) structure with dimensions of $w_2 = 7.13$ mm and $l_2 = 6$ mm; (b) simulated S parameter response of the crossover for the input at port 1.

The designed 90° hybrid coupler and crossover are used to construct the Butler matrix. The phase shifters are designed using the curved SIW lines. The structure of the Butler matrix and a photograph of the fabricated Butler matrix are shown in Figure 12. The simulated and measured S parameter response of the Butler matrix is shown in Figure 13.

The simulated phases from ports 5 to 8 for the input at port 1 are approximately 20.82° , -9.53° , -38.58° , and -92.60° respectively at 30 GHz. The measured phases from ports 5 to 8 for input at port 1 are approximately -26.06° , -15.07° , -44.48° , and -170.00° , respectively, at 30 GHz. The final fabricated structure of the Butler matrix with CRLH antenna is shown in Figure 14. The same Rogers RO4003c substrate that was used in the fabrication of the CRLH antenna is also used to fabricate the Butler matrix with the CRLH antenna.

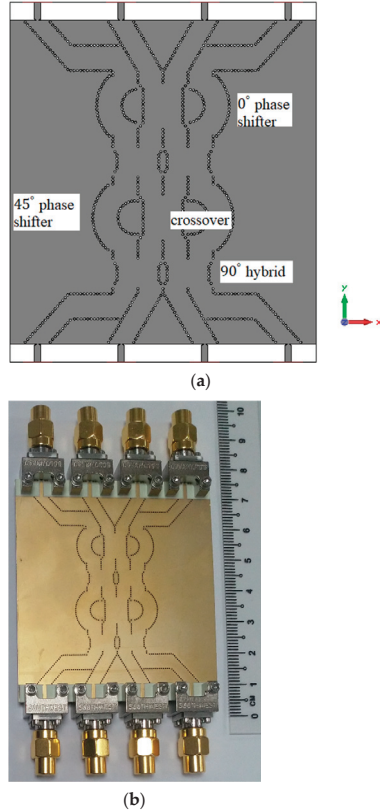


Figure 12. The 4×4 SIW Butler matrix (a) structure; (b) photograph of the fabricated structure.

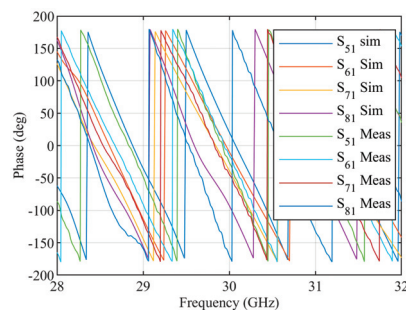


Figure 13. Measured and simulated S parameter responses of the 4×4 SIW Butler matrix for port 1 excitation.

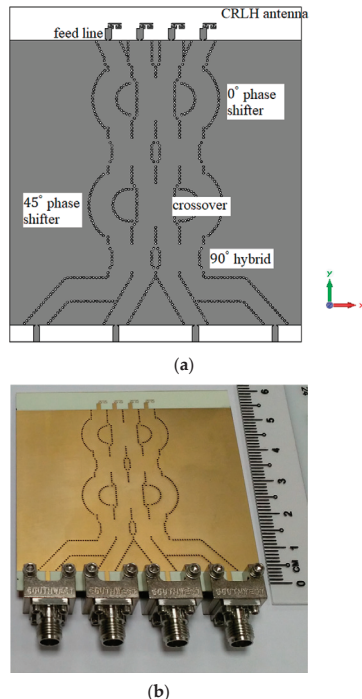


Figure 14. The Butler matrix with a CRLH antenna (a) structure; (b) photograph of the fabricated structure.

The CRLH antenna described in Section 2 is added as the radiating element for a 4×4 Butler matrix at the four output ports. The CRLH antenna is designed without via holes to obtain the radiation in the broad side direction. The distance between the antennas is $0.75 \lambda_g$. The simulated electric field of the Butler matrix during port 1 excitation is shown in Figure 15. From the electric field distribution, it can be found that the waves from port 1 reach the four output ports at different phases to tilt the radiated beam in the desired direction. The radiation pattern of the antenna in the XZ ($\varphi = 0^\circ$) plane for excitations in the four input ports is shown in Figure 16. The simulated total realized gain is above 7 dBi in all input port excitations, and the simulated scanning angles are 12° for port 1 excitation, -68° for port 2 excitation, 64° for port 3 excitation, and -11° for port 4 excitation.

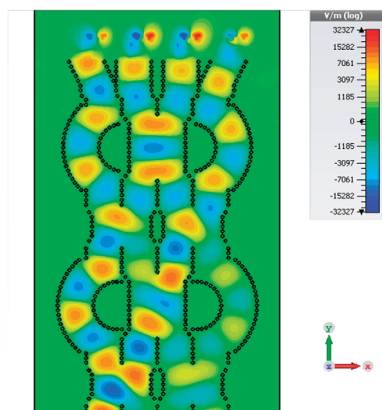


Figure 15. Simulated electric distribution of the Butler matrix with an antenna in SIW.

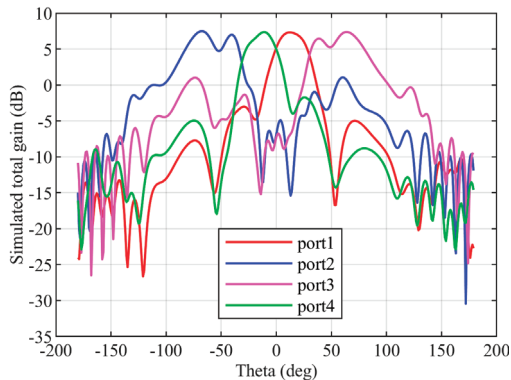


Figure 16. Simulated radiation pattern of the CRLH antenna with the Butler matrix from port 1 to port 4 excitations.

4. Conclusions

A CRLH resonant antenna without metallic vias has been designed and experimentally demonstrated to have patch-like radiation in the broadside direction. By utilizing the new CRLH resonator, patch-type radiation can be achieved. The antenna has a low profile and a radiated efficiency of around 87%. The designed antenna has no spurious resonance over a bandwidth of 10 GHz. A passive beamforming array has been designed and fabricated using the Butler matrix and the CRLH antennas. The CRLH antennas are attached to the output ports of the 4×4 SIW Butler matrix, and the performance of the CRLH antenna and the 4×4 SIW Butler matrix is verified. It has potential applications in 5G communication, wireless power transfer, and IoT sensing.

Author Contributions: M.P.M. and M.F.K. jointly conceived the idea. M.P.M., H.C. and A.A. designed the system and built the experimental setup. M.P.M. and H.C. performed the experiments. M.P.M., M.F.K. and A.A. assisted with the theory. All authors contributed to the discussion of experimental results. M.F.K., A.A. and H.C. supervised and coordinated all the work. M.P.M. and M.F.K. wrote the manuscript with contributions from all co-authors. All authors have read and agreed to the published version of the manuscript.

Funding: This study is supported under the Future Communications Research and Development Programme (FCP) Research Grant-FCP-NTU-RG-2022-013.

Institutional Review Board Statement: Not applicable.

Informed Consent Statement: Not applicable.

Data Availability Statement: Not applicable.

Acknowledgments: We thank Nasimuddin for the support in the measurements.

Conflicts of Interest: The authors declare no conflict of interest.

References

1. Ladan, S.; Guntupalli, A.B.; Wu, K. A High-Efficiency 24 GHz Rectenna Development Towards Millimeter-Wave Energy Harvesting and Wireless Power Transmission. *IEEE Trans. Circuits Syst. I Regul. Pap.* **2014**, *61*, 3358–3366. [CrossRef]
2. Hu, H.; Karim, M.F.; Ong, L.C.; Leyman, A.R.; Luo, B.; Chiam, T.M.; Guo, Y.X.; Zhu, X.H. All Authors Millimeter wave imaging using SAR modeling. In Proceedings of the 2013 IEEE MTT-S International Microwave Workshop Series on RF and Wireless Technologies for Biomedical and Healthcare Applications (IMWS-BIO), Singapore, 9–11 December 2013; pp. 1–3. [CrossRef]
3. Chandrasekaran, K.T.; Nasimuddin; Leong, S.W.; Chan, K.S.; Luo, B.; Karim, M.F.; Alphones, A.; Agarwal, K.; Ong, M.L.C. Millimeter-wave System-in-Package (SiP) for Non-Destructive Testing of Metallic Structures under Multilayered Composites using Backward-to-Forward Beamscanning Leaky Wave Antenna. In Proceedings of the 2019 16th European Radar Conference (EuRAD), Paris, France, 1–3 October 2019; pp. 389–392.
4. Fallahpour, M.; Zoughi, R. Antenna Miniaturization Techniques: A Review of Topology- and Material-Based Methods. *IEEE Antennas Propag. Mag.* **2018**, *60*, 38–50. [CrossRef]

5. Caloz, C.; Itoh, T. *Electromagnetic Metamaterial: Transmission Line Theory and Microwave Applications*; Wiley: Hoboken, NJ, USA, 2005.
6. Lai, A.; Leong, K.M.K.H.; Itoh, T. Infinite Wavelength Resonant Antennas with Monopolar Radiation Pattern Based on Periodic Structures. *IEEE Trans. Antennas Propag.* **2007**, *55*, 868–876. [CrossRef]
7. Sanada, A.; Kimura, M.; Awai, I.; Caloz, C.; Itoh, T. A planar zeroth-order resonator antenna using a left-handed transmission line. In Proceedings of the 34th European Microwave Conference 2004, Amsterdam, The Netherlands, 12–14 October 2004; pp. 1341–1344.
8. Otto, S.; Rennings, A.; Caloz, C.; Waldow, P.; Itoh, T. Composite right/left-handed /spl lambda/-resonator ring antenna for dual-frequency operation. In Proceedings of the 2005 IEEE Antennas and Propagation Society International Symposium, Washington, DC, USA, 3–8 July 2005; Volume 1A, pp. 684–687. [CrossRef]
9. Zhang, C.; Gong, J.; Li, Y.; Wang, Y. Zeroth-Order-Mode Circular Microstrip Antenna With Patch-Like Radiation Pattern. *IEEE Antennas Wirel. Propag. Lett.* **2018**, *17*, 446–449. [CrossRef]
10. Ko, S.-T.; Lee, J.-H. Hybrid Zeroth-Order Resonance Patch Antenna with Broad E-Plane Beamwidth. *IEEE Trans. Antennas Propag.* **2013**, *61*, 19–25. [CrossRef]
11. Yan, S.; Vandenbosch, G.A.E. Radiation Pattern-Reconfigurable Wearable Antenna Based on Metamaterial Structure. *IEEE Antennas Wirel. Propag. Lett.* **2016**, *15*, 1715–1718. [CrossRef]
12. Yan, S.; Vandenbosch, G.A.E. Zeroth-order resonant circular patch antenna based on periodic structures. *IET Microw. Antennas Propag.* **2014**, *8*, 1432–1439. [CrossRef]
13. Chi, P.; Shih, Y. Compact and Bandwidth-Enhanced Zeroth-Order Resonant Antenna. *IEEE Antennas Wirel. Propag. Lett.* **2015**, *14*, 285–288. [CrossRef]
14. El Atrash, M.; Abdalla, M.A.; Elhennawy, H.M. A Compact Highly Efficient Π -Section CRLH Antenna Loaded With Textile AMC for Wireless Body Area Network Applications. *IEEE Trans. Antennas Propag.* **2021**, *69*, 648–657. [CrossRef]
15. Liu, C.; Menzel, W. Broadband Via-Free Microstrip Balun Using Metamaterial Transmission Lines. *IEEE Microw. Wirel. Compon. Lett.* **2008**, *18*, 437–439. [CrossRef]
16. Song, Y.; Liu, H.; Zhao, W.; Wen, P.; Wang, Z. Compact Balanced Dual-Band Bandpass Filter with High Common-Mode Suppression Using Planar Via-Free CRLH Resonator. *IEEE Microw. Wirel. Compon. Lett.* **2018**, *28*, 996–998. [CrossRef]
17. Butler, J.; Lowe, R. Beam-forming matrix simplifies design of electronically scanned antennas. *Electron. Design* **1961**, *9*, 170–173.
18. Cassivi, Y.; Perregnini, L.; Arcioni, P.; Bressan, M.; Wu, K.; Conciauro, G. Dispersion characteristics of substrate integrated rectangular waveguide. *IEEE Microw. Wirel. Compon. Lett.* **2002**, *12*, 333–335. [CrossRef]
19. Xu, F.; Wu, K. Guided-wave and leakage characteristics of substrate integrated waveguide. *IEEE Trans. Microw. Theory Tech.* **2005**, *53*, 66–73. [CrossRef]
20. Deslandes, D.; Wu, K. Accurate modeling, wave mechanisms, and design considerations of a substrate integrated waveguide. *IEEE Trans. Microw. Theory Tech.* **2006**, *54*, 2516–2526. [CrossRef]
21. Bozzi, M.; Georgiadis, A.; Wu, K. Review of substrate-integrated waveguide circuits and antennas. *IET Microw. Antennas Propag.* **2011**, *5*, 909–920. [CrossRef]
22. Deslandes, D.; Wu, K. Design Consideration and Performance Analysis of Substrate Integrated Waveguide Components. In Proceedings of the 2002 32nd European Microwave Conference, Milan, Italy, 23–26 September 2002; pp. 1–4. [CrossRef]
23. Deslandes, D.; Wu, K. Integrated microstrip and rectangular waveguide in planar form. *IEEE Microw. Wirel. Compon. Lett.* **2001**, *11*, 68–70. [CrossRef]
24. Deslandes, D. Design equations for tapered microstrip-to-Substrate Integrated Waveguide transitions. In Proceedings of the 2010 IEEE MTT-S International Microwave Symposium, Anaheim, CA, USA, 23–28 May 2010; pp. 704–707. [CrossRef]
25. Taringou, F.; Dousset, D.; Bornemann, J.; Wu, K. Substrate-integrated waveguide transitions to planar transmission-line technologies. In Proceedings of the 2012 IEEE/MTT-S International Microwave Symposium Digest, Montreal, QC, Canada, 17–22 June 2012; pp. 1–3. [CrossRef]
26. Rotman, W.; Turner, R. Wide-angle microwave lens for line source applications. *IEEE Trans. Antennas Propag.* **1963**, *11*, 623–632. [CrossRef]
27. Mosca, S.; Biliotti, F.; Toscano, A.; Vegni, L. A novel design method for Blass matrix beam-forming networks. *IEEE Trans. Antennas Propag.* **2002**, *50*, 225–232. [CrossRef]
28. Djerafi, T.; Fonseca, N.J.G.; Wu, K. Planar Ku -Band 4 × 4 Nolen Matrix in SIW Technology. *IEEE Trans. Microw. Theory Tech.* **2010**, *58*, 259–266. [CrossRef]
29. Djerafi, T.; Wu, K. A Low-Cost Wideband 77-GHz Planar Butler Matrix in SIW Technology. *IEEE Trans. Antennas Propag.* **2012**, *60*, 4949–4954. [CrossRef]
30. Karamzadeh, S.; Rafii, V.; Kartal, M.; Virdee, B.S. Compact and Broadband 4 × 4 SIW Butler Matrix With Phase and Magnitude Error Reduction. *IEEE Microw. Wirel. Compon. Lett.* **2015**, *25*, 772–774. [CrossRef]
31. Cao, Y.; Chin, K.-S.; Che, W.; Yang, W.; Li, E.S. A Compact 38 GHz Multibeam Antenna Array With Multifolded Butler Matrix for 5G Applications. *IEEE Antennas Wirel. Propag. Lett.* **2017**, *16*, 2996–2999. [CrossRef]
32. Lian, J.-W.; Ban, Y.-L.; Xiao, C.; Yu, Z.-F. Compact Substrate-Integrated 4 × 8 Butler Matrix With Sidelobe Suppression for Millimeter-Wave Multibeam Application. *IEEE Antennas Wirel. Propag. Lett.* **2018**, *17*, 928–932. [CrossRef]
33. Zhong, L.-H.; Ban, Y.-L.; Lian, J.-W.; Yang, Q.-L.; Guo, J.; Yu, Z.-F. Miniaturized SIW Multibeam Antenna Array Fed by Dual-Layer 8 × 8 Butler Matrix. *IEEE Antennas Wirel. Propag. Lett.* **2017**, *16*, 3018–3021. [CrossRef]

34. Wu, M.; Zhang, B.; Zhou, Y.; Huang, K. A Double-Fold 7×8 Butler Matrix-Fed Multibeam Antenna With a Boresight Beam for 5G Applications. *IEEE Antennas Wirel. Propag. Lett.* **2022**, *21*, 516–520. [CrossRef]
35. Yang, Q.-L.; Ban, Y.-L.; Lian, J.-W.; Yu, Z.-F.; Wu, B. SIW Butler Matrix with Modified Hybrid Coupler for Slot Antenna Array. *IEEE Access* **2016**, *4*, 9561–9569. [CrossRef]
36. Chen, C.-J.; Chu, T.-H. Design of a 60-GHz Substrate Integrated Waveguide Butler Matrix—A Systematic Approach. *IEEE Trans. Microw. Theory Tech.* **2010**, *58*, 1724–1733. [CrossRef]
37. Mohan, M.P.; Karim, M.F.; Hong, C.; Alphones, A.; Liu, A.Q. A 30 GHz SIW based 4×4 Butler Matrix. In Proceedings of the 2020 IEEE International Symposium on Antennas and Propagation and North American Radio Science Meeting, Montreal, QC, Canada, 5–10 July 2020; pp. 429–430. [CrossRef]
38. El-Nady, S.; Elsharkawy, R.R.; Afifi, A.I.; Abd El-Hameed, A.S. Performance Improvement of Substrate Integrated Cavity Fed Dipole Array Antenna Using ENZ Metamaterial for 5G Applications. *Sensors* **2022**, *22*, 125. [CrossRef]
39. Pozar, D.M. *Microwave Engineering*, 4th ed.; Wiley: Hoboken, NJ, USA, 2012.
40. Yamamoto, S.; Hirokawa, J.; Ando, M. A half-sized post-wall short-slot directional coupler with hollow rectangular holes in a dielectric substrate. *IEICE Trans. Electron.* **2005**, *88*, 1387–1394. [CrossRef]

Disclaimer/Publisher’s Note: The statements, opinions and data contained in all publications are solely those of the individual author(s) and contributor(s) and not of MDPI and/or the editor(s). MDPI and/or the editor(s) disclaim responsibility for any injury to people or property resulting from any ideas, methods, instructions or products referred to in the content.



Article

Multifunctional THz Graphene Antenna with 360° Continuous ϕ -Steering and θ -Control of Beam

Victor Dmitriev *, Rodrigo M. S. de Oliveira *, Rodrigo R. Paiva and Nilton R. N. M. Rodrigues

Graduate Program in Electrical Engineering (PPGEE), Institute of Technology (ITEC), Federal University of Pará (UFPA), Rua Augusto Corrêa, 01, Belém 66075-110, PA, Brazil; rods.paiva26@gmail.com (R.R.P.); niltonrodolfo@ufpa.br (N.R.N.M.R.)
* Correspondence: victor@ufpa.br (V.D.); rmso@ufpa.br (R.M.S.d.O.)

Abstract: A novel graphene antenna composed of a graphene dipole and four auxiliary graphene sheets oriented at 90° to each other is proposed and analyzed. The sheets play the role of reflectors. A detailed group-theoretical analysis of symmetry properties of the discussed antennas has been completed. Through electric field control of the chemical potentials of the graphene elements, the antenna can provide a quasi-omnidirectional diagram, a one- or two-directional beam regime, dynamic control of the beam width and, due to the vertical orientation of the dipole with respect to the base substrate, a 360° beam steering in the azimuth plane. An additional graphene layer on the base permits control of the radiation pattern in the θ -direction. Radiation patterns in different working states of the antenna are considered using symmetry arguments. We discuss the antenna parameters such as input reflection coefficient, total efficiency, front-to-back ratio, and gain. An equivalent circuit of the antenna is suggested. The proposed antenna operates at frequencies between 1.75 THz and 2.03 THz. Depending on the active regime defined by the chemical potentials set on the antenna graphene elements, the maximum gain varies from 0.86 to 1.63.

Keywords: THz communications; dipole graphene antenna; multifunctional antenna; reconfigurable radiation pattern; beam steering

Citation: Dmitriev, V.; de Oliveira, R.M.S.; Paiva, R.R.; Rodrigues, N.R.N.M. Multifunctional THz Graphene Antenna with 360° Continuous ϕ -Steering and θ -Control of Beam. *Sensors* **2023**, *23*, 6900. <https://doi.org/10.3390/s23156900>

Academic Editor: Naser Ojaroudi Parchin

Received: 17 June 2023

Revised: 29 July 2023

Accepted: 29 July 2023

Published: 3 August 2023



Copyright: © 2023 by the authors. Licensee MDPI, Basel, Switzerland. This article is an open access article distributed under the terms and conditions of the Creative Commons Attribution (CC BY) license (<https://creativecommons.org/licenses/by/4.0/>).

1. Introduction

Terahertz (THz) communication systems, operating in the frequency range of 0.1 THz to 10 THz, have emerged as a promising solution to address the ever-increasing demand for high-speed wireless communication. This frequency range, known as the THz gap, lies between the traditional microwave and infrared bands, offering unique opportunities for a wide range of applications, including sensing [1], imaging [2], spectroscopy [3], and high-speed data transmission antennas [4–7].

Graphene is a material formed by a single layer of carbon atoms arranged in a honeycomb lattice [8]. Graphene possesses specific electronic and electrical properties, in particular, voltage-controlled chemical potential and, consequently, the possibility for dynamic control of its complex electric conductivity [9,10]. Application of graphene has led to significant technical advances in several fields [9,11–14], including design of nanoantennas for various applications [4], such as intra- and inter-chip communications. In the THz region, graphene supports surface plasmon polaritons (SPPs) [9], providing the small dimensions of circuit components. During the last decade, different types of graphene antennas have been suggested in the literature, starting from a simple dipole one to more complex structures presenting combinations of graphene with metal elements or with dielectric resonators. Many of them have been projected by analogy with microwave [15] and optical antennas [16], such as bow-tie, loop, Yagi-Uda, spiral, and log-periodic ones.

A review of microwave beam-switchable antennas is presented in [17]. The methods of beam switching in the microwave frequency region are based on the use of phased array antennas, liquid metal antennas, antennas based on active frequency selective surfaces, and

electronically controlled quasi-Yagi array antennas. Notice that some of these methods can also be applied in the THz region using graphene as a tunable material.

Today, the number of the papers devoted to graphene antenna technology is in the hundreds. Detailed descriptions of many graphene and graphene-based antennas are given, as in the review papers [4,18]. In [18], the author discusses graphene antenna theory and experiments at that early stage, such as the graphene patch, plasmonic resonant antennas, and reflectarrays. A detailed discussion of graphene antenna technology is presented in a recently published review paper [4]. There, one can find a wide spectrum of issues, starting from the fundamental principles of the graphene antenna theory to the description of the technology in fabrication of graphene–metal nanoantennas. Many graphene antenna structures are presented in the reference paper. A considerable part of the paper is devoted to the methods for radiation beam scanning and beam reconfigurability. Hence, there is no need to discuss the published literature in detail. Therefore, we decided to restrict our literature review to recent publications that did not appear in the existing review papers and to the works where the suggested antennas possess some functionalities similar to our proposal.

In paper [19], a monopole source antenna is surrounded by six hexagonal active frequency selective surfaces. These surfaces permit stepwise 0° , $\pm 60^\circ$, $\pm 120^\circ$, and 180° -switching of the beam in two different frequency bands of 0.96 THz and 1.21 THz. However, the proposed antenna is very complex in its biasing graphene scheme and has a complex geometry and large dimensions defined by the hexagonal screen. The THz antennas proposed in [20,21], based on the Yagi–Uda antenna concept, consist of two graphene-based dipoles and graphene-based parasitic elements. These elements can act as directors or reflectors by controlling their surface conductivity. The antennas can direct the main lobe into four orthogonal θ -directions: 0° , $\pm 90^\circ$, or 180° .

The antenna in [22] consists of a graphene dipole with two coplanar graphene parasites placed on the SiO_2 substrate. Working in the frequency range of 1.94–2.13 THz, the antenna has four radiation operation states that can be selected by setting specific chemical potentials using the external electric field on the graphene elements. In state 1, a dipole-like radiation diagram is produced. States 2 and 3 are characterized by specific directional radiation patterns. By selecting the operation state 4, the antenna is switched off. In [5], a rectangular graphene loop antenna placed on a dielectric substrate for the THz band is proposed and analyzed. Symmetry properties of the antenna in terms of currents and the radiated fields are investigated. The maximum total efficiency of the proposed antenna is about 57%, and its fractional bandwidth is 96%, with the central frequency 1.74 THz. This bandwidth is approximately twice that of the graphene dipole antenna.

Recently, an antenna containing an active radiating graphene patch and a non-radiating graphene ring was analyzed in [23], where the radiation pattern can be steered by controlling gate voltages over the ring. A reconfigurable graphene leaky-wave antenna with electronic beam scanning for a THz communications system is proposed in [24]. It consists of graphene strips printed on a silicon oxide substrate and fed by a planar H-plane horn antenna. The tunable graphene conductivity using DC-bias is used to control the radiated beam direction. By selecting the periodicity of the biased/unbiased graphene strips of the antenna, the beam direction, scanning range, and gain can be controlled. The radiated beam is electronically scanned from -68° to 26° at the frequency 2 THz. A THz beam steering microstrip patch antenna is demonstrated in [25]. The metallic radiating patch is surrounded by six parasitic graphene ribbons located at the lateral, upper, and lower sides of the radiating patch. The graphene ribbons are employed to change the beam orientation in the θ -constant plane. The chemical potentials for graphene elements are switched between 0 and 1 eV to produce beam steering. Two lateral ribbons act as director elements, whereas four upper and lower parasitic elements take on the reflector role, resulting in a beam deflected into the opposite direction. As a result, an overall 120° beam steering at the frequency of 1.47 THz is obtained.

In [26], opto-electronic simulation is carried out, and the emission intensity spectrum is determined in a graphene-based THz bow-tie dipole antenna on a substrate with photonic band gap structure. The directivity of the proposed antenna with photonic V is found to be 13.7 dBi, which is a 10 dB improvement over the conventional design, and an efficiency of 95% is achieved. A Ti–Au dipole antenna on a GaAs substrate is designed in [27] for THz emission. A spectral width of 120 GHz is obtained from the emission spectrum. In order to compare the spectral characteristics, a graphene dipole antenna is designed on the same substrate. It is observed that the graphene dipole yields a narrower spectral width of 70 GHz due to its high Q-factor.

A graphene multiple-input multiple-output (MIMO) microstrip patch antenna in [28] contains graphene E-shaped elements placed between the graphene radiating patches. It provides a higher isolation between the unit cells. At the frequency 1.9 THz, the antenna produces the radiated beam, allowing it to steer in different directions within the angle interval $\pm 60^\circ$. The reconfigurable process is carried out by changing the chemical potential of the antenna elements.

In [29], a sub-THz emitter based on a large-bandwidth silicon-plasmonic graphene photodetector integrated with a broadband rounded bow-tie THz antenna was fabricated. The sub-THz emitter is experimentally demonstrated to emit sub-THz waves with a radiation spectrum from 50 to 300 GHz. A maximum sub-THz emission power of 5.4 nW is obtained at 145 GHz with 3 mW input light power. The emitter can be fabricated by a CMOS-compatible process.

In this paper, we propose a very simple antenna consisting of a graphene dipole, two coplanar reflectors, and two orthogonal reflectors also made of graphene. The main peculiarity of our antenna is its multifunctionality. We will show that it can work in the omnidirectional state and in five other discrete states that differ in the form of the diagram pattern. The control of these states is fulfilled by a simple change to the chemical potential of the graphene elements. In addition to these states, due to vertical orientation of the dipole with respect to the base substrate, there is a possibility of continuous 360° ϕ -steering of the beam and also θ -control of it. The analysis of the published literature presented above demonstrates that only a stepwise 360° control of the THz beam in graphene antennas has been suggested up to now. The reported continuous beam steering is restricted by a relatively small ϕ -angle around $\pm 60^\circ$. Our proposed antenna is very simple; it is small and has a high level of reconfigurability that has not been achieved until now.

The paper is organized as follows. The antenna description is presented in Section 2. Graphene parameters used in calculations are discussed in Section 3. Section 4 is devoted to symmetry analysis of the proposed antenna. Section 5 provides the qualitative analysis of currents and fields in the antenna. In Section 6, we present the design of the dipole antenna. The design of the antenna with four reflectors is discussed in Section 7. The results of the numerical simulations are detailed in Section 8. A discussion and conclusions end the paper with Sections 9 and 10, respectively.

2. Antenna Description

Geometry of the proposed antenna in free space is presented in Figure 1.

The device is formed by an active graphene dipole antenna (measuring $l_0 \times w_0$), which is fed by a photomixer [30] placed in the gap between the dipole arms. The photomixer and the metallic electrodes are 5 μm and 0.5 μm in width, respectively. Two orthogonal reflectors with respect to the plane of the dipole with dimensions l_{r2}, w_{r2}, l_{r4} , and w_{r4} , and two coplanar graphene reflectors, measuring $l_{r1} \times w_{r1}$ and $l_{r3} \times w_{r3}$, are also a part of the device. The distance between the dipole antenna and each coplanar reflector is d_x , while d_y is the separation between the dipole and each orthogonal reflector. The dipole arms and orthogonal reflectors are made of three-layer graphene sheets, while each coplanar reflector consists of a single-layer sheet.

Thus, the discussed system consists of a common graphene dipole antenna shown in Figure 1a and four graphene reflectors oriented at 90° to each other (see Figure 1b). The

reflectors that provide beam shaping present equal rectangular graphene sheets placed symmetrically with respect to the active dipole element. The geometric configuration among the graphene dipole and reflectors and the vertical orientation of the graphene dipole antenna with respect to the base substrate, as discussed later, provide the possibility of 360° beam steering. A possible implementation of chemical potential tuning is discussed in Section 9.

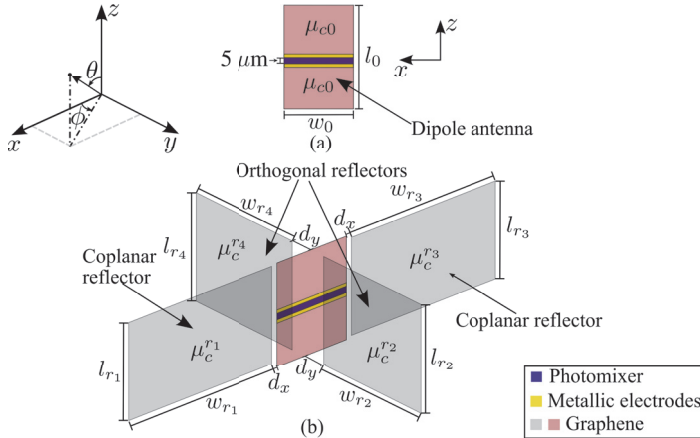


Figure 1. The proposed device: (a) dipole antenna and (b) dipole and four reflectors.

3. Graphene Parameters

The chemical potential of the dipole antenna is μ_{c0} , while chemical potentials of orthogonal reflectors are μ_c^{r2} and μ_c^{r4} . Coplanar reflector chemical potentials are μ_c^{r1} and μ_c^{r3} (see Figure 1). In the THz band, the complex conductivity of a single layer of graphene is properly described by its intraband conductivity contribution [5,9], given by

$$\sigma_g = \frac{q_e^2 k_B T}{\pi \hbar^2 (j\omega + 2\Gamma_g)} \left[\frac{\mu_c}{k_B T} + 2 \ln \left(1 + e^{-\mu_c/k_B T} \right) \right], \quad (1)$$

where q_e is the electron charge, k_B and \hbar are the Boltzmann's and the reduced Planck's constants, T is temperature, $j = \sqrt{-1}$, ω is angular frequency, μ_c is chemical potential, and $\Gamma_g = (2\tau)^{-1}$ is the scattering rate (τ is relaxation time). The conductivity of a graphene sheet with $N \leq 5$ layers is $\sigma_N = N\sigma_g$, as detailed in [9,31,32].

4. Symmetry Analysis

4.1. The Full 3D Symmetry of the Antenna

The physical symmetry of the discussed antenna is defined by the geometric symmetry of the structure and by the symmetry of chemical potentials of the reflectors. The resulting symmetry defines the distribution of currents in the graphene elements and, consequently, the distribution of the electromagnetic field around the antenna. Therefore, symmetry of the radiation pattern (RP) of the antenna, which is the main subject of our work, depends on the resulting symmetry of the antenna.

Group theory greatly simplifies the description, calculations, and analysis of the systems with high symmetry. The highest symmetry of the free-standing antenna in Figure 1b is described by the three-dimensional (3D) point group D_{2h} (in Schoenflies notation [33]). This group consists of the following elements: e is the unit element; C_{2z} is a twofold principal symmetry axis z ; C'_2 and C''_2 are two twofold symmetry axes orthogonal to the principal axis; i is inversion through a center of symmetry; σ_x is the vertical plane $y = 0$ aligned with the principal symmetry axis; σ_y is the vertical plane $x = 0$ aligned

with the principal symmetry axis; and σ_z is a horizontal plane intersecting the principal symmetry axis.

The group D_{2h} can be presented as the direct product $D_{2h} = C_{2v} \otimes C_s$ of two lower groups. The 2D group C_{2v} describes symmetry in the plane $x0y$, and the group C_s , consisting of the unit element e and the plane of symmetry σ_z , describes symmetry in the third coordinate z . The plane of symmetry σ_z allows one to consider only the upper ($z > 0$) or lower ($z < 0$) half-space. In Section 8.5, we demonstrate the effect of symmetry reduction, deleting the plane σ_z . In the following, we restrict ourselves to the group C_{2v} . This group contains the elements e , C_2 , σ_x , and σ_y .

4.2. Effect of Dielectric Substrates on Antenna Symmetry

The symmetry elements of the group C_{2v} are shown in Figure 2a. Symmetry of the discussed antenna can be reduced when we add some dielectric elements to the antenna. The symmetry C_{2v} is preserved if every graphene element is placed between two equal supporting dielectric layers, i.e., it is a sandwich-like element (see Figure 2b).

If the graphene elements of the reflectors are placed on one side of the dielectric substrate, the symmetry is reduced to group C_2 with only the two-fold rotational axis C_{2z} without planes of symmetry (see Figure 2c). Antennas described by group C_s with the plane of symmetry σ_x and σ_y are shown in Figure 2d and 2e, respectively. Notice that groups C_{2z} and C_s are subgroups of group C_{2v} . If all the graphene elements are placed on one side of the substrates, no 2D symmetry is left in the antenna shown in Figure 2f. In this case, however, the horizontal plane of symmetry σ_z can be present.

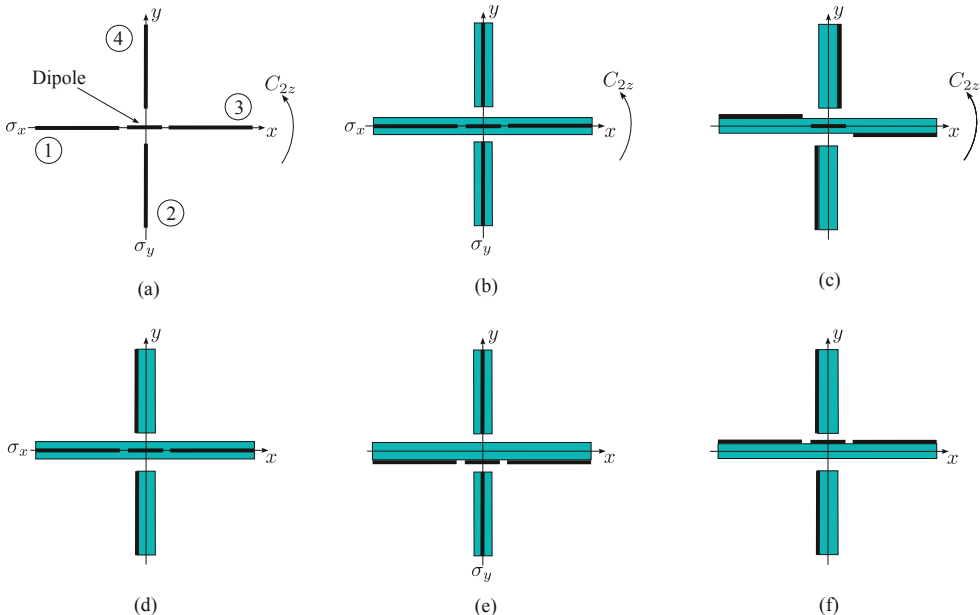


Figure 2. Symmetry of antennas in the $x0y$ plane; the thick lines correspond to graphene layers, and the thin lines delineate the dielectric substrates. (a) Free-standing antenna, group C_{2v} ; the numbers 1 and 3 denote coplanar reflectors with the dipole between them, and numbers 2 and 4 correspond to the orthogonal reflectors; (b) antenna with graphene elements between dielectric layers, group C_{2v} ; (c) antenna with reflectors on substrates, group C_2 ; (d) antenna with the symmetry C_s and the plane of symmetry σ_x ; (e) antenna with the symmetry C_s and the plane of symmetry σ_y ; (f) antenna with the symmetry C_1 , i.e., no symmetry elements.

4.3. Effect of Chemical Potentials on Antenna Symmetry

Symmetry of the antenna system is defined not only by geometry but also by its physical parameters, in particular, by chemical potentials. First, we shall consider the antenna without dielectric substrates in free space with C_{2v} symmetry. With equal chemical potentials on the reflectors, the symmetry is also described by group C_{2v} . This symmetry is preserved if the reflectors in each pair of the coplanar and orthogonal reflectors have the same chemical potential. If only one pair of reflectors has the same potential, this yields C_s symmetry. If the chemical potentials of all the reflectors are different, the antenna loses all the elements of symmetry C_{2v} (except the unit element e , which does not provide any information).

4.4. Resulting Symmetry of Antenna

From the point of view of group theory, the resulting symmetry of the structure depends on the combined effect of the dielectric substrates and of the chemical potentials. This can be determined using Curie's principle of symmetry superposition [33]. This principle states that the symmetry of a complex object is defined by the highest common subgroup of all the groups describing the object. In our case, it is defined by intersection from one side of the group of symmetry of the antenna with substrates with chemical potentials equal to zero, and from the other side, of the group of symmetry of the chemical potentials, for example, $C_{2v} \cap C_{2v} = C_{2v}$, $C_{2v} \cap C_s = C_s$, $C_2 \cap C_s = C_1$.

Notice that with the small thickness of the substrates and low dielectric constants of the dielectric material, the influence of the substrates on the symmetry can be very small, and the resulting symmetry of the antenna will be defined mostly by the chemical potentials. Different resulting symmetries allow us to realize different RPs using the same antenna, as shown by numerical calculations in Section 8.

4.5. Symmetry of Currents and Fields: Group C_{2v}

The irreducible representations (IRREPs) of group C_{2v} are given in Table 1. The transformations of the graphene currents \mathbf{j} , the electric field \mathbf{E} , and the magnetic field \mathbf{H} are defined by this table as follows. Let us consider, for example, the currents in the coplanar reflector 1 of Figure 1a. Due to the 2D nature of graphene, only two components of the current can exist in the layer, namely, j_x and j_z . The component j_z belongs to IRREP A_1 where all the representations are equal to 1; therefore, after application of all symmetry operators, j_z preserves its sign. This means that the j_z components in the symmetrical points of the two coplanar (and also in the two orthogonal) reflectors will be the same. On the other side, the component j_x belongs to IRREP B_1 ; therefore, after rotation by π (the symmetry element C_2), j_x multiplied by the IRREP -1 preserves its modulus but changes the sign. By reflection σ_x , the current j_x is not changed (it is the same current in the same graphene reflector). However, after reflection σ_y , one comes from reflector 1 to the symmetrical point in reflector 3 and, multiplying by -1 , one has the current in this reflector.

Table 1. IRREPs of group C_{2v} ; current and field transformations.

C_{2v}	e	C_2	σ_x	σ_y	Current \mathbf{j}	Field \mathbf{E}	Field \mathbf{H}
A_1	1	1	1	1	j_z	E_z	
A_2	1	1	-1	-1			H_z
B_1	1	-1	1	-1	j_x	E_x	H_y
B_2	1	-1	-1	1	j_y	E_y	H_x

In the case of the electromagnetic fields \mathbf{E} and \mathbf{H} , one can consider their symmetry at any point of the space. Due to the relation $\mathbf{j} = \sigma_g \mathbf{E}$, where σ_g is the conductivity of graphene, the symmetry of the electric field \mathbf{E} on the graphene elements coincides with the symmetry of the current \mathbf{j} .

4.6. Symmetry of Currents and Fields: Groups C_2 and C_s

The symmetry degeneration Table 2 provides the correspondence between the IRREPs of group C_{2v} and the IRREPs of its subgroups C_2 and C_s [34]. As a result, one can assign different components of current and fields to IRREPs C_2 or C_s using the corresponding IRREPs of group C_{2v} . Notice that, in the case of group C_s , one needs to consider two variants with different orientations of the planes of symmetry separately, namely, one is within the plane of symmetry σ_x (group C_s^x), and the other within the plane σ_y (group C_s^y).

Table 2. Symmetry degeneration table of group C_{2v} .

C_{2v}	C_2	C_s^x	C_s^y
A_1	A	A	A
A_2	A	B	B
B_1	B	A	B
B_2	B	B	A

For example, the components belonging to the IRREPs A_1 and A_2 of C_{2v} will belong to the IRREP A of C_2 . However, A_1 of C_{2v} degenerates to the IRREP A of C_s^x , but A_2 degenerates to the IRREP B of C_s^x . The IRREP A in the C_s^x group describes an even symmetry, but the IRREP B corresponds to the odd symmetry with respect to the plane σ_x . The presented information allows us to create Tables 3–5. Additionally, we present in Table 6 the transformation properties of the currents in the graphene elements as well as the electric and magnetic fields with respect to the plane σ_z .

Table 3. IRREPs of group C_2 ; current and field transformations.

C_2	e	C_2	Current \mathbf{j}	Field E	Field H
A	1	1	j_z	E_z	H_z
B	1	-1	j_x, j_y	E_x, E_y	H_x, H_y

Table 4. IRREPs of group C_s^x , plane of symmetry σ_x ; current and field transformations.

C_s^x	e	σ_x	Current \mathbf{j}	Field E	Field H
A	1	1	j_x, j_z	E_x, E_z	H_y
B	1	-1	j_y	E_y	H_x, H_z

Table 5. IRREPs of group C_s^y , plane of symmetry σ_y ; current and field transformations.

C_s^y	e	σ_y	Current \mathbf{j}	Field E	Field H
A	1	1	j_y, j_z	E_y, E_z	H_x
B	1	-1	j_x	E_x	H_y, H_z

Table 6. IRREPs of group C_s^z , plane of symmetry σ_z ; current and field transformations.

C_s^z	e	σ_z	Current \mathbf{j}	Field E	Field H
A	1	1	j_z	E_z	H_x, H_y
B	1	-1	j_x, j_y	E_x, E_y	H_z

5. Qualitative Analysis of the Currents and Fields

Qualitative analysis of both the near and far fields of the antennas can be completed using the elaborated Tables 1 and 3–6. A special line is the vertical axis z with the parameters $x = 0$ and $y = 0$. Due to the two-fold rotation axis C_2 in groups C_{2v} and C_2 , the components that are odd with respect to this element (see Tables 1 and 3, the field

components E_x , E_y and also H_x and H_y) are equal to zero on the axis z because these components change their sign on the axis. Therefore, the Poynting vector in the z -direction is equal to zero, and the antenna does not radiate in this direction. However, groups of symmetry C_s^x and C_s^y do not prohibit the existence of the Poynting vector in the z -direction. For example, in Table 4, for group C_s^x , the components E_x and H_y are even with respect to the plane σ_x , i.e., they can exist on the axis z , thus providing the Poynting vector in the z -direction.

Now, we consider the restrictions produced by the planes of symmetry. If, for example, a current or field component is odd with respect to the plane of symmetry σ_x , it means that this component is zero in this plane. The same is true for the planes σ_y and σ_z . For example, in Figure 3b, obtained by numerical calculations, one can see that in the plane $z = 0$, the graphene currents $j_y = 0$ because this current is odd with respect to this plane. The field E_x in Figure 4 is odd with respect to the plane σ_y and, therefore, it is equal to zero in this plane. The argument results obtained by symmetry are exact and can be used as references in numerical calculations.

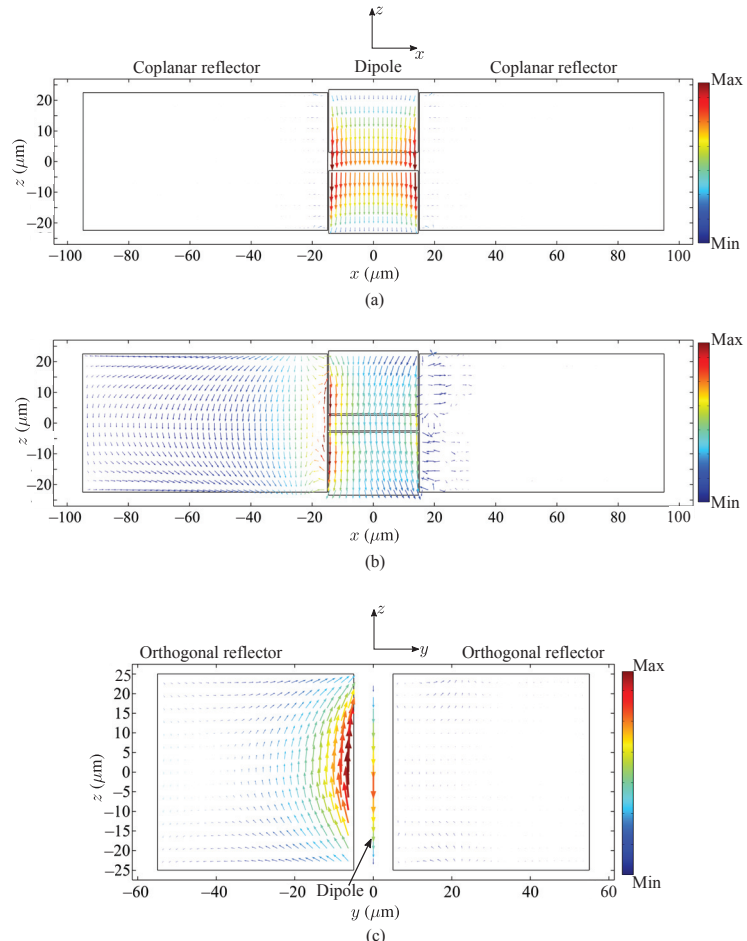


Figure 3. Current distributions on graphene parts at 1.89 THz: (a) on the dipole and on the coplanar reflectors (state 0, plane $x0z$), (b) on the dipole and on the coplanar reflectors (state 1, plane $x0z$), (c) on the dipole and orthogonal reflectors (state 2, plane $y0z$).

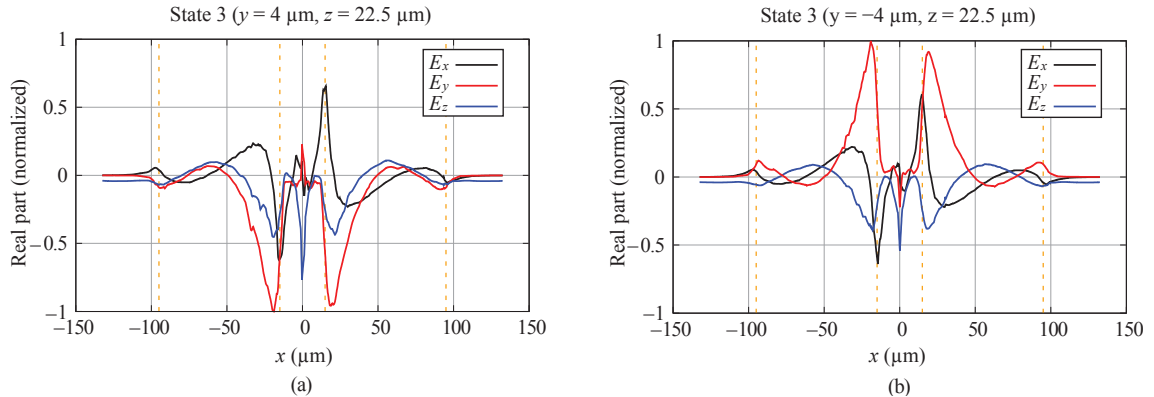


Figure 4. The x -dependence of E_x , E_y , and E_z field components, state 3, $f = 1.89$ THz. The coordinates $z = 22.5$ μm , (a) $y = 4$ μm , (b) $y = -4$ μm . The vertical dotted lines delineate the regions of the dipole and the reflectors.

6. Pre-Optimization Design of Graphene Dipole Antenna (Without Reflectors)

Few studies in the literature provide equations for designing terahertz graphene dipole antennas and predicting their plasmonic resonance frequency. In [35], a Fabry-Perot model is presented to estimate the resonance frequency of a graphene-based nano-patch antenna based on its length. That antenna was modeled as an infinitely wide graphene patch suspended in the air, and the results were verified by means of numerical simulations. To take into account the finite width of a realistic graphene-based nano-patch antenna, a partial element equivalent circuit (PEEC) model was developed in [36] to calculate absorption cross-section peaks, which can be used to obtain the device resonance frequencies. That approach is validated using data from [37,38]; however, it does not consider antenna feeding mechanisms. In [39], an RLC resonant circuit model for graphene-based bow-tie antennas was proposed, which was fed by a THz photomixer between its arms. More recently, a circuit model for nanoscale graphene dipole antennas was presented in [40]. Despite permitting prompt physical analysis, the evaluation of antenna performance, and simplified optimization procedures for obtaining a desired set of antenna characteristics, the parameters of antenna circuit models must often be extracted from full-wave simulation data. Furthermore, in addition to the strong influence of the basic graphene parameters (dimensions and chemical potential) and dipole feeding structures, substrate electromagnetic parameters play a fundamental role in defining the operational characteristics of the antenna.

In [41], semi-analytical equations were developed to facilitate the design of rectangular terahertz graphene-based dipole antennas mounted on glass substrates. The equations allow for the direct calculation of the dipole length needed to achieve resonance at a given frequency f_r , given the antenna width w_0 , graphene chemical potential μ_{c0} , and the dimensions of the feeding structure. The formulation is a combination of the graphene electrostatic scaling law [42,43] and the least squares method [44], which were used with finite-difference time-domain (FDTD) [45,46] simulations, taking into account the dipole feeding mechanism of Figure 1 and various combinations of antenna dimensions and chemical potential values.

A coplanar plate capacitor is formed by the graphene dipole metallic electrodes. Its capacitance (ignoring graphene contribution) is given by $C = \epsilon_{\text{eff}} w_0 K(\sqrt{1 - k^2}) / K(k)$, as detailed in [47,48], in which ϵ_{eff} is the effective permittivity around the structure, $K(.)$ is the complete first kind elliptic integral [49], $k = d_{\text{gap}} / L_s$, d_{gap} is the distance between metallic plates, d_{metal} is the plate width, and $L_s = d_{\text{gap}} + 2d_{\text{metal}}$. Furthermore, the self-inductance of the metallic electrodes [50] is given by $L = 2 \cdot 10^{-9} L_s [\log(2L_s/w_0) + 0.5 + 0.2235w_0/L_s]$. Thus, the resonance frequency f_m , solely regarding the pair of metallic feed contacts

composing the graphene dipole, can be approximately calculated by employing the well-known LC circuit equation $f_m = (2\pi\sqrt{LC})^{-1}$. Considering the graphene sheets as part of the structure, the resonance frequency f_m can be used to calculate the phase contribution of the source and the metallic parts, overall measuring L_s , which is obtained by $\theta_s = \pi f_r / f_m$, where f_r is the graphene dipole first resonance frequency. Thus, the half-cycle contribution θ_g of both graphene sheets in the dipole antenna is $\theta_g = \pi - \theta_s$. Therefore, one can see that the total length of the pair of graphene sheets L_g is given by $L_g = \theta_g / \beta$, where β is the graphene plasmonic phase constant. Clearly, the total length of the graphene dipole antenna is $l_0 = L_s + L_g$.

As is shown in detail by [41], β can be obtained using an adapted version of the quasi-electrostatic scaling parameter [43] for cases in which condition $w_0 \ll \lambda_{\text{spp}}$ is not met (such as in the cases of the antennas in this paper). The adapted scaling parameter η is given by $\eta = \text{Im}[\sigma(f_r)] / (f_r w_0 \epsilon_{\text{eff}})$, in which f_r is the graphene dipole resonance frequency. In [41], several graphene dipole antennas were simulated using the FDTD method, from which f_r has been numerically computed and η has been calculated using the given definition. Finally, it can be shown that $\beta \approx \eta^a e^b / w_0$, in which e is Euler's number and a and b are functions of μ_c and w_0 [41]. Thus, since the values of f_r , μ_c , and w_0 were previously defined, β and L_g can be calculated.

For designing a pre-optimization model of our THz graphene dipole antenna, resonating at $f_r = 1.5$ THz, a high level of efficiency must be assured. It is known that, for low THz applications, the width of graphene nanoribbons should measure tens of micrometers because the imaginary part of the effective refractive index is importantly reduced by increasing the graphene sheet width [51]. As a consequence, the radiation efficiency of the graphene dipole antenna also substantially improves with dipole width in the THz range from approximately 16% to 80%, at resonance frequency, by increasing the dipole width from 2 μm to 32 μm (with $\mu_{c0} = 1$ eV and $l_0 = 41$ μm) [41]. For this reason, we have selected the dipole width $w_0 = 30$ μm for our pre-optimization dipole model. However, w_0 should be smaller than l_0 for avoiding undesired width-related resonances. Further fixed parameters in our design are: $d_{\text{gap}} = 5$ μm , $d_{\text{metal}} = 0.5$ μm , $\epsilon_r = 3.8$ (glass substrate relative permittivity), and $\mu_{c0} = 1.2$ eV. Thus, for our device, by using the given parameters, definitions, and expressions, we obtain $\eta \approx 1.372 \times 10^{-10}$, $a \approx -0.594$, $b \approx -12.722$, $\beta \approx 7.129 \times 10^4$, and $L_g = \theta_g / \beta \approx 35.4$ μm ; finally, the dipole length is estimated to be $l_0 = (d_{\text{gap}} + 2d_{\text{metal}}) + L_g \approx 41.4$ μm to produce the desired resonance frequency and high radiation efficiency [41]. Finally, note that the term pre-optimization is used in this section due to the fact that the reflectors are not yet being considered at this point. The uncoupled dipole design is optimized, but once reflectors are present and coupled to the active antenna, dipole dimensions along with dimensions of reflectors and chemical potentials of all graphene parts must be optimized for working as a single device. This is explored in the following section.

7. Design of Graphene Dipole Antenna with Reflectors

Graphene reflectors are passive elements that can be used to improve and control the gain of a given antenna (such as a graphene dipole). This can be achieved by placing the reflectors at specific distances d_i from the dipole, forming a parasitically coupled antenna. Chemical potentials of reflectors can be regulated in order to define maximum gain direction by tuning electromagnetic coupling among the active element (dipole) and passive parts (reflectors). However, the antenna operation spectral range may also be affected due to alterable electromagnetic coupling characteristics. Fortunately, the operation spectral range can be maintained if the chemical potential of the graphene dipole is regulated along with those of the reflectors.

For defining geometric parameters of the antenna in Figure 1b, full-wave numerical electromagnetic simulations were performed using the software CST Studio Suite 2019. In order to minimize computational requirements, graphene elements composing the dipole antenna and reflectors are modeled using a surface impedance boundary condition [9]. The

surface impedance boundary condition is commonly used in electromagnetic simulations of graphene sheets to model the behavior of the graphene with interfaces to surrounding media, such as air or dielectric materials. The surface impedance boundary condition allows the representation of graphene as a thin layer of material, i.e., it is represented as a 2D material in a computational mesh. It takes into account the electromagnetic properties of the interface by considering the complex conductivity of the graphene sheet. By defining the surface impedance boundary condition appropriately, the simulation can accurately model the electromagnetic behavior of the thin graphene sheet and the antenna and can predict the performance of the device. The chosen graphene parameters are $\tau = 0.5$ ps [52,53] and room temperature $T = 300$ K. As an optimization starting point for defining the device dimensions, the pre-optimization dimensions formerly calculated for the graphene dipole antenna were used ($w_0 = 30$ μm and $l_0 = 40.4$ μm). Then, reflectors were included in the model. Dimensions of the dipole antenna and reflectors were optimized to preserve the operation band by taking into account the reflectors' influence (whether they were activated or not). We consider a graphene sheet to be electrically deactivated if its chemical potential is zero and activated otherwise. The dimensions of the graphene elements of the proposed antenna obtained via parametric optimization are shown in Table 7. Note that the operation band of the proposed antenna is chosen to be centered at 1.89 THz, around the second resonance frequency of the dipole, since its radiation efficiency is higher than radiation efficiency seen around $f_r = 1.5$ THz.

Table 7. Optimized dimensions of graphene elements of the proposed antenna.

Parameter	Dimension (μm)	Parameter	Dimension (μm)
w_0	29.32	w_{r_2}	50
l_0	46.92	w_{r_4}	50
l_{r_1}	45	l_{r_2}	50
l_{r_3}	45	l_{r_4}	50
w_{r_1}	80	d_x	0.33
w_{r_3}	80	d_y	5

8. Numerical Simulations and Equivalent Circuit Analysis

8.1. Comparison of Radiation Patterns of the Graphene Dipole Antenna and Quasi-Omnidirectional Antenna with Reflectors

Symmetry of a common linear wire antenna oriented in the z -direction, in the plane $x0y$, is described by the continuous group $C_{\infty v}$ with the axis C_z of the infinite order. This symmetry provides omnidirectional RP. The graphene antenna without reflectors is, in fact, a rectangular one with a one-atom thickness. Symmetry of this antenna in the $x0y$ plane is C_{2v} , which is a subgroup of $C_{\infty v}$. As a result of symmetry reduction, the corresponding RP is not omnidirectional. The elliptic-like diagram of such a graphene dipole antenna is shown in Figure 5a. The geometric dimensions of the antenna in this example are given in Section 7.

As a first demonstration of the effect of the reflectors in RP, we show that it is possible to transform the elliptic-like RP of the graphene antenna in Figure 5a to the quasi-omnidirectional one by applying certain chemical potentials on the reflectors. With $\mu_c^{r_2} = \mu_c^{r_4} = 0$ eV and $\mu_c^{r_1} = \mu_c^{r_3} = 0.11$ eV on the reflectors, the RP is transformed to an almost circular RP, as shown in Figure 5b. Quantitatively, the ratio of the minor axis to the major one for the antenna without reflectors is 0.8, but this parameter for the antenna with reflectors increases to 0.93.

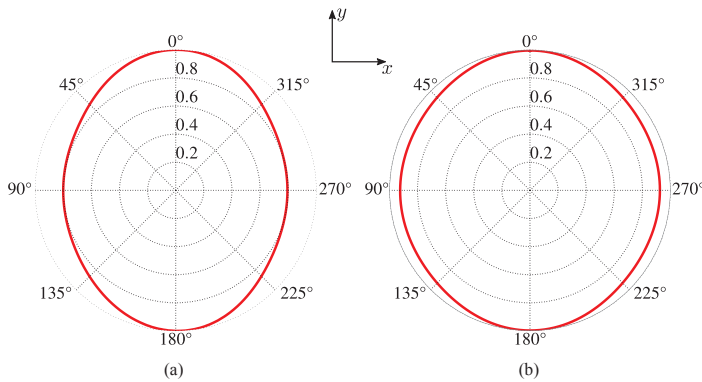


Figure 5. The normalized RP (red curves) in the x_0y plane: (a) dipole antenna with the chemical potential of the dipole $\mu_{c0} = 0.55$ eV and the chemical potentials of all the reflectors equal to 0, i.e., $\mu_c^{r1} = \mu_c^{r2} = \mu_c^{r3} = \mu_c^{r4} = 0$ eV, (b) dipole with the chemical potential $\mu_{c0} = 0.55$ eV and the chemical potentials of the reflectors $\mu_c^{r2} = \mu_c^{r4} = 0$ eV and $\mu_c^{r1} = \mu_c^{r3} = 0.11$ eV. The RPs in both cases were calculated at the frequency 1.89 THz.

8.2. Operation States and Characteristics of the Antenna

The activation setup of the reflectors defines the following six antenna operation states:

(state 0) coplanar and orthogonal reflectors are electrically deactivated ($\mu_c^{r_i} = 0$ eV, for $1 \leq i \leq 4$), which gives the symmetry elements of the antenna C_{2z} as σ_x and σ_y ;

(state 1) a single coplanar reflector is exclusively activated ($\mu_c^{r1} = 1.2$ eV and $\mu_c^{r3} = 0$ eV, or vice versa), and in this case the symmetry element is σ_x ;

(state 2) only one orthogonal reflector is activated ($\mu_c^{r4} = 0.4$ eV and $\mu_c^{r2} = 0$ eV, or vice versa), and the symmetry element is σ_y ;

(state 3) the pair of coplanar reflectors is uniquely activated ($\mu_c^{r1} = \mu_c^{r3} = 0.6$ eV), and the symmetry elements are C_{2z} , σ_x , and σ_y ;

(state 4) activation is limited to the pair of orthogonal reflectors ($\mu_c^{r2} = \mu_c^{r4} = 0.4$ eV), and the symmetry elements are C_{2z} , σ_x , and σ_y ;

(state 5) coplanar reflectors ($\mu_c^{r1} = \mu_c^{r3} = 1.2$ eV) and one orthogonal reflector ($\mu_c^{r2} = 0.5$ eV or $\mu_c^{r4} = 0.5$ eV) are activated, and the symmetry element is σ_y .

The antenna can also operate in the beam steering regime (BSR), where only one coplanar reflector and one orthogonal reflector are properly activated, with no elements in 2D symmetry. For instance, the main lobe azimuth angle is set to 45° when $\mu_c^{r1} = 1.2$ eV and $\mu_c^{r4} = 0.3$ eV.

In state 1 and BSR, the dipole chemical potential μ_{c0} is set to 0.4 eV and, in state 4, $\mu_{c0} = 0.8$ eV. For all other states, $\mu_{c0} = 1.2$ eV. This correction of μ_{c0} is required for preserving the central frequency of the antenna $f_c = 1.89$ THz.

Figure 6 shows antenna input impedances Z , while Figure 7 demonstrates total efficiency η_t , magnitude of input reflection coefficients Γ and maximum gains calculated for each device operation state and BSR from 1 THz to 3 THz. The antenna operating range of frequencies was defined such that $|\Gamma| \leq -5$ dB (see Figure 7b). In Figures 6 and 7, the operation band $[f_l, f_h]$ is highlighted (it is valid for all operation states and BSR). Since the lower frequency of the band is $f_l = 1.75$ THz and the higher frequency is $f_h = 2.03$ THz, the antenna fractional bandwidth is $BW(\%) = 200(f_h - f_l)/(f_l + f_h) \approx 14.8\%$.

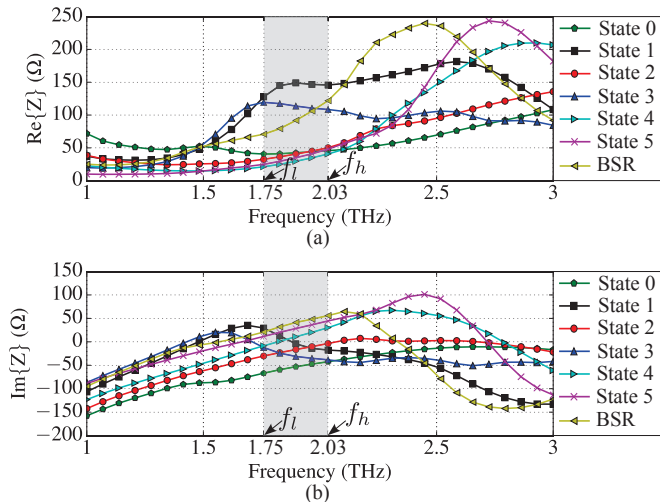


Figure 6. Antenna input impedances for the six states and BSR: (a) resistances and (b) reactances. The gray shadow defines the operation band ($f_c = 1.89$ THz).

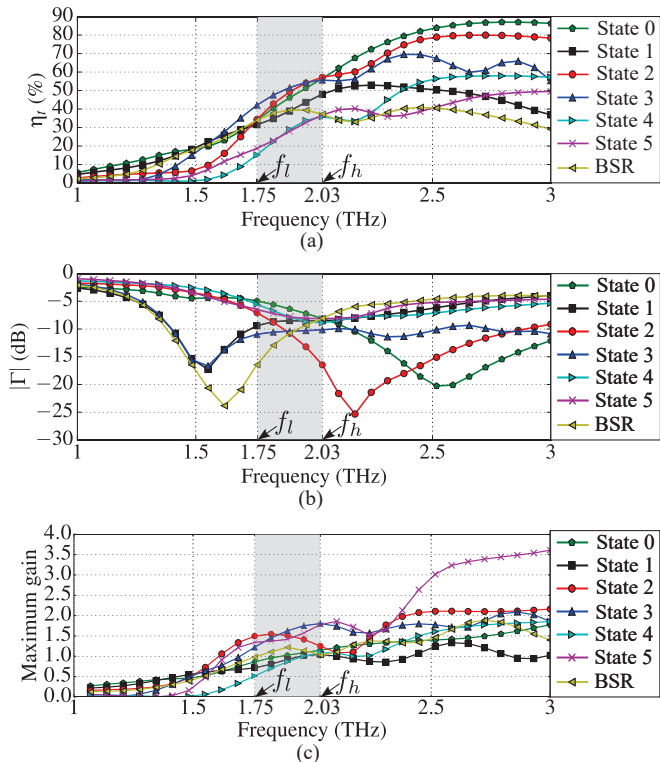


Figure 7. Antenna characteristics for each of the six operation states and BSR as functions of frequency: (a) total efficiencies η_t and (b) magnitudes of reflection coefficients Γ (dB) and (c) maximum gains. The gray shadow defines the operation band ($f_c = 1.89$ THz).

The parameters Γ and η_t were calculated using as the reference impedance Z_0 the arithmetic mean of the input resistances obtained at $f = 1.8$ THz for all states and BSR. The calculated impedance $Z_0 = 67.6 \Omega$ can be obtained using the photomixer described in [30] by properly setting the chemical potential of its graphene emitter.

The RPs of the proposed antenna on azimuth plane $x0y$ for the fixed states and BSR are depicted in Figure 8.

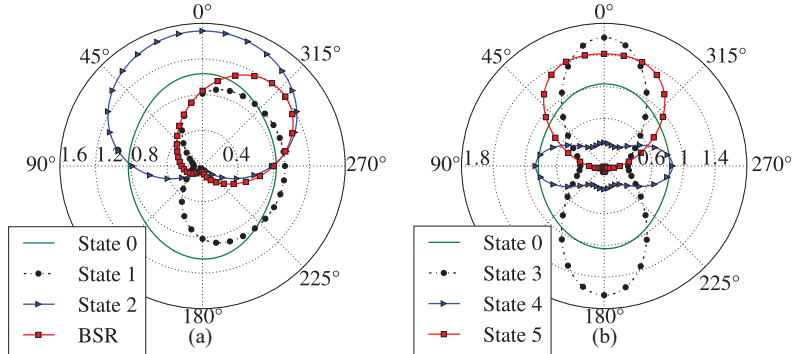


Figure 8. Antenna radiation patterns at $f_c = 1.89$ THz on azimuth plane $x0y$: (a) for states 0 (reference), 1, 2, and BSR, (b) states 0 (reference), 3, 4, and 5.

In state 0, by deactivating coplanar and orthogonal reflectors, the antenna operates in its non-directional state, as expected due to partial transparency of deactivated graphene. The diagram is slightly different from the omnidirectional one due to the absence of full rotational symmetry around the z -axis (see Section 8.1).

The antenna diagram for state 1 has its main lobe with maximum radiation directed parallel to versor $-\hat{x}$ (see Figure 8a and Table 8). Thus, state 1 is a directive one. By permuting the chemical potentials of the coplanar reflectors, the main radiation lobe can be flipped by 180° , i.e., maximum radiation is aligned with \hat{x} . For state 2, the main lobe is oriented as \hat{y} due to the conductivity of the activated graphene orthogonal reflector ($\mu_c^{r4} = 0.4$ eV), as seen in Figure 8a and Table 8. Similarly to state 1, the main lobe can be directed along $-\hat{y}$ by permuting the chemical potentials of the orthogonal reflectors.

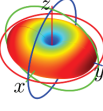
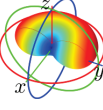
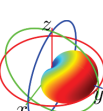
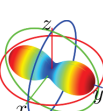
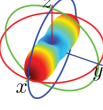
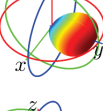
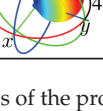
For states 3 and 4, the radiation lobes are narrower (i.e., with lower half-power beam width HPBW) along the x - and y -axes, as illustrated by Figure 8b. This is due to the simultaneous activation of coplanar reflectors in state 3 and orthogonal reflectors in state 4.

Similarly, for state 5, due to the simultaneous activation of coplanar reflectors and an orthogonal reflector, the main radiation lobe is oriented parallel to \hat{y} and is more directive than in state 2 (see Figure 8).

In BSR, due to the simultaneous activation of an orthogonal reflector and a coplanar reflector, the main lobe can be rotated by 45° with respect to $\pm\hat{y}$. Thus, the antenna in this regime has its main radiation lobe with the azimuth angle of 45° measured from the y -axis when $\mu_c^{r4} = 0.3$ eV and $\mu_c^{r1} = 1.2$, as demonstrated in Figure 8a. Conversely, by activating an orthogonal reflector ($\mu_c^{r2} = 0.3$ eV) and a coplanar reflector ($\mu_c^{r1} = 1.2$ eV), the main lobe is rotated by 45° with respect to versor \hat{y} .

Table 8 summarizes the fundamental parameters, the symmetry, and the respective 3D RPs of the proposed device calculated for all states at the central frequency $f_c = 1.89$ THz. The highest values of η_t and gain are produced in state 3, while the highest value of the front-to-back ratio (FBR) is produced in state 5. FBR is the ratio of maximum gain in the main radiation lobe and the maximum gain in the opposite direction. The minimum of $|\Gamma|$ is observed in state 2.

Table 8. Fundamental parameters and characteristics of the antenna at the central frequency 1.89 THz.

State	FBR	Maximum gain	$ \Gamma $ (dB)	η_t (%)	Chemical Potential of Reflectors	HPBW ($\theta = 90^\circ$)	Symmetry Elements	Radiation Pattern
0	1	1.04	-6.38	46.2	$\mu_c^{r_1} = \mu_c^{r_2} = 1.2$ eV, $\mu_c^{r_3} = \mu_c^{r_4} = 0$ eV, $\mu_{c0} = 1.2$ eV	—	$C_{2z}, \sigma_x,$ σ_y	
1	9.73	0.93	-8.49	38.9	$\mu_c^{r_1} = 1.2$ eV, $\mu_c^{r_3} = 0$ eV, (flipped lobe if permuted), $\mu_c^{r_2} = \mu_c^{r_4} = 0$ eV, $\mu_{c0} = 0.4$ eV	239°	σ_x	
2	17.3	1.51	-10.8	49.3	$\mu_c^{r_4} = 0.4$ eV, $\mu_c^{r_2} = 0$ eV, (flipped lobe if permuted), $\mu_c^{r_1} = \mu_c^{r_3} = 0$ eV, $\mu_{c0} = 1.2$ eV	183°	σ_y	
3	1	1.63	-10.4	51.6	$\mu_c^{r_1} = \mu_c^{r_3} = 0.6$ eV, $\mu_c^{r_2} = \mu_c^{r_4} = 0$ eV, $\mu_{c0} = 1.2$ eV	79°	$C_{2z}, \sigma_x,$ σ_y	
4	1	0.86	-7.85	29.1	$\mu_c^{r_2} = \mu_c^{r_4} = 0.4$ eV, $\mu_c^{r_1} = \mu_c^{r_3} = 0$ eV, $\mu_{c0} = 0.8$ eV	73°	$C_{2z}, \sigma_x,$ σ_y	
5	17.8	1.42	-7.83	27.9	$\mu_c^{r_1} = \mu_c^{r_3} = 1.2$ eV, $\mu_c^{r_4} = 0.5$ eV, $\mu_c^{r_2} = 0$ eV, $\mu_{c0} = 1.2$ eV	120°	σ_y	
BSR ($\phi = 45^\circ$)	10.1	1.22	-10.7	39.5	$\mu_c^{r_1} = 1.2$ eV, $\mu_c^{r_4} = 0.3$ eV, $\mu_c^{r_2} = \mu_c^{r_3} = 0$ eV, $\mu_{c0} = 0.4$ eV	134°		

Finally, for the sake of illustration of lobe rotation capabilities of the proposed device, we present in Figure 9 three radiation patterns with maximum gain angle ϕ_{\max} set to 0° , 45° , and 90° . The necessary chemical potentials for each graphene part of the antenna for producing the lobes shown are given in Table 9. Note that the 360° main lobe rotation is possible due to the demonstrated symmetry properties of the device.

Table 9. Chemical potentials of graphene parts for setting maximum gain angle ϕ_{\max} to 0° , 45° , and 90° .

ϕ_{\max}	Chemical Potentials
0°	$\mu_c^{r_1} = 0$ eV, $\mu_c^{r_3} = 1.2$ eV, $\mu_c^{r_2} = \mu_c^{r_4} = 0$ eV, and $\mu_{c0} = 0.4$ eV
45°	$\mu_c^{r_1} = 0$ eV, $\mu_c^{r_3} = 1.2$ eV, $\mu_c^{r_2} = 0$ eV, $\mu_c^{r_4} = 0.3$ eV, and $\mu_{c0} = 0.4$ eV
90°	$\mu_c^{r_1} = \mu_c^{r_3} = 0$ eV, $\mu_c^{r_2} = 0$ eV, $\mu_c^{r_4} = 0.4$ eV, and $\mu_{c0} = 1.2$ eV

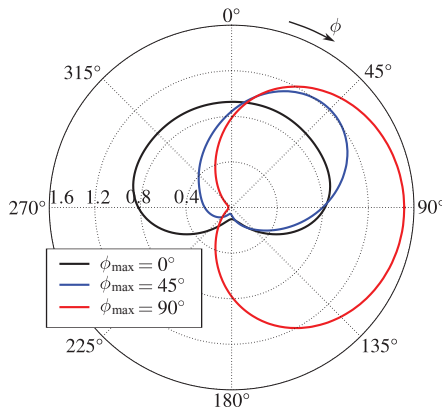


Figure 9. Radiation patterns of the proposed device in free space illustrating lobe rotation capabilities: ϕ_{\max} is the angle of maximum gain.

8.3. Near Field in the Antenna

The proposed graphene antenna electromagnetic field distribution is distinct from that of the metal wire dipole because of its different composition and geometry. Here, we consider the antenna with symmetry C_{2v} . In order to discuss the peculiarities of the field, we calculated the distribution of the fields along the line oriented in the x -direction for state 3, $f = 1.89$ THz. The line is fixed at the coordinate $z = 22.5$ μ m. The components E_x , E_y , and E_z at $y = 4$ μ m are presented in Figure 4a and at $y = -4$ μ m in Figure 4b. The components H_x , H_y , and H_z for the same coordinates are given in Figure 10a,b.

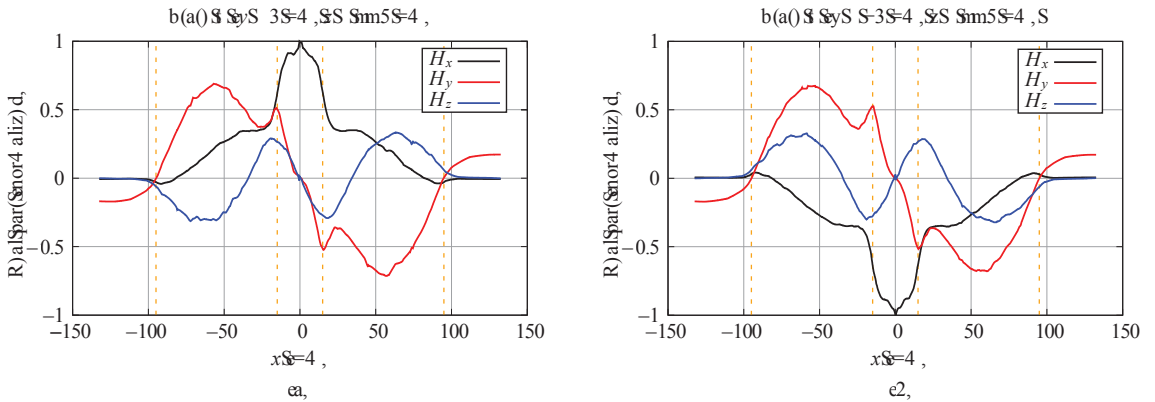


Figure 10. The x -dependence of H_x , H_y , and H_z field components, state 3, $f = 1.89$ THz. The coordinates $z = 22.5$ μ m, (a) $y = 4$ μ m, (b) $y = -4$ μ m. The vertical dotted lines delineate the regions of the dipole and the reflectors.

Analyzing these graphics, one can see that the symmetry of the field components is in accordance with the results of the group-theoretical predictions in Section 4.5 and the discussion in Section 5. Small discrepancies in the absolute values of the fields in the symmetric points are due the limits in accuracy of the numerical method.

The near field in the antenna contains all components of the electric and magnetic fields of high intensity, which vary rapidly in space. The presence of the reflectors where the excited currents produce the fields significantly changes the structure of the near field in comparison with the antenna without reflectors (not presented here). The components E_z and H_y (more specifically, E_θ and H_ϕ) for $|x| > 95$ μ m provide the Poynting vector of the outgoing wave. Notice that the components of the resonant near fields in the region of

the antenna and the reflectors are much higher than the corresponding components of the radiated field.

8.4. Circuit Representation of Graphene Dipole Antenna with Reflectors

Circuit representations of the antenna with its reflectors can be used to study the frequency characteristics of the antenna. As demonstrated in [5], a graphene dipole antenna can be represented by an RLC circuit fed by an electric source representing the dipole photomixer excitation. In [54], asynchronously tuned coupled-resonator circuits are presented for analysis of electromagnetically coupled resonators that may resonate at different frequencies. This is the same case as the proposed graphene antenna when one of the reflectors is activated.

A graphene patch surface impedance is defined by $Z_p(\omega) = 1/(N\sigma_g(\omega))$, where $\sigma_g(\omega)$ is given by (1) and N is the number of graphene layers composing the patch [9]. Notice that $\sigma_g(\omega)$ is dependent on the graphene electrochemical potential, which is specifically set for each graphene patch depending on the proposed device operating state (see Table 8). Thus, the graphene resonance frequency depends on sheet dimensions, on $\sigma_g(\omega)$, and on the surrounding media parameters [9,41].

The graphene dipole and the activated graphene reflector act as electromagnetically coupled resonators, resonating at different frequencies. Therefore, a suitable equivalent circuit representation [54] for the proposed graphene antenna in Figure 1b, with only one activated graphene reflector, is depicted by Figure 11. The graphene dipole circuit elements are R_d (resistance of graphene dipole), L_d (dipole inductance), and C_d (dipole capacitance). Furthermore, R_{r_n} , L_{r_n} , and C_{r_n} are, respectively, the equivalent resistance, inductance, and capacitance associated with the discussed graphene reflector. Circuit parameters C_m and L_m are coupling capacitance and coupling inductance established respectively by electric and magnetic field coupling between the dipole and the activated graphene reflector. Finally, the graphene dipole terminals are associated with nodes A and B in the circuit of Figure 11. A photomixer is used to convert optical signals to electrical current, which feeds the antenna [30]. Thus, the current source represents the optically-induced photomixer current.

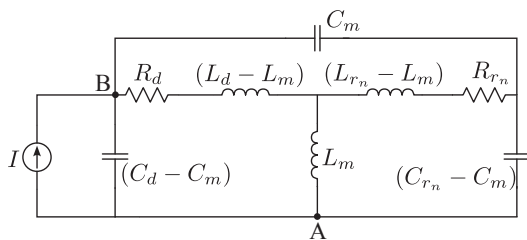


Figure 11. Circuit representation of the graphene dipole antenna coupled with the activated graphene reflector placed near the dipole.

In order to estimate circuit lumped parameters, we suppose that our device is operating in state 1. For this specific case, only a coplanar reflector is activated (i.e., $\mu_c^{r_1} = 1.2$ eV), and the graphene dipole chemical potential is set to $\mu_{c0} = 0.4$ eV.

Since the circuit model is based on the idea of two electromagnetically coupled resonators [54], we initially simulate the dipole antenna with our full-wave model considering all reflectors deactivated (their chemical potentials are set to zero), i.e., the dipole is practically decoupled from the reflectors, and we set $\mu_{c0} = 0.4$ eV. This condition allows us to estimate the lumped circuit parameters for the dipole (R_d , L_d and C_d) when it is decoupled from all reflectors. Analyzing the circuit in Figure 11, one can see that the dipole circuit is decoupled from the reflector when $R_{r_1} \rightarrow \infty$, $L_{r_1} \rightarrow 0$, $C_{r_1} \rightarrow 0$, $C_m \rightarrow 0$, and $L_m \rightarrow 0$. The aforementioned decoupling conditions are obtained when the graphene conductivity of the reflector is small, since $\mu_c^{r_1} = 0$.

The full-wave dipole simulation provides the impedance shown in Figure 12, from which we see that the decoupled dipole's first resonance frequency is $f_1^d \approx 1.316$ THz. At the frequency f_1^d , we obtain, from Figure 12, $R_d \approx \text{Re}\{Z\}(f_1^d) \approx 37.9 \Omega$. Furthermore, in order to obtain the dipole circuit parameters L_d and C_d , we extract the values of $\text{Im}\{Z\}$ obtained at the frequencies around f_1^d . At $f_L = 1.25$ THz and $f_H = 1.35$ THz, one has $\text{Im}\{Z\}(f_L) \approx -16.27 \Omega$ and $\text{Im}\{Z\}(f_H) \approx 8.89 \Omega$. Therefore, we may write two circuital equations: $\omega_L L_d - \omega_L^{-1} C_d^{-1} = -16.27$ and $\omega_H L_d - \omega_H^{-1} C_d^{-1} = 8.89$, where $\omega_L = 2\pi f_L$ and $\omega_H = 2\pi f_H$. By solving the above-formed linear system for L_d and C_d^{-1} , one gets $L_d \approx 1.98 \times 10^{-11} \text{ H}$ and $C_d \approx 7.41 \times 10^{-16} \text{ F}$.

Decoupled activated coplanar reflector lumped parameters can be estimated by determining the reflector resonance frequency f_1^{r1} . In this work, we employ the procedure described in [37] for numerically calculating a finite-length graphene plate extinction cross-section σ_{ext} , whose peak is associated with the sheet resonance frequency. The numerical procedure starts by simulating the graphene sheet excited by a plane wave, as illustrated by Figure 13a. Then, ratios of surface integrals involving Poynting vectors of the total, scattered, and incident fields are numerically computed [37], producing, in our case, the curve shown in Figure 13b, in which we see that $f_1^{r1} \approx 2.0$ THz. It is important to point out that the z-polarization of plane wave is so defined for agreeing with the stronger current direction of the coupled coplanar reflector, as shown in Figure 3b. In order to estimate the lumped circuit parameters for the coplanar reflector, we use the calculated values of the dipole lumped parameters as a reference. Because the coplanar reflector length is greater than the dipole dimensions, we estimate that $L_{r1} \approx 2.45L_d \approx 4.851 \times 10^{-11} \text{ H}$. This estimation provides $C_{r1} = [1/(2\pi f_1^{r1})^2]/L_{r1} \approx 1.305 \times 10^{-16} \text{ F}$. Furthermore, since the chemical potential is higher on the reflector in state 1, we estimate that $R_{r1} \approx R_d/5$.

Finally, the electromagnetic coupling circuital parameters L_m and C_m were obtained in this work by manual parametric optimization. We found that $L_m \approx 1.20L_d \approx 2.376 \times 10^{-11} \text{ H}$ and $C_m \approx 0.80C_d \approx 5.928 \times 10^{-16} \text{ F}$. By comparing the full-wave antenna impedance for the electromagnetically coupled dipole-reflector device with the equivalent circuit impedance, we observed that R_d should be slightly reduced from 37.9Ω to $R_d = 33.0 \Omega$ for better fitting. Figure 14 shows a comparison between the antenna impedance while operating in state 1 (the graphene dipole and the activated coplanar reflector are electromagnetically coupled), obtained by means of the full-wave CST simulation, and the impedance of its equivalent circuit obtained with the calculated lumped circuit parameters. As one can see in Figure 14, the procedure suggested in this work for estimating the lumped circuit parameters produced a good agreement between the full-wave and equivalent circuit models.

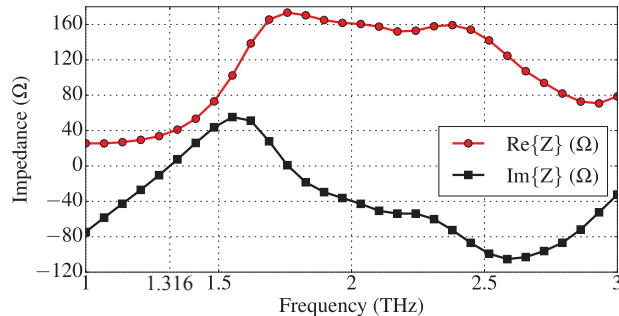


Figure 12. Graphene dipole impedance obtained via full-wave CST simulation (dipole with $\mu_{c0} = 0.4 \text{ eV}$ and deactivated reflectors). The dipole first resonance frequency is $f_1^d = 1.316 \text{ THz}$, at which $\text{Re}\{Z\}(f_1^d) = 37.9 \Omega$ and $\text{Im}\{Z\}(f_1^d) = 0$.

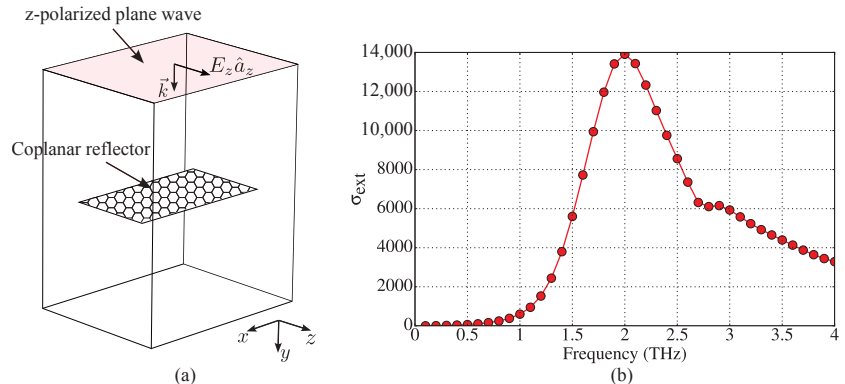


Figure 13. Numerical calculation of resonance frequency of graphene coplanar reflector in free space: (a) simulation geometry and (b) extinction cross-section of the reflector ($\mu_c^{r_1} = 1.2$ eV). Coplanar reflector resonance frequency is $f_1^{r_1} = 2.0$ THz.

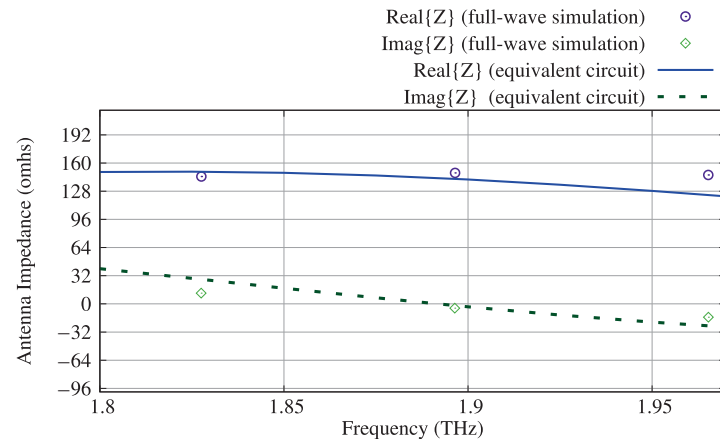


Figure 14. Antenna impedance obtained via full-wave CST simulation of graphene dipole with an activated coplanar graphene reflector (state 1) and the impedance of its equivalent circuit.

8.5. Effect of Substrates and Base and θ -Control of RP

The above analysis of the antenna was completed for the case of absence of any substrate. As a result, due to the plane of symmetry σ_z , for example, the maximum of the RP is always situated in the $x0y$ plane. In practice, the graphene reflectors are placed on substrates, and the antenna as a whole is placed on a supporting base. These dielectric elements modify the parameters and RP of the antenna.

One possible practical realization of the proposed antenna is shown in Figure 15. The coplanar reflectors, dipole, and the orthogonal reflectors are placed on SiO_2 substrates with relative permittivity $\epsilon_r = 3.8$ and thickness 5 μm . The whole structure is mounted on a SiO_2 base infinite in x - and y -directions with thickness 40 μm . Because of the presence of the dielectric substrates and the base, as well as the applied chemical potentials, all possible symmetry elements of the antenna in this case are absent.

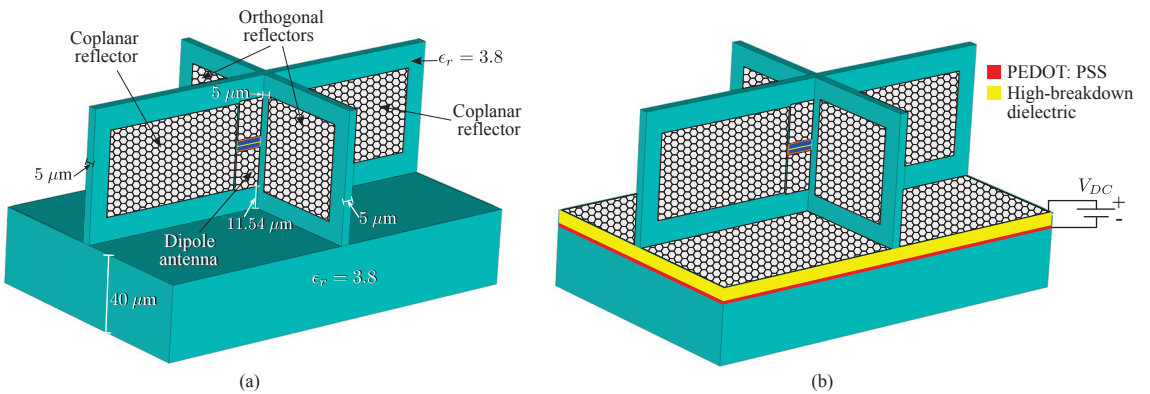


Figure 15. Antenna (a) with dielectric substrates and dielectric base, where a system of the chemical potential control is not shown; (b) with additional graphene layer on the base and the base control system. Navy blue represents the dielectric material.

Figure 16a shows the radiation patterns of the antenna operating in free space, and Figure 16b shows it with SiO_2 base and substrates.

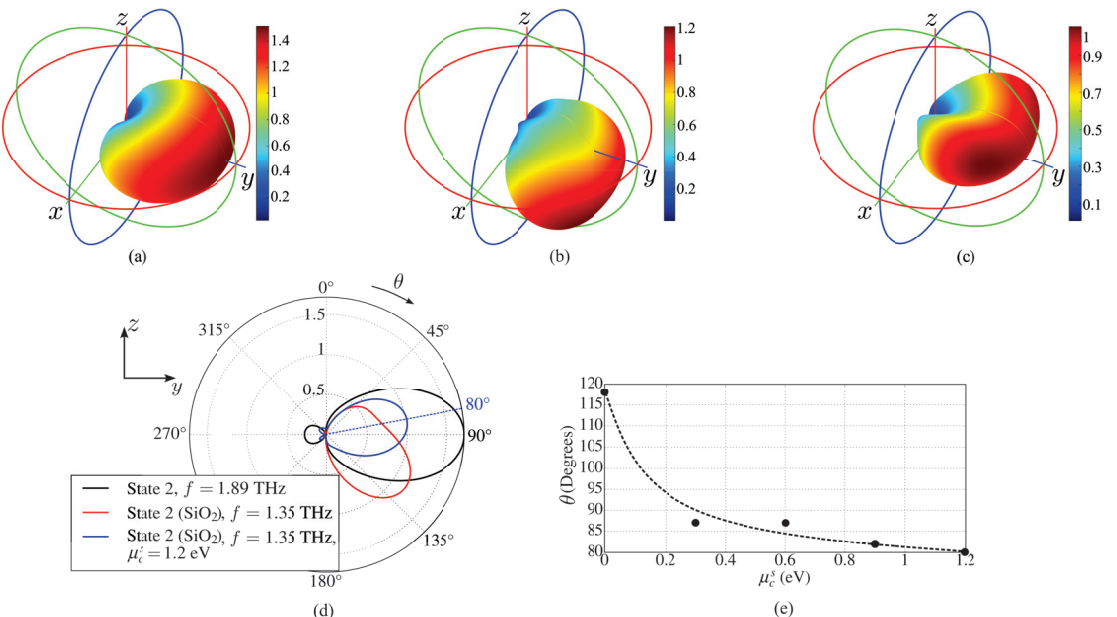


Figure 16. Comparison of antenna radiation patterns in state 2: (a) in free space, (b) with dielectric supporting substrates for reflectors and with dielectric base, (c) the dielectric base is covered by an additional graphene layer with $\mu_c^s = 1.2 \text{ eV}$, gain is mapped by the color bars, (d) RPs in the plane $y0z$ for the cases (a–c), (e) μ_c^s dependence of the RP inclination angle θ (the points are the result of numerical calculations).

For the free space case, the radiation pattern is calculated at $f_c = 1.89 \text{ THz}$ (see Table 1, state 2) and, when dielectric elements are included, $f_c = 1.35 \text{ THz}$. The thin reflector substrates have a relatively small influence on the antenna characteristics. However, the resonance frequency lowers due to the Purcell effect and, as expected [55] due to the optically denser massive dielectric base, the main radiation lobe tilts towards the base with

$\theta = 117^\circ$, as can be seen in Figure 16b,d. Figure 16d,e demonstrate that it is possible to correct the angle θ by using the chemical potential μ_c^s of the additional graphene layer placed on the base.

9. Discussion

The wavelength in free space for the frequency $f = 1.89$ THz is $\lambda \approx 160$ μm . The length of the graphene dipole $l_0 = 46.92$ μm is 3.4 times less than λ . The volume $l_x \times l_y \times l_z$ occupied by the discussed antenna in physical space is $160.66 \mu\text{m} \times 110 \mu\text{m} \times 50 \mu\text{m}$. Thus, the highest dimension of the antenna is defined by the reflectors. It is approximately equal to the free-space wavelength λ .

Now, we shall provide several comments on the presented material. First, the control of the chemical potential in every graphene element can be fulfilled by applying a tunable DC voltage V_{DC} between the graphene sheet and a thin polysilicon layer [56] embedded in the dielectric substrate. This layer with relatively high conductivity is used as a gate electrode [57,58]. The thickness of the layer is very small, and it was shown that its effect on the parameters of the corresponding device is negligible [59]. Therefore, we did not include this element in our model. A choice of the dielectric material between graphene and the gate electrode (such as, for example, HfO_2 , TiO_2 , Al_2O_3 , and ion gel gate dielectrics) allows one to change the Fermi energy up to 1.3 eV without voltage breakdown [60]. An example of the graphene layer biased by the electric field is given in Figure 15b. Notice that the same scheme can also be used for biasing of the dipole and reflector graphene sheets of Figure 1 (for simplicity, it is not shown in Figure 15b). Some other problems of graphene technology are discussed in recent review papers [61,62].

Secondly, applying a variable voltage to the coplanar and orthogonal reflectors in the beam steering regime (BSR) in the form of, for example, $\sin(\Omega_s t)$ and $\cos(\Omega_s t)$, where Ω_s is a sweeping frequency and t is time, one can provide a continuous angular rotation of the antenna beam, maintaining reasonable levels of the principal parameters of the antenna.

Thirdly, the suggested antenna can be optimized. The optimization parameters can be the geometrical dimensions of the active dipole antenna, the dimensions of the reflectors, the gaps between the dipole and reflectors, the number of graphene layers, the chemical potentials of the dipole and the reflectors, and the dimensions of the dielectric substrates and their physical parameters. Depending on application of the antenna, the objective function (or functions) can be different for example, the parameters FBR, gain, $|\Gamma|$, η_t , the antenna bandwidth, and the beam width. Thus, it can be a multi-objective and a multi-parametric optimization problem which requires special consideration. This is planned in future work.

The group-theoretical approach developed in our work allows one to reduce the volume of numerical calculus. For example, in the case of C_{2v} symmetry, it is sufficient to consider only one-eighth of the whole physical space. Such a reduction allows one to greatly accelerate the optimization process of the antenna.

10. Conclusions

In this paper, a novel smart graphene antenna with a simple design and dynamic control of its characteristics was suggested and analyzed. Group-theoretical analysis of the antenna presented in this work allows one to predict the main properties of the radiation diagram of the antenna without solving the corresponding boundary-value problem and also to reduce the volume of numerical calculations.

We have shown that, by tuning chemical potentials of the graphene reflectors and the graphene dipole, one can change the antenna radiation pattern, preserving the antenna operation band. In our work, we have calculated the main parameters of the antenna such as input reflection coefficient, total efficiency, front-to-back ratio, and gain for different operation states of the antenna. Due to the vertical orientation of the dipole with respect to the dielectric base and the presence of the four reflectors, the antenna can provide 360° beam steering of its radiation pattern. Also, with an additional graphene layer on the base,

a certain control of the radiation pattern in the θ -direction is possible. Additionally, an equivalent circuit of the antenna for analysis of its frequency characteristics is suggested. Many numerical calculations confirm the presented theoretical results.

One of the key contributions of our proposed graphene antenna is its ability to achieve continuous 360° beam steering on the azimuth plane and also continuous beam steering on elevation plane. This feature sets our antenna apart from existing THz antennas, as it allows for seamless and uninterrupted beam control over the entire azimuthal range. The ability to steer the beam continuously provides enhanced flexibility and adaptability in a wide range of applications. For instance, in THz communication systems, the antenna can dynamically track a moving receiver or transmitter, maintaining a stable and robust link. Furthermore, since THz waves can penetrate certain materials, providing valuable information in fields like medical imaging and security screening, continuous beam steering allows for more efficient scanning and mapping of the target area, enabling quick and automatic data acquisition along with improved imaging resolution.

In future work, we intend to perform optimization of radiation efficiency as well as other parameters and characteristics of the proposed device. We hope that the suggested antenna can find versatile applications.

Author Contributions: Conceptualization, V.D. and R.M.S.d.O.; methodology, V.D. and R.M.S.d.O.; software, R.R.P. and N.R.N.M.R.; validation, V.D. and R.M.S.d.O.; formal analysis, V.D. and R.M.S.d.O.; investigation, V.D., R.M.S.d.O. and R.R.P.; resources, V.D. and R.M.S.d.O.; data curation, R.R.P. and N.R.N.M.R.; writing—original draft preparation, V.D., R.M.S.d.O. and R.R.P.; writing—review and editing, V.D., R.M.S.d.O., R.R.P. and N.R.N.M.R.; visualization, R.R.P.; supervision, V.D. and R.M.S.d.O.; project administration, V.D. and R.M.S.d.O.; funding acquisition, R.M.S.d.O. All authors have read and agreed to the published version of the manuscript.

Funding: The APC was funded by CNPq via *taxa de bancada* (the student extra support funding) of doctoral scholarship of Rodrigo R. Paiva. Authors are grateful to CNPq for the support.

Institutional Review Board Statement: Not applicable.

Informed Consent Statement: Not applicable.

Data Availability Statement: Data is contained within the article.

Acknowledgments: The authors are grateful to Brazilian agency CNPq and Federal University of Pará (UFPA) for their support.

Conflicts of Interest: The authors declare no conflict of interest.

References

- Wang, Y.; Chang, B.; Xue, J.; Cao, X.; Xu, H.; He, H.; Cui, W.; He, Z. Sensing and slow light applications based on graphene metasurface in terahertz. *Diam. Relat. Mater.* **2022**, *123*, 108881. [CrossRef]
- Auton, G.; But, D.B.; Zhang, J.; Hill, E.; Coquillat, D.; Consejo, C.; Nouvel, P.; Knap, W.; Varani, L.; Teppe, F.; et al. Terahertz Detection and Imaging Using Graphene Ballistic Rectifiers. *Nano Lett.* **2017**, *17*, 7015–7020. [CrossRef] [PubMed]
- Prabhu, S.S. Chapter 4—Terahertz Spectroscopy: Advances and Applications. In *Molecular and Laser Spectroscopy*; Gupta, V., Ed.; Elsevier: Amsterdam, The Netherlands, 2018; pp. 65–85.
- Ullah, Z.; Witjaksono, G.; Nawi, I.; Tansu, N.; Irfan Khattak, M.; Junaid, M. A Review on the Development of Tunable Graphene Nanoantennas for Terahertz Optoelectronic and Plasmonic Applications. *Sensors* **2020**, *20*, 1401. [CrossRef]
- Dmitriev, V.; Rodrigues, N.R.N.M.; de Oliveira, R.M.S.; Paiva, R.R. Graphene Rectangular Loop Antenna for Terahertz Communications. *IEEE Trans. Antennas Propag.* **2020**, *69*, 3063–3073. [CrossRef]
- Shihzad, W.; Ullah, S.; Ahmad, A.; Abbasi, N.A.; Choi, D.y. Design and Analysis of Dual-Band High-Gain THz Antenna Array for THz Space Applications. *Appl. Sci.* **2022**, *12*, 9231. [CrossRef]
- Chemweno, E.; Kumar, P.; Afullo, T. Design of high-gain wideband substrate integrated waveguide dielectric resonator antenna for D-band applications. *Optik* **2023**, *272*, 170261. [CrossRef]
- Grigorenko, A.; Polini, M.; Novoselov, K. Graphene plasmonics. *Nat. Photonics* **2012**, *6*, 749–758. [CrossRef]
- Gonçalves, P.A.D.; Peres, N.M.R. *An Introduction to Graphene Plasmonics*; World Scientific Publishing: Singapore, 2016.
- Dash, S.; Patnaik, A.; Kaushik, B.K. Performance enhancement of graphene plasmonic nanoantennas for THz communication. *IET Microwaves Antennas Propag.* **2019**, *13*, 71–75. [CrossRef]

11. Rudrapati, R. Graphene: Fabrication Methods, Properties, and Applications in Modern Industries. In *Graphene Production and Application*; Ameen, S., Akhtar, M.S., Shin, H.S., Eds.; IntechOpen: London, UK, 2020; Chapter 2.
12. Goyal, R.; Vishwakarma, D.K. Design of a graphene-based patch antenna on glass substrate for high-speed terahertz communications. *Microw. Opt. Technol. Lett.* **2018**, *60*, 1594–1600. [CrossRef]
13. Ye, R.; James, D.K.; Tour, J.M. Laser-induced graphene: From discovery to translation. *Adv. Mater.* **2019**, *31*, 1803621. [CrossRef]
14. Catania, F.; Marras, E.; Giorelli, M.; Jagdale, P.; Lavagna, L.; Tagliaferro, A.; Bartoli, M. A Review on Recent Advancements of Graphene and Graphene-Related Materials in Biological Applications. *Appl. Sci.* **2021**, *11*, 614. [CrossRef]
15. Balanis, C.A. *Antenna Theory: Analysis and Design*; Wiley-Interscience: Hoboken, NJ, USA, 2005.
16. Novotny, L.; van Hulst, N. Antennas for light. *Nat. Photonics* **2011**, *5*, 83–90. [CrossRef]
17. Chang, Y.-L.; Chu, Q.-X.; Li, Y. Reconfigurable dipole antenna array with shared parasitic elements for 360° beam steering. *Int. J. Microw. Comput.-Aided Eng.* **2020**, *30*, e22435.
18. Perruisseau-Carrier, J. Graphene for antenna applications: Opportunities and challenges from microwaves to THz. In Proceedings of the 2012 Loughborough Antennas & Propagation Conference (LAPC), Leicestershire, UK, 12–13 November 2012; pp. 1–4.
19. Yang, Y.-J.; Wu, B.; Zhao, Y.-T.; Chi-Fan. Dual-band beam steering THz antenna using active frequency selective surface based on graphene. *EPJ Appl. Metamat.* **2021**, *8*, 1–7. [CrossRef]
20. Wu, Y.; Qu, M.; Jiao, L.; Liu, Y.; Ghassemlooy, Z. Graphene-based Yagi-Uda antenna with reconfigurable radiation patterns. *AIP Adv.* **2016**, *6*, 065308. [CrossRef]
21. Dash, S.; Psomas, C.; Patnaik, A.; Krikidis, I. An ultra-wideband orthogonal-beam directional graphene-based antenna for THz wireless systems. *Sci. Rep.* **2022**, *12*, 22145. [CrossRef]
22. Rodrigues, N.R.N.M.; de Oliveira, R.M.S.; Dmitriev, V. Smart Terahertz Graphene Antenna: Operation as an Omnidirectional Dipole and as a Reconfigurable Directive Antenna. *IEEE Antennas Propag. Mag.* **2018**, *60*, 26–40. [CrossRef]
23. Varshney, G. Reconfigurable graphene antenna for THz applications: A mode conversion approach. *Nanotechnology* **2020**, *31*, 135208. [CrossRef]
24. Al-Shalaby, N.A.; Elhenawy, A.S.; Zainud-Deen, S.H.; Malhat, H.A. Electronic Beam-Scanning Strip-Coded Graphene Leaky-Wave Antenna Using Single Structure. *Plasmonics* **2021**, *16*, 1427–1438.
25. Basiri, R.; Zareian-Jahromi, E.; Aghazade-Tehrani, M. A reconfigurable beam sweeping patch antenna utilizing parasitic graphene elements for terahertz applications. *Photonics Nanostruct.-Fundam. Appl.* **2022**, *51*, 101044 [CrossRef]
26. Shalini, M.; Madhan, M.G. Photoconductive bowtie dipole antenna incorporating photonic crystal substrate for Terahertz radiation. *Opt. Commun.* **2022**, *517*, 128327. [CrossRef]
27. Nissiyah, G.J.; Madhan, M.G. A narrow spectrum terahertz emitter based on graphene photoconductive antenna. *Plasmonics* **2019**, *14*, 2003–2011.
28. Khaleel, S.A.; Hamad, E.K.; Parchin, N.O.; Saleh, M.B. Programmable Beam-Steering Capabilities Based on Graphene Plasmonic THz MIMO Antenna via Reconfigurable Intelligent Surfaces (RIS) for IoT Applications. *Electronics* **2022**, *12*, 164.
29. Jiang, Z.; Wang, Y.; Chen, L.; Yu, Y.; Yuan, S.; Deng, W.; Wang, R.; Wang, Z.; Yan, Q.; Wu, X.; et al. Antenna-integrated silicon-plasmonic graphene sub-terahertz emitter. *APL Photonics* **2021**, *6*, 066102.
30. Chen, P.Y.; Alù, A. A terahertz photomixer based on plasmonic nanoantennas coupled to a graphene emitter. *Nanotechnology* **2013**, *24*, 455202. [CrossRef]
31. Casiraghi, C.; Hartschuh, A.; Lidorikis, E.; Qian, H.; Harutyunyan, H.; Gokus, T.; Novoselov, K.S.; Ferrari, A. Rayleigh imaging of graphene and graphene layers. *Nano Lett.* **2007**, *7*, 2711–2717. [CrossRef]
32. Hosseininejad, S.E.; Neshat, M.; Faraji-Dana, R.; Lemme, M.; Haring Bolivar, P.; Cabellos-Aparicio, A.; Alarcon, E.; Abadal, S. Reconfigurable THz Plasmonic Antenna Based on Few-Layer Graphene with High Radiation Efficiency. *Nanomaterials* **2018**, *8*, 577. [CrossRef]
33. Barybin, A.A.; Dmitriev, V.A. *Modern Electrodynamics and Coupled-Mode Theory: Application to Guided-Wave Optics*; Rinton: Princeton, NJ, USA, 2002.
34. Overvig, A.C.; Malek, S.C.; Carter, M.J.; Shrestha, S.; Yu, N. Selection rules for quasibound states in the continuum. *Phys. Rev. B* **2020**, *102*, 035434. [CrossRef]
35. Martí, I.L.; Kremers, C.; Cabellos-Aparicio, A.; Jornet, J.M.; Alarcón, E.; Chigrin, D.N. Scattering of terahertz radiation on a graphene-based nano-antenna. In Proceedings of the AIP Conference Proceedings. American Institute of Physics, Bad Honnef, Germany, 26–28 October 2011; Volume 1398, pp. 144–146.
36. Cao, Y.S.; Jiang, L.J.; Ruehli, A.E. An equivalent circuit model for graphene-based terahertz antenna using the PEEC method. *IEEE Trans. Antennas Propag.* **2016**, *64*, 1385–1393. [CrossRef]
37. Llatser, I.; Kremers, C.; Cabellos-Aparicio, A.; Jornet, J.M.; Alarcón, E.; Chigrin, D.N. Graphene-based nano-patch antenna for terahertz radiation. *Photonics Nanostruct.-Fundam. Appl.* **2012**, *10*, 353–358. [CrossRef]
38. Llatser, I.; Kremers, C.; Chigrin, D.N.; Jornet, J.M.; Lemme, M.C.; Cabellos-Aparicio, A.; Alarcon, E. Radiation characteristics of tunable graphennas in the terahertz band. *Radioengineering* **2012**, *21*, 946–953.
39. Zhang, B.; Zhang, J.; Liu, C.; Wu, Z.P.; He, D. Equivalent resonant circuit modeling of a graphene-based bowtie antenna. *Electronics* **2018**, *7*, 285. [CrossRef]
40. Rakheja, S.; Sengupta, P.; Shakiah, S.M. Design and Circuit Modeling of Graphene Plasmonic Nanoantennas. *IEEE Access* **2020**, *8*, 129562–129575. [CrossRef]

41. Garcia, M.E.C.; de Oliveira, R.M.S.; Rodrigues, N.R.N.M. Semi-analytical Equations for Designing Terahertz Graphene Dipole Antennas on Glass Substrate. *J. Microwaves, Optoelectron. Electromagn. Appl.s* **2022**, *21*, 11–34.
42. Christensen, J.; Manjavacas, A.; Thongrattanasiri, S.; Koppens, F.H.L.; de Abajo, F.J.G. Graphene Plasmon Waveguiding and Hybridization in Individual and Paired Nanoribbons. *ACS Nano* **2012**, *6*, 431–440.
43. Correas-Serrano, D.; Gomez-Diaz, J.S.; Perruisseau-Carrier, J.; Alvarez-Melcon, A. Graphene-based plasmonic tunable low-pass filters in the terahertz band. *IEEE Trans. Nanotechnol.* **2014**, *13*, 1145–1153. [CrossRef]
44. Powell, M.J.D. *Approximation Theory and Methods*; Cambridge University Press: Cambridge, UK, 1981.
45. de Oliveira, R.M.S.; Rodrigues, N.R.N.M.; Dmitriev, V. FDTD Formulation for Graphene Modeling Based on Piecewise Linear Recursive Convolution and Thin Material Sheets Techniques. *IEEE Antennas Wirel. Propag. Lett.* **2015**, *14*, 767–770. [CrossRef]
46. Tafove, A.; Hagness, S.C. *Computational Electrodynamics, The Finite-Difference Time-Domain Method*, 3rd ed.; Artech House: Norwood, MA, USA, 2005.
47. Gevorgian, S.; Berg, H. Line Capacitance and Impedance of Coplanar-Strip Waveguides on Substrates with Multiple Dielectric Layers. In Proceedings of the 2001 31st European Microwave Conference, London, UK, 24–26 September 2001; pp. 1–4.
48. Binns, K.J.; Lawrenson, P.J. *Analysis and Computation of Electric and Magnetic Field Problems*; Pergamon International Library of Science, Technology, Engineering and Social Studies: 2013. Available online: <https://www.sciencedirect.com/book/9780080166384/analysis-and-computation-of-electric-and-magnetic-field-problems> (accessed on 28 July 2023).
49. Gradshteyn, I.S.; Ryzhik, I.M. *Tables of Integrals, Series, and Products*, 6th ed.; Academic Press: Cambridge, MA, USA, 2000.
50. Whitaker, J.C., Ed. *The Electronics Handbook*, 2nd ed.; Electrical Engineering Handbook; CRC Press: Boca Raton, FL, USA, 2005.
51. Dmitriev, V.; Castro, W.; Melo, G.; Oliveira, C. Controllable graphene W-shaped three-port THz circulator. *Photonics Nanostruct.-Fundam. Appl.* **2020**, *40*, 100795.
52. Huang, J.; Song, Z. Terahertz graphene modulator based on hybrid plasmonic waveguide. *Phys. Scr.* **2021**, *96*, 125525.
53. Hou, H.; Teng, J.; Palacios, T.; Chua, S. Edge plasmons and cut-off behavior of graphene nano-ribbon waveguides. *Opt. Commun.* **2016**, *370*, 226–230. [CrossRef]
54. Hong, J.S.; Lancaster, M.J. *Microstrip Filters for RF/Microwave Applications*; Wiley Series in Microwave and Optical Engineering; John Wiley & Sons: Nashville, TN, USA, 2001.
55. Li, D.; Huang, Y.; Shen, Y.C.; Khiabani, N. Effects of substrate on the performance of photoconductive THz antennas. In Proceedings of the 2010 International Workshop on Antenna Technology, Lisbon, Portugal, 1–3 March 2010; pp. 1–4.
56. Adekoya, G.J.; Sadiku, R.E.; Ray, S.S. Nanocomposites of PEDOT:PSS with Graphene and its Derivatives for Flexible Electronic Applications: A Review. *Macromol. Mater. Eng.* **2021**, *306*, 1–21.
57. Gomez-Diaz, J.; Moldovan, C.; Capdevila, S.; Romeu, J.; Bernard, L.; Magrez, A.; Ionescu, A.; Perruisseau-Carrier, J. Self-biased reconfigurable graphene stacks for terahertz plasmonics. *Nat. Commun.* **2015**, *6*, 6334. [CrossRef] [PubMed]
58. Li, Y.; Yu, H.; Dai, T.; Jiang, J.; Wang, G.; Yang, L.; Wang, W.; Yang, J.; Jiang, X. Graphene-Based Floating-Gate Nonvolatile Optical Switch. *IEEE Photonics Technol. Lett.* **2016**, *28*, 284–287.
59. Fuscaldo, W.; Burghignoli, P.; Baccarelli, P.; Galli, A. Graphene Fabry-Perot Cavity Leaky-Wave Antennas: Plasmonic Versus Nonplasmonic Solutions. *IEEE Trans. Antennas Propag.* **2017**, *65*, 1651–1660.
60. McPherson, J.W.; Kim, J.; Shanware, A.; Mogul, H.; Rodriguez, J. Trends in the ultimate breakdown strength of high dielectric-constant materials. *IEEE Trans. Electron Devices* **2003**, *50*, 1771–1778. [CrossRef]
61. Kong, W.; Kum, H.; Bae, S.H.; Shim, J.; Kim, H.; Kong, L.; Meng, Y.; Wang, K.; Kim, C.; Kim, J. Path towards graphene commercialization from lab to market. *Nat. Nanotechnol.* **2019**, *14*, 927–938.
62. Meng, Y.; Feng, J.; Han, S.; Xu, Z.; Mao, W.; Zhang, T.; Kim, J.S.; Roh, I.; Zhao, Y.; Kim, D.H.; et al. Photonic van der Waals integration from 2D materials to 3D nanomembranes. *Nat. Rev. Mater.* **2023**, 1–20. [CrossRef]

Disclaimer/Publisher’s Note: The statements, opinions and data contained in all publications are solely those of the individual author(s) and contributor(s) and not of MDPI and/or the editor(s). MDPI and/or the editor(s) disclaim responsibility for any injury to people or property resulting from any ideas, methods, instructions or products referred to in the content.

Communication

Suppression of Common-Mode Resonance in Multiband Base Station Antennas

Madiha Farasat *, Dushmantha Thalakotuna, Yang Yang, Zhonghao Hu and Karu Esselle

School of Electrical and Data Engineering, University of Technology, Ultimo, Sydney 2007, Australia

* Correspondence: madiha.farasat@student.uts.edu.au

Abstract: 5G demands a significant increment in the number of connected devices. As a result, gNodeBs are constantly pushed to serve more spectrum and smaller sectors. These increased capacity demands are met by using multiband antennas in base stations. One of the key challenges with multiband antennas is the pattern distortions due to the presence of other surrounding antenna element structures. This work provides a novel approach to address the challenge of pattern distortion in the lower frequency band 690–960 MHz due to common-mode (CM) currents in the high-frequency-band antenna element operating in the 1810–2690 MHz band. A common-mode suppression circuit is integrated with the impedance matching network of the high-band antenna element to reduce these common-mode currents. The experimental results verified that the common-mode suppression circuit reduces the common-mode currents at low-band frequencies by moving the common-mode resonance frequency outside the low frequency band, resulting in cleaner low-band patterns meeting pattern specifications.

Keywords: base station antenna; common-mode resonance; common-mode suppression; radiation pattern distortion; wideband matching; 5G; 4G; gNB

1. Introduction

5G access network marks a significant milestone in the evolution of mobile communication. The 5G access network is designed to handle an increased traffic demand [1]. In mobile communication, antennas play a vital role translating the analog circuit signals to electromagnetic waves to propagate through air [2]. These antennas in the last access element, i.e., gNBs in 5G or NodeBs in 4G, are commonly referred to as base station antennas (BSA) [3]. BSAs have evolved from omni-directional single-band antennas from early generations to sectorized multiband multibeam antennas in 5G [4]. To meet the capacity demands for operators, the base station antenna needs to be multiband as this improves the resource utilization. On top, the size of a multiband antenna shall not vary a lot compared to a legacy single-band antenna. Thus, within the same size constraints, a 5G BSA should support multiple frequency bands such as 617 MHz–960 MHz (Low Band), 1695 MHz–2180 MHz (High Band 1), 2490 MHz–2690 MHz (High Band 2), and 3300 MHz–3800 MHz (High Band 3) [5].

Common practice is to have separate antenna arrays to cover each of these bands. In doing so, antenna arrays will be interspersed on the same ground plane. The challenges in such designs include pattern distortions [6] due to scattering from nearby elements. The pattern distortions can be of two types. First is the high-band (HB) pattern distortions due to nearby low-band (LB) antenna elements. The second is the LB pattern distortions due to the HB antenna element radiating in its common mode (CM). The first is overcome by introducing choking techniques [7], implementation of metal baffles [8,9] and frequency-selective surfaces [10,11]. However, the second challenge of HB common-mode radiation at LB [12] has not been investigated extensively.

The LB pattern distortions due to HB CM is observed through the impacts on 3dB beamwidth and cross-polarization levels. The 3dB beamwidth of LB patterns will exhibit a

Citation: Farasat, M.; Thalakotuna, D.; Yang, Y.; Hu, Z.; Esselle, K. Suppression of Common-Mode Resonance in Multiband Base Station Antennas. *Sensors* **2023**, *23*, 2905. <https://doi.org/10.3390/s23062905>

Academic Editor: Naser Ojaroudi Parchin

Received: 9 December 2022

Revised: 27 February 2023

Accepted: 2 March 2023

Published: 7 March 2023



Copyright: © 2023 by the authors. Licensee MDPI, Basel, Switzerland. This article is an open access article distributed under the terms and conditions of the Creative Commons Attribution (CC BY) license (<https://creativecommons.org/licenses/by/4.0/>).

significant widening, and cross-polarization levels can be high due to CM radiation. Often it is attempted to reduce the common-mode (CM) resonance by tuning the dimensions of the HB elements. The common approaches are to include capacitive element in the feed, thus moving the CM resonance to higher frequency or out of band [12]. This approach causes broadening of the azimuth beamwidth at lower frequency for commonly used LB radiators.

In this work, we propose a novel approach to reduce the CM resonance by adding a CM suppression circuit. We introduce a CM suppression circuit to the impedance matching network of the HB radiator to minimize the induced CM currents at LB frequencies. This CM suppression circuit is designed to present a high impedance to the HB matching circuit in order for it to appear as an open circuit.

2. The Effect of Common Mode on Low-Band Patterns

Typical interspersed HB and LB elements in a modern day multiband BSA are shown in Figure 1a. Due to the use of $\pm 45^\circ$ polarized elements, the dipoles are oriented in a slant configuration.

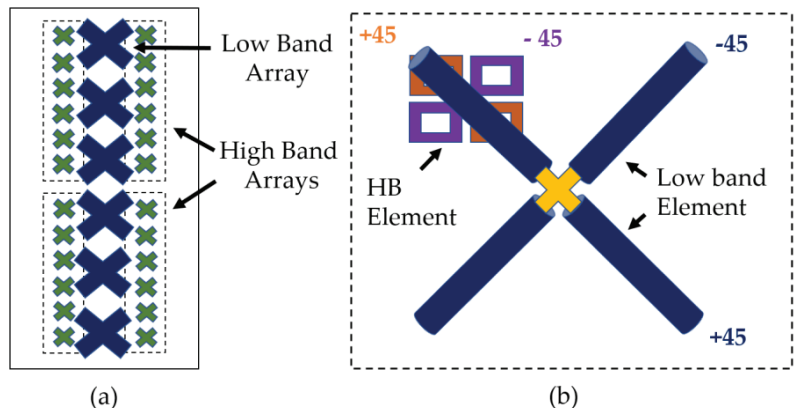


Figure 1. (a) Slant dipole configuration used in traditional interspersed scheme for dual-band dual-polarized BSA (b) Schematic of the experimental setup with one LB and one HB element.

In such an interspersed arrangement, there are two types of resonances that can cause pattern distortions, namely common-mode (CM) resonance and differential mode (DM) resonance. The presence of these resonances is not a problem as long as they occur outside the frequency bands of interest. However, since the total length of the HB feed circuit and the dipoles are approximately a quarter wavelength of LB, when LB radiates it can induce strong common-mode currents on HB elements as shown in Figure 2. Due to these high CM currents, the HB dipole operates as a quarter-wave monopole at LB frequencies. This monopole-like radiation pattern from HB elements at LB frequencies distorts the LB radiation patterns. Here, to clearly present the impact of HB element on performance of the LB element, a parametric study is performed whose results are listed in Table 1. The LB element patterns in the absence of HB element have a half-power beamwidth (HPBW) around $65 \pm 5^\circ$, as shown in Figure 3a. However, with the CM resonance caused by the HB element, the HPBW broadens to $75^\circ\text{--}85^\circ$, as indicated in Figure 3a,b.

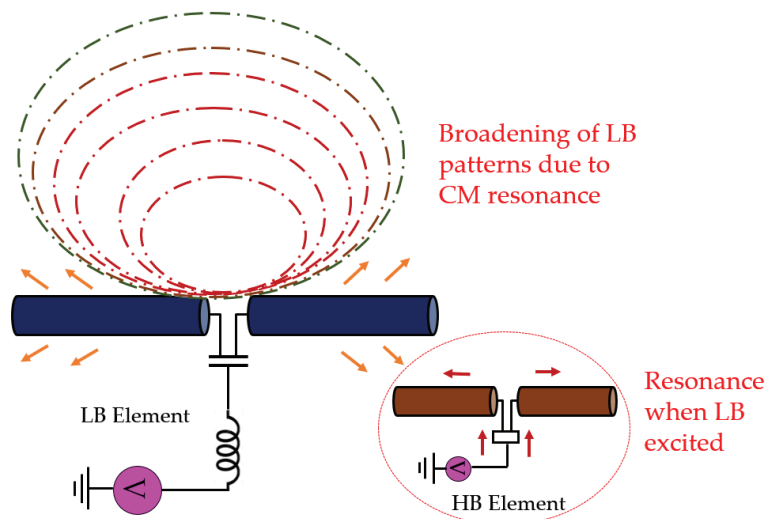


Figure 2. Artistic impression of the common-mode currents induced in nearby High-band (HB) elements impacting the patterns.

Table 1. LB key patterns performance parameters impacted due to HB element.

Frequency (GHz)	Beamwidth (Deg.)	Squint (Deg.)
0.66	82.5	-6
0.67	82.1	-5
0.72	86.4	10
0.75	77.7	16
0.77	75	14
0.85	68.8	5
0.90	66.1	2

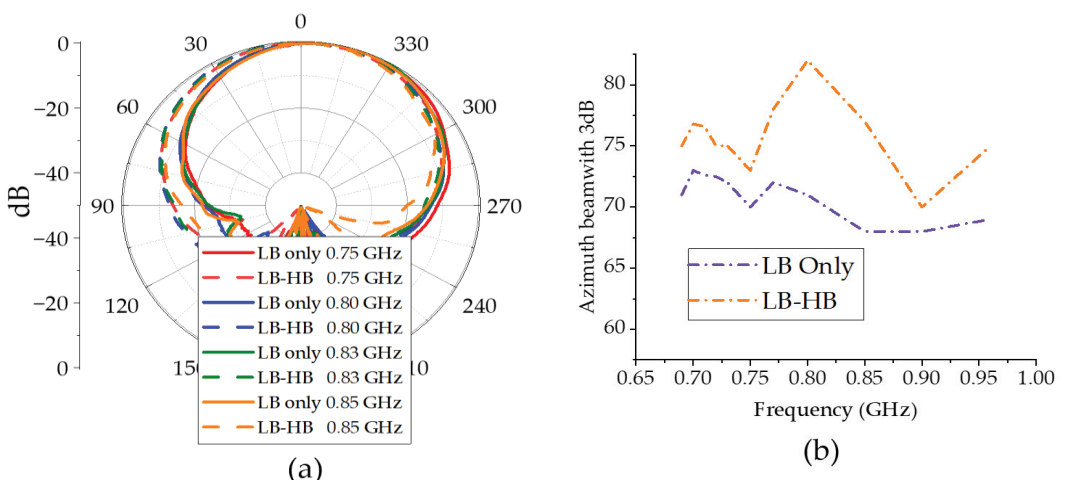


Figure 3. (a) Low-band-only (LB-only) and low-band with an HB antenna element (LB-HB) azimuth +45 co-pol patterns. (b) Measured 3dB azimuth beamwidth of LB element.

In order to demonstrate the effect of CM resonance, a simpler dual-band antenna setup is constructed. A schematic representation of this antenna setup is shown in Figure 1b. Only one LB element and one HB element are used from the interspersed array to keep the simulation setup simpler. As demonstrated later, the CM effects are observed even with only one HB element. The LB patterns were measured in the 690–960 MHz band, as it covers the typical BSA LB frequencies.

3. The Working Principle of CM Suppression Circuit

A careful observation of the current distribution on the HB dipole shows that the currents on the feed board (stalk) and dipoles travel in the same direction, mimicking the current distribution of a monopole, as shown in Figure 4a,b, when LB patterns are distorted. Only the current distribution at 0.69GHz on an HB antenna is shown in the Figure 4a,b. The currents on HB elements show similar behavior for other frequencies where LB patterns are distorted. An LB antenna element is located near the HB antenna element in this simulation setup and is differentially excited. In order to minimize this CM resonance, the effective resonance length of the HB antenna element at the LB frequencies needs to be altered. At the moment, the length of the HB dipole and the height of the stalk is 35mm, which is $\lambda_{\text{glb}}/4$ at LB frequencies, where $\lambda_{\text{glb}}/4$ is the guided wavelength at low-band mid frequency.

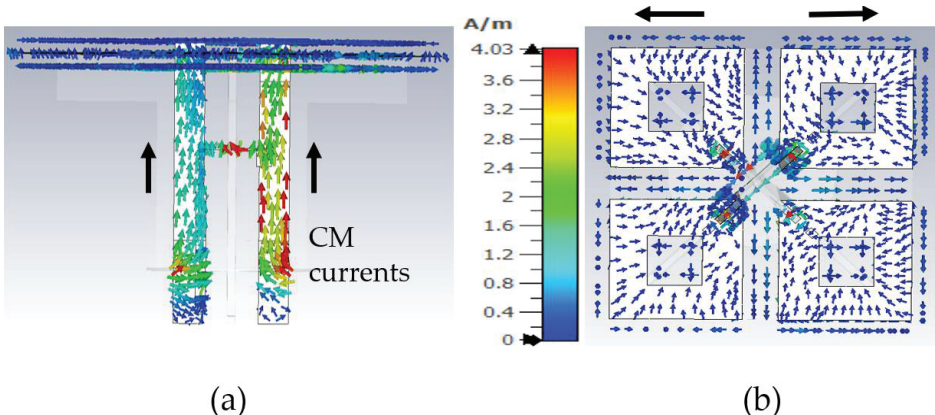


Figure 4. Currents on high-band antenna element at LB frequency 0.69GHz: (a) side view; (b) top view showing the HB dipole.

A typical HB antenna feed with the dipole is shown in Figure 5a. The feed point of the HB antenna is at the bottom of the TL (transmission line) below the ground plane. The TL and OL (open line) act as an impedance transformer from unbalanced to balanced feed; the balanced SL (short line) and TL1(transmission line 1) are printed at the back of the substrate. Further details on this Balun design can be found in [13].

In order to avoid LB currents in the HB stalk, we introduce a common-mode suppression circuit (CMSC) between the dipoles and the balanced feed as shown in Figure 5b. Effectively, the CM suppression circuit should allow all the HB currents to flow as usual while the LB currents are bypassed. The introduction of C1 in the CMSC provides a high series impedance to the LB currents and forces them to flow to ground via the series transmission line L2. Just having a C1 is not sufficient to avoid common-mode currents at LB for this dipole. Therefore, providing a shorting path for LB currents through L2 is necessary. The L2 length is selected such that it is approximately $\lambda_{\text{gHB}}/4$ at HB, where λ_{gHB} is the guided wavelength at HB. Since one end of this L2 is shorted to the ground, it presents an open circuit to HB currents, forcing them to go through C1. The value of the C1 is tuned in CST such that it provides low impedance at HB frequencies and high impedance at LB

frequencies. This will ensure that the HB feed circuit operates as a conventional HB feed without a CMSC.

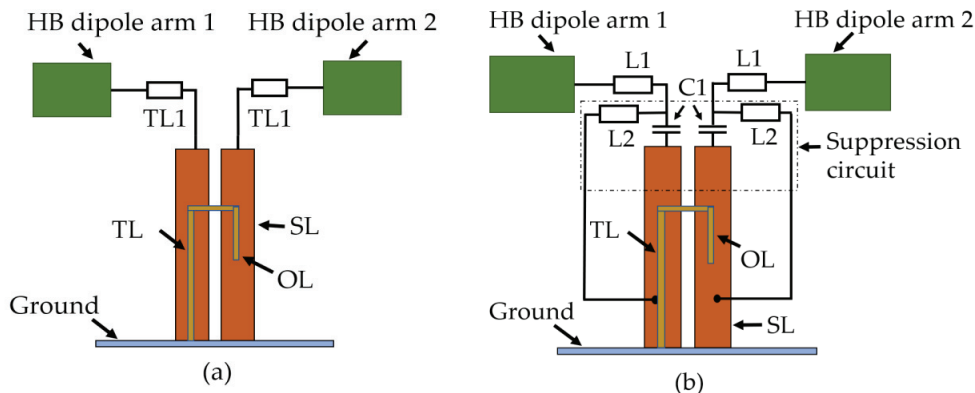


Figure 5. Schematic diagram of (a) typical HB antenna feed with the dipoles; (b) modified HB antenna feed with the CM suppression circuit. The TL refers to (transmission line); OL (open line); and SL (short line).

4. Implementation of CM Suppression Circuit on HB

A conventional HB antenna element feed without the CMSC is shown in Figure 6. Implementing C1 on the feed board can be done either as printed capacitor or an external lumped capacitor while the latter is undesirable due to cost and additional effort for assembly. Implementing the C1 as a parallel plate capacitor using PCB technology is in fact cost-effective and requires no additional effort during the assembly process. The C1 is therefore printed as a parallel plate capacitor as shown in Figure 7.

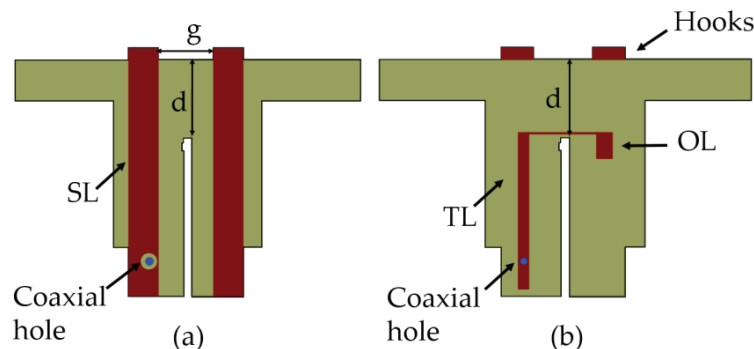


Figure 6. Schematic representation of a typical HB antenna element with impedance matching circuit (a) Back view, (b) Front view.

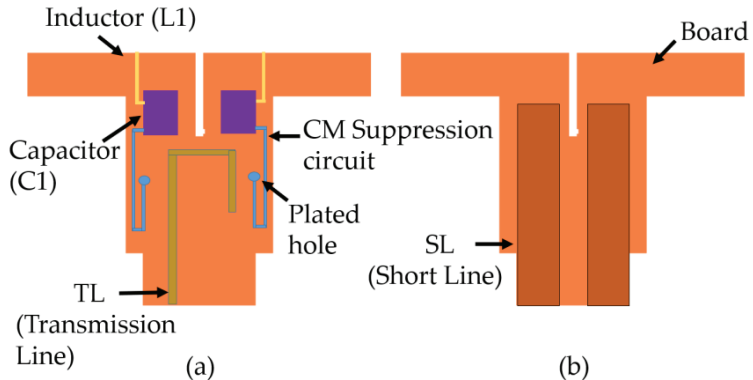


Figure 7. Schematic representation of HB antenna element stalk with CMSC **(a)** Front view, **(b)** Back view.

The realized capacitance of the C1 is 0.58pF . The capacitance C1 and length of the L2 transmission line were tuned during the simulation to minimize CM LB currents while observing pattern performance during parametric study. The LB CM currents on the HB antenna element are not visible anymore with the CMSC as shown in Figure 8; only differential currents are observed on the HB antenna element, which does not radiate effectively due to mismatch.

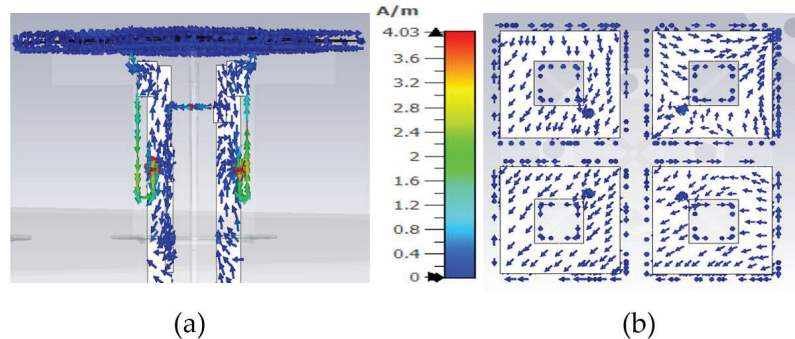


Figure 8. Currents on high-band antenna element with CMSC at LB frequency 0.69 GHz : **(a)** side view; **(b)** top view showing the HB dipole.

5. Experimental Results

The experimental setup consists of one LB element and one HB element as shown in Figure 9a. Based on simulations, it was found even one HB element near the LB element was sufficient to cause pattern distortions. A conventional slant LB dipole [14] was used as the LB element. The LB dipole impedance matching from $690\text{--}960\text{ MHz}$ is based on a feed network design that includes series, shunt resonators, and a quasi-quarter-wavelength transmission line (TL2). A circuit theory model of matching circuit and implementation is proposed in [15]. Both the HB and LB antenna elements achieved $S_{11} < -10\text{ dB}$ across the frequency band of interest as shown in Figure 10. The optimized dimensions of the structure are provided in Table 2.

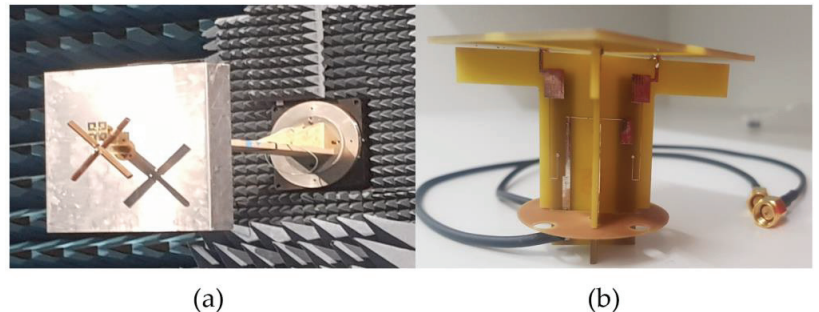


Figure 9. (a) The experimental setup consisting of one LB element and one HB element; (b) fabricated HB antenna element containing CMSC.

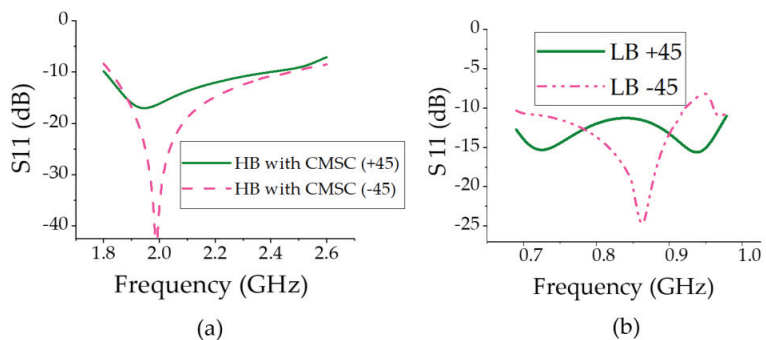


Figure 10. The measured return loss of the (a) HB element and (b) LB element.

Table 2. Optimized parameters of the proposed antenna.

Parameters	Values HB (mm)	Description
W-SL	6	Width of SL
L-SL	43	Length of SL
W-TL	1.3	Width of TL
L-TL	15	Length of TL
W-TL1	1	Width of TL1
L-TL1	5.5	Length of TL1
W-TL2	0.2	Width of TL2
L-TL2	20	Length of TL2
W-OL	2.8	Width of OL
L-OL	6	Length of OL
g	11	Gap between SL

Figure 11a shows the measured far field patterns at LB. With the inclusion of CMSC in HB elements, the LB radiation patterns in Figure 11a show a significant improvement compared to patterns in Figure 3a. As indicated in Figure 11b, the 3dB beamwidth is very close to the 3dB beamwidth of the LB element alone, completely removing the broadening effect due to common-mode currents. The HB patterns with and without the CMSC are shown in Figure 12. It is shown that the HB patterns are almost identical and show no impact due to the CMSC. The interband isolation between the LB and HB elements is

measured as shown in Figure 13. For clarity, the isolation between HB +45 polarization from the LB polarizations is shown. Without the CMSC, both LB +45 and −45 slant polarizations have high coupling at the bottom of the low-band frequencies. With the CMSC, the coupling is reduced by over 10dB for the same polarization, while it is more than 20dB for opposite polarizations. This significant decoupling also provides an indication of transparency of the HB antenna element to LB frequencies. The simulated values also agree very closely with the measurements from the experimental setup. To address the advantages of the proposed design, a comparison of results with the previous work on mutual coupling suppression techniques is tabulated in Table 3.

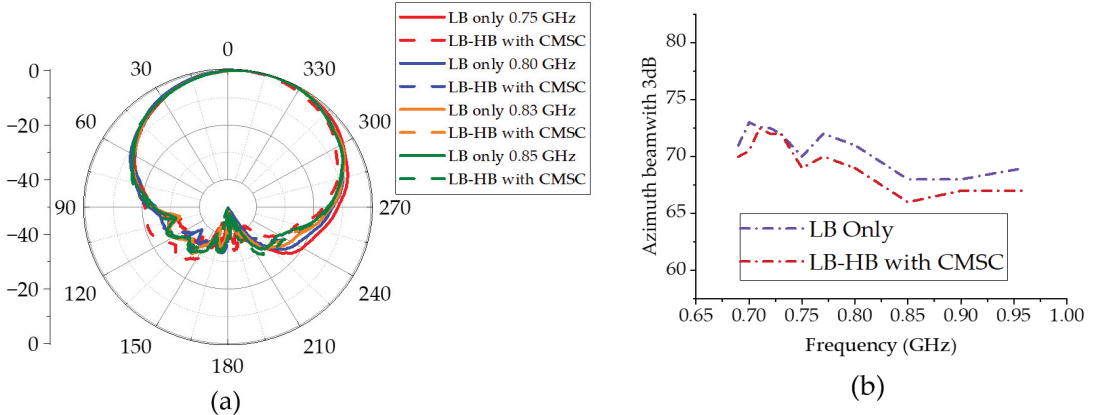


Figure 11. (a) Low-band-only (LB only) and low-band with HB antenna element containing CMSC (LB-HB with CMSC) azimuth +45 co-pol patterns. (b) Measured 3dB azimuth beamwidth of LB patterns.

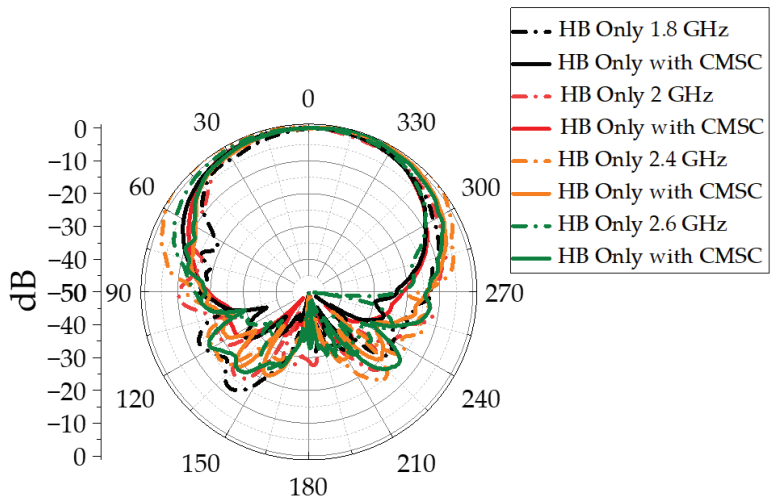


Figure 12. High-band-only antenna element azimuth co-pol patterns.

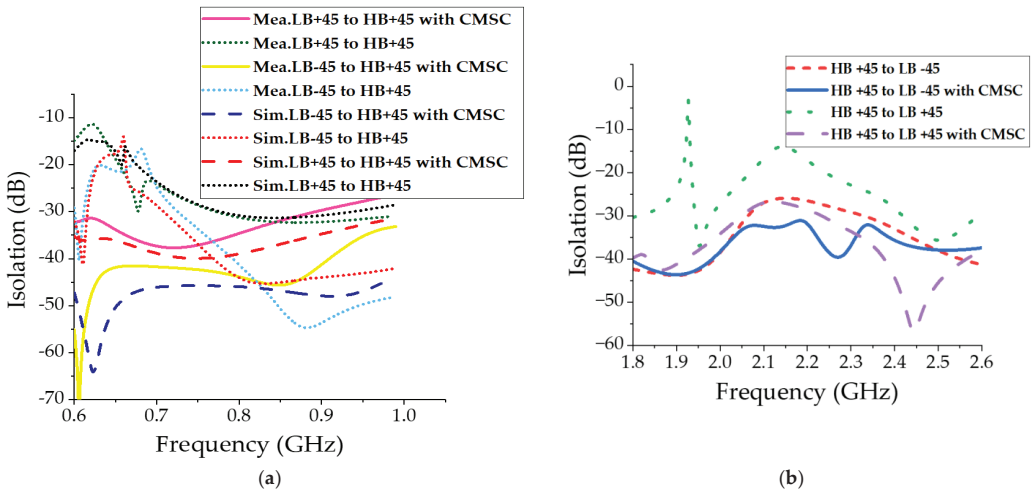


Figure 13. Interband isolation between LB and HB at (a) LB frequencies and (b) HB frequencies.

Table 3. Comparison of recent state-of-the-art works with proposed work.

References	Mutual Coupling Suppression Techniques	Frequency Band (GHz)	Isolation (dB)	HPBW (Measured)
[2]	Passive dipoles + baffles	0.69–0.96 1.7–2.7	>27 >22	$72^\circ \pm 2^\circ$ $65^\circ \pm 5^\circ$
[10]	Frequency-selective surface	0.69–0.96 3.5–4.9	>28 >25	60° 75°
[11]	Frequency-selective surface	2.3–2.7 3.3–3.8	>25 23.5	44° – 48° 66° – 69°
[12]	Capacitance-loading technique/chokes	0.70–0.96 1.7–2.2	>20	75° + 5° 64° + 5°
[16]	Filtering antenna elements	1.71–1.88 1.9–2.17	>30	$65^\circ \pm 5^\circ$
[17]	Decoupling network	2.3–2.4 2.4–2.483	>25	$60^\circ \pm 5^\circ$ $65^\circ \pm 5^\circ$
[18]	Metal baffles	0.77–0.98 1.65–2.9	<23 17.5	64.5° – 57.1° 84.4° – 74.1°
[19]	Capacitance-loaded HB element	0.69–0.96 1.7–2.2	>20	75° + 5° 64° + 5°
Proposed Work	Common mode suppression circuit	0.69–0.96 1.8–2.6	>30 >25	65° + 5° $65^\circ \pm 5^\circ$

6. Conclusions

The LB pattern distortions in multiband antennas occur due to common-mode resonance currents induced in HB antenna elements. This causes significant distortions in LB radiation patterns. This is very undesirable for the network performance as it leads to inter-cell interference in adjacent sectors due to coverage overlaps, resulting in degradation of network quality. The common mode is suppressed by introducing a capacitor with a quarter-wavelength short line at LB frequencies to the HB feed network. This suppresses the LB currents at resonance frequencies without significantly changing the HB current distribution at HB frequencies. As a result, CM resonance behavior of the HB dipole is no longer visible, resulting in cleaner patterns at low-band frequencies. The 3 dB beamwidth variation is 65° + 5° . The HB patterns are not affected and the HB element impedance matching below 10 dB can be obtained.

Author Contributions: Investigation, M.F.; Supervision, D.T., Y.Y., Z.H. and K.E. All authors conceived and proposed the idea. All authors have read and agreed to the published version of the manuscript.

Funding: This research received no external funding.

Institutional Review Board Statement: Not applicable.

Informed Consent Statement: Not applicable.

Data Availability Statement: Not applicable.

Conflicts of Interest: The authors declare no conflict of interest.

References

- Osseiran, A.; Parkvall, S.; Persson, P.; Zaidi, A.; Magnusson, S.; Balachandran, K. *5G Wireless Access: An Overview*; 1/28423-FGB1010937; Ericsson: Stockholm, Sweden, 2020.
- Huang, H.; Li, X.; Liu, Y. A dual-broadband base station antenna with ikebana-like arrangement scheme. *Microw. Opt. Technol. Lett.* **2020**, *62*, 708–713. [CrossRef]
- Farasat, M.; Thalakotuna, D.N.; Hu, Z.; Yang, Y. A review on 5G sub-6 GHz base station antenna design challenges. *Electronics* **2021**, *10*, 2000. [CrossRef]
- Beckman, C.; Lindmark, B. The evolution of base station antennas for mobile communications. In Proceedings of the 2007 International Conference on Electromagnetics in Advanced Applications, Turin, Italy, 17–21 September 2007; pp. 85–92.
- Thalakotuna, D.N.; Karmokar, D.K.; Hu, Z.; Esselle, K.P.; Matekovits, L. Improving Cross-Band Isolation in MultiBand Antennas. In Proceedings of the 2021 International Conference on Electromagnetics in Advanced Applications (ICEAA), Honolulu, HI, USA, 9–13 August 2021; p. 68.
- Sun, H.-H.; Ding, C.; Zhu, H.; Jones, B.; Guo, Y.J. Suppression of Cross-Band Scattering in Multiband Antenna Arrays. *IEEE Trans. Antennas Propag.* **2019**, *67*, 2379–2389. [CrossRef]
- Sun, H.-H.; Zhu, H.; Ding, C.; Jones, B.; Guo, Y.J. Scattering suppression in a 4G and 5G base station antenna array using spiral chokes. *IEEE Antennas Wirel. Propag. Lett.* **2020**, *19*, 1818–1822. [CrossRef]
- Huang, H.; Liu, Y.; Gong, S. A Dual-Broadband, Dual-Polarized Base Station Antenna for 2G/3G/4G Applications. *IEEE Antennas Wirel. Propag. Lett.* **2017**, *16*, 1111–1114. [CrossRef]
- He, Y.; Pan, Z.; Cheng, X.; He, Y.; Qiao, J.; Tentzeris, M.M. A Novel Dual-Band, Dual-Polarized, Miniaturized and Low-Profile Base Station Antenna. *IEEE Trans. Antennas Propag.* **2015**, *63*, 5399–5408. [CrossRef]
- Zhu, Y.; Chen, Y.; Yang, S. Decoupling and Low-Profile Design of Dual-Band Dual-Polarized Base Station Antennas Using Frequency-Selective Surface. *IEEE Trans. Antennas Propag.* **2019**, *67*, 5272–5281. [CrossRef]
- Yang, S.J.; Zhang, X.Y. Frequency Selective Surface-Based Dual-Band Dual-Polarized High-Gain Antenna. *IEEE Trans. Antennas Propag.* **2021**, *70*, 1663–1671. [CrossRef]
- Sun, H.-H.; Jones, B.; Guo, Y.J.; Lee, Y.H. Dual-Band Base Station Antenna Array with Suppressed Cross-Band Mutual Scattering. In Proceedings of the 2021 IEEE International Symposium on Antennas and Propagation and USNC-URSI Radio Science Meeting (APS/URSI), Singapore, 4–10 December 2021; pp. 1–2.
- Ding, C.; Sun, H.; Ziolkowski, R.W.; Guo, Y.J. Simplified Tightly-Coupled Cross-Dipole Arrangement for Base Station Applications. *IEEE Access* **2017**, *5*, 27491–27503. [CrossRef]
- Ding, C.; Jones, B.; Guo, Y.J.; Qin, P.Y. Wideband Matching of Full-Wavelength Dipole with Reflector for Base Station. *IEEE Trans. Antennas Propag.* **2017**, *65*, 5571–5576. [CrossRef]
- Farasat, M.; Thalakotuna, D.; Hu, Z.; Yang, Y. A Simple and Effective Approach for Scattering Suppression in Multiband Base Station Antennas. *Electronics* **2022**, *11*, 3423. [CrossRef]
- Zhang, Y.; Zhang, X.Y.; Ye, L.; Pan, Y. Dual-Band Base Station Array Using Filtering Antenna Elements for Mutual Coupling Suppression. *IEEE Trans. Antennas Propag.* **2016**, *64*, 3423–3430. [CrossRef]
- Zhao, L.; Qian, K.W.; Wu, K.L. A Cascaded Coupled Resonator Decoupling Network for Mitigating Interference Between Two Radios in Adjacent Frequency Bands. *IEEE Trans. Microw. Theory Tech.* **2014**, *62*, 2680–2688. [CrossRef]
- Huang, H.; Liu, Y.; Gong, S. A Novel Dual-Broadband and Dual-Polarized Antenna for 2G/3G/LTE Base Stations. *IEEE Trans. Antennas Propag.* **2016**, *64*, 4113–4118. [CrossRef]
- Sun, H.-H.; Jones, B.; Guo, Y.J.; Lee, Y.H. Suppression of cross-band scattering in interleaved dual-band cellular base-station antenna arrays. *IEEE Access* **2020**, *8*, 222486–222495. [CrossRef]

Disclaimer/Publisher’s Note: The statements, opinions and data contained in all publications are solely those of the individual author(s) and contributor(s) and not of MDPI and/or the editor(s). MDPI and/or the editor(s) disclaim responsibility for any injury to people or property resulting from any ideas, methods, instructions or products referred to in the content.



Article

A Shorted Stub Loaded UWB Flexible Antenna for Small IoT Devices

Esraa Mousa Ali ^{1,†}, Wahaj Abbas Awan ^{2,*†}, Mohammed S. Alzaidi ³, Abdullah Alzahrani ³, Dalia H. Elkamchouchi ⁴, Francisco Falcone ^{5,6,7} and Sherif S. M. Ghoneim ³

- ¹ Faculty of Aviation Sciences, Amman Arab University, Amman 11953, Jordan
² Department of Information and Communication Engineering, Chungbuk National University, Cheongju 28644, Republic of Korea
³ Department of Electrical Engineering, College of Engineering Taif University, P.O. Box 11099, Taif 21944, Saudi Arabia
⁴ Department of Information Technology, College of Computer and Information Sciences, Princess Nourah bint Abdulrahman University, P.O. Box 84428, Riyadh 11671, Saudi Arabia
⁵ Electrical Engineering and Communications Department, Universidad Pública de Navarra, Campus Arrosadia, E-31006 Pamplona, Spain
⁶ Institute of Smart Cities, Universidad Pública de Navarra, Campus Arrosadia, E-31006 Pamplona, Spain
⁷ Tecnológico de Monterrey, School of Engineering and Sciences, Monterrey 64849, Mexico
* Correspondence: wahajabbasawan@chungbuk.ac.kr
† These authors contributed equally to this work.

Abstract: In this manuscript, a compact in size yet geometrically simple Ultra-Wideband (UWB) antenna is demonstrated. The flexible-by-nature substrate ROGERS 5880, having a thickness of 0.254 mm, is utilized to design the proposed work. The antenna configuration is an excerpt of a traditional rectangular monopole antenna resonating at 5 GHz. Initially, a pair of triangular slots are employed to extend the impedance bandwidth of the antenna. In addition, a semi-circular-shaped, short-ended stub is connected at the upper edges of the patch to further increase the operational bandwidth. After optimization, the proposed antenna offers UWB ranging from 2.73–9.68 GHz, covering almost the entire spectrum allocated globally for UWB applications. Further, the antenna offers a compact size of $15 \times 20 \text{ mm}^2$ that can easily be integrated into small, flexible electronics. The flexibility analysis is done by bending the antenna on both the x and y axes. The antenna offers performance stability in terms of return loss, radiation pattern, and gain for both conformal and non-conformal conditions. Furthermore, the strong comparison between simulated and measured results for both rigid and bent cases of the antenna, along with the performance comparison with the state-of-the-art, makes it a potential candidate for present and future compact-sized flexible devices.

Citation: Ali, E.M.; Awan, W.A.; Alzaidi, M.S.; Alzahrani, A.; Elkamchouchi, D.H.; Falcone, F.; Ghoneim, S.S.M. A Shorted Stub Loaded UWB Flexible Antenna for Small IoT Devices. *Sensors* **2023**, *23*, 748. <https://doi.org/10.3390/s23020748>

Academic Editor: Andrea Randazzo

Received: 15 October 2022

Revised: 30 December 2022

Accepted: 4 January 2023

Published: 9 January 2023



Copyright: © 2023 by the authors. Licensee MDPI, Basel, Switzerland. This article is an open access article distributed under the terms and conditions of the Creative Commons Attribution (CC BY) license (<https://creativecommons.org/licenses/by/4.0/>).

1. Introduction

The UWB (ultra-wideband) radio demonstrates features such as broad bandwidth, low power spectrum levels, high data-rate transmission, good phase linearity, and auspicious radiation performance [1]. As a result, the UWB technology has promising prospects in diverse applications, such as the Internet of Things (IoT), surveillance systems, wireless sensor networks, and medical applications [2,3]. Since the year 2002, researchers have intensified their efforts in this area after the allocation of the frequency range 3.1–10.6 GHz for unlicensed UWB indoor wireless communication by the United States Federal Communication Commission (FCC) [4]. Whereas, the Electronic Communication Committee (ECC) has designated the 6–8.5 GHz band spectrum for UWB applications [5].

In addition, with the progression of wireless communication standards, an enormous number of devices and gadgets are required to be connected to the internet. The assortment of interconnected devices accelerated the idea of designing flexible and robust antennas

capable of being mounted on curved or wearable devices [6–8]. Moreover, various conductive and substrate materials have been investigated to be employed as flexible substrates, such as Kapton, paper, polyethylene terephthalate (PET), polydimethylsiloxane (PDMS), polyamide, and textile fabric [9–13]. Flexible antennas are desired to have acceptable radiation characteristics in conformal and rigid configurations.

Recently, numerous approaches have been reported in the literature for attaining the UWB characteristics [5–7] and [14–16]. However, very few UWB antennas have been presented with flexible substrates [17–22]. For instance, the reported work in [17] is made up of a co-planar waveguide (CPW)-fed circular monopole antenna designed using a liquid crystalline polymer (LCP)-based substrate. The antenna offers a wideband of 2.5–11 GHz along with an average gain of 2 dB and an overall size of $40 \times 22 \times 0.1$ mm³. On the other hand, an inkjet-printed flexible Multiple-Input, Multiple-Output (MIMO) antenna is presented in [18]. It has a relatively compact size of $22 \times 31 \times 0.125$ mm³ and offers a wide bandwidth ranging from 3.43–10.1 GHz, accompanied by an average gain of 1.7 dBi. Similarly, in [19], a flexible antenna having physical dimensions of $38 \times 22 \times 0.1$ mm³ is proposed for wearable applications. Although the antenna offers a wideband of 2.8 GHz (5.8–8.6 GHz), this work cannot be used for UWB applications requiring bandwidth ranging from 3.1 to 10 GHz. Another intriguing report conducted in [20] describes a photo paper-based inkjet-printed antenna for IoT applications. The antennas offer a wideband over 3.2–15 GHz, having an average gain of 4.87 dB along with an overall dimension of $33.1 \times 32.7 \times 0.254$ mm³.

Further, in [21], a flexible antenna is designed on a polyimide substrate for UWB applications. The polyimide substrate-based antenna is designed after the surface modification by utilizing an *in situ* self-metallization technique. The antenna offers an ultra-wide bandwidth of 1.35–16.4 GHz as well as a high realized gain of >2.8 dB in the operational region. Lastly, a nanocomposite material-based organic antenna is presented for UWB and flexible applications [22]. The antenna comprises $48 \times 34.9 \times 0.13$ mm³ and has an operational impedance bandwidth of 2–7 GHz, along with mismatched performance for unbent and bent conditions. Thus, it can be concluded from the aforementioned decision that the UWB antennas proposed in [17–22] exhibit larger dimensions. Furthermore, the reported work in [21,22] involves costly substrates and complex fabrication methodologies. As the state-of-the-art systems require compact antennas, it would therefore be advantageous to employ a more compact UWB antenna with conformal capabilities for diverse services to comply with the commercial and functional requirements.

Therefore, this work offers the design of a miniaturized UWB antenna realized on a flexible substrate. The overall substrate dimensions of the proposed design are $20 \times 15 \times 0.254$ mm³, which is relatively compact compared to the state-of-the-art. The proposed structure exhibits adequate radiation characteristics for both rigid and conformal arrangements. Therefore, the suitability of the proposed antenna is ascertained for both rigid and conformal electronic devices. The forthcoming parts of the paper are split as follows: Section 2 describes the methodology used to design the proposed antenna, while Section 3 discusses the performance parameters of the proposed antenna. Finally, Section 4 concludes the manuscript, which is accompanied by references.

2. Methodology of the Proposed Antenna and Methodology

2.1. UWB Antenna

Figure 1 depicts the layout of the proposed antenna. The radiating structure is placed at the top of the flexible material ROGERS 5880, which has an electric permittivity of 2.2 along with a loss tangent of 0.0009. The radiator is fed using the CPW feeding technique, owing to the advantage of its uniplanar structure, which increases its potential for use with electronic circuits [23]. Furthermore, because of the similar structure, CPW feed aids in achieving a compact antenna size as well as ease of fabrication [24]. The antenna radiator consists of a rectangular-shaped quarter-wave monopole whose both sides are truncated using triangular-shaped slots. Afterwards, a semi-circular-shaped short stub is inserted at the top

of the radiator, which helps in achieving an ultra-wideband. The working principle of the antenna is explained in the forthcoming section, along with the results of various design techniques utilized to achieve the proposed UWB antenna.

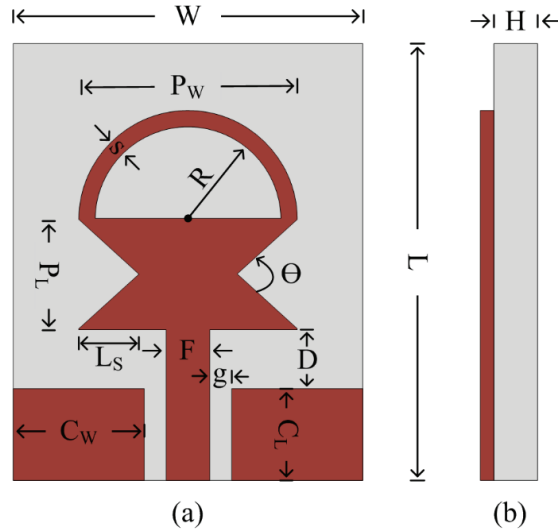


Figure 1. Geometry of the proposed antenna: (a) front view; (b) side view $L = 20$ mm; $W = 15$ mm; $C_L = 5.5$ mm; $C_W = 6$ mm; $g = 0.5$ mm; $F = 2$ mm; $D = 2$ mm; $H = 0.254$ mm; $P_L = 5$ mm; $P_w = 13$ mm; $L_s = 2.5$ mm; $R = 4.5$ mm; $s = 1.5$ mm; $\theta = 90^\circ$.

2.2. Antenna Design Methodology

Figure 2 portrays the geometrical structure of various antennas utilized to design the proposed work. The design methodology consists of three major steps.

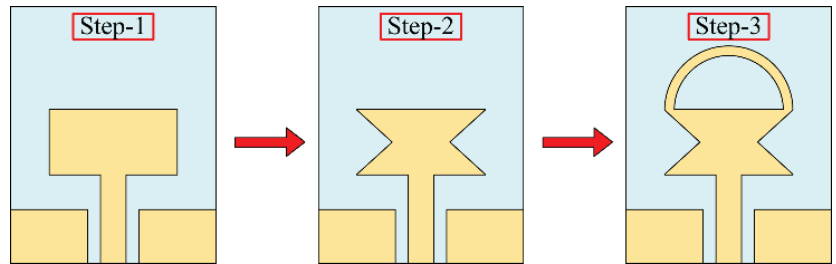


Figure 2. Different antennas are utilized to achieve the proposed UWB antenna design.

Step-1: The design of a compact size conventional quarter-wave monopole antenna.

Step-2: Band enhancement of the quarter-wave monopole antenna by truncating the sides of the radiator.

Step-3: Further operational band enhancement of the truncated monopole antenna by loading the short-ended stub. Initially, a CPW-fed, rectangular-haped quarter-wave monopole antenna is designed. The length (P_L) of the radiator for any desired resonance (f_0) can be estimated by utilizing Equations (1) and (2), as proven in [25]:

$$P_L = \frac{c}{4f_0\sqrt{\epsilon_{eff}}} \quad (1)$$

Here ϵ_{eff} is the effective permittivity of the substrate, which is given as:

$$\epsilon_{eff} \approx \frac{\epsilon_r + 1}{2} + \frac{\epsilon_r + 1}{2}(1 + 12(\frac{P_w}{H}))^{-0.5} \quad (2)$$

Here, ϵ_r is the permittivity of the substrate, P_w is the width of the radiator, and H is the thickness of the substrate.

Besides, for broadband antenna, the lower cut-off frequency (F_L) of the monopole antenna can be estimated by the following expression provided in [26]:

$$F_L = \frac{7.2}{(l + r + p) \times k} \quad (3)$$

for proposed antenna, the parameters in the above equations are:

$$l = \frac{P_w}{2} r = \frac{P_L}{4\pi} p = Dk = \sqrt{\epsilon_{eff}}$$

After putting the parameters into Equation (3), the equations become:

$$F_L = \frac{7.2}{(\frac{P_w}{2} + \frac{P_L}{4\pi} + D) \times \sqrt{\epsilon_{eff}}} \quad (4)$$

Equation (4) gives the lower cut-off frequency of 4.19 GHz, which is remarkably close to the simulated results having a lower cut-off frequency of 4.23 GHz, as depicted in Figure 3. Furthermore, Equation (4) also shows that the lower cut-off frequency of a monopole antenna can be adjusted by varying the length and width of the patch along with the space between the radiator and CPW ground, denoted by D.

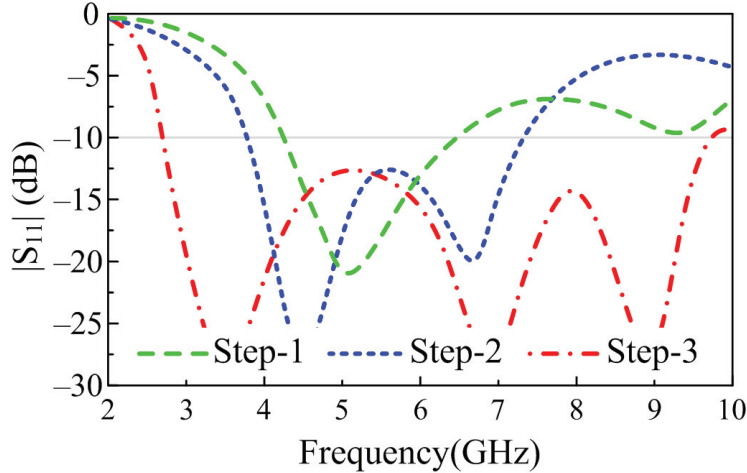


Figure 3. $|S_{11}|$ of the various antenna involve in designing of proposed work.

However, due to the size limitation of the antenna, further variation was not possible, and the optimized antenna offers a broadband of 4.23–6.64 GHz, as illustrated in Figure 3. In order to broaden the bandwidth of the radiator even further, truncating the corners of the radiator is utilized. Various techniques, including etching slots [27], inserting vias [28], and loading open-ended stubs [29], are widely studied to achieve wide bandwidth. However,

etching slots requires a bigger radiator, inserting vias requires a ground plane at the back of the radiator, and open-ended stubs require more space. Therefore, instead of utilizing conventional techniques, the truncated corner technique is exploited. Furthermore, rather than truncating the corners of the radiator as utilized in [8,10,28], the sides of the radiator are truncated by using a triangular-shaped structure, as depicted in Figure 2. The variation in the shape of the radiator due to the etched slot causes the flow of current to redistribute itself across the surface of the radiator, and with optimization, it results in the generation of a wide band ranging from 3.8–7.35 GHz, as depicted in Figure 3.

In a decisive step, a semi-circular-shaped stub was added at the top-corner of the radiator. The loading of the stub introduces additional impedance that can be approximated by the following relationship [30]:

$$Z_{SC} = j Z_O \tan(\beta l) \quad (5)$$

Here, Z_O is the input impedance of 50Ω , β is the per-unit change in length and can be computed as $\beta = 2\pi/\lambda$, l is the physical length of the stub and can be computed by using the arc length (L_A) formula of $L_A = \pi/180 \times \theta \times R$, and j is the unit imaginary number.

The addition of extra impedance due to the insertion of the stub provides a good match with the transmission line and results in more current flow through the surface of the antenna, which consequently increases the impedance bandwidth of the antenna, as depicted in Figure 3. From Figure 4, it can be seen that with each modification, the more current induced in the radiator causes the resonance at the selected frequency, thereby eventually increasing the bandwidth of the proposed antenna. The final antenna after optimization has a wide $|S_{11}| > -10$ dB impedance bandwidth at 6.95 GHz ranging from 2.73–9.68 GHz, as illustrated in Figure 3.

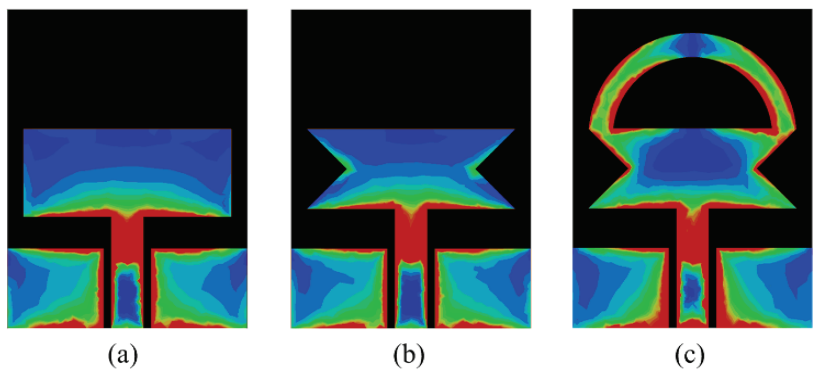


Figure 4. Surface current distribution at 3.5 GHz (a) step-1 (b) step-2 (c) step-3.

2.3. Optimization and Design Procedure

The generic value of various parameters, including the length and width of the monopole antenna, along with CPW-feeding parameters as well as the impedance of the stub, can be estimated by various equations. However, due to the presence of various materials and connector losses, these values must be optimized to achieve the desired results. In the literature, various optimization techniques were used. However, due to its ease of use and lustiness, the CST Genetic Algorithm (GA) is utilized. Figure 5 depicts the working flow chart of the GA. The detailed description and working methodology of the GA are fully explained in [31].

The design methodology of the proposed flexible UWB antenna is shown in Figure 6. The antenna can be summarized as the following three steps:

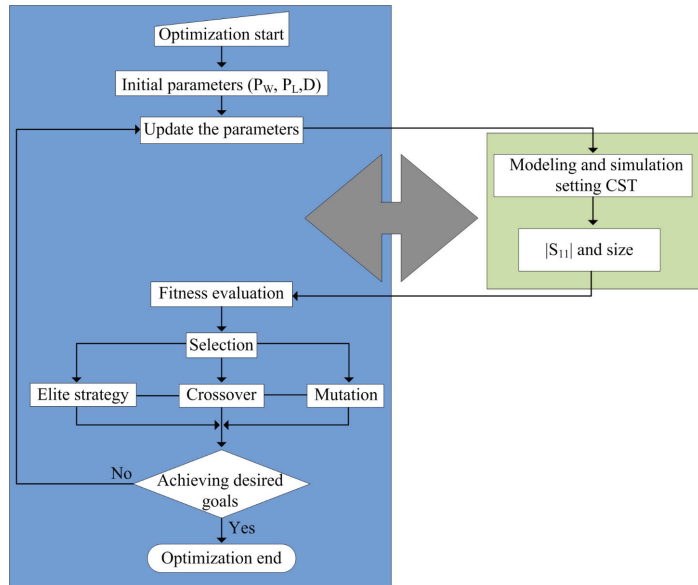


Figure 5. Flow chart explaining the optimization algorithm utilized for the proposed antenna.

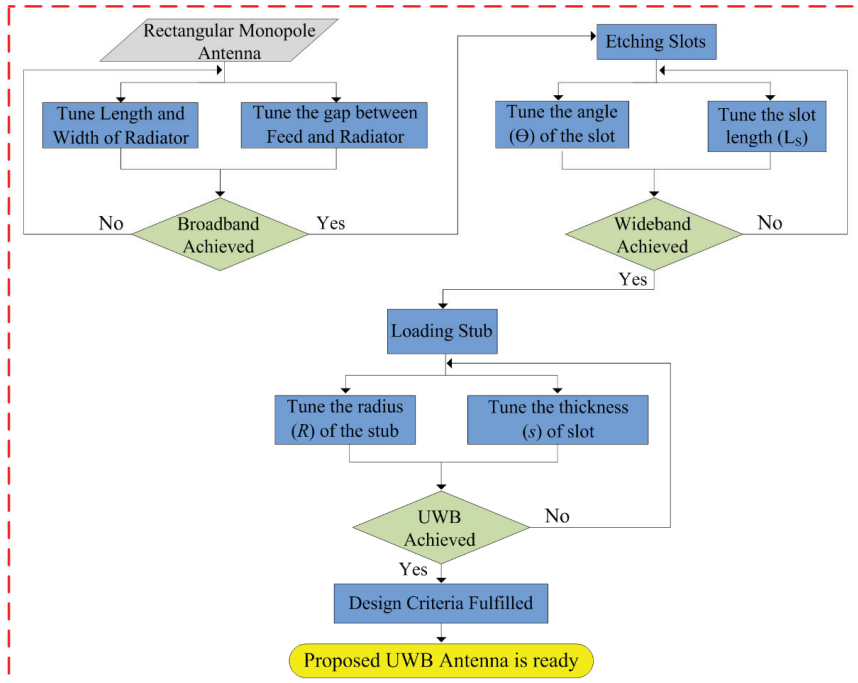


Figure 6. Flow chart explaining the optimization algorithm utilized for the proposed antenna.

Step-1: Initially, a quarter-wave monopole antenna is designed using the equations provided in the literature. Afterwards, the length, width, and gap between CPW ground and the radiator are optimized using GA to achieve the maximum possible bandwidth without affecting the overall size of the antenna.

Step-2: Later, the etching slot technique is utilized to achieve wideband behavior, where a simple structure is employed to avoid any structural complexity. Then, the length and angle of the slot are optimized to achieve wideband behavior. It is important to note that the length and width of the radiator, as well as the gap between the radiator and CPW ground, remain constant as of step 1.

Step-3: Finally, a shorted stub is loaded at the top edges of the antenna to improve the impedance matching of the antenna. The resultant antenna offers UWB behavior while covering almost 95% of the band spectrum allocated globally for UWB applications. In this step, the thickness and internal radius of the stub are optimized initially, along with a slight optimization of the angle and length of the slot.

By following the aforementioned steps 1, 2, and 3, a compact-sized antenna with incredibly low structural complexity as well as UWB bandwidth can be designed. A detailed theoretical analysis and mathematical equation validate the proposed work's scientific contribution.

3. Performance Parameters of the Antenna

3.1. Reflection Coefficient

In order to substantiate the theoretically proven results, a prototype of the antenna was fabricated using a standard chemical etching process. A gold-plated SMA connector having an impedance of $50\ \Omega$ is utilized for excitation of the antenna, as depicted in Figure 7. The reflection coefficient of the proposed UWB antenna is measured using an E5063A Vector Network Analyzer (VNA) by KEYSIGHT Technologies, with a maximum frequency range of up to 18 GHz. Figure 7 provides the comparison between theoretical and measured results; it can be observed that the measured results are in good agreement with the simulated results. The measured results offer an UWB of 7.05 GHz, which is 140% of the initial central frequency of 5 GHz. The proposed work, as shown in Figure 7, provides $|S_{11}| > -10$ dB impedance bandwidth ranges from 2.70–9.75 GHz.

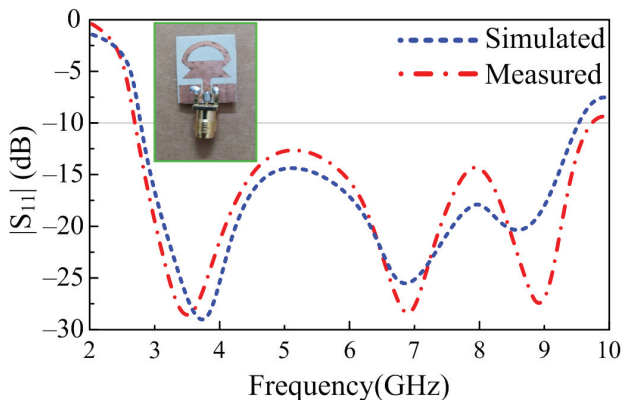


Figure 7. Comparison among the predicted and measured reflection coefficients of the proposed work.

3.2. Conformal Analysis

In working effectively with the flexible electronics, the antenna should offer a stable result in both conformal and non-conformal conditions. The antenna is bent in both the X and Y axes for this purpose, as shown in Figures 8 and 9, respectively. The bending radius for both simulation and measurements is chosen to be 10 mm. Figure 9 depicts the comparison between the simulated and measured results of antennas under bending conditions. It can be observed from Figure 9a that when the antenna is bent along the X-axis, the return loss of the antenna gets further improved as compared to the antenna without any bending. Furthermore, the bandwidth remains identical to the rigid case. On the other hand, when the antenna is bent along the Y-axis, as shown in Figure 9b, a

slight improvement in bandwidth as well as return loss is observed, similar to the results observed in non-conformal conditions. Thus, it can be concluded that the antenna offers almost identical results in both scenarios, which shows the performance stability of the proposed work. Furthermore, the strong agreement between simulated and measured results also highlights the performance stability of the antenna in terms of return loss.

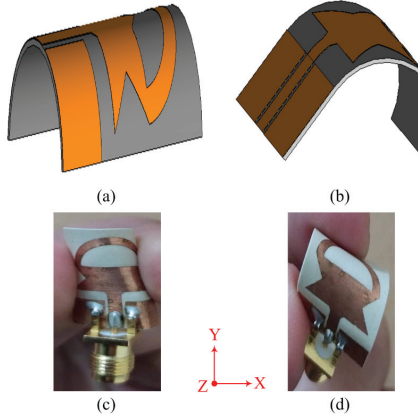


Figure 8. Simulation setup for conformal structure (a) X-axis (b) Y-axis; fabricated prototype of the proposed antenna bent along (c) X-axis (d) Y-axis.

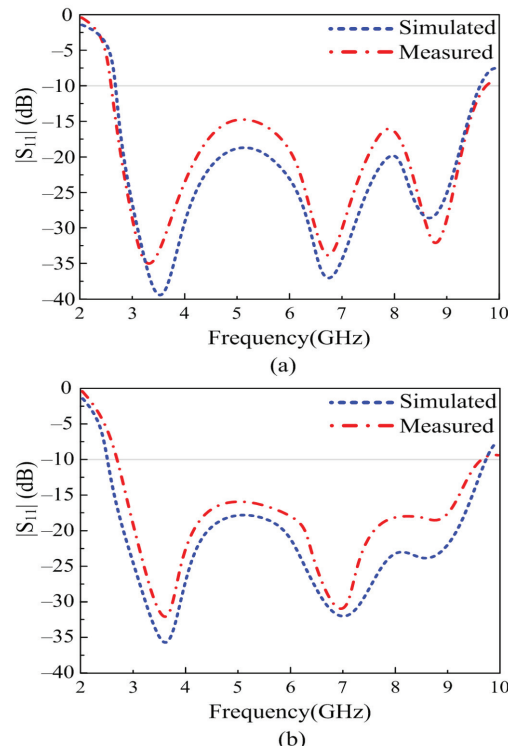


Figure 9. Comparison between predicted and measured reflection coefficients of the antenna under conformal conditions along the (a) X-axis and (b) Y-axis.

3.3. Far-Field Analysis

3.3.1. Measurement Setup

The fabricated prototype is further utilized to measure the far-field parameters of the proposed work. In order to this, the antenna was placed inside the anechoic chamber in front of the reference Horn antenna, which has a broadband of up to 12 GHz. The measurement setup, along with a close snap of the proposed work, is depicted in Figure 10.

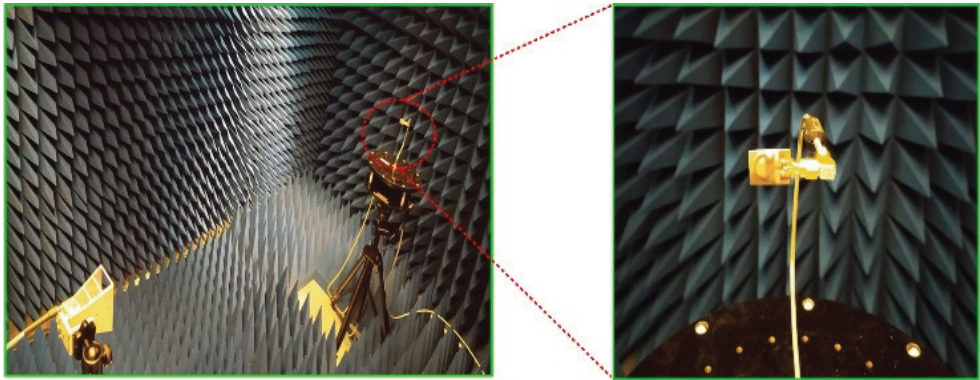


Figure 10. Measurement setup for far-field analysis of the propped flexible UWB antenna.

3.3.2. Radiation Pattern

Figure 11a–c depict the radiation pattern of the proposed antenna at the selected frequencies of 3.5 GHz, 6.8 GHz, and 9 GHz, respectively. In all the selected frequencies, the antenna provides an omnidirectional radiation pattern in the h-plane, while in the e-plane, the antenna provides a monopole-like bidirectional radiation pattern. It can also be seen that as the frequency increases, the radiation pattern becomes slightly distorted, owing to the fact that the antenna size grows relatively large. Furthermore, the measured results offer a strong agreement with the simulated results over all frequencies, as depicted in Figure 11.

3.3.3. Radiation Pattern under Conformability

The prototype is then used to measure the radiation pattern under bending conditions. The radiation is measured at the selected frequencies of 3.5 GHz, 6.8 GHz, and 9 GHz while bending the antenna along the x - and y -axes, as shown in Figure 12. It can be observed that at all selected frequencies, the antenna offers a nearly identical radiation pattern as compared to the antenna under normal conditions. A little deviation from the original pattern is due to conformability in the radiating structure. Moreover, the simulated and measured results also show strong agreement with each other, stating the performance stability of the proposed antenna in terms of radiation pattern.

3.3.4. Gain of UWB Antenna

The gain of the proposed antenna is also measured for both conformal and non-conformal conditions. It can be observed from Figure 13 that the antenna offers a gain of 2.5 dB in operational bandwidth. Moreover, it can also be observed that for conformal conditions, a slight increase in gain is achieved. It is due to a slight deviation in the radiation pattern. Furthermore, a strong agreement is observed between the theoretical and measured values of the gain.

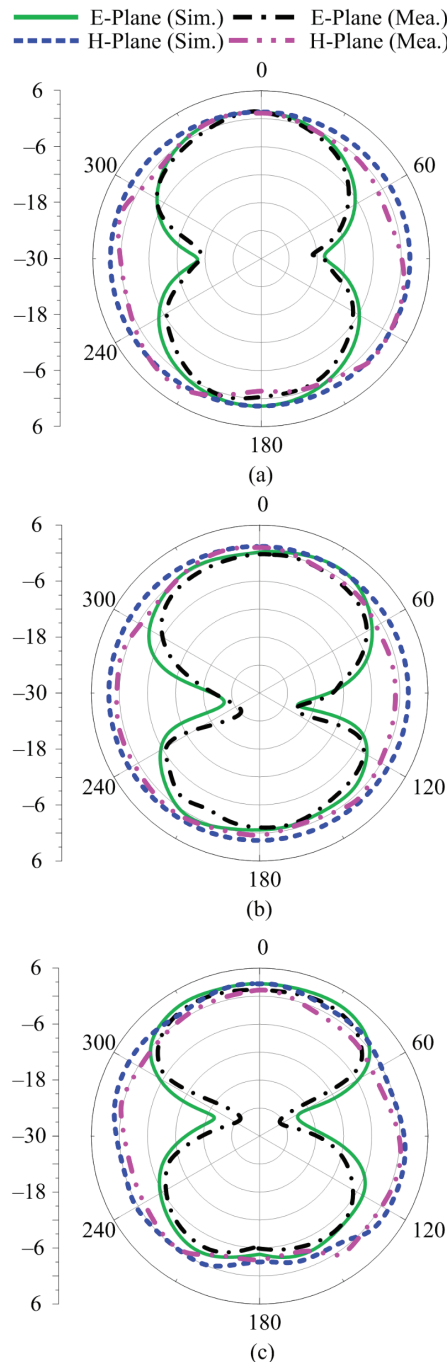


Figure 11. Comparison of predicted and measured radiation patterns at (a) 3.5 GHz, (b) 6.8 GHz, and (c) 9 GHz.

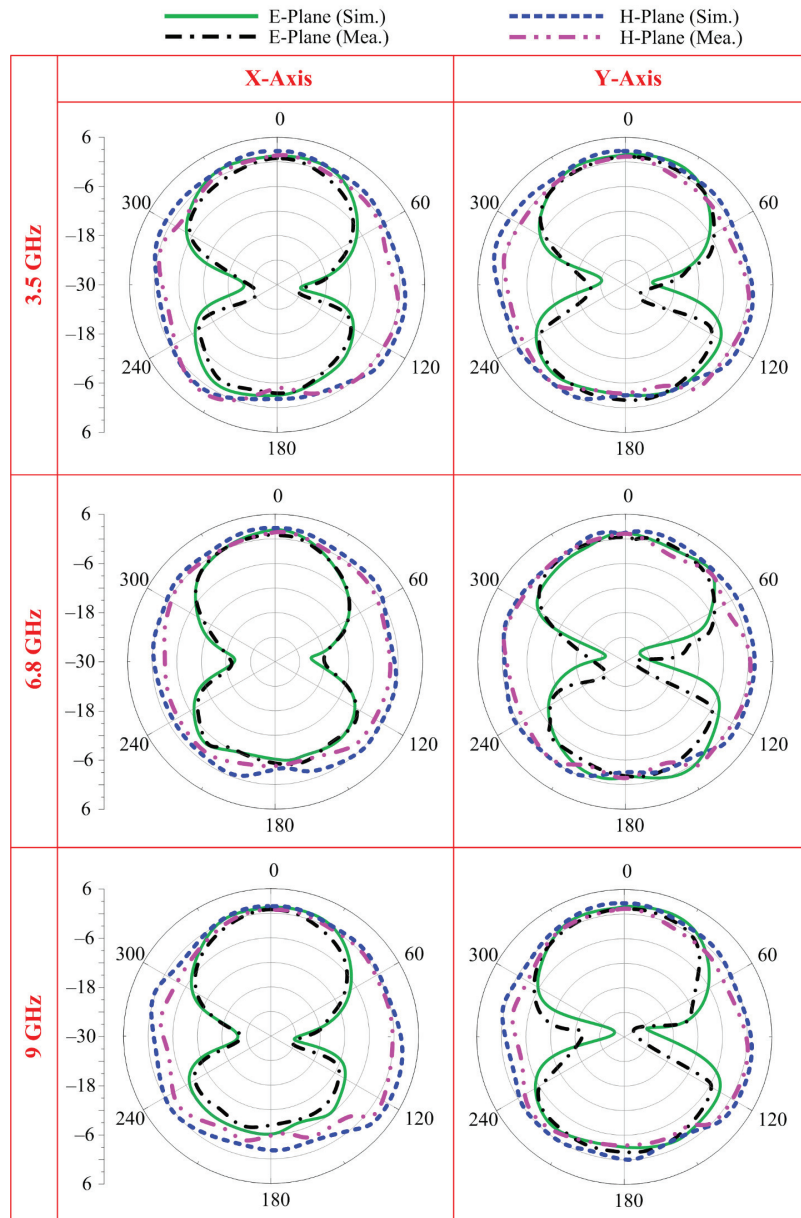


Figure 12. Comparison between predicted and measured radiation patterns of the proposed antenna.

3.4. Group Delay

The time-domain analyses are another crucial factor while designing the UWB antenna, as they are useful to understand the propagation through the antenna. The group delay of any UWB can be calculated by using change in phase with respect to change in frequency and can be estimated by using the following relation provided in [32].

$$\text{Group Delay} = -\frac{1}{2\pi} \frac{d\theta}{df} \quad (6)$$

In order to work efficiently, the UWB antenna should possess a constant group delay, ideally. However, due to the presence of various losses in the materials used for designing the antenna, a little deviation is acceptable. The proposed antenna offers a group delay range of 0.4–0.6 nS with an average value of 0.5 nS over the entire bandwidth, as shown in Figure 14.

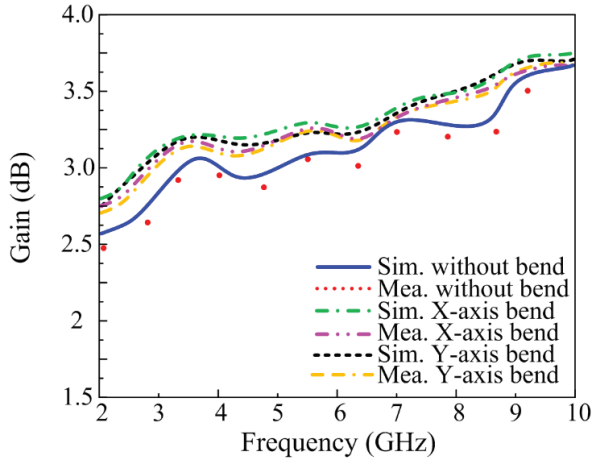


Figure 13. Gain of the proposed work for conformal and non-conformal scenarios.

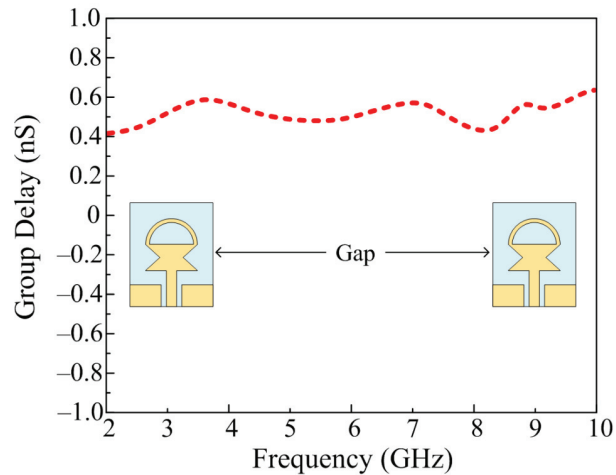


Figure 14. Group delay of the proposed UWB antenna.

3.5. Comparison with State-of-the-Art

Table 1 presents the comparison of the proposed antenna with the state-of-the-art. It can be observed from Table 1 that the antenna reported in [13–22] offers a bigger size as compared to the proposed work, while the antenna reported in [13–19] also offers structural complexity. Moreover, the antenna reported in [14–19,22] exhibits low gain as compared to the presented work. Therefore, it can be concluded that the proposed work over-performs the related work by offering a good combination of compact size, wideband, moderate gain, low structural complexity, and strong comparisons among simulated and measured results in both rigid and bending conditions.

Table 1. Comparison with State-of-the-Art.

Ref. no.	Size (mm ³)	Bandwidth (GHz)	Gain (dB)	Structural Complexity	Flexibility
[13]	59.8 × 59.8 × 3.4	2–3	>2.5	High	No
[14]	39 × 39 × 1.6	2–13	>0.5	High	No
[15]	80 × 67 × 3.4	3.68–10.1	>0.9	High	Yes
[16]	28.1 × 17.1 × 1.4	5–14	>2	Moderate	No
[17]	40 × 22 × 0.1	2.5–11	>2	Moderate	Yes
[18]	33 × 22 × 0.125	4–10	>1	High	Yes
[19]	38 × 22 × 0.1	4–11	>0.3	Moderate	Yes
[20]	33.1 × 32.7 × 0.254	4–15	>2.5	Low	Yes
[21]	34 × 32.6 × 0.05	2–10	>2.8	Low	Yes
[22]	48 × 34.9 × 0.05	2–8	>−2.1	Low	Yes
Proposed Work	20 × 15 × 0.254	2.73–9.68	>2.5	Low	Yes

4. Conclusions

This article presents the design of a compact-sized UWB antenna extracted from a conventional rectangular monopole by etching a pair of slots and a loading stub. The antenna is designed using ROGERS 5880, a flexible material with an extremely low dielectric loss of 0.0009, a thickness of 0.254 mm, and a dielectric constant of 2.2. Additionally, by means of two triangular slots along with a semi-circular-shaped short-ended stub, a narrow band antenna is converted to a UWB antenna without increasing the structural complexity. The antenna covers the band spectrum ranging from 2.73–9.68 GHz, has a minimum gain of >2.5 dBi, and has an omni-directional radiation pattern. Furthermore, when the antenna is bent along the *x* and *y* axes, its performance remains identical to that of the unbent antenna. Along with that, the strong comparison between simulated and measured results for both conformal and non-conformal scenarios shows the performance stability of the proposed UWB antenna. Moreover, the comparison with the state of the art shows that the presented work outperforms the related work. Thus, owing to the advantage of the CPW-feeding technique providing ease of integration with other electronics circuits and its size, compactness, wideband, and stable performance for both non-conforming and conforming scenarios, the proposed work is a strong potential candidate for wireless networks and small flexible as well as rigid devices requiring UWB antenna.

Author Contributions: Conceptualization, W.A.A.; methodology, software and validation, E.M.A., M.S.A. and A.A.; formal analysis, investigation, resources and data curation, E.M.A., W.A.A. and D.H.E.; writing—original draft preparation, E.M.A., W.A.A., M.S.A. and D.H.E.; writing—review and editing, W.A.A., A.A., F.F. and S.S.M.G.; project administration and funding acquisition, D.H.E., F.F. and W.A.A. All authors have read and agreed to the published version of the manuscript.

Funding: This work was supported by Ministerio de Ciencia, Innovación y Universidades, Gobierno de España (Agencia Estatal de Investigación, Fondo Europeo de Desarrollo Regional -FEDER-, European Union) under the research grant of PID2021-127409OB-C31 CONDOR and by Princess Nourah bint Abdulrahman University Researchers Supporting Project number (PNURSP2023R238), Princess Nourah bint Abdulrahman University, Riyadh, Saudi Arabia.

Institutional Review Board Statement: Not applicable.

Informed Consent Statement: Not applicable.

Data Availability Statement: Not applicable.

Acknowledgments: Princess Nourah bint Abdulrahman University Researchers Supporting Project number (PNURSP2023R238), Princess Nourah bint Abdulrahman University, Riyadh, Saudi Arabia.

Conflicts of Interest: The authors declare no conflict of interest.

References

1. Fontana, R.J. Recent system applications of short-pulse ultra-wideband (UWB) technology. *IEEE Trans. Microw. Theory Techn.* **2004**, *52*, 2087–2104. [CrossRef]
2. Matin, M.A. *Ultra-Wideband Current Status and Future Trends*; Intech Open: London, UK, 2012.
3. Galvan-Tejada, G.M.; Peyrot-Solis, M.A.; Aguilar, H.J. *Ultra-Wideband Antennas: Design, Methodologies, and Performance*; CRC Press: Boca Raton, FL, USA, 2015.
4. FCC. *FCC 1st Report and Order on Ultra-Wideband Technology*; FCC: Washington, DC, USA, 2002.
5. Wei, Q.H.; Ruan, C.L.; Xue, Q. A planar folded ultrawideband antenna with gap-loading. *IEEE Trans. Antennas Propag.* **2007**, *55*, 216–220.
6. Hussain, N.; Awan, W.A.; Naqvi, S.I.; Ghaffar, A.; Zaidi, A.; Naqvi, S.A.; Iftikhar, A.; Li, X.J. A compact flexible frequency reconfigurable antenna for heterogeneous applications. *IEEE Access* **2020**, *8*, 173298–173307. [CrossRef]
7. Hussain, N.; Ghaffar, A.; Naqvi, S.I.; Iftikhar, A.; Anagnostou, D.E.; Tran, H.H. A conformal frequency reconfigurable antenna with multiband and wideband characteristics. *Sensors* **2022**, *22*, 2601. [CrossRef]
8. Awan, W.A.; Hussain, N.; Le, T.T. Ultra-thin flexible fractal antenna for 2.45 GHz application with wideband harmonic rejection. *AEU Int. J. Electron. Commun.* **2019**, *110*, e152851. [CrossRef]
9. Saeed, S.M.; Balanis, C.A.; Birtcher, C.R.; Durgun, A.C.; Shaman, H.N. Wearable flexible reconfigurable antenna integrated with artificial magnetic conductor. *IEEE Antennas Wirel. Propag. Lett.* **2017**, *16*, 2396–2399. [CrossRef]
10. Ghaffar, A.; Li, X.J.; Awan, W.A.; Naqvi, A.H.; Hussain, N.; Alibakhshikenari, M.; Limiti, E. A flexible and pattern reconfigurable antenna with small dimensions and simple layout for wireless communication systems operating over 1.65–2.51 GHz. *Electronics* **2021**, *10*, 601. [CrossRef]
11. Hamouda, Z.; Wojkiewicz, J.L.; Pud, A.A.; Koné, L.; Bergheul, S.; Lasri, T. Magnetodielectric nanocomposite polymer-based dual-band flexible antenna for wearable applications. *IEEE Trans. Antennas Propag.* **2018**, *66*, 3271–3277. [CrossRef]
12. Rizwan, M.; Khan, M.W.A.; Sydänheimo, L.; Virkkilä, J.; Ukkonen, L. Flexible and stretchable brush-painted wearable antenna on a three-dimensional (3-D) printed substrate. *IEEE Antennas Wirel. Propag. Lett.* **2017**, *16*, 3108–3112. [CrossRef]
13. Simorangkir, R.B.V.B.; Yang, Y.; Esselle, K.P.; Zeb, B.A. A method to realize robust flexible electronically tunable antennas using polymer-embedded conductive fabric. *IEEE Trans. Antennas Propag.* **2017**, *66*, 50–58. [CrossRef]
14. Tang, Z.; Wu, X.; Zhan, J.; Hu, S.; Xi, Z.; Liu, Y. Compact UWB-MIMO antenna with high isolation and triple band-notched characteristics. *IEEE Access* **2019**, *7*, 19856–19865. [CrossRef]
15. Simorangkir, R.B.V.B.; Kiourtzi, A.; Esselle, K.P. UWB wearable antenna with a full ground plane based on PDMS-embedded conductive fabric. *IEEE Antennas Wirel. Propag. Lett.* **2018**, *17*, 493–496. [CrossRef]
16. Saha, T.K.; Goodbody, C.; Karacolak, T.; Sekhar, P.K. A compact monopole antenna for ultra-wideband applications. *Microw. Opt. Technol. Lett.* **2019**, *61*, 182–186. [CrossRef]
17. Zahran, S.R.; Abdalla, M.A.; Gaafar, A. Time domain analysis for foldable thin UWB monopole antenna. *AEU Int. J. Electron. Commun.* **2018**, *83*, 253–262. [CrossRef]
18. Li, W.; Hei, Y.; Grubb, P.M.; Shi, X.; Chen, R.T. Compact inkjet-printed flexible MIMO antenna for UWB applications. *IEEE Access* **2018**, *6*, 50290–50298. [CrossRef]
19. Zahran, S.R.; Gaafar, A.; Abdalla, M.A. A flexible UWB low profile antenna for wearable applications. In *IEEE International Symposium on Antennas and Propagation (APSURSI)*; IEEE: Piscataway, NJ, USA, 2016; pp. 1931–1932.
20. Saha, T.K.; Knaus, T.N.; Khosla, A.; Sekhar, P.K. A CPW-fed flexible UWB antenna for IoT applications. *Microsys. Technol.* **2018**, *28*, 5–11. [CrossRef]
21. Wang, Z.; Qin, L.; Chen, Q.; Yang, W.; Qu, H. Flexible UWB antenna fabricated on polyimide substrate by surface modification and in situ self-metallization technique. *Microelectron. Eng.* **2019**, *6*, 12–16. [CrossRef]
22. Hamouda, Z.; Wojkiewicz, J.L.; Pud, A.A.; Kone, L.; Bergheul, S.; Lasri, T. Flexible UWB organic antenna for wearable technologies application. *IET Microw. Antennas Propag.* **2018**, *12*, 160–166. [CrossRef]
23. Ray, K.P.; Tiwari, S. Ultra-wideband printed hexagonal monopole antennas. *IET Microw. Antennas Propag.* **2010**, *4*, 437–445.
24. Kundu, S. Balloon-shaped CPW fed printed UWB antenna with dual frequency notch to eliminate WiMAX and WLAN interferences. *Microw. Opt. Technol. Lett.* **2018**, *60*, 1744–1750. [CrossRef]
25. Du, C.; Li, X.; Zhong, S. Compact liquid crystal polymer based tri-band flexible antenna for WLAN/WiMAX/5G applications. *IEEE Access* **2019**. [CrossRef]
26. Govindan, T.; Palaniswamy, S.K.; Kanagasabai, M.; Rao, T.R.; Alsath, M.; Kumar, S.; Marey, M.; Aggarwal, A. On the design and performance analysis of wristband MIMO/diversity antenna for smart wearable communication applications. *Sci. Rep.* **2021**, *11*, 21917. [CrossRef] [PubMed]
27. Hussain, N.; Jeong, M.J.; Park, J.; Kim, N. A broadband circularly polarized fabry-perot resonant antenna using a single-layered PRS for 5G MIMO applications. *IEEE Access* **2019**, *7*, 42897–42907. [CrossRef]
28. Sufian, M.A.; Hussain, N.; Abbas, A.; Lee, J.; Park, S.G.; Kim, N. Mutual coupling reduction of a circularly polarized MIMO antenna using parasitic elements and DGS for V2X communications. *IEEE Access* **2022**, *10*, 56388–56400. [CrossRef]
29. Abbas, A.; Hussain, N.; Sufian, M.A.; Jung, J.; Park, S.M.; Kim, N. Isolation and gain improvement of a rectangular notch UWB-MIMO antenna. *Sensors* **2022**, *22*, 1460. [CrossRef]
30. May, C. Transmission lines. In *Passive Circuit Analysis with LTspice®*; Springer: Cham, Switzerland, 2020; pp. 417–444.

31. Awan, W.A.; Zaidi, A.; Hussain, M.; Hussain, N.; Syed, I. The design of a wideband antenna with notching characteristics for small devices using a genetic algorithm. *Mathematics* **2021**, *9*, 2113. [CrossRef]
32. Dwivedi, R.P.; Khan, M.Z.; Kommuri, U.K. UWB circular cross slot AMC design for radiation improvement of UWB antenna. *AEU-Int. J. Electron. Commun.* **2020**, *117*, 153092. [CrossRef]

Disclaimer/Publisher's Note: The statements, opinions and data contained in all publications are solely those of the individual author(s) and contributor(s) and not of MDPI and/or the editor(s). MDPI and/or the editor(s) disclaim responsibility for any injury to people or property resulting from any ideas, methods, instructions or products referred to in the content.



Article

Near Field Models of Spatially-Fed Planar Arrays and Their Application to Multi-Frequency Direct Layout Optimization for mm-Wave 5G New Radio Indoor Network Coverage

Daniel R. Prado

Group of Signal Theory and Communications, Department of Electrical Engineering, Universidad de Oviedo, 33203 Gijón, Spain; drprado@uniovi.es

Abstract: Two near field models for the analysis of spatially fed planar array antennas are presented, compared and applied to a multi-frequency wideband direct layout optimization for mm-Wave 5G new radio (NR) indoor network coverage. One model is based on the direct application of the radiation equations directly derived from the A and F vector potentials. The second model is based on the superposition of far field contributions of all array elements, which are modelled as rectangular apertures with constant field. Despite the different assumptions made to develop both models, the degree of agreement between them in the computation of the radiated near field is very high. The relative error between the models is equal or lower than 3.2% at a plane 13λ from the array, and it decreases as the near field is computed further away from the array. Then, the faster model is employed in a general direct layout optimization procedure to shape the electromagnetic near field for application in an indoor femtocell to provide coverage with constant power in a private office. Results show that a magnitude ripple better than 1.5 dB can be achieved in an enlarged coverage area covering the whole n257 band of the 5G NR, corresponding to a 10.7% relative bandwidth.

Citation: Prado, D.R. Near Field Models of Spatially-Fed Planar Arrays and Their Application to Multi-Frequency Direct Layout Optimization for mm-Wave 5G New Radio Indoor Network Coverage. *Sensors* **2022**, *22*, 8925. <https://doi.org/10.3390/s22228925>

Academic Editor: Naser Ojaroudi Parchin

Received: 10 October 2022

Accepted: 15 November 2022

Published: 18 November 2022

Publisher's Note: MDPI stays neutral with regard to jurisdictional claims in published maps and institutional affiliations.



Copyright: © 2022 by the author. Licensee MDPI, Basel, Switzerland. This article is an open access article distributed under the terms and conditions of the Creative Commons Attribution (CC BY) license (<https://creativecommons.org/licenses/by/4.0/>).

Keywords: spatially fed array; reflectarray antenna; transmitarray; near field; radiation equations; radiated field synthesis; optimization; electromagnetic field shaping; generalized intersection approach

1. Introduction

Wireless communications within the 3rd Generation Partnership Project (3GPP) 5G New Radio (NR) paradigm have introduced new concepts and technologies, including ultra-dense networking, massive machine communications, all-spectrum access, full-duplexing, and massive MIMO [1,2], for applications in the industry 4.0 [3], smart cities [4], Internet of Things (IoT) [5], precision agriculture [6], and self-driving cars [7], among others [8]. These applications require higher data rates, higher channel capacity, and lower latency than those achieved with previous generations of mobile networks [9]. To that end, the 3GPP 5G NR technical specification [10] identifies two frequency ranges (FR) for the implementation of the 5G networks, namely, FR1 (0.41–7.125 GHz) and FR2 (24.25–71 GHz), each of them divided into several bands. From the point of view of frequency allocation, the FR1 spectrum is already very crowded, by now providing services that range from cellular and satellite communications, to wireless local area networks [9]. Thus, the mm-wave ranges provided by the FR2, with their readily available wide spectrum, have become increasingly interesting for the deployment of 5G NR networks. In particular, there is special interest in the three lower bands in FR2, n257 (26.5–29.5 GHz), n258 (24.25–27.5 GHz), and n261 (27.5–28.35 GHz) since they have been released by the most countries, including the United States, the European Union, China, Japan, and South Korea [9]. However, the use of frequencies in the FR2 presents some challenges, such as path loss due to higher losses and shadowing due to blockage by physical objects that act as barriers for the propagating wave [11]. To overcome these issues, the use of femtocells with increased line of sight

connectivity [12,13] has been proposed as a means of enhancing the cellular coverage while offloading the macro cell traffic in places with higher density.

Spatially fed arrays have been proposed within the intelligent reflective surface (IRS) paradigm [14–16], specifically reflectarray antennas for both indoor [17] and outdoor scenarios [18]. Transmitarrays have also been proposed as a solution to provide coverage in indoor femtocells [19,20]. In order to improve the coverage in indoor scenarios for transfer of information, power, or both simultaneously, near field beam-shaping techniques for the enlargement of coverage areas have been proposed. For instance, in [17] a phase-only synthesis (POS) based on the generalized intersection approach [21] was carried out to design two reflectarray antennas, one providing coverage in an outdoor scenario by considering a squared-cosecant beam in elevation and sectorial beam in azimuth, while the other reflectarray provides coverage in an indoor scenario. In [19], a novel near field POS algorithm was developed in which the far field resulting from the truncated near field according to specifications is computed as an intermediate step before recovering the field at the aperture by means of the fast Fourier transform (FFT). It was employed to design a 3D-printed dielectric transmitarray antenna that provides a very narrow coverage area. This algorithm was later extended [22] to include simultaneous near and far field constraints. Another near field POS is carried out in [20] to enlarge the coverage area provided by a multi-fed transmitarray antenna.

The techniques employed in the previous works are very efficient for the near field beam-shaping of spatially fed arrays at a single frequency. However, they present some shortcomings. One common characteristic of the previous works is that they perform a POS, where a phase-shift for each array element is obtained at a single frequency such that the array radiates the desired near field. From those phases, the chosen unit cell is tuned in such a way that it produces the required phase-shift [23]. One obvious limitation of such an approach is the narrow bandwidth nature of the obtained arrays. Indeed, since the POS and layout design only consider a single frequency, the in-band behaviour of the array rapidly deteriorates [24]. Moreover, due to the intermediate step of computing the far field in the near field synthesis of [19,22], that algorithm is restricted to a single near field plane that is parallel to the array aperture.

In order to overcome those limitations, this work proposes a general near field beam-shaping technique for the wideband optimization of spatially fed arrays. Specifically, the new analysis technique allows computation of the near field in a volume with an arbitrary local coordinate system rotated by three angles with regard to the array, as well as to perform a wideband direct layout optimization by taking into account the full electromagnetic response of the unit cell at several frequencies as provided by the use of a full-wave electromagnetic tool assuming local periodicity directly in the optimization loop. To that end, first two near field models for spatially fed arrays are presented. One model is based on the radiation equations directly derived from the A and F vector potentials [25]. The volumetric integrals are particularized to planar arrays discretized into a number of constituent elements. The resulting surface integrals are evaluated by means of the mid point quadrature, evaluating their convergence for different discretization grids. The second model is based on the superposition of the far fields radiated by each array element, which are modelled as small rectangular apertures with constant field on them. The far field is obtained with Love's principle of equivalence for aperture antenna [26]. In addition, a formulation is given to have the possibility of computing the near field in an arbitrary local coordinate system which is rotated and translated with regard to the array local coordinate system, which might be useful depending on the application. Both near field models are then compared by considering the near field radiated by a transmitarray antenna, showing a high degree of agreement between the two models. Then, the faster model is applied to a novel technique for the wideband near field beam-shaping based on the generalized intersection approach (GIA) [21]. This technique performs a direct layout optimization employing a method of moments based on local periodicity (MoM-LP) directly in the optimization loop to account for the real electromagnetic response of the

unit cell at several frequencies of interest, including mutual coupling between the array elements. In this way, a general near field multi-frequency optimization algorithm is obtained. As an example of application, it is applied to an indoor scenario in which it is desired to provide coverage in a private office with a 5G NR femtocell working in the n257 band, which comprises the frequency range 26.5–29.5 GHz, corresponding to a 10.7% relative bandwidth. The optimization procedure with the GIA is divided into several stages to facilitate convergence towards a suitable solution. The final optimized array presents a maximum magnitude ripple in the enlarged coverage area of 1.5 dB over the whole n257 bandwidth, showing the suitability of the proposed methodology for the wideband near field beam-shaping of spatially fed array antennas.

2. Statement of the Problem

Let us consider a spatially fed planar array, namely a reflectarray or transmitarray, comprised of N elements with a regular periodicity of $p_x \times p_y$. The goal is to calculate the near field radiated by the array in a volume discretized in M points in front of the antenna and to shape the near field such that it complies with certain specifications for a given application. To that end, Figure 1 shows a sketch of the near field model for the two considered arrays. From the point of view of the analysis of the array, both spatially fed arrays are analysed in the same way, considering their own local coordinate system (ACS, array coordinate system) defined by $(\hat{x}_a, \hat{y}_a, \hat{z}_a)$. The location (i.e., centre) of the i -th array element is given by $\vec{r}'_i = (x'_i, y'_i, z'_i = 0)$, which is a point in the surface of the planar array, and $\vec{r} = (x, y, z)$ is a point in space in front of the array, i.e., with $z > 0$. Both \vec{r}'_i and \vec{r} are defined in the ACS, and $\vec{R} = \vec{r} - \vec{r}'_i$.

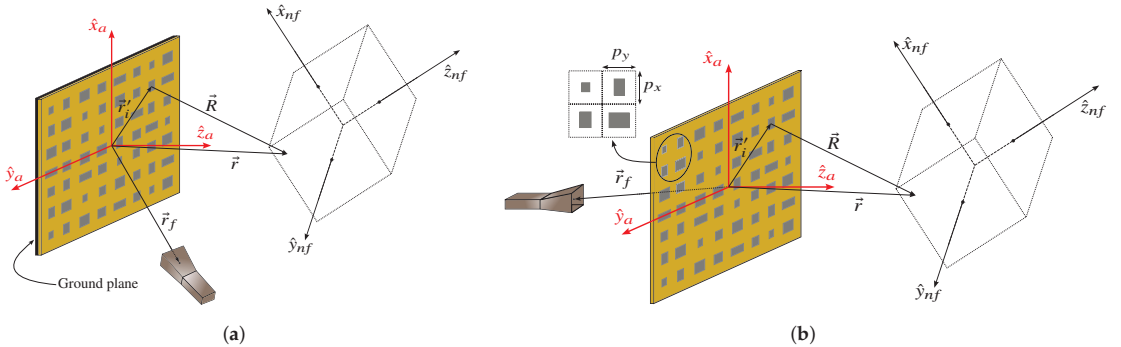


Figure 1. Sketch of the (a) reflectarray and (b) transmitarray scenarios. The goal is to obtain the near field radiated by the arrays in a volume in front of the antenna. The analysis of the arrays is carried out in the array coordinate system (ACS) defined by $(\hat{x}_a, \hat{y}_a, \hat{z}_a)$, while the radiated field will be obtained in the near field coordinate system (NFCS) defined by $(\hat{x}_{nf}, \hat{y}_{nf}, \hat{z}_{nf})$. The transformation between ACS and NFCS may be consulted in Appendix A.

On the other hand, the radiated field is referred to a rotated—and translated—coordinate system (NFCS, near field coordinate system) noted as $(\hat{x}_{nf}, \hat{y}_{nf}, \hat{z}_{nf})$. The relation between the ACS and NFCS is given by matrix T , which is derived in Appendix A. Since the analysis of the array is carried out in the ACS, the calculated radiated field will have to be transformed so that it is referenced to the NFCS.

In the following section, two near field models will be developed. One is based on the exact radiated field equations, while the other is based on the superposition of the far field radiated by each array element. In both cases, the radiation element is modelled as a small rectangular aperture with constant field on it.

3. Near Field Models of Reflectarray and Transmitarray Antennas

3.1. Field at the Aperture

Before presenting the two near field models, the field at the aperture needs to be calculated, since it is used as the source from which the radiated field is obtained. First, a feed whose phase center is placed at $\vec{r}_f = (x_f, y_f, z_f)$ in the ACS generates a tangential incident field on the surface of the array, which can be written for the i -th element as:

$$\vec{E}_{\text{inc}}(\vec{r}_i') = E_{\text{inc},x}(\vec{r}_i')\hat{x}_a + E_{\text{inc},y}(\vec{r}_i')\hat{y}_a, \quad (1)$$

with $i = 1, \dots, N$. In order to alleviate the notation, the dependence on \vec{r}_i' of the field components will be dropped from here on. From the incident field, the field at the aperture may be calculated as:

$$\vec{E}_{\text{ap}}(\vec{r}_i') = M_i \vec{E}_{\text{inc}}(\vec{r}_i') \quad (2)$$

where M_i is a 2×2 matrix of complex numbers which depends on the considered array. For reflectarrays, M_i is the matrix of reflection coefficients:

$$M_i = \begin{pmatrix} \rho_{xx,i} & \rho_{xy,i} \\ \rho_{yx,i} & \rho_{yy,i} \end{pmatrix}, \quad (3)$$

and the field at the aperture \vec{E}_{ap} would correspond to the reflected field. In the case of transmitarrays, M_i is the matrix of transmission coefficients:

$$M_i = \begin{pmatrix} \tau_{xx,i} & \tau_{xy,i} \\ \tau_{yx,i} & \tau_{yy,i} \end{pmatrix}, \quad (4)$$

and the field at the aperture would correspond to the transmitted field. For both cases, M_i is computed using a full-wave analysis tool assuming local periodicity. In addition, M_i depends on the working frequency, unit cell topology, periodicity, substrate characteristics, and angles of incidence of the plane wave employed in the analysis [27].

Once the tangential electric field at the aperture has been obtained with (2), the tangential magnetic field may be calculated with:

$$\vec{H}_{\text{ap}}(\vec{r}_i') = \frac{\vec{k} \times \vec{E}_{\text{ap}}(\vec{r}_i')}{\omega \mu_0}, \quad (5)$$

where

$$\vec{k} = k_x \hat{x}_a + k_y \hat{y}_a + k_z \hat{z}_a = -k_0 (\sin \theta_i \cos \varphi_i \hat{x}_a + \sin \theta_i \sin \varphi_i \hat{y}_a - \cos \theta_i \hat{z}_a), \quad (6)$$

$\omega = 2\pi f$, f is the frequency, μ_0 is the free-space permeability, k_0 is the free-space wavenumber, and (θ_i, φ_i) is the angle of incidence of the plane wave for the i -th array element (see Figure 1). The \hat{z} component of \vec{E}_{ap} , necessary to solve (5), is obtained by solving the plane wave equation $\vec{k} \cdot \vec{E}_{\text{ap}} = 0$. Then, the components of the reflected tangential magnetic field are:

$$H_{\text{ap},x} = -K_1 E_{\text{ap},x} - K_2 E_{\text{ap},y}, \quad (7a)$$

$$H_{\text{ap},y} = K_3 E_{\text{ap},x} + K_1 E_{\text{ap},y}, \quad (7b)$$

with:

$$K_1 = \frac{k_x k_y}{\omega \mu_0 k_z}, \quad (8a)$$

$$K_2 = \frac{k_y^2 + k_z^2}{\omega \mu_0 k_z}, \quad (8b)$$

$$K_3 = \frac{k_x^2 + k_z^2}{\omega \mu_0 k_z}. \quad (8c)$$

In this way, the tangential field at the aperture is fully characterized by:

$$\vec{E}_{\text{ap}}(\vec{r}_i') = E_{\text{ap},x} \hat{x}_a + E_{\text{ap},y} \hat{y}_a, \quad (9a)$$

$$\vec{H}_{\text{ap}}(\vec{r}_i') = H_{\text{ap},x} \hat{x}_a + H_{\text{ap},y} \hat{y}_a, \quad (9b)$$

where $\vec{E}_{\text{ap}}(\vec{r}_i')$ is obtained from (2) and $\vec{H}_{\text{ap}}(\vec{r}_i')$ from (5) and may be readily employed as a source for the calculation of the radiated field.

Sometimes, the electric (\vec{j}) and magnetic (\vec{M}) current densities are required. Since planar arrays are considered, the notation \vec{j}_s and \vec{M}_s is employed. They can be obtained from the tangential field at the aperture as follows:

$$\vec{j}_s(\vec{r}_i') = \hat{n} \times \vec{H}_{\text{ap}}(\vec{r}_i') = H_{\text{ap},x} \hat{y}_a - H_{\text{ap},y} \hat{x}_a, \quad (10a)$$

$$\vec{M}_s(\vec{r}_i') = -\hat{n} \times \vec{E}_{\text{ap}}(\vec{r}_i') = -E_{\text{ap},x} \hat{y}_a + E_{\text{ap},y} \hat{x}_a, \quad (10b)$$

where $\hat{n} = \hat{z}_a$ is the unit vector normal to the surface of the planar array. Please notice that the surface current densities are also tangential vectors, and thus the longitudinal components are zero, i.e., $J_z = M_z = 0$.

3.2. Near Field from the Radiation Equations

The first near field model is based on the radiation equations obtained as superposition of the contributions of the vector potentials \vec{A} and \vec{F} [25]:

$$\vec{E}_{\text{NF}}(\vec{r}) = \vec{E}_A(\vec{r}) + \vec{E}_F(\vec{r}), \quad (11a)$$

$$\vec{H}_{\text{NF}}(\vec{r}) = \vec{H}_A(\vec{r}) + \vec{H}_F(\vec{r}), \quad (11b)$$

where

$$\vec{E}_A(\vec{r}) = E_{A,x} \hat{x}_a + E_{A,y} \hat{y}_a + E_{A,z} \hat{z}_a \quad (12a)$$

$$\vec{E}_F(\vec{r}) = E_{F,x} \hat{x}_a + E_{F,y} \hat{y}_a + E_{F,z} \hat{z}_a \quad (12b)$$

$$\vec{H}_A(\vec{r}) = H_{A,x} \hat{x}_a + H_{A,y} \hat{y}_a + H_{A,z} \hat{z}_a \quad (12c)$$

$$\vec{H}_F(\vec{r}) = H_{F,x} \hat{x}_a + H_{F,y} \hat{y}_a + H_{F,z} \hat{z}_a \quad (12d)$$

In (12) and subsequent equations, the dependence of the field components on the observation point \vec{r} has been dropped to alleviate the notation. There are a total of 12 field components in (11), for which an integral of field sources must be evaluated. An example of one such component is:

$$E_{F_z} = -\frac{1}{4\pi} \iiint_V [(y - y') M_x - (x - x') M_y] \frac{1 + j\beta R}{R^3} e^{-j\beta R} dx' dy' dz', \quad (13)$$

where R is the distance from a source point in the volume V to the observation point, and β is the phase constant that in this case is equal to the free-space wavenumber k_0 . The rest of

the integrals may be consulted in [25] (pp. 285–286). Since the arrays are planar, (13) can be reduced to:

$$E_{F_z} = -\frac{1}{4\pi} \iint_S [(y - y')M_x - (x - x')M_y] \frac{1 + j\beta R}{R^3} e^{-j\beta R} dx' dy', \quad (14)$$

where S is the surface of the array. The array is divided into N unit cells, where the elements of matrix M_i , and thus the field at the aperture and surface currents, are computed. Thus, we express the integral as a sum of the integral over each array element:

$$E_{F_z} = -\frac{1}{4\pi} \sum_{i=1}^N \iint_{S_i} [(y - y')M_{x_i} - (x - x')M_{y_i}] \frac{1 + j\beta R_i}{R_i^3} e^{-j\beta R_i} dx' dy', \quad (15)$$

where S_i is the surface of the i -th unit cell, and:

$$R_i = |\vec{r} - \vec{r}_i'| = \sqrt{(x - x_i')^2 + (y - y_i')^2 + z^2}. \quad (16)$$

To finally obtain E_{F_z} in (15), the double integral may be evaluated by any quadrature method, for instance, the mid point quadrature. With this technique, the integral is approximated by a double sum:

$$\begin{aligned} V_i &= \iint_{S_i} [(y - y')M_{x_i} - (x - x')M_{y_i}] \frac{1 + j\beta R_i}{R_i^3} e^{-j\beta R_i} dx' dy' \approx \sum_{h=1}^{N_x} \sum_{k=1}^{N_y} [(y - y')M_{x_i} \\ &\quad (x - x')M_{y_i}] \frac{1 + j\beta R_{ihk}}{R_{ihk}^3} e^{-j\beta R_{ihk}} \Delta x \Delta y, \end{aligned} \quad (17)$$

where surface S_i is divided into $N_x N_y$ rectangles of length $\Delta_x = p_x/N_x$ and width $\Delta_y = p_y/N_y$, and:

$$R_{ihk} = \sqrt{(x - x_{ih})^2 + (y - y_{ki})^2 + z^2}, \quad (18)$$

with:

$$x_{ih} = -p_x/2 + (h - 1/2)\Delta_x + x_i', \quad (19a)$$

$$y_{ik} = -p_y/2 + (k - 1/2)\Delta_y + y_i'. \quad (19b)$$

Thus, the function is evaluated at the center of each rectangle. By substituting (17) into (15), we finally obtain:

$$E_{F_z} = -\frac{1}{4\pi} \sum_{i=1}^N \sum_{h=1}^{N_x} \sum_{k=1}^{N_y} [(y - y')M_{x_i} - (x - x')M_{y_i}] \frac{1 + j\beta R_{ihk}}{R_{ihk}^3} e^{-j\beta R_{ihk}} \Delta x \Delta y. \quad (20)$$

The same process can be applied to the other 11 integrals in [25] (pp. 285–286), taking into account that the planar arrays are placed at the plane $z' = 0$ and that the longitudinal components of the surface currents are zero ($J_z = M_z = 0$). For the sake of completeness, the final expressions for all the integrals particularized for spatially fed planar arrays are gathered next:

$$E_{A_x} = \frac{-j\eta}{4\pi\beta} \sum_{i=1}^N \sum_{h=1}^{N_x} \sum_{k=1}^{N_y} \left\{ G_1 J_{x_i} + (x - x') G_2 [(x - x') J_{x_i} + (y - y') J_{y_i}] \right\} e^{-j\beta R_{ihk}} \Delta x \Delta y, \quad (21a)$$

$$E_{A_y} = \frac{-j\eta}{4\pi\beta} \sum_{i=1}^N \sum_{h=1}^{N_x} \sum_{k=1}^{N_y} \left\{ G_1 J_{y_i} + (y - y') G_2 [(x - x') J_{x_i} + (y - y') J_{y_i}] \right\} e^{-j\beta R_{ihk}} \Delta x \Delta y, \quad (21b)$$

$$E_{A_z} = \frac{-j\eta}{4\pi\beta} \sum_{i=1}^N \sum_{h=1}^{N_x} \sum_{k=1}^{N_y} z G_2 [(x - x') J_{x_i} + (y - y') J_{y_i}] e^{-j\beta R_{ihk}} \Delta x \Delta y, \quad (21c)$$

$$E_{F_x} = \frac{-1}{4\pi} \sum_{i=1}^N \sum_{h=1}^{N_x} \sum_{k=1}^{N_y} z M_{y_i} \frac{1+j\beta R_{ihk}}{R_{ihk}^3} e^{-j\beta R_{ihk}} \Delta x \Delta y, \quad (21d)$$

$$E_{F_y} = \frac{-1}{4\pi} \sum_{i=1}^N \sum_{h=1}^{N_x} \sum_{k=1}^{N_y} -z M_{x_i} \frac{1+j\beta R_{ihk}}{R_{ihk}^3} e^{-j\beta R_{ihk}} \Delta x \Delta y, \quad (21e)$$

$$E_{F_z} = \frac{-1}{4\pi} \sum_{i=1}^N \sum_{h=1}^{N_x} \sum_{k=1}^{N_y} [(y-y')M_{x_i} - (x-x')M_{y_i}] \frac{1+j\beta R_{ihk}}{R_{ihk}^3} e^{-j\beta R_{ihk}} \Delta x \Delta y, \quad (21f)$$

$$H_{A_x} = \frac{1}{4\pi} \sum_{i=1}^N \sum_{h=1}^{N_x} \sum_{k=1}^{N_y} z J_{y_i} \frac{1+j\beta R_{ihk}}{R_{ihk}^3} e^{-j\beta R_{ihk}} \Delta x \Delta y, \quad (21g)$$

$$H_{A_y} = \frac{1}{4\pi} \sum_{i=1}^N \sum_{h=1}^{N_x} \sum_{k=1}^{N_y} -z J_{x_i} \frac{1+j\beta R_{ihk}}{R_{ihk}^3} e^{-j\beta R_{ihk}} \Delta x \Delta y, \quad (21h)$$

$$H_{A_z} = \frac{1}{4\pi} \sum_{i=1}^N \sum_{h=1}^{N_x} \sum_{k=1}^{N_y} [(y-y')J_{x_i} - (x-x')J_{y_i}] \frac{1+j\beta R_{ihk}}{R_{ihk}^3} e^{-j\beta R_{ihk}} \Delta x \Delta y, \quad (21i)$$

$$H_{F_x} = \frac{-j}{4\pi\beta\eta} \sum_{i=1}^N \sum_{h=1}^{N_x} \sum_{k=1}^{N_y} \left\{ G_1 M_{x_i} + (x-x')G_2 [(x-x')M_{x_i} + (y-y')M_{y_i}] \right\} e^{-j\beta R_{ihk}} \Delta x \Delta y, \quad (21j)$$

$$H_{F_y} = \frac{-j}{4\pi\beta\eta} \sum_{i=1}^N \sum_{h=1}^{N_x} \sum_{k=1}^{N_y} \left\{ G_1 M_{y_i} + (y-y')G_2 [(x-x')M_{x_i} + (y-y')M_{y_i}] \right\} e^{-j\beta R_{ihk}} \Delta x \Delta y, \quad (21k)$$

$$H_{F_z} = \frac{-j}{4\pi\beta\eta} \sum_{i=1}^N \sum_{h=1}^{N_x} \sum_{k=1}^{N_y} z G_2 [(x-x')M_{x_i} + (y-y')M_{y_i}] e^{-j\beta R_{ihk}} \Delta x \Delta y, \quad (21l)$$

where η is the free-space impedance, and:

$$G_1 = \frac{-1 - j\beta R_{ihk} + \beta^2 R_{ihk}^2}{R_{ihk}^3}, \quad (22a)$$

$$G_2 = \frac{3 + 3j\beta R_{ihk} - \beta^2 R_{ihk}^2}{R_{ihk}^5}. \quad (22b)$$

3.3. Near Field as Superposition of Far Field Contributions

To develop this model, we have to consider each unit cell in the array as a unit of radiation and calculate its far field. In such a case, the total near field will be the superposition of the far fields radiated by each element:

$$\vec{E}_{\text{NF}}(\vec{r}) = \sum_{i=1}^N \vec{E}_{\text{FF},i}(\vec{r}) \quad (23a)$$

$$\vec{H}_{\text{NF}}(\vec{r}) = \sum_{i=1}^N \vec{H}_{\text{FF},i}(\vec{r}), \quad (23b)$$

where $\vec{E}_{\text{FF},i}$ and $\vec{H}_{\text{FF},i}$ are calculated as the far field radiated by an aperture [26]. The electric far field is:

$$\vec{E}_{\text{FF},i} = E_{\theta,i} \hat{\theta} + E_{\varphi,i} \hat{\varphi}, \quad (24)$$

and its components according to Love's equivalent principle:

$$E_{\theta,i} = \frac{j k_0 e^{-jk_0 R_i}}{4\pi R_i} [P_{x,i} \cos \varphi_i + P_{y,i} \sin \varphi_i - \eta \cos \theta_i (Q_{x,i} \sin \varphi_i - Q_{y,i} \cos \varphi_i)], \quad (25a)$$

$$E_{\varphi,i} = -\frac{j k_0 e^{-jk_0 R_i}}{4\pi R_i} [\eta (Q_{x,i} \cos \varphi_i + Q_{y,i} \sin \varphi_i) + \cos \theta_i (P_{x,i} \sin \varphi_i - P_{y,i} \cos \varphi_i)], \quad (25b)$$

where the angles θ_i and φ_i are defined in Figure 2.

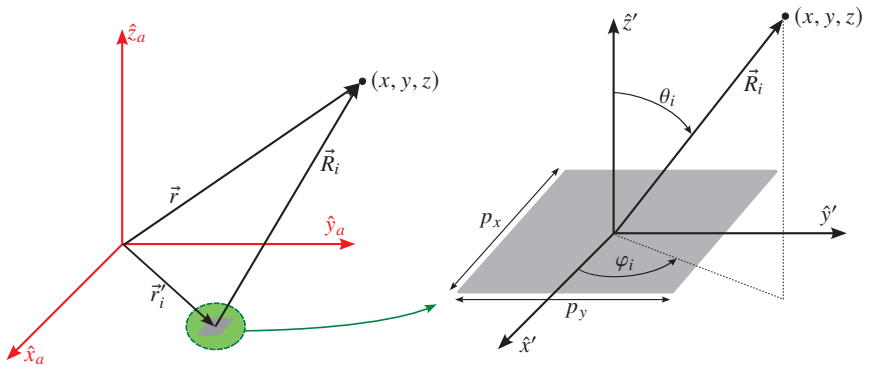


Figure 2. The definition of the angles θ_i and φ_i for the computations of the far field radiated by an array element are defined in the element coordinate system $(\hat{x}', \hat{y}', \hat{z}')$, which is the same as the ACS but translated by \vec{r}'_i .

P and Q are known as the spectrum functions, and they are the Fourier transform of the field at the aperture:

$$\begin{aligned} P_{x/y,i} &= \iint_{S_i} E_{\text{ap},x/y,i}(x, y) e^{j k_0(ux+vy)} dx dy, \\ Q_{x/y,i} &= \iint_{S_i} H_{\text{ap},x/y,i}(x, y) e^{j k_0(ux+vy)} dx dy, \end{aligned} \quad (26)$$

where $u = \sin \theta_i \cos \varphi_i$ and $v = \sin \theta_i \sin \varphi_i$. Since the aperture is element i of the array, we consider a constant field, which comes out of the integral, yielding:

$$P_{x/y,i} = E_{\text{ap},x/y,i} \iint_{S_i} e^{j k_0(ux+vy)} dx dy, \quad (27a)$$

$$Q_{x/y,i} = H_{\text{ap},x/y,i} \iint_{S_i} e^{j k_0(ux+vy)} dx dy. \quad (27b)$$

The double integral in (27) can be solved analytically yielding [28]:

$$\iint_{S_i} e^{j k_0(ux+vy)} dx dy = p_x p_y \operatorname{sinc}\left(\frac{k_0 u p_x}{2}\right) \operatorname{sinc}\left(\frac{k_0 v p_y}{2}\right), \quad (28)$$

where $\operatorname{sinc} x = \sin x / x$ is the unnormalized sinc function.

Once the electric far field has been obtained, the magnetic far field may be obtained using the plane wave relation:

$$\vec{H}_{\text{FF},i} = \frac{\hat{r} \times \vec{E}_{\text{FF},i}}{\eta} = \frac{E_{\varphi,i} \hat{\theta} + E_{\theta,i} \hat{\phi}}{\eta}. \quad (29)$$

The far field of an array element obtained with (24) and (29) is expressed in spherical coordinates, while we are interested in obtaining the near field in a Cartesian basis. Thus, to perform the superposition of (23), the far field of an array element must be expressed as:

$$\vec{E}_{\text{FF},i} = E_{\text{FF},x,i} \hat{x}_a + E_{\text{FF},y,i} \hat{y}_a + E_{\text{FF},z,i} \hat{z}_a, \quad (30a)$$

$$\vec{H}_{\text{FF},i} = H_{\text{FF},x,i} \hat{x}_a + H_{\text{FF},y,i} \hat{y}_a + H_{\text{FF},z,i} \hat{z}_a, \quad (30b)$$

where the Cartesian components are found with:

$$\begin{pmatrix} E_{\text{FF},x,i} \\ E_{\text{FF},y,i} \\ E_{\text{FF},z,i} \end{pmatrix} = \begin{pmatrix} \cos \theta_i \cos \varphi_i & -\sin \varphi_i \\ \cos \theta_i \sin \varphi_i & \cos \varphi_i \\ -\sin \theta_i & 0 \end{pmatrix} \begin{pmatrix} E_\theta \\ E_\varphi \end{pmatrix}. \quad (31)$$

The same procedure is applied to the \vec{H}_{FF} field.

3.4. Change of Coordinates

The near field obtained with either (11) or (23) is referenced to the ACS. Moreover, to compute the near field following the equations derived in the previous subsections, the point in space $\vec{r} = (x, y, z)$ must also be expressed in the ACS. However, the goal is to obtain the near field in the NFCS, since the array may be rotated with regard to the desired local coordinate system (for instance, if the reflectarray is placed on a wall, and it is desired to provide indoor coverage on a table).

In general, the coordinates of the points where the near field is to be computed will be initially given in the NFCS. Thus, in order to compute the near field with (11) and (23), these coordinates need to be transformed from the NFCS to the ACS as detailed in Appendix A. Then, after the near field is computed in the ACS, it needs to be transformed to the NFCS as follows:

$$\vec{E}_{\text{NF}}(\vec{r}) \Big|_{\text{NFCS}} = T \vec{E}_{\text{NF}}(\vec{r}) \Big|_{\text{ACS}}, \quad (32a)$$

$$\vec{H}_{\text{NF}}(\vec{r}) \Big|_{\text{NFCS}} = T \vec{H}_{\text{NF}}(\vec{r}) \Big|_{\text{ACS}}, \quad (32b)$$

where T is defined in Appendix A, and $\vec{E}_{\text{NF}}(\vec{r}) \Big|_{\text{ACS}}$ and $\vec{H}_{\text{NF}}(\vec{r}) \Big|_{\text{ACS}}$ are the same as in (11) and (23).

3.5. Comparison of the Near Field Models

To compare the near field predicted by both models, let us consider a center-fed square planar transmitarray comprised of 60×60 elements in a regular grid of periodicity 3.84 mm^2 . The feed is modelled as a $\cos^q \theta$ function [29] with $q = 22$ and placed at $\vec{r}_f = (0, 0, -180) \text{ mm}$ in the ACS (see Figure 1). The working frequency is 39 GHz. For the analysis, the phases of the direct transmission coefficients in (4) are set to:

$$\angle \tau_{xx} = \angle \tau_{yy} = k_0(d_i - (x' \cos \varphi_0 + y' \sin \varphi_0) \sin \theta_0), \quad (33)$$

where d_i is the distance from the feed phase center to the i -th array element, and (θ_0, φ_0) is the pointing direction of the far field pencil beam defined by the phases of τ_{xx} and τ_{yy} . For the present example, (θ_0, φ_0) is set to $(0^\circ, 0^\circ)$.

The radiated near field will be calculated with the two models in planes parallel to the array with z constant and values $z = 0.1 \text{ m}, 1 \text{ m}$. Thus, the matrix of change of coordinates from the ACS to the NFCS is the identity. In addition, in the case of the model based on the radiation equations, it will be evaluated for several values of N_x and N_y , specifically for $N_x = N_y = 1, 3, 5$ to assess the convergence of the integrals. Finally, each plane is divided into a grid of 150×150 points (22,500 in total) where the near field is computed.

Figure 3 shows the main cuts in x for $y = 0$ for the near field component E_x in magnitude and phase for both z planes. The agreement between both models is in general very good. In the case of the magnitude, the model based on the radiation equations with $N_x = N_y = 1$ presents some discrepancies in the plane $z = 0.1 \text{ m}$ with the rest of the models, albeit for very low values, 60 dB lower than the peak magnitude. In the case of the phase, the model based on the superposition of the far field radiated by each array element presents a small discrepancy in the plane $z = 0.1 \text{ m}$. In this case, the shape of the phase is the same as in the other models, but it has a shift of approximately 1.3 deg . Both discrepancies disappear when the field is calculated further away from the array.

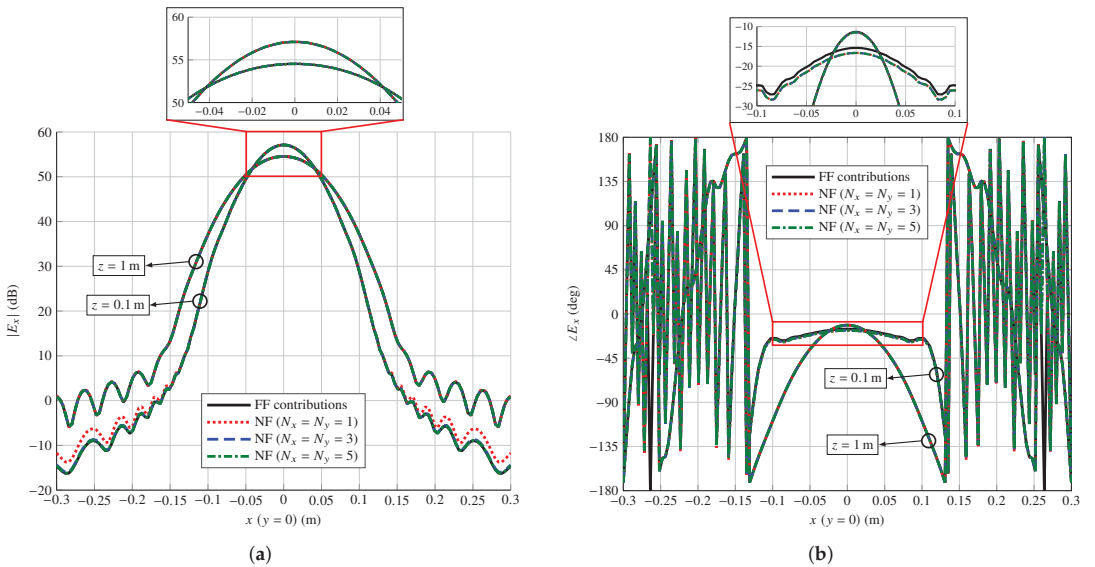


Figure 3. Comparison of the near field radiated by a center-fed transmitarray in (a) magnitude and (b) phase at the different z planes as calculated by the near field model based on the superposition of far field (FF) contributions of each array element, and the near field (NF) model based on the radiation equations for different values of N_x and N_y to assess the convergence in the numerical evaluation of the double integrals. Near field is plotted in the NFCS.

Figure 4 shows the magnitude and phase of the field components E_x and E_y as calculated by the models based on far field superposition (top row) and the radiation equations with $N_x = N_y = 5$ (bottom row) for the plane $z = 0.1$ m. As can be seen, visually the results are practically the same.

A better way of assessing the similarities between both models is to compute the relative error in the calculated near fields. To that end, the following expression is employed:

$$\text{RE} = 100 \frac{\left\| E_{x|y|z} - \tilde{E}_{x|y|z} \right\|}{\left\| E_{x|y|z} \right\|}, \quad (34)$$

where $\|\cdot\|$ is the Euclidean norm; E is one component of the near field computed with the model based on the radiation equations with $N_x = N_y = 5$, which is considered as reference to compute the relative error in percentage; and \tilde{E} is the same component of the near field computed with any other model. Table 1 shows the relative error for both models. It shows the relative errors for the three components of the near field for both planes. In the case of the model based on the radiation equations, even a value of $N_x = N_y = 1$ shows a sufficiently low error. As the near field is computed further away from the array, the error decreases. The use of $N_x = N_y = 1$ means that the double integrals in (15) are just evaluated at the center of the array element, i.e., considering only one sample, effectively reducing the triple summation in (21) to a single sum, considerably accelerating computations without barely affecting accuracy in the prediction of the near field. In the case of the near field model based on the superposition of the far fields radiated by each array element, the relative error is slightly larger, and it also decreases as the near field is computed further away from the array. However, even for a plane at $z = 0.1$ m, which is 13λ at the working frequency, the error is very low.

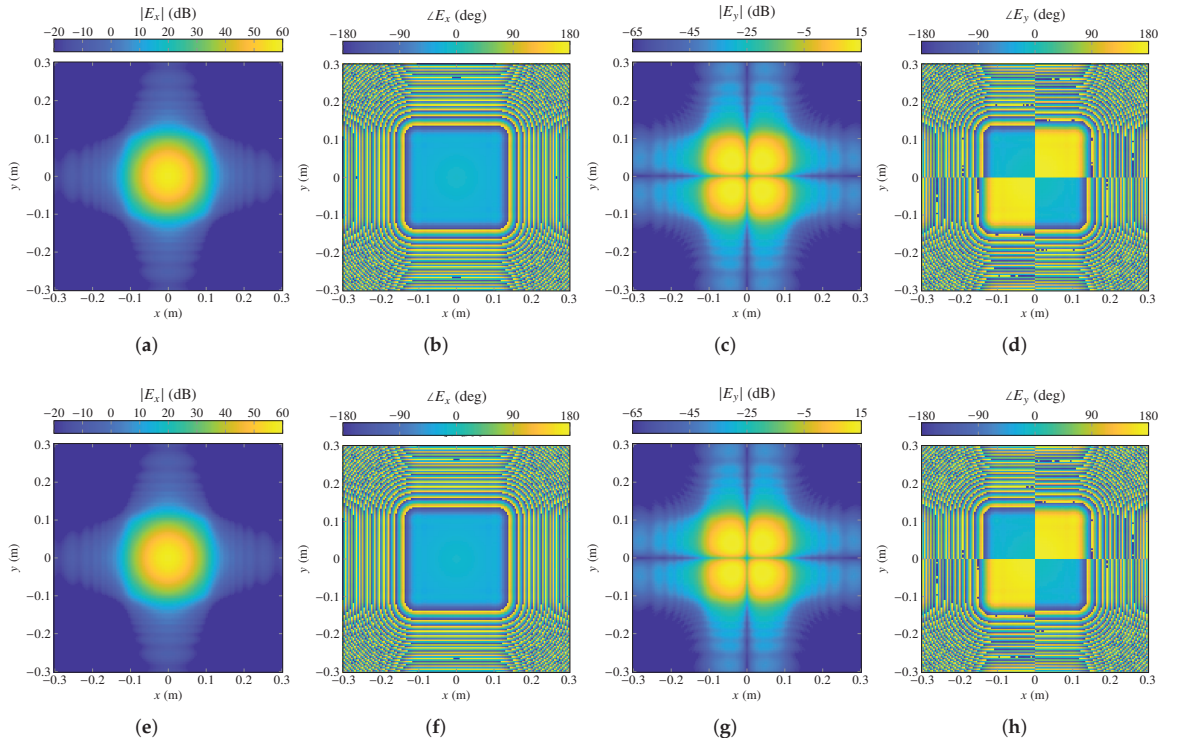


Figure 4. Comparison of the near field radiated by a center-fed transmitarray in magnitude and phase for the plane $z = 0.1$ m generated by the model based on the superposition of far field contributions of each array element (**top row**), and the near field model based on the radiation equations for $N_x = N_y = 5$ (**bottom row**). The relative error between both simulations taking the bottom row as reference is 2.2% for both components of the field. Near field is plotted in the NFCS.

Table 1. Relative error of the field components calculated with the different near field models when compared with the model based on the radiation equations with $N_x = N_y = 5$, which is taken as reference.

	$z = 0.1$ m			$z = 1$ m		
	E_x	E_y	E_z	E_x	E_y	E_z
FF contributions	2.22%	2.21%	3.20%	0.22%	0.22%	0.32%
NF ($N_x = N_y = 1$)	0.09%	0.33%	3.10%	0.06%	0.14%	0.15%
NF ($N_x = N_y = 3$)	0.01%	0.02%	0.18%	0.00%	0.01%	0.01%

In light of these results, it is clear that both models offer practically the same results in the computation of the near field for spatially fed planar arrays. However, from a computational point of view, the model based on the superposition of far fields is more interesting. Indeed, as shown in Table 2, this model is at least one order of magnitude faster than the model based on the radiation equations. This is particularly important when employing the model in optimization procedures to shape the near field, since the analysis routine where the near field is computed is invoked many times. Then, the model based on the radiation equations could be used, if desired, to assess the validity of the results that were obtained employing the approximate model based on superposition of the far fields radiated by the array elements.

Table 2. Computational performance of each algorithm in the computation of the near field in a total of 22,500 points employing an Intel i9-9900 CPU working at 3.1 GHz. Computations are parallelized with OpenMP [30].

Model	Time (s)
FF contributions	1.40
NF ($N_x = N_y = 1$)	24.65
NF ($N_x = N_y = 3$)	168.45
NF ($N_x = N_y = 5$)	455.89

4. Wideband near Field Shaping with Application to Indoor Femtocell Coverage

4.1. Scenario Definition and Antenna Specifications

As an example of application of the developed models for near field beam-shaping, let us consider the scenario depicted in Figure 5, where the goal is to provide coverage on top of an office desktop. The coverage area is a rectangle of dimensions $0.9 \times 0.5 \text{ m}^2$ on the right side of the table. The reflectarray that provides the coverage is placed on the ceiling, at a distance of 2 m from the center of the coverage area, while the feed is placed on a shelf to illuminate the reflectarray. The goal is to achieve a maximum magnitude ripple in the coverage area of 2 dB in the whole 5G NR n257 band (26.5–29.5 GHz) in dual-linear polarization.

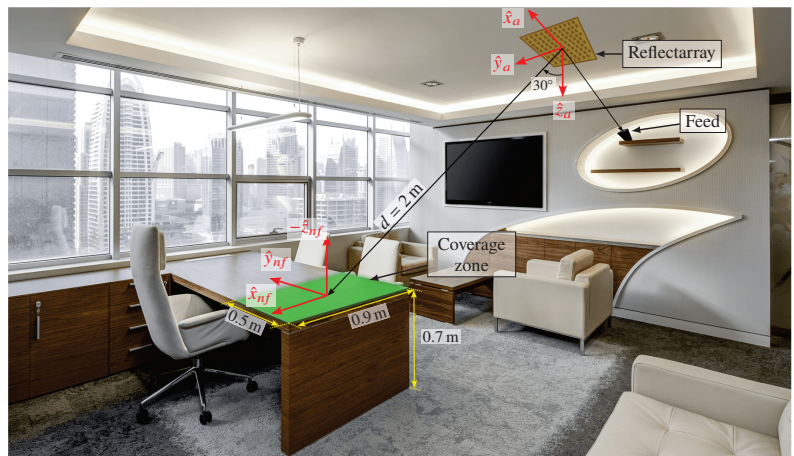


Figure 5. Proposed scenario for indoor femtocell coverage. A reflectarray provides a coverage on top of an office desktop with a maximum desired magnitude ripple of 2 dB. Picture adapted from [31].

The considered reflectarray is square and comprised of $N = 1936$ elements in a regular grid of 44×44 . The periodicity is 5.35 mm in both dimensions, which is approximately half a wavelength at the central frequency of operation, 28 GHz. The phase center of the feed is placed at $\vec{r}_f = (-0.16, 0, 0.24) \text{ m}$ with regard to the reflectarray center and generates an average edge illumination taper between -14.7 dB and -16.5 dB in the range 26.5–29.5 GHz.

4.2. Unit Cell Characterization

In order to be able to successfully perform a wideband direct layout optimization, the chosen unit cell should be able to provide a large enough phase-shift range as well as enough degrees of freedom for the optimization. In this regard, a unit cell comprised of only one rectangular patch would not provide enough phase-shift and degrees of freedom for its use in a wideband optimization procedure [32]. However, by stacking two rectangular patches, the range of the phase-shift can be increased. Thus, the chosen unit cell consists

of two stacked rectangular patches backed by a ground plane as shown in Figure 6a. Both layers employ the same substrate, the Rogers DiClad 870 with relative permittivity $\epsilon_r = 2.33$, loss tangent $\tan \delta = 0.005$, and thickness $h = 30$ mil. A CuClad 6250 bonding film between the two layers with the same electrical characteristics as the DiClad 870 is considered in the simulations. The substrate has been chosen such that a large enough phase-shift range is achieved.

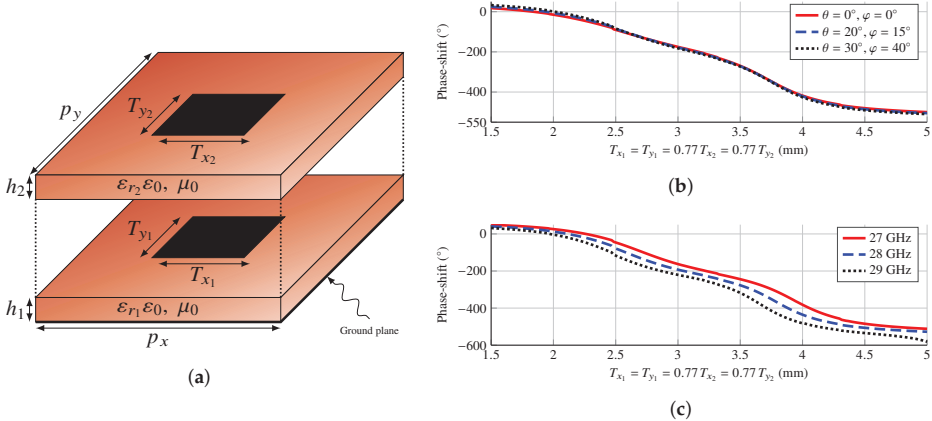


Figure 6. (a) Sketch of the employed unit cell, consisting of two stacked rectangular patches backed by a ground plane. The periodicity is $p_x = p_y = 5.35$ mm, and both layers use the same substrate from Rogers Co., DiClad 870 with thickness of 30 mil; (b) phase response of the unit cell for normal and oblique incidence, showing that the unit cell response is stable with the angle of incidence; (c) phase response of the unit cell for three different frequencies for oblique incidence with $(\theta = 40^\circ, \varphi = 30^\circ)$.

For the initial layout design after the POS (see Section 4.3), a fixed relative size of the stacked patches is kept, with $T_{x_1} = 0.77 T_{x_2}$ and $T_{y_1} = 0.77 T_{y_2}$. The scaling factors were found after performing a parametric study to obtain a smooth variation of the phase-shift for $T_{x_1} = T_{y_1}$ at several frequencies and angles of incidence. Figure 6b shows the phase response of the unit cell at 28 GHz for normal and oblique incidence. The total phase-shift provided by the cell with the selected substrate is around 500° , and it can be seen that it is stable with the angle of incidence. Conversely, Figure 6c shows the unit cell phase response at three different frequencies for oblique incidence with $(\theta = 40^\circ, \varphi = 30^\circ)$. From these curves, it can be seen that the unit cell also provides around 500° of phase-shift at several frequencies, making it suitable for a multi-frequency optimization.

4.3. Phase-Only Synthesis at 28 GHz

Figure 7 shows the proposed wideband near field optimization strategy for spatially fed array antennas. It is divided into several stages in order to facilitate convergence towards a suitable solution. After defining the antenna and near field specifications, a phase-only synthesis is carried out at central frequency. Afterwards, the geometrical features of the unit cell are tuned so each element produces the desired phase-shift obtained from the POS. After this point, the near field radiated by the antenna closely complies with the specifications at central frequency. However, due to the narrow bandwidth nature of planar spatially fed arrays, it does not comply at other frequencies. Thus, this initial layout is used in a multi-stage direct layout optimization (DLO) at several frequencies, finally obtaining an optimized wideband layout. To obtain an array working in dual-linear polarization, the POS is carried out independently for both polarizations, while the DLO is performed considering specifications in both polarizations simultaneously.

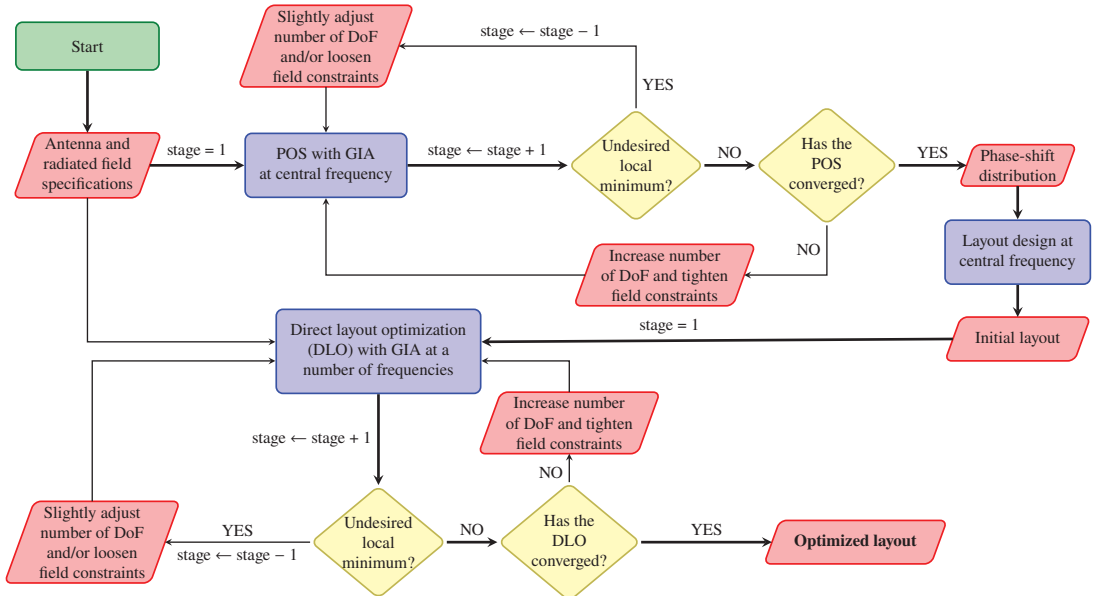


Figure 7. Proposed wideband optimization strategy for spatially fed arrays using the generalized intersection approach (GIA). First, a phase-only synthesis (POS) at central frequency is carried out in order to obtain a phase-shift distribution from which the initial layout is obtained. Then, the layout is used in a direct layout optimization (DLO) at multiple frequencies until specifications are met.

For the POS, the generalized intersection approach (GIA) [33] will be employed. The POS assumes an ideal phase-shifter simplification in matrix M_i , in which there are no losses ($|\rho_{xx,i}| = |\rho_{yy,i}| = 1$ for reflectarrays, or $|\tau_{xx,i}| = |\tau_{yy,i}| = 1$ for transmitarrays) and no cross-polarization ($\rho_{xy,i} = \rho_{yx,i} = 0$ for reflectarrays, or $\tau_{xy,i} = \tau_{yx,i} = 0$ for transmitarrays). In this way, only the phases of the direct coefficients are considered as optimization variables. Once the POS has converged to a near field that complies (or it is close to compliance) with the imposed specifications at central frequency, the sizes of the rectangular patches of the unit cell are adjusted such that the unit cell provides the required phase-shift that was obtained in the POS. This procedure can be summarized as follows. First, and for each reflectarray element, two phase shift tables are generated independently for each polarization. Then, the dimensions of the rectangular patches are adjusted using a linear equation. Finally, a zero-finding routine is employed to adjust both dimensions at the same time. During this process, a fixed relative size between the stacked patches is kept, $T_{x_1} = 0.77T_{x_2}$ and $T_{y_1} = 0.77T_{y_2}$. Further details on the GIA applied to POS may be found in [21,33].

Since the employed algorithm is a local optimizer, the starting point of the optimization is very important. Thus, the starting phase-shift distribution will be such that it provides a focused near field at the center of the coverage zone. To that end, the conjugate-phase approach [34] is employed, which establishes that the phase of the field at the aperture should be:

$$\angle \vec{E}_{ap,i} = k_0 |\vec{r} - \vec{r}'_i|, \quad (35)$$

for $i = 1, \dots, N$. On the other hand, the phase of the field at the aperture is also equal to the phase introduced by the unit cell plus the phase of the incident field from the feed [32]:

$$\angle \vec{E}_{ap,i} = -k_0 d_i + \angle \rho, \quad (36)$$

where d_i is the distance from the feed phase center to the i -th unit cell, and ρ is a direct reflection coefficient (either ρ_{xx} or ρ_{yy} , depending on the polarization). Thus, by combining (35) and (36), we can obtain the phase-shift introduced by each reflectarray element to focus the near field at a point $\vec{r} = (x, y, z)$:

$$\angle\rho = k_0(d_i + |\vec{r} - \vec{r}_i'|) = k_0\left(d_i + \sqrt{(x - x_i)^2 + (y - y_i)^2 + z^2}\right). \quad (37)$$

Figure 8a shows the focused near field for linear polarization X when the phases in (37) are implemented. The magnitude of the field is concentrated in the middle of the coverage zone, but it presents an important drop towards the edges of the coverage zone. Indeed, the ripple in this case is 48 dB for polarization X and 38 dB for polarization Y. After the POS is completed, a phase-shift distribution is obtained such that the ripple is considerably reduced at 28 GHz. A layout is obtained from this phase-shift distribution by following the steps described above and in [23] and using the MoM-LP described in [35]. When this layout is simulated, the near field shown in Figure 8b is obtained. As can be seen, the near field presents a more uniform distribution in the coverage area when compared to that of the starting point of the POS shown in Figure 8a. Now, the ripple for polarizations X and Y is 2.66 dB and 2.48 dB, respectively. Although it does not comply with the specifications of a maximum ripple of 2 dB, it is a net improvement over the starting point.

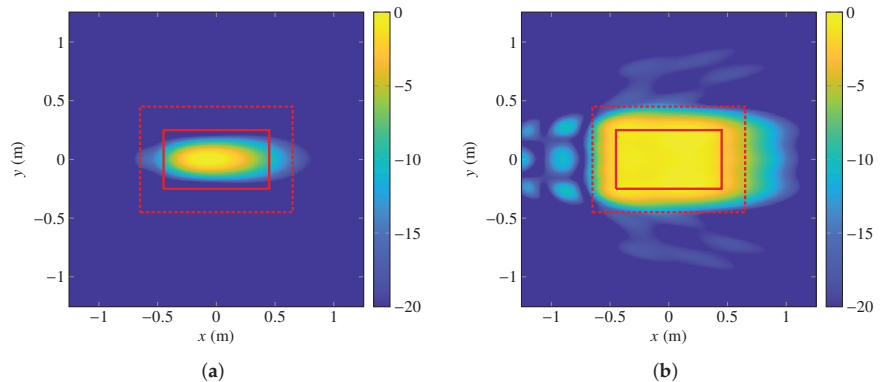


Figure 8. Normalized magnitude of the electric field (a) for the starting point of the POS and (b) the result of the POS simulated with a MoM-LP at 28 GHz. Coverage zone is represented by a solid red line and transition zone by a dashed red line. Near field is plotted in the NFCS.

However, we are also interested in the performance in the 5G NR n257 band (26.5–29.5 GHz). To that end, Table 3 gathers the results at seven equispaced frequencies, showing the maximum achieved ripple as well as the percentage of the coverage area that complies with a 1 dB, 2 dB, or 3 dB ripple. As can be seen, the best results are obtained at the frequency of design, 28 GHz. For frequencies 500 MHz above and below 28 GHz, the results deteriorate slightly. However, as the frequency moves further away from the design one, the results quickly worsen, showing the narrow bandwidth behaviour of the reflectarray antenna and the need for a wideband optimization.

Table 3. Performance of the layout obtained after a POS at 28 GHz in the whole 5G NR n257 band. X dB (%) indicates what percentage of the coverage area complies with a ripple of X dB.

Frequency (GHz)	Polarization X				Polarization Y			
	Ripple (dB)	1 dB (%)	2 dB (%)	3 dB (%)	Ripple (dB)	1 dB (%)	2 dB (%)	3 dB (%)
26.5	5.34	42.45	63.35	82.03	5.92	30.40	58.80	78.97
27.0	3.79	47.17	71.23	98.79	3.97	43.83	73.20	98.45
27.5	2.53	43.63	93.75	100	2.53	48.57	89.96	100
28.0	2.66	51.28	96.44	100	2.48	45.14	99.10	100
28.5	3.74	58.82	86.04	96.40	3.58	52.70	90.61	98.49
29.0	6.39	33.76	54.02	81.71	5.03	54.69	81.71	89.96
29.5	9.19	26.42	44.32	57.55	7.37	37.15	63.18	77.81

4.4. Multi-Frequency Optimization of the Near Field

The multi-frequency optimization of the near field consists in a direct layout optimization using the GIA [21]. To accommodate specifications at a number of frequencies, the cost function (F) in the backward projector of the GIA is modified in the following fashion [36]:

$$F_{\Omega} = \sum_{f=1}^{N_f} \sum_{l=1}^L w_f(\vec{r}_l) \left(\left| \vec{E}_{\text{NF},f}(\vec{r}_l) \right|^2 - \left| \tilde{\vec{E}}_{\text{NF},f}(\vec{r}_l) \right|^2 \right)^2 \Delta\Omega, \quad (38)$$

where Ω is the region where the near field is computed; N_f is the total number of frequencies at which the direct layout optimization is performed; L is the number of points in which the region Ω is discretized; w_f is a weighting function that depends on the frequency and observation point \vec{r}_l ; $\vec{E}_{\text{NF},f}(\vec{r}_l)$ is the computed near field at each iteration of the GIA and frequency; $\tilde{\vec{E}}_{\text{NF},f}(\vec{r}_l)$ is the reference near field in region Ω resulting from applying the specification templates at a given frequency; and $\Delta\Omega$ is the step of the discretization. Further details on the specifics of the optimization algorithm may be consulted elsewhere [21].

Unlike in POS, where the optimizing variables (sometimes also referred to as degrees of freedom or DoF) were the phases of the direct coefficients, the direct layout optimization employs the geometrical features of the unit cell as optimizing variables. In the present case, the dimensions of the rectangular patches are employed, T_{x_1} , T_{x_2} , T_{y_1} , and T_{y_2} (see Figure 6). Thus, a total of 7744 DoF are available for the optimization. Moreover, the direct layout optimization will be carried out in several stages in order to facilitate convergence towards a suitable solution. First, only variables T_{x_1} , and T_{x_2} will be considered at three frequencies, 27 GHz, 28 GHz and 29 GHz. In the second stage, the near field is optimized at the same three frequencies, but this time only considering as variables T_{y_1} and T_{y_2} . Finally, in the third stage, all four variables per element are used in the optimization at the same seven frequencies of Table 3. In all stages, the specifications for both linear polarizations are imposed. In addition, the MoM-LP tool is directly employed in the optimization loop to obtain the real electromagnetic response of the unit cell at each considered frequency. In order to accelerate computations, the differential contributions technique [37] is used.

The improvement in the coverage zone can be visually seen in Figure 9, where the normalized magnitude of the electric field for linear polarization X is represented at three different frequencies (26.5 GHz, 28 GHz, and 29.5 GHz) before and after the direct layout optimization. The field is only plotted at those points that comply with the requirement of 2 dB of ripple. Although the starting layout does not radiate a near field that fully complies with specifications at 28 GHz, Figure 9b shows that most of the coverage zone does comply, and only at one edge is the ripple higher than 2 dB, demonstrating the successful optimization carried out by the POS. However, due to the intrinsic narrow bandwidth behaviour of the reflectarray, at other frequencies, it does not comply. Nevertheless, after the direct layout optimization, in which the sizes of the two stacked rectangular patches are

directly optimized, the antenna is able to provide full coverage in the designated area with a maximum ripple lower than 2 dB.

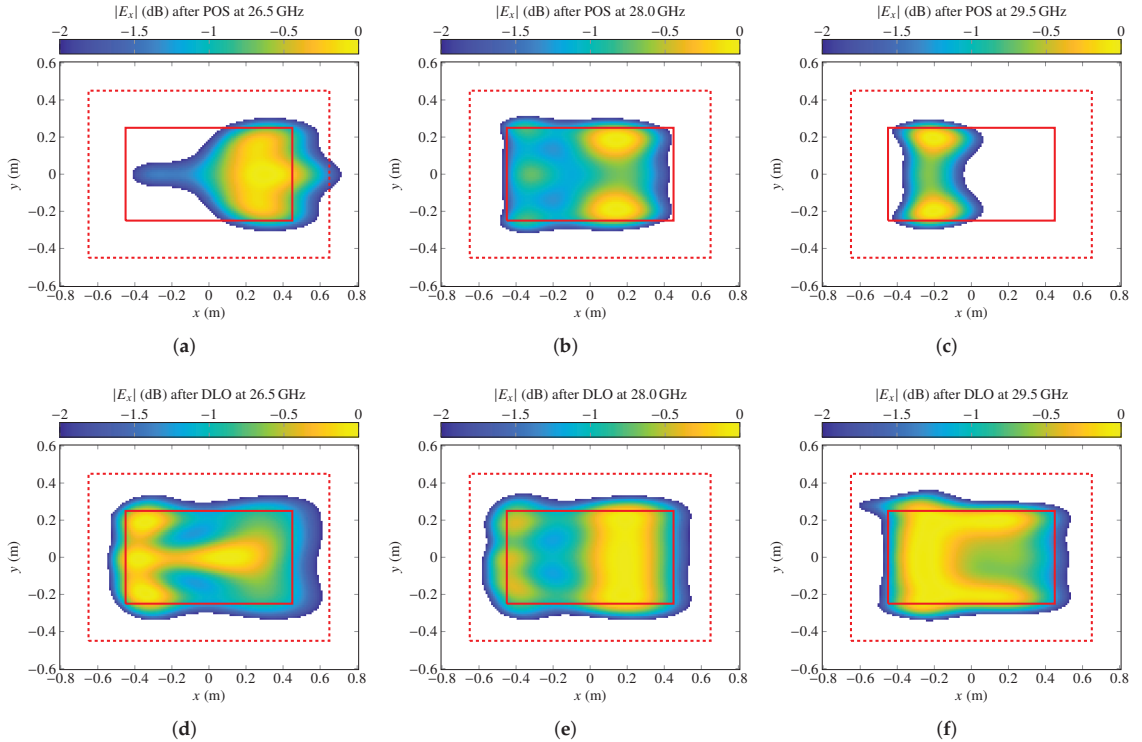


Figure 9. Representation of the normalized electric field magnitude for linear polarization X that complies with a ripple of 2 dB at 26.5 GHz (left column), 28 GHz (middle column), and 29.5 GHz (right column) generated by the layout obtained after the POS (top row) and after the direct layout optimization (DLO) with the GIA (bottom row). Coverage zone is represented by a solid red line and transition zone by a dashed red line. Near field is plotted in the NFCS.

Table 4 gathers the performance of the optimized layout at seven equispaced frequencies covering the whole 5G NR n257 band. Now, a compliance of 100% is achieved in the whole band for a ripple of 2 dB. Indeed, the worst achieved ripple is 1.5 dB at 29.5 GHz for polarization X. When compared with the results shown in Table 3, the worst ripple has been reduced more than 7.5 dB, and even the compliance for a ripple of 1 dB, although not considered a requirement, has improved from the lowest value of 26.4% for polarization X at 29.5 GHz to 76.7% for polarization X at 28.5 GHz. In the case of the 2 dB compliance columns, the minimum value before the direct layout optimization was 44.3%, which was improved to a 100% compliance after a successful wideband optimization.

Table 4. Performance of the optimized layout in the whole 5G NR n257 band. X dB (%) indicates what percentage of the coverage area complies with a ripple of X dB.

Frequency (GHz)	Polarization X				Polarization Y			
	Ripple (dB)	1 dB (%)	2 dB (%)	3 dB (%)	Ripple (dB)	1 dB (%)	2 dB (%)	3 dB (%)
26.5	1.30	80.89	100	100	0.82	100	100	100
27.0	1.03	99.63	100	100	0.84	100	100	100
27.5	1.08	95.63	100	100	0.96	100	100	100
28.0	1.23	84.90	100	100	0.96	100	100	100
28.5	1.26	76.73	100	100	1.02	99.07	100	100
29.0	1.25	96.72	100	100	1.16	93.67	100	100
29.5	1.50	89.05	100	100	1.49	90.52	100	100

4.5. Discussion

The proposed wideband near field beam-shaping technique was able to achieve a maximum ripple of 1.5 dB in the whole 5G NR n257 band, corresponding to a 10.7% relative bandwidth. It is worth mentioning that specifications have been met employing a unit cell consisting of two stacked rectangular microstrip patches backed by a ground plane, offering up to four degrees of freedom to perform a direct layout optimization. However, bandwidth could be further improved by employing a more suitable unit cell. For instance, the three stacked patches configuration is known to offer higher bandwidth of operation than only two layers [38]. Alternatively, a unit cell comprised of two layers of parallel and coplanar dipoles is known to be able to offer, after a direct layout optimization, relative bandwidths of up to 20% [36]. When applied to near field beam-shaping, this would allow offering coverage in both the n257 and n258 bands, covering from 24.25 GHz up to 29.5 GHz, which represents 19.5% of relative bandwidth. Additionally, even though the use of a MoM-LP tool directly in the optimization loop penalizes computational performance to achieve wideband results, some techniques could be employed to accelerate the process. In this work, the differential contributions technique [37] was used to accelerate some building blocks of the GIA. However, the unit cell analysis could also be sped up by substituting the MoM-LP with a database of reflection coefficients [39] or the use of machine learning techniques [40].

5. Conclusions

This work has presented two near field models for the analysis of spatially fed array antennas, namely, reflectarrays and transmitarrays. The first model is based on the direct application of the radiation equations directly derived from the A and F vector potentials. The volumetric integrals are particularized for a planar array discretized into a number of rectangular unit cells, and thus they are reduced to a summation of a double integral over each unit cell. In turn, this integral is numerically evaluated by a quadrature method, for instance, the mid point quadrature. The second model is based on the superposition of the far field radiated by each array element. The far field is computed using Love's principle of equivalence assuming a constant field at each unit cell. Both near field models were compared by computing the field radiated by a transmitarray antenna. For the model based on the radiation equations, the near field was also computed for several discretizations of the unit cell for the numerical computation of the double integrals. Both models provide very similar results. When the model based on the radiation equations is used as reference, the relative error in the radiated field obtained with the other model quickly drops as the field is computed further away from the array. With relative errors lower than 3% in the computed tangential near field at 13λ or further from the array, the model is effectively validated for subsequent use in optimization algorithms for near field beam-shaping.

Then, the model based on far field superposition was applied to perform near field beam-shaping. The considered scenario is aimed at providing indoor coverage in an office for mm-Wave 5G NR networks in the n257 band. The proposed wideband near field opti-

mization strategy is composed of several stages to facilitate convergence towards a suitable solution. First, a phase-only synthesis (POS) was carried out to obtain a reflectarray layout that provides coverage at central frequency (28 GHz). Due to the narrow bandwidth nature of spatially fed planar array antennas, poor compliance is achieved at other frequencies within the n257 band. Thus, a multi-frequency optimization was then carried out employing a method of moments based on local periodicity (MoM-LP) directly in the optimization loop along with the near field model. The cost function of the optimization algorithm was modified to include requirements at several frequencies in the near field region of interest. At the same time, the optimization was carried out in several stages, gradually increasing the number of DoF to improve convergence. Eventually, the optimized antenna complied with the imposed specifications, achieving a magnitude ripple equal or lower than 1.5 dB in the whole 5G NR n257 band, corresponding to a 10.7% relative bandwidth, showing the suitability of the proposed methodology for the wideband near field beam-shaping of spatially fed arrays.

Funding: This work was supported in part by the Ministerio de Ciencia, Innovación y Universidades under project IJC2018-035696-I; by the Ministerio de Ciencia e Innovación and the Agencia Estatal de Investigación within project ENHANCE-5G (PID2020-114172RB-C21/AEI/10.13039/501100011033); by Gobierno del Principado de Asturias under project AYUD/2021/51706.

Institutional Review Board Statement: Not applicable.

Informed Consent Statement: Not applicable.

Data Availability Statement: Not applicable.

Acknowledgments: The author would like to thank J. A. Encinar for providing the MoM-LP software.

Conflicts of Interest: The author declares no conflict of interest.

Abbreviations

The following abbreviations are used in this manuscript:

5G NR	Fifth generation new radio
ACS	Array coordinate system
DLO	Direct layout optimization
DoF	Degrees of freedom
FF	Far field
FFT	Fast Fourier transform
FR	Frequency Range
GIA	Generalized intersection approach
MoM-LP	Method of moments based on local periodicity
NF	Near field
NFCS	Near field coordinate system
POS	Phase-only synthesis

Appendix A

Computations of the radiated field by the array were carried out in the ACS ($\hat{x}_a, \hat{y}_a, \hat{z}_a$). However, the final field must be expressed in the NFCS ($\hat{x}_{nf}, \hat{y}_{nf}, \hat{z}_{nf}$). In general, the rotation of the NFCS with regard to the ACS can be expressed by three angles, θ , φ , and ψ , as described in [41]. The definition of θ and φ in spherical coordinates is the usual, while ψ defines a rotation around axis \hat{z}_2 , as shown in Figure A1.

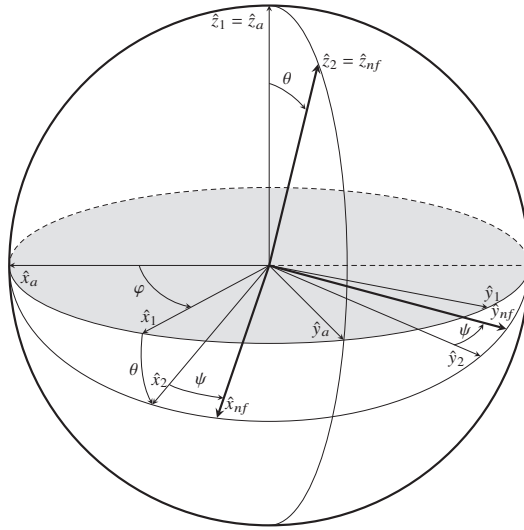


Figure A1. Rotation of the array coordinate system (ACS) $(\hat{x}_a, \hat{y}_a, \hat{z}_a)$ to obtain the near field coordinate system (NFCS) $(\hat{x}_{nf}, \hat{y}_{nf}, \hat{z}_{nf})$. This rotation is specified by angles θ , φ , and ψ .

The unit vectors of the rotated coordinate system are defined as [41]:

$$\hat{x}_{nf} = \hat{\theta} \cos(\varphi - \psi) - \hat{\varphi} \sin(\varphi - \psi), \quad (\text{A1a})$$

$$\hat{y}_{nf} = \hat{\theta} \sin(\varphi - \psi) + \hat{\varphi} \cos(\varphi - \psi), \quad (\text{A1b})$$

$$\hat{z}_{nf} = \hat{r}, \quad (\text{A1c})$$

where

$$\hat{\theta} = \hat{x}_a \cos \theta \cos \varphi + \hat{y}_a \cos \theta \sin \varphi - \hat{z}_a \sin \theta, \quad (\text{A2a})$$

$$\hat{\varphi} = -\hat{x}_a \sin \varphi + \hat{y}_a \cos \varphi, \quad (\text{A2b})$$

$$\hat{r} = \hat{x}_a \sin \theta \cos \varphi + \hat{y}_a \sin \theta \sin \varphi + \hat{z}_a \cos \theta. \quad (\text{A2c})$$

Substituting (A2) into (A1) yields:

$$\begin{aligned} \hat{x}_{nf} &= \hat{x}_a [\cos \theta \cos \varphi \cos(\varphi - \psi) + \sin \varphi \sin(\varphi - \psi)] + \\ &\quad \hat{y}_a [\cos \theta \sin \varphi \cos(\varphi - \psi) - \cos \varphi \sin(\varphi - \psi)] - \\ &\quad \hat{z}_a \sin \theta \cos(\varphi - \psi), \end{aligned} \quad (\text{A3a})$$

$$\begin{aligned} \hat{y}_{nf} &= \hat{x}_a [\cos \theta \cos \varphi \sin(\varphi - \psi) - \sin \varphi \cos(\varphi - \psi)] + \\ &\quad \hat{y}_a [\cos \theta \sin \varphi \cos(\varphi - \psi) - \cos \varphi \sin(\varphi - \psi)] - \\ &\quad \hat{z}_a \sin \theta \sin(\varphi - \psi), \end{aligned} \quad (\text{A3b})$$

$$\hat{z}_{nf} = \hat{x}_a \sin \theta \cos \varphi + \hat{y}_a \sin \theta \sin \varphi + \hat{z}_a \cos \theta. \quad (\text{A3c})$$

Then, if $\vec{r}_a = (x, y, z)_{\text{ACS}}$ is a point in the ACS, and $\vec{r}_{nf} = (x, y, z)_{\text{NFCS}}$ is the same point in the NFCS, the matrix of change of coordinates from the ACS to the NFCS is:

$$\vec{r}_{nf} = T \vec{r}_a, \quad (\text{A4})$$

with:

$$T = \begin{pmatrix} \hat{x}_{nf} \cdot \hat{x}_a & \hat{x}_{nf} \cdot \hat{y}_a & \hat{x}_{nf} \cdot \hat{z}_a \\ \hat{y}_{nf} \cdot \hat{x}_a & \hat{y}_{nf} \cdot \hat{y}_a & \hat{y}_{nf} \cdot \hat{z}_a \\ \hat{z}_{nf} \cdot \hat{x}_a & \hat{z}_{nf} \cdot \hat{y}_a & \hat{z}_{nf} \cdot \hat{z}_a \end{pmatrix}. \quad (\text{A5})$$

Conversely, to perform a change of coordinates from the NFCS to the ACS we can calculate:

$$\vec{r}_a = T^T \vec{r}_{nf}, \quad (\text{A6})$$

where T^T is the transpose of T , which is an orthogonal matrix, i.e., $T^T = T^{-1}$.

References

1. Ly, A.; Yao, Y.D. A Review of Deep Learning in 5G Research: Channel Coding, Massive MIMO, Multiple Access, Resource Allocation, and Network Security. *IEEE Open J. Commun. Soc.* **2021**, *2*, 396–408.
2. Boccardi, F.; Heath, R.W.; Lozano, A.; Marzetta, T.L.; Popovski, P. Five disruptive technology directions for 5G. *IEEE Commun. Mag.* **2014**, *52*, 74–80. [CrossRef]
3. Attaran, M. The impact of 5G on the evolution of intelligent automation and industry digitization. *J. Ambient Intell. Humaniz. Comput.* **2021**. [CrossRef]
4. Gohar, A.; Nencioni, G. The Role of 5G Technologies in a Smart City: The Case for Intelligent Transportation System. *Sustainability* **2021**, *13*, 5188. [CrossRef]
5. Wijethilaka, S.; Liyanage, M. Survey on Network Slicing for Internet of Things Realization in 5G Networks. *IEEE Commun. Surv. Tutor.* **2021**, *23*, 957–994. [CrossRef]
6. Arrubla-Hoyos, W.; Ojeda-Beltrán, A.; Solano-Barliza, A.; Rambauth-Ibarra, G.; Barrios-Ulloa, A.; Cama-Pinto, D.; Arrabal-Campos, F.M.; Martínez-Lao, J.A.; Cama-Pinto, A.; Manzano-Agugliaro, F. Precision Agriculture and Sensor Systems Applications in Colombia through 5G Networks. *Sensors* **2022**, *22*, 7295. [CrossRef]
7. Szalay, Z.; Ficzere, D.; Tihanyi, V.; Magyar, F.; Soós, G.; Varga, P. 5G-Enabled Autonomous Driving Demonstration with a V2X Scenario-in-the-Loop Approach. *Sensors* **2020**, *20*, 7344. [CrossRef]
8. Rischke, J.; Sossalla, P.; Itting, S.; Fitzek, F.H.P.; Reisslein, M. 5G Campus Networks: A First Measurement Study. *IEEE Access* **2021**, *9*, 121786–121803. [CrossRef]
9. Hong, W.; Jiang, Z.H.; Yu, C.; Hou, D.; Wang, H.; Guo, C.; Hu, Y.; Kuai, L.; Yu, Y.; Jiang, Z.; et al. The Role of Millimeter-Wave Technologies in 5G/6G Wireless Communications. *IEEE J. Microw.* **2021**, *1*, 101–122. [CrossRef]
10. 3GPP. Technical Specification Group Radio Access Network; NR; User Equipment (UE) Radio Transmission and Reception; Part 2: Range 2 Standalone (Release 17); Technical Report; 3GPP: Sophia Antipolis, France, 2022. Available online: https://www.3gpp.org/ftp/Specs/archive/38_series/38.101-2/ (accessed on 6 October 2022).
11. Zheng, K.; Wang, D.; Han, Y.; Zhao, X.; Wang, D. Performance and Measurement Analysis of a Commercial 5G Millimeter-Wave Network. *IEEE Access* **2020**, *8*, 163996–164011. [CrossRef]
12. Poularakis, K.; Iosifidis, G.; Sourlas, V.; Tassiulas, L. Exploiting Caching and Multicast for 5G Wireless Networks. *IEEE Trans. Wirel. Commun.* **2016**, *15*, 2995–3007. [CrossRef]
13. Soleimani, B.; Sabbaghian, M. Cluster-Based Resource Allocation and User Association in mmWave Femtocell Networks. *IEEE Trans. Commun.* **2020**, *68*, 1746–1759. [CrossRef]
14. Nemat, M.; Park, J.; Choi, J. RIS-Assisted Coverage Enhancement in Millimeter-Wave Cellular Networks. *IEEE Access* **2020**, *8*, 188171–188185. [CrossRef]
15. Okogbaa, F.C.; Ahmed, Q.Z.; Khan, F.A.; Abbas, W.B.; Che, F.; Zaidi, S.A.R.; Alade, T. Design and Application of Intelligent Reflecting Surface (IRS) for Beyond 5G Wireless Networks: A Review. *Sensors* **2022**, *22*, 2436. [CrossRef]
16. Pérez-Adán, D.; Fresnedo, O.; González-Coma, J.P.; Castedo, L. Intelligent Reflective Surfaces for Wireless Networks: An Overview of Applications, Approached Issues, and Open Problems. *Electronics* **2021**, *10*, 2345. [CrossRef]
17. Imaz-Lueje, B.; Vaquero, A.F.; Prado, D.R.; Pino, M.R.; Arrebola, M. Shaped-Pattern Reflectarray Antennas for mm-Wave Networks Using a Simple Cell Topology. *IEEE Access* **2022**, *10*, 12580–12591. [CrossRef]
18. Martínez-De-Rioja, D.; Encinar, J.A.; Martínez-De-Rioja, E.; Vaquero, A.F.; Arrebola, M. A Simple Beamforming Technique for Intelligent Reflecting Surfaces in 5G Scenarios. In Proceedings of the International Workshop on Antenna Technology (iWAT), Dublin, Ireland, 16–18 May 2022; pp. 249–252. [CrossRef]
19. Loredo, S.; León, G.; Plaza, E.G. A Fast Approach to Near-Field Synthesis of Transmitarrays. *IEEE Antennas Wirel. Propag. Lett.* **2021**, *20*, 648–652. [CrossRef]
20. Vaquero, A.F.; Pino, M.R.; Arrebola, M. Evaluation of a transmit-array base station for mm-wave communications in the Fresnel region. In Proceedings of the IEEE International Symposium on Antennas and Propagation (AP-S), Denver, CO, USA, 10–15 July 2022; pp. 788–789. [CrossRef]
21. Prado, D.R. The Generalized Intersection Approach for Electromagnetic Array Antenna Beam-Shaping Synthesis: A Review. *IEEE Access* **2022**, *10*, 87053–87068. [CrossRef]

22. Loredo, S.; Plaza, E.G.; León, G. Fast Transmitarray Synthesis with Far-Field and Near-Field Constraints. *Sensors* **2022**, *22*, 4355. [CrossRef]
23. Prado, D.R.; López-Fernández, J.A.; Arrebola, M.; Pino, M.R.; Goussetis, G. General Framework for the Efficient Optimization of Reflectarray Antennas for Contoured Beam Space Applications. *IEEE Access* **2018**, *6*, 72295–72310. [CrossRef]
24. Vaquero, A.F.; Arrebola, M.; Pino, M.R. Bandwidth response of a reflectarray antenna working as a Compact Antenna Test Range probe. In Proceedings of the AMTA 41st Annual Meeting & Symposium, San Diego, CO, USA, 6–11 October 2019; pp. 1–6. Available online: <http://hdl.handle.net/10651/54227> (accessed on 9 September 2022).
25. Balanis, C.A. *Advanced Engineering Electromagnetics*, 2nd ed.; John Wiley & Sons: Hoboken, NJ, USA, 2012.
26. Stutzman, W.L.; Thiele, G.A. *Antenna Theory and Design*, 3rd ed.; John Wiley & Sons: Hoboken, NJ, USA, 2012.
27. Mittra, R.; Chan, C.H.; Cwik, T. Techniques for analyzing frequency selective surfaces—A review. *Proc. IEEE* **1988**, *76*, 1593–1615. [CrossRef]
28. Prado, D.R.; Arrebola, M.; Pino, M.R.; Las-Heras, F. An efficient calculation of the far field radiated by non-uniformly sampled planar fields complying Nyquist theorem. *IEEE Trans. Antennas Propag.* **2015**, *63*, 862–865. [CrossRef]
29. Lo, Y.T.; Lee, S.W. (Eds.) *Antenna Handbook*; Van Nostrand Reinhold: New York, NY, USA, 1993; Volume 1, Chapter 1, pp. 28–29.
30. Sato, M. OpenMP: Parallel programming API for shared memory multiprocessors and on-chip multiprocessors. In Proceedings of the 15th International Symposium on System Synthesis, Kyoto Japan, 2–4 October 2002; pp. 109–111. [CrossRef]
31. MagicDesk. Office Sitting Room Executive Business Desk. Available online: <https://pixabay.com/photos/office-sitting-room-executive-730681/> (accessed on 9 September 2022).
32. Huang, J.; Encinar, J.A. *Reflectarray Antennas*; John Wiley & Sons: Hoboken, NJ, USA, 2008.
33. Prado, D.R.; Arrebola, M.; Pino, M.R.; Las-Heras, F. Improved Reflectarray Phase-Only Synthesis Using the Generalized Intersection Approach with Dielectric Frame and First Principle of Equivalence. *Int. J. Antennas Propag.* **2017**, *2017*, 3829390. [CrossRef]
34. Nepa, P.; Buffi, A. Near-Field-Focused Microwave Antennas: Near-field shaping and implementation. *IEEE Antennas Propag. Mag.* **2017**, *59*, 42–53. [CrossRef]
35. Wan, C.; Encinar, J.A. Efficient computation of generalized scattering matrix for analyzing multilayered periodic structures. *IEEE Trans. Antennas Propag.* **1995**, *43*, 1233–1242. [CrossRef]
36. Prado, D.R.; Arrebola, M.; Pino, M.R.; Goussetis, G. Broadband Reflectarray with High Polarization Purity for 4K and 8K UHDTV DVB-S2. *IEEE Access* **2020**, *8*, 100712–100720. [CrossRef]
37. Prado, D.R.; Vaquero, A.F.; Arrebola, M.; Pino, M.R.; Las-Heras, F. Acceleration of Gradient-Based Algorithms for Array Antenna Synthesis with Far Field or Near Field Constraints. *IEEE Trans. Antennas Propag.* **2018**, *66*, 5239–5248. [CrossRef]
38. Encinar, J.A.; Zornoza, J.A. Three-layer printed reflectarrays for contoured beam space applications. *IEEE Trans. Antennas Propag.* **2004**, *52*, 1138–1148. [CrossRef]
39. Prado, D.R.; López-Fernández, J.A.; Arrebola, M. Efficient General Reflectarray Design and Direct Layout Optimization with a Simple and Accurate Database Using Multilinear Interpolation. *Electronics* **2022**, *11*, 191. [CrossRef]
40. Prado, D.R.; López-Fernández, J.A.; Arrebola, M.; Goussetis, G. Support Vector Regression to Accelerate Design and Crosspolar Optimization of Shaped-Beam Reflectarray Antennas for Space Applications. *IEEE Trans. Antennas Propag.* **2019**, *67*, 1659–1668. [CrossRef]
41. Pontoppidan, K. *GRASP9 Technical Description*; TICRA: Copenhagen, Denmark, 2008.

Article

Design of a mmWave Antenna Printed on a Thick Vehicle-Glass Substrate Using a Linearly Arrayed Patch Director and a Grid-Slotted Patch Reflector for High-Gain Characteristics

Changhyeon Im ¹, Tae Heung Lim ^{2,*} and Hosung Choo ¹

¹ Department of Electronic and Electrical Engineering, Hongik University, Seoul 04066, Korea

² Department of Electrical Engineering, Ulsan National Institute of Science and Technology (UNIST), Ulsan 44919, Korea

* Correspondence: limth0105@unist.ac.kr

Abstract: This paper proposes a 5G glass antenna that can be printed on the thick window glass of a vehicle. The proposed antenna consists of a coplanar waveguide (CPW), a printed monopole radiator, parasitic elements, a linearly arrayed patch director, and a grid-slotted patch reflector. The linearly arrayed patch director and grid-slotted patch reflector are applied to improve the bore-sight gain of the antenna. To verify the performance improvement and feasibility, the proposed antenna is fabricated, and a reflection coefficient and a radiation pattern are measured and compared with the simulation results. The measured reflection coefficient shows broadband characteristics of less than -10 dB from 24.1 GHz to 31.0 GHz (fractional bandwidth of 24.6%), which agrees well with the simulation results. The reflection coefficients are -33.1 dB by measurement and -25.7 dB by simulation, and the maximum gains are 6.2 dBi and 5.5 dBi at 28 GHz, respectively. These results demonstrate that the proposed antenna has high-gain characteristics being suitable for 5G wireless communications.

Citation: Im, C.; Lim, T.H.; Choo, H. Design of a mmWave Antenna Printed on a Thick Vehicle-Glass Substrate Using a Linearly Arrayed Patch Director and a Grid-Slotted Patch Reflector for High-Gain Characteristics. *Sensors* **2022**, *22*, 6187. <https://doi.org/10.3390/s22166187>

Academic Editor: Naser Ojaroudi
Parchin

Received: 21 July 2022

Accepted: 15 August 2022

Published: 18 August 2022

Publisher's Note: MDPI stays neutral with regard to jurisdictional claims in published maps and institutional affiliations.



Copyright: © 2022 by the authors. Licensee MDPI, Basel, Switzerland. This article is an open access article distributed under the terms and conditions of the Creative Commons Attribution (CC BY) license (<https://creativecommons.org/licenses/by/4.0/>).

Keywords: linearly arrayed patch director; grid-slotted patch reflector; glass antenna; high-gain; 5G vehicle application

1. Introduction

With the recent development of autonomous vehicle technologies, considerable efforts are devoted to employing 5G wireless communication systems for vehicle applications [1–6]. 5G vehicle wireless communication systems essentially require mmWave antennas that can stably maintain vehicle wireless communication links according to the signal transmission/reception environments while the vehicle is driving. To meet such requirements, many studies on the mmWave vehicle antennas have investigated by employing multiple antennas inside or outside vehicles [7–12], using a roof-top antenna for the coupling reduction with the vehicle body [13–15], and mounting the antennas inside the shark-fin radome [16,17]. These antennas have good impedance matching and high-gain characteristics for improving the reliability of 5G signal reception. However, it is difficult to practically use such antenna design techniques in vehicle applications because the change in the vehicle structures creates enormous costs in the vehicle manufacturing process. To resolve these problems, research on low-cost mmWave antennas that print various shapes such as a rectangular patch, a helical antenna, and a slot antenna on glass substrates, has been carried out [18–20]. Nevertheless, these antennas generally adopt thin glass substrates to reduce pattern distortion and radiation loss, and it is still difficult to apply them to thick glass substrates of actual vehicles. Although some mmWave antennas printed on very thick vehicle-glass substrates have been recently introduced, these vehicle-glass antennas generally exhibit low bore-sight gain characteristics [21–23].

In this paper, we propose an mmWave antenna printed on thick vehicle glass with a linearly arrayed patch director and a grid-slotted patch reflector for high-gain characteristics. The proposed antenna consists of a coplanar waveguide (CPW), a printed monopole

radiator, parasitic elements, the linearly arrayed patch director, and the grid-slotted patch reflector. The monopole radiator with the parasitic elements is printed on the top surface of the thick vehicle glass. In addition, the linearly arrayed patch director is designed on the same surface with the monopole using seven rectangular patch elements to enhance the bore-sight gain. On the other side, the grid-slotted patch reflector, which consists of 5×4 rectangular patches, is printed to further improve the bore-sight gain and reduce the pattern distortion. This reflector can operate as a frequency selective surface (FSS), which reflects electromagnetic waves at a specific frequency [24,25]. The critical design parameters of the proposed antenna are then optimized using the CST Studio Suite EM simulation software [26] and re-validated by HFSS [27] and FEKO EM simulation software tool [28]. To verify the feasibility, it is fabricated and measured in a full anechoic chamber to obtain the antenna characteristics, such as reflection coefficients, gains, and radiation patterns. These results demonstrate that the proposed antenna on the thick vehicle glass has high-gain characteristics being suitable for 5G wireless communications.

2. Proposed Antenna Design

Figure 1 shows the geometry of the proposed on-glass antenna for the vehicle applications. The proposed antenna consists of a CPW transmission line, a printed monopole radiator, parasitic elements, a linearly arrayed patch director, and a grid-slotted patch reflector. Herein, the geometry and concept of the proposed antenna are modeled based on the previous research [23]. The CPW transmission line has an inner conductor with a length and a width of l_1 and w_4 , and the rectangular grounds ($l_1 \times w_5$) are designed on both sides of the inner line having a gap of g_3 . This CPW transmission line is printed on the top of a thick vehicle-glass substrate ($\epsilon_r = 6.9$, $\tan\delta = 0.03$ at 28 GHz) having a thickness of t . Note that if the vehicle-glass substrate thickness becomes thicker, it is difficult to use the conventional monopole antenna due to performance degradations such as pattern distortion and gain reduction, which will be specifically discussed in Section 3. The CPW transmission line is usually less affected by the substrate thickness compared to other transmission lines (i.e., a microstrip line, a strip line, and a CPW with a ground), so that it is advantageous for use as a feeder in the proposed antenna employing the thick vehicle-glass substrate. The printed monopole radiator has a length of l_3 and a width of w_4 and is directly connected to the CPW inner conductor [29–31]. Four identical parasitic elements with a rectangular patch shape ($l_2 \times w_3$) are located at distances of g_2 from the CPW ground and g_3 from the monopole radiator. The parasitic elements are indirectly coupled by electromagnetic fields from the monopole radiator, and surface current distributions near the parasitic elements can enlarge an effective aperture resulting in the improved radiation efficiency. On the same surface as the monopole and parasitic elements, seven rectangular patches having a width of w_2 are linearly arrayed with an identical interval of g_1 to model a director that can reduce the pattern distortion by focusing the electromagnetic fields at the bore-sight direction. The grid-slotted patch reflector with an $M \times N$ rectangular configuration is printed on the bottom of the thick vehicle-glass substrate, where M and N represent the number of reflector patches along the x - and y -axis, respectively. Each patch has a width w_6 and an equal distance g_4 between the adjacent patches, and the reflector can more improve the bore-sight gain by reflecting the back radiation field to make a constructive interference at the main lobe direction. The proposed antenna is modeled, and its critical design parameters are optimized using the CST Studio Suite EM simulator. The optimized parameters are listed in Table 1.

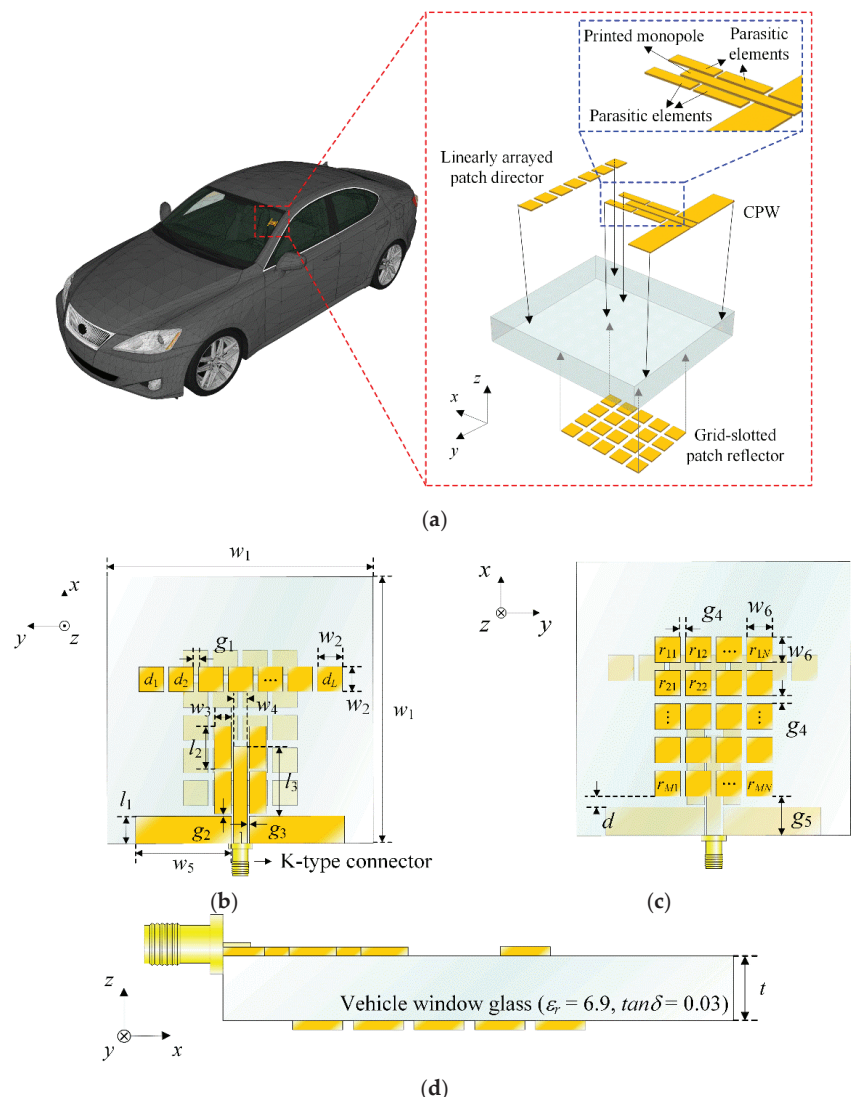


Figure 1. Geometry of the proposed antenna: (a) isometric view; (b) top view; (c) bottom view; (d) side view.

Table 1. Design parameters of the proposed antenna.

Parameters	Values	Parameters	Values
w_1	25 mm	g_1	0.5 mm
w_2	2 mm	g_2	0.13 mm
w_3	0.8 mm	g_3	0.13 mm
w_4	0.5 mm	g_4	0.5 mm
w_5	9.62 mm	d	1.06 mm
w_6	2 mm	L	7
l_1	2 mm	M	5
l_2	1.4 mm	N	4
l_3	2.03 mm	t	3.2 mm

3. Analysis

Figure 2 presents the reflection coefficients according to the distance d from the end edge of the CPW ground to the starting edge of the grid-slotted patch reflector along the x -axis. The resonance of the proposed antenna can be adjusted by the overlapping area between the reflector and the printed monopole radiator with the parasitic elements, since the overlapping area can confine the strong electromagnetic fields inside the thick vehicle-glass substrate. Figure 3 illustrates the maximum gain and the main lobe direction θ_0 in the upper hemisphere of the radiation pattern in accordance with a variation of d . The resulting maximum gain shows a peak level at the optimized distance of $d = 1.06$ mm, which allows the main lobe direction of θ_0 to be approximately 0° .

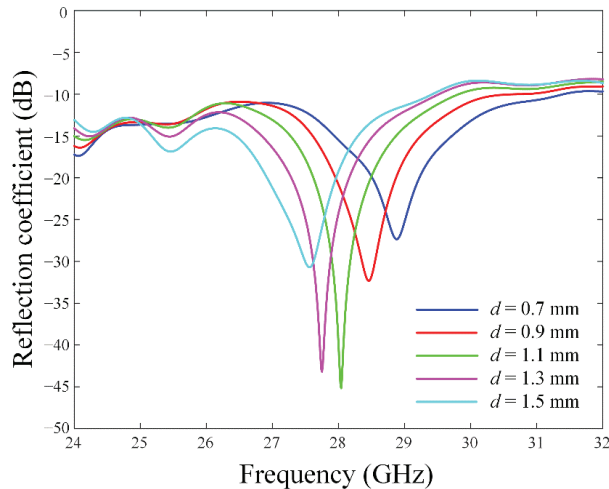


Figure 2. Reflection coefficients in accordance with the parameter d .

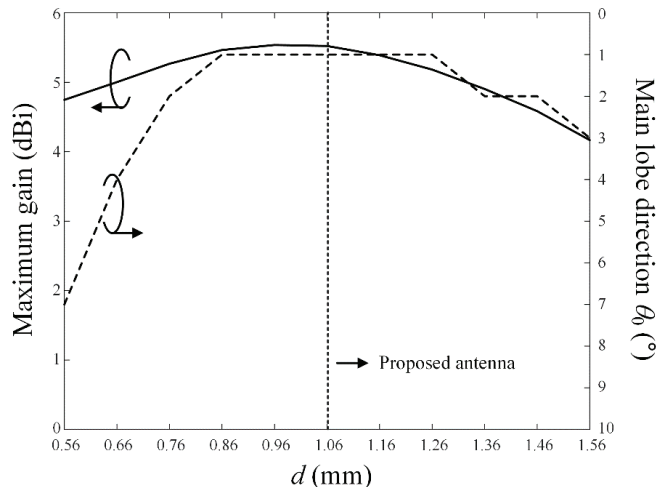


Figure 3. The maximum gain and main lobe direction θ_0 in accordance with the parameter d at 28 GHz.

Figure 4 shows the reflection coefficients according to the printed monopole length l_3 . The resonance frequency increases when l_3 varies from 1.63 mm to 2.43 mm since the overlapping area between the printed monopole radiator and the reflector become larger.

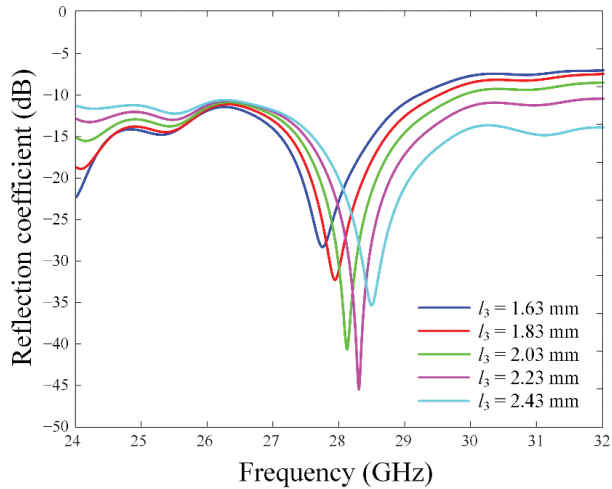


Figure 4. Reflection coefficients in accordance with the parameter l_3 .

To observe antenna characteristics according to the shape of the director, the bore-sight gain is simulated by changing the number of patch elements along the x - and y -axis, as shown in Figure 5. L_x and L_y specify the number of the patches in the x - and y -axis, respectively. High bore-sight gains are obtained when L_x is 1, which means the director is a linear array, and L_y of 7 is decided to have the maximum bore-sight gain of 5.5 dBi. Figure 6 shows the simulated bore-sight gains according to g_1 and w_2 , while L_x and L_y are fixed to be 1 and 7. The bore-sight gains are examined in the parameter ranges of $0.1 \text{ mm} \leq g_1 \leq 1 \text{ mm}$ and $1.5 \text{ mm} \leq w_2 \leq 2.5 \text{ mm}$. The peak gain of 5.5 dBi is obtained when the optimal values of g_1 and w_2 are 0.5 mm ($0.125\lambda_0$) and 1.9 mm ($0.48\lambda_0$), where λ_0 is the wavelength at the operating frequency of 28 GHz.

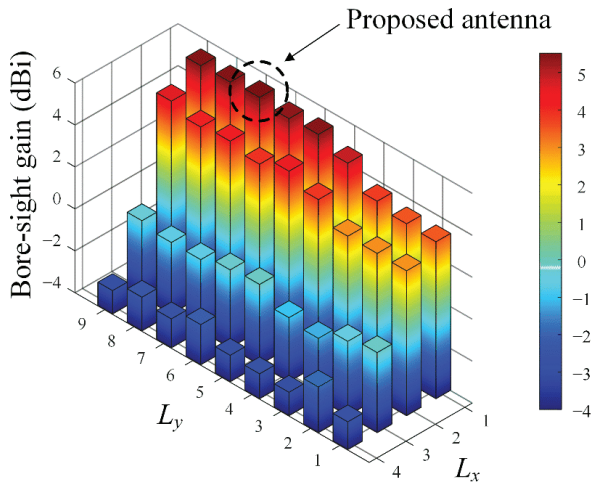


Figure 5. Bore-sight gain in accordance with the number of patch elements in the director.

Figure 7 illustrates the bore-sight gain in accordance with the gap (g_4) and the width (w_6) of the grid-slotted patch reflector. For a fixed $M = 5$ and $N = 4$, the bore-sight gain is observed in the ranges of $0.1 \text{ mm} \leq g_4 \leq 1 \text{ mm}$ and $1.5 \text{ mm} \leq w_6 \leq 2.5 \text{ mm}$. Figure 8 shows the reflection coefficient and transmission coefficient of the grid-slotted patch reflector. The

reflection coefficient is -1.7 dB, and the transmission coefficient is -10.1 dB at 28 GHz. These results mean that electromagnetic waves of 28 GHz are reflected well, thereby increasing the bore-sight gain [24,32,33].

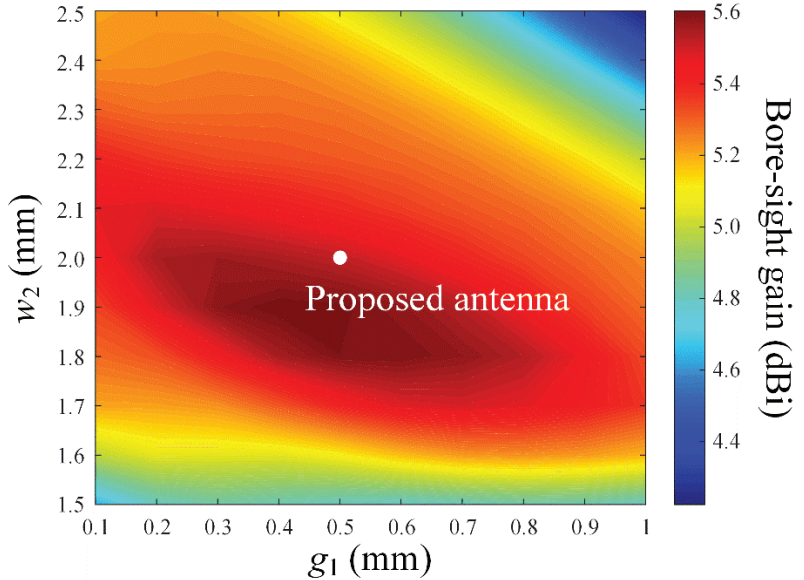


Figure 6. Bore-sight gain in accordance with parameters g_1 and w_2 .

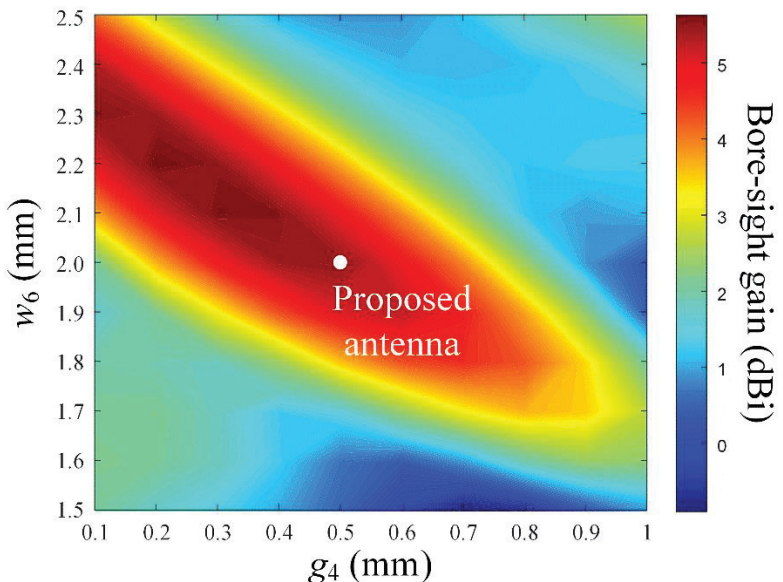


Figure 7. Bore-sight gain in accordance with parameters g_4 and w_6 .

Figure 9a,b present the maximum gain and the main lobe direction θ_0 of the conventional printed monopole antenna in comparison with the proposed antenna according to the glass thickness t . For the conventional monopole antenna, the trends of the maximum gain and main lobe direction are considerably irregular. In particular, at a conventional ve-

hicle glass thickness of 3.2 mm, θ_0 is significantly tilted more than 150° from the bore-sight direction. On the other hand, for the proposed antenna, the main lobe direction θ_0 is less than 10° in the range of $0.8 \text{ mm} \leq t \leq 1.1 \text{ mm}$ and $2.75 \text{ mm} \leq t \leq 3.5 \text{ mm}$. In Figure 10, gain characteristics of the proposed antenna are observed according to variations of w_1 from $2.5\lambda_0$ to $15\lambda_0$. The bore-sight gain fluctuates slightly when w_1 is less than $5\lambda_0$, and it saturates to 4.5 dBi when w_1 is more than $10\lambda_0$. The results confirm that the proposed antenna can be suitable for use in the large vehicle glass.

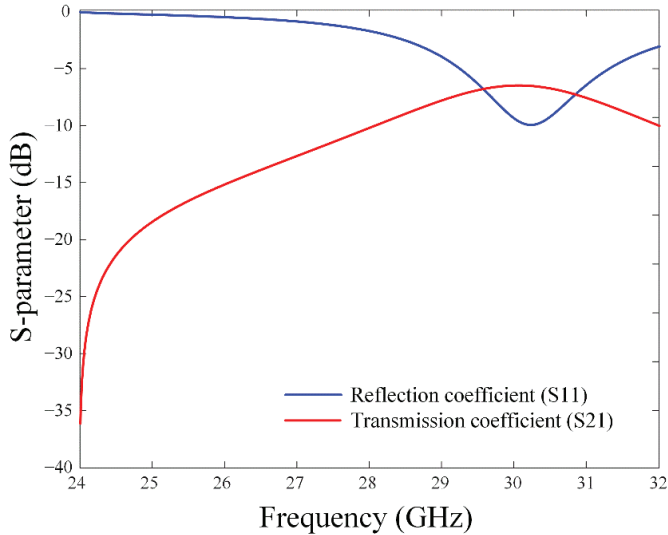
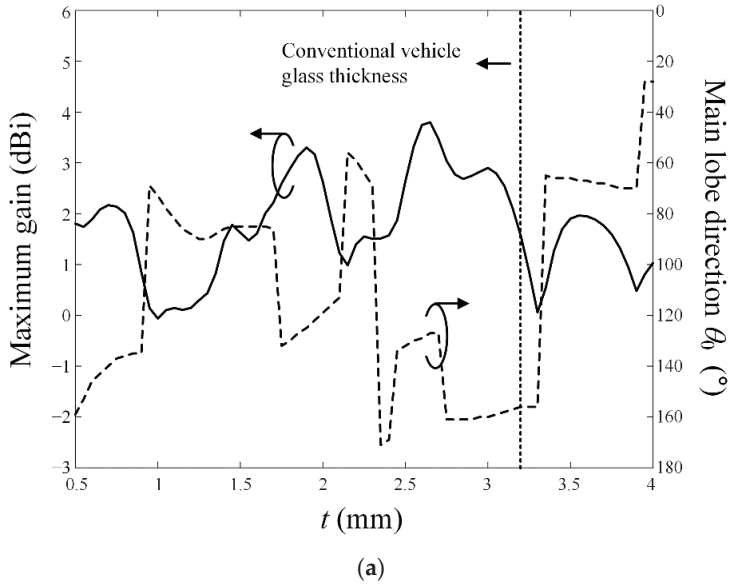


Figure 8. Reflection coefficient and transmission coefficient of the grid-slotted patch reflector.



(a)

Figure 9. Cont.

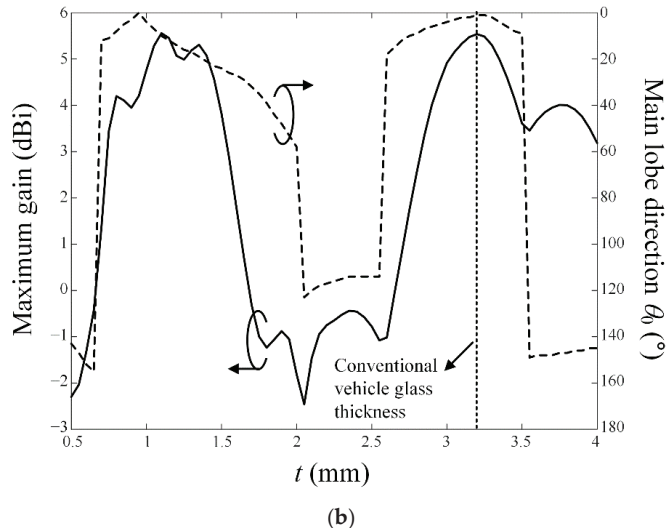


Figure 9. The maximum gain and main lobe direction θ_0 in accordance with parameter t : (a) conventional printed monopole antenna; (b) proposed antenna.

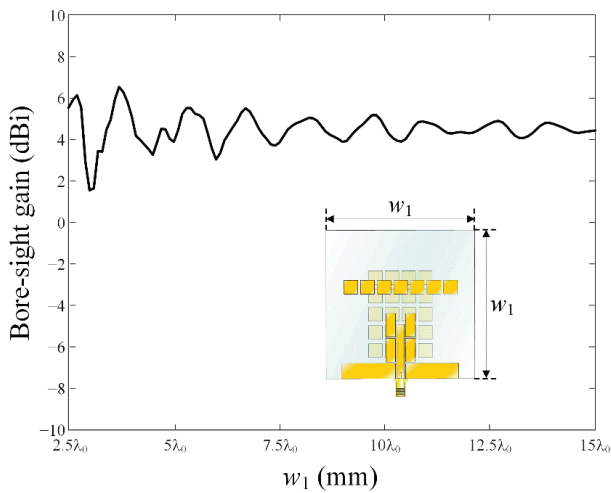


Figure 10. Bore-sight gain in accordance with the parameter w_1 .

4. Fabrication and Measurement

Figure 11a,b shows the fabricated mmWave on-glass antenna with the linearly arrayed patch director and the grid-slotted patch reflector. The proposed antenna is fabricated using a thermosetting adhesive to strongly attach the printed antenna copper layers to the glass substrate. The proposed antenna is fed by a K-type (2.92 mm) connector operating at up to 40 GHz. The inner and outer conductors of the connector are electrically connected to the inner conductor and rectangular grounds of the CPW line by soldering. Figure 11c shows a photograph of the measurement setup, and antenna characteristics such as reflection coefficients and radiation patterns are measured in the full anechoic chamber.

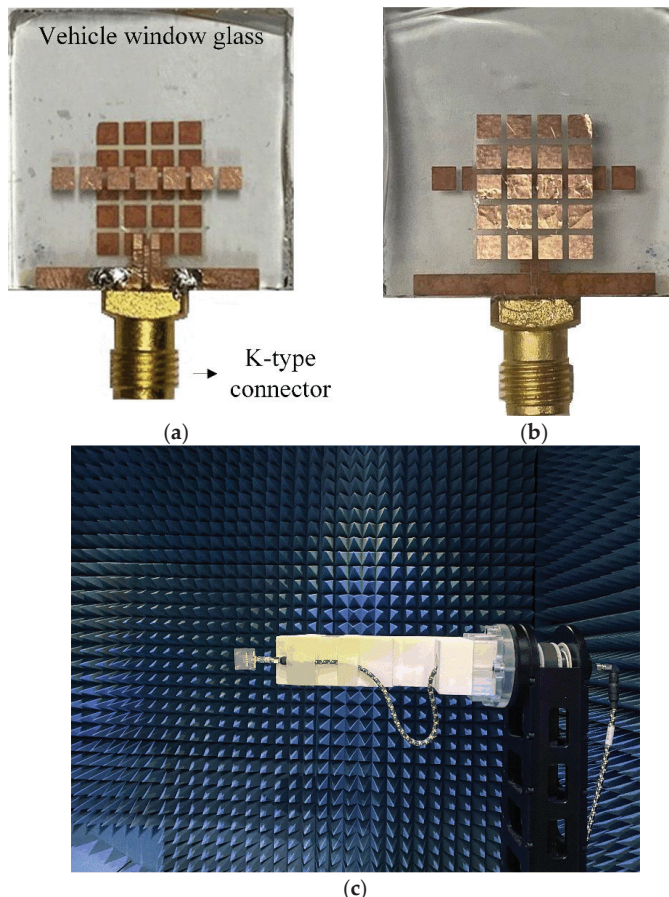


Figure 11. Photographs of the proposed antenna and measurement setup: (a) top view; (b) bottom view; (c) measurement setup.

As shown in Figure 12, the measured reflection coefficient shows broadband characteristics of less than -10 dB from 24.1 GHz to 31.0 GHz (fractional bandwidth of 24.6%), which agrees well with the simulation results. At 28 GHz, the measured reflection coefficient is -33.1 dB, while simulated reflection coefficients are -25.7 dB by CST, -23.8 dB by HFSS, and -27.9 dB by FEKO. Figure 13 illustrates maximum gains with or without the linearly arrayed patch director and the grid-slotted patch reflector. At 28 GHz, simulated result of the proposed antenna shows an improved maximum gain of 5.52 dBi. It is higher than the gain of 1.9 dBi without the reflector and the gain of 2.9 dBi without the director. The measurement results also agree well with the simulation, and the maximum measured gain is 6.20 dBi at 28 GHz. The radiation efficiency of the proposed antenna is 39%, which is higher than 31% without the reflector and 38% without the director.

Figure 14 shows the current distributions of the proposed antenna without the director and without the reflector. When the grid-slotted patch reflector is employed, the current distributions of the reflector are increased at 28 GHz.

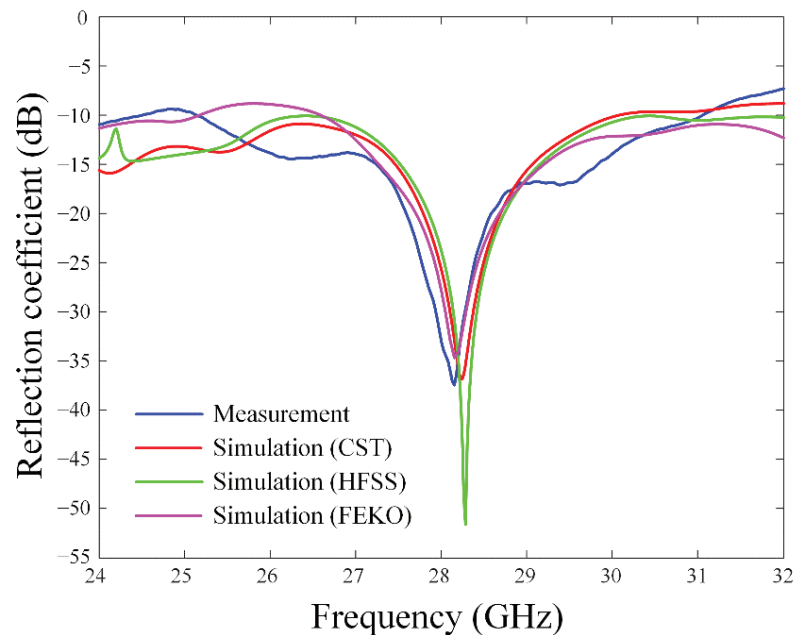


Figure 12. Measured and simulated reflection coefficients of the proposed antenna.

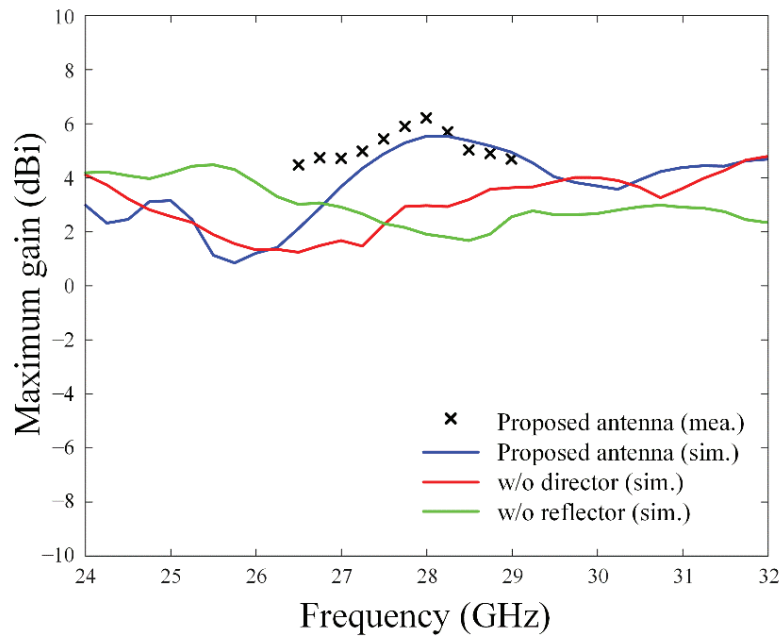


Figure 13. Maximum gains with and without the director and the reflector.

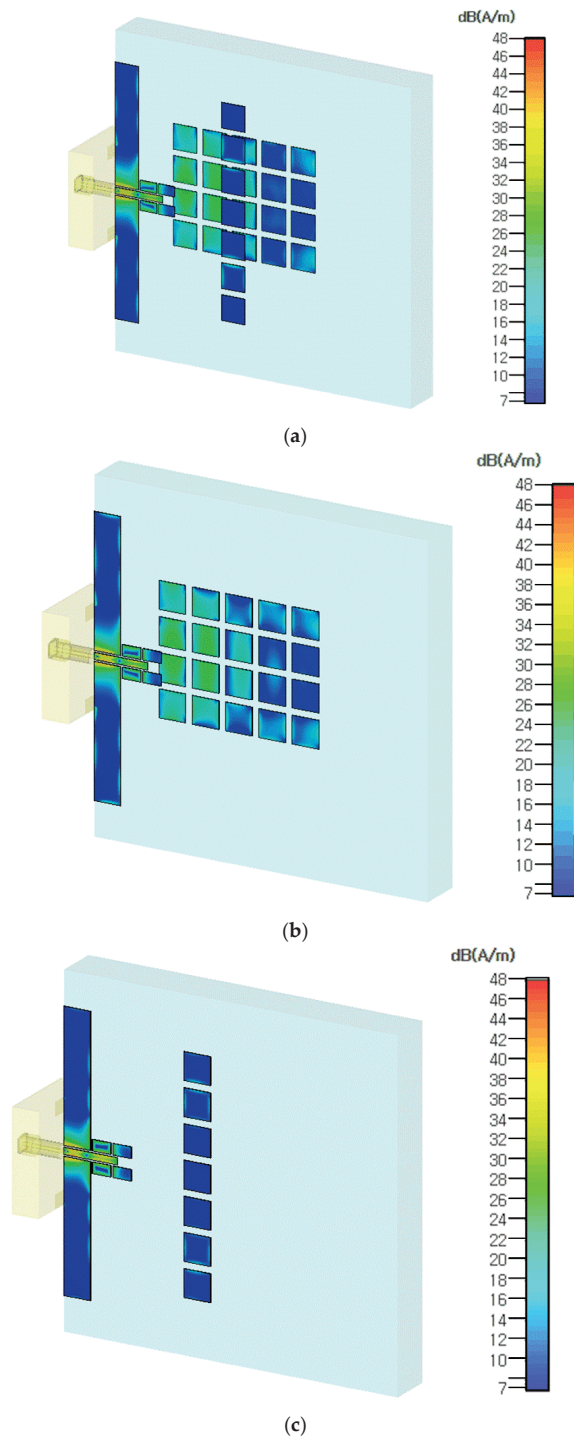


Figure 14. Current distributions: (a) proposed antenna; (b) without the director; (c) without the reflector.

Figure 15 shows two-dimensional (2-D) radiation patterns in zx - and zy -planes at 28 GHz. The measured maximum gain in the zx -plane is 6.20 dBi at $\theta = 14^\circ$, and the simulated maximum gain is 5.54 dBi at $\theta = -2^\circ$ by CST. In the zy -plane, the measured maximum gain is 3.24 dBi at $\theta = -3^\circ$, and simulated result is 5.52 dBi at $\theta = 0^\circ$ by CST. Figure 16 illustrates simulated 3-D radiation patterns according to the presence of the director and the reflector. The resulting 3-D radiation beam shapes obviously show that the bore-sight gain is improved by adding both the reflector and the director.

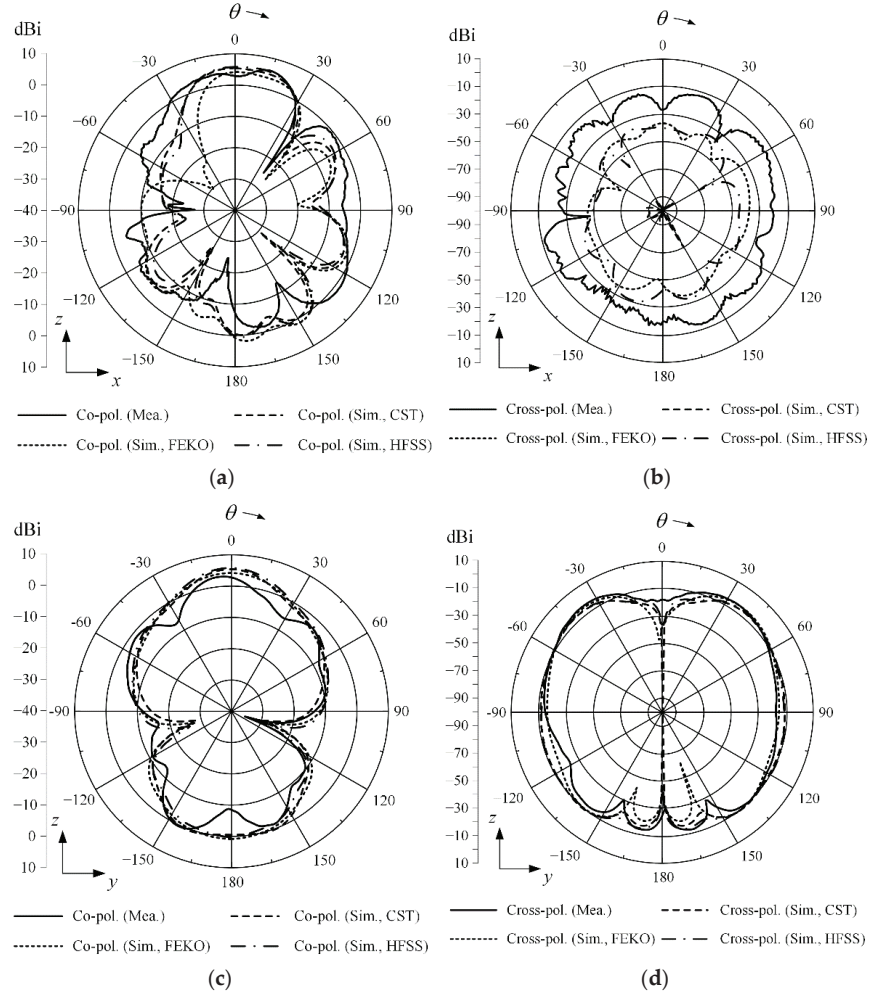


Figure 15. Measured and simulated 2-D radiation patterns of the proposed antenna at 28 GHz: (a) zx -plane co-polarization; (b) zx -plane cross-polarization; (c) zy -plane co-polarization; (d) zy -plane cross-polarization.

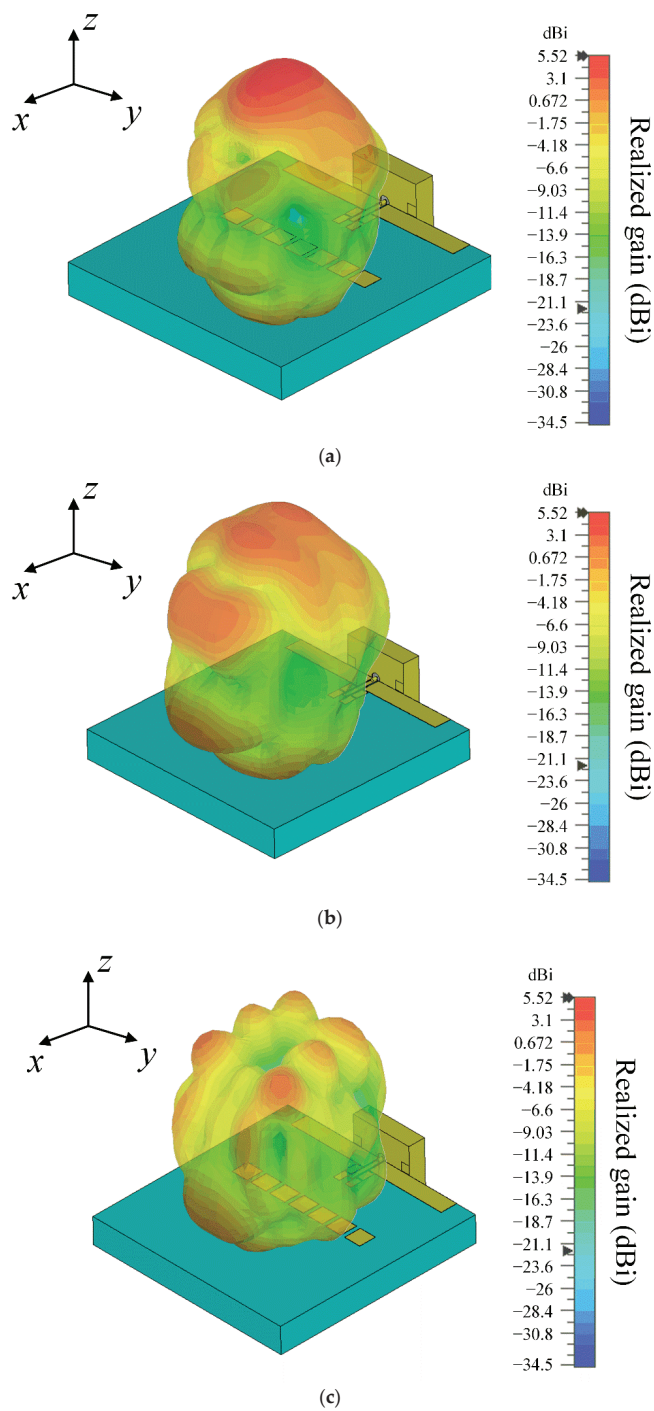


Figure 16. 3-D radiation patterns by simulation: (a) proposed antenna; (b) without the director; (c) without the reflector.

5. Conclusions

We proposed an mmWave on-glass antenna with a linearly arrayed patch director and a grid-slotted patch reflector. The proposed antenna was printed on the thick vehicle-glass substrate, which did not require the remodeling of the vehicle structures. To improve the bore-sight gain, the linearly arrayed patch director and the grid-slotted patch reflector were employed. The director and reflector were optimized to achieve high-gain characteristics on the thick glass substrate. The measured reflection coefficient of the proposed antenna was -33.1 dB, and the maximum gain was 6.2 dBi at 28 GHz. In addition, it was confirmed that the bore-sight gain was saturated to 4.5 dBi even when the size of the glass window was increased. Through the results, we verified that the proposed antenna achieving the high-gain characteristics could be suitable for $5G$ wireless communications.

Author Contributions: Conceptualization, C.I., T.H.L. and H.C.; methodology, C.I. and T.H.L.; software, C.I.; validation, C.I., T.H.L. and H.C.; formal analysis, C.I., T.H.L. and H.C.; investigation, C.I. and T.H.L.; resources, C.I.; data curation, C.I.; writing—original draft preparation, C.I., T.H.L. and H.C.; writing—review and editing, C.I., T.H.L. and H.C.; visualization, C.I.; supervision, H.C.; project administration, H.C.; funding acquisition, H.C. All authors have read and agreed to the published version of the manuscript.

Funding: This research was funded by the Basic Science Research Program through the National Research Foundation of Korea (NRF) funded by the Ministry of Education (no. NRF-2017R1A5A1015596), and the NRF grant funded by the Korea government (no. 2015R1A6A1A03031833).

Institutional Review Board Statement: Not applicable.

Informed Consent Statement: Not applicable.

Data Availability Statement: Not applicable.

Conflicts of Interest: The authors declare no conflict of interest.

References

- Minovski, D.; Åhlund, C.; Mitra, K. Modeling quality of IoT experience in autonomous vehicles. *IEEE Internet Things J.* **2020**, *7*, 3833–3849. [CrossRef]
- Wang, P.; Di, B.; Zhang, H.; Bian, K.; Song, L. Cellular V2X communications in unlicensed spectrum: Harmonious coexistence with VANET in 5G systems. *IEEE Trans. Wirel. Commun.* **2018**, *17*, 5212–5224. [CrossRef]
- Alalewi, A.; Dayoub, I.; Cherkaoui, S. On 5G-V2X use cases and enabling technologies: A comprehensive survey. *IEEE Access* **2021**, *9*, 107710–107737. [CrossRef]
- Lou, L.; Li, Q.; Zhang, Z.; Yang, R.; He, W. An IoT-driven vehicle detection method based on multisource data fusion technology for smart parking management system. *IEEE Internet Things J.* **2020**, *7*, 11020–11029. [CrossRef]
- Condoluci, M.; Gallo, L.; Mussot, L.; Kousaridas, A.; Spapis, P.; Mahlouji, M.; Mahmoodi, T. 5G V2X system-level architecture of 5GCAR project. *Future Internet* **2019**, *11*, 217. [CrossRef]
- Oh, S.S.; Choi, J.W.; Kim, D.W.; Lee, Y.C.; Cho, B.L. Comparison of 0.75–24-GHz reach distances and ratios using propagation path loss measurements from urban and rural line-of-sight environments. *J. Electromagn. Eng. Sci.* **2021**, *21*, 1–7. [CrossRef]
- Venkateswara Rao, M.; Madhav, B.T.P.; Krishna, J.; Usha Devi, Y.; Anilkumar, T.; Prudhvi Nadh, B. CSRR-loaded T-shaped MIMO antenna for 5G cellular networks and vehicular communications. *Int. J. RF Microw. Comput. Aid. Eng.* **2019**, *29*, e21799. [CrossRef]
- Devi, Y.U.; Rukmini, M.S.S.; Madhav, B.T.P. Liquid crystal polymer based flexible and conformal 5G antenna for vehicular communication. *Mater. Res. Express.* **2018**, *6*, 016306. [CrossRef]
- Feng, B.; Chen, J.; Yin, S.; Sim, C.-Y.-D.; Zhao, Z. A tri-polarized antenna with diverse radiation characteristics for 5G and V2X communications. *IEEE Trans. Veh. Technol.* **2020**, *69*, 10115–10126. [CrossRef]
- Cheng, Y.; Lu, J.; Wang, C. Design of a multiple band vehicle-mounted antenna. *Int. J. Antennas Propag.* **2019**, *2019*, 11. [CrossRef]
- Sun, Y.-X.; Leung, K.W.; Lu, K. Compact dual microwave/millimeter-wave planar shared-aperture antenna for vehicle-to-vehicle/5G Communications. *IEEE Trans. Veh. Technol.* **2021**, *70*, 5071–5076. [CrossRef]
- Awan, W.A.; Naqvi, S.I.; Naqvi, A.H.; Abbas, S.M.; Zaidi, A.; Hussain, N. Design and characterization of wideband printed antenna based on DGS for 28 GHz 5G applications. *J. Electromagn. Eng. Sci.* **2021**, *21*, 177–183. [CrossRef]
- Artner, G.; Kotterman, W.; Galdo, G.D.; Hein, M.A. Conformal automotive roof-top antenna cavity with increased coverage to vulnerable road users. *IEEE Antennas Wirel. Propag. Lett.* **2018**, *17*, 2399–2403. [CrossRef]
- Artner, G.; Langwieser, R.; Mecklenbrauker, C.F. Concealed CFRP vehicle chassis antenna cavity. *IEEE Antennas Wirel. Propag. Lett.* **2017**, *16*, 1415–1418. [CrossRef]

15. Artner, G.; Kotterman, W.; Galdo, G.D.; Hein, M.A. Automotive antenna roof for cooperative connected driving. *IEEE Access* **2019**, *7*, 20083–20090. [CrossRef]
16. Khalifa, M.O.; Yacoub, A.M.; Aloisio, D.N. A multiwideband compact antenna design for vehicular sub-6 GHz 5G wireless systems. *IEEE Trans. Antennas Propag.* **2021**, *69*, 8136–8142. [CrossRef]
17. Yacoub, A.M.; Khalifa, M.O.; Aloisio, D.N. Wide band raised printed monopole for automotive 5G wireless communications. *IEEE Antennas Propag. Mag.* **2022**, *3*, 502–510. [CrossRef]
18. Goyal, R.; Vishwakarma, D.K. Design of a graphene-based patch antenna on glass substrate for high-speed terahertz communications. *Microw. Opt. Technol. Lett.* **2018**, *60*, 1594–1600. [CrossRef]
19. Naqvi, A.H.; Park, J.; Baek, C.; Lim, S. V-Band end-fire radiating planar micromachined helical antenna using through-glass silicon via (TGSV) technology. *IEEE Access* **2019**, *7*, 87907–87915. [CrossRef]
20. Cil, E.; Dumanli, S. The design of a reconfigurable slot antenna printed on glass for wearable applications. *IEEE Access* **2020**, *8*, 95417–95423. [CrossRef]
21. Jang, D.; Kong, N.K.; Choo, H. Design of an on-glass 5G monopole antenna for a vehicle window glass. *IEEE Access* **2021**, *9*, 152749–152755. [CrossRef]
22. Youn, S.; Jang, D.; Kong, N.K.; Choo, H. Design of a printed 5G monopole antenna with periodic patch director on the laminated window glass. *IEEE Antennas Wirel. Propag. Lett.* **2022**, *21*, 297–301. [CrossRef]
23. Im, C.; Lim, T.-H.; Jang, D.; Kong, N.-K.; Choo, H. Design of a printed 5G monopole antenna on vehicle window glass using parasitic elements and a lattice-structure reflector for gain enhancement. *Appl. Sci.* **2021**, *11*, 9953. [CrossRef]
24. Alwareth, H.; Ibrahim, I.M.; Zakaria, Z.; Al-Gburi, A.J.A.; Ahmed, S.; Nasser, Z.A. A wideband high-gain microstrip array antenna integrated with frequency-selective surface for Sub-6 GHz 5G applications. *Micromachines* **2022**, *13*, 1215. [CrossRef]
25. Mohyuddin, W.; Kim, D.H.; Choi, H.C.; Kim, K.W. Comparative study of square and circular loop frequency selective surfaces for millimeter-wave imaging diagnostics systems. *Sensors* **2018**, *18*, 3079. [CrossRef]
26. CST Microwave Studio. Available online: <http://www.cst.com> (accessed on 10 October 2021).
27. Available online: <http://www.ansys.com/products/electronics/ansys-hfss> (accessed on 30 July 2019).
28. Altair. FEKO. Available online: <http://www.altair.com> (accessed on 29 March 2022).
29. Pan, C.-Y.; Horng, T.-S.; Chen, W.-S.; Huang, C.-H. Dual wideband printed monopole antenna for WLAN/WiMAX applications. *IEEE Antennas Wirel. Propag. Lett.* **2007**, *6*, 149–151. [CrossRef]
30. Ahmed, O.; Sebak, A. A printed monopole antenna with two steps and a circular slot for UWB applications. *IEEE Antennas Wirel. Propag. Lett.* **2008**, *7*, 411–413. [CrossRef]
31. Kuo, Y.-L.; Wong, K.-L. Printed double-T monopole antenna for 2.4/5.2 GHz dual-band WLAN operations. *IEEE Trans. Antennas Propag.* **2003**, *51*, 2187–2192.
32. Chatterjee, A.; Parui, S.K. Performance enhancement of a dual-band monopole antenna by using a frequency-selective surface-based corner reflector. *IEEE Trans. Antennas Propag.* **2016**, *64*, 2165–2171. [CrossRef]
33. Ranga, Y.; Matekovits, L.; Esselle, K.P.; Weily, A.R. Multi octave frequency selective surface reflector for ultrawideband antennas. *IEEE Antennas Wirel. Propag. Lett.* **2011**, *10*, 219–222. [CrossRef]

Review

Advancements and Challenges in Antenna Design and Rectifying Circuits for Radio Frequency Energy Harvesting

Martins Odiamenhi *, Haleh Jahanbakhsh Basherlou, Chan Hwang See, Naser Ojaroudi Parchin *, Keng Goh and Hongnian Yu

School of Computing, Engineering and the Built Environment, Edinburgh Napier University, Edinburgh EH10 5DT, UK; haleh.jahanbakhshbasherlou@napier.ac.uk (H.J.B.); c.see@napier.ac.uk (C.H.S.); k.goh@napier.ac.uk (K.G.); h.yu@napier.ac.uk (H.Y.)

* Correspondence: m.odiamenhi@napier.ac.uk (M.O.); n.ojaroudiparchin@napier.ac.uk (N.O.P.)

Abstract: The proliferation of smart devices increases the demand for energy-efficient, battery-free technologies essential for sustaining IoT devices in Industry 4.0 and 5G networks, which require zero maintenance and sustainable operation. Integrating radio frequency (RF) energy harvesting with IoT and 5G technologies enables real-time data acquisition, reduces maintenance costs, and enhances productivity, supporting a carbon-free future. This survey reviews the challenges and advancements in RF energy harvesting, focusing on far-field wireless power transfer and powering low-energy devices. It examines miniaturization, circular polarization, fabrication challenges, and efficiency using the metamaterial-inspired antenna, concentrating on improving diode nonlinearity design. This study analyzes key components such as rectifiers, impedance matching networks, and antennas, and evaluates their applications in biomedical and IoT devices. The review concludes with future directions to increase bandwidth, improve power conversion efficiency, and optimize RF energy harvesting system designs.

Keywords: RF energy harvesting; antenna design; rectifying circuit; nonlinearity; IoT applications; wireless power transfer

Citation: Odiamenhi, M.; Jahanbakhsh Basherlou, H.; Hwang See, C.; Ojaroudi Parchin, N.; Goh, K.; Yu, H. Advancements and Challenges in Antenna Design and Rectifying Circuits for Radio Frequency Energy Harvesting. *Sensors* **2024**, *24*, 6804. <https://doi.org/10.3390/s24216804>

Academic Editor: Shah Nawaz
Burokur

Received: 10 September 2024

Revised: 11 October 2024

Accepted: 17 October 2024

Published: 23 October 2024



Copyright: © 2024 by the authors. Licensee MDPI, Basel, Switzerland. This article is an open access article distributed under the terms and conditions of the Creative Commons Attribution (CC BY) license (<https://creativecommons.org/licenses/by/4.0/>).

1. Introduction

Electronic devices and wireless sensors play critical roles in healthcare, sports monitoring, environmental sensing, wearable technology, and implants. However, their widespread adoption is limited by the constraints of conventional batteries, which have short lifespans and are difficult to replace in many use cases [1,2]. Addressing these issues is crucial for the longevity of Internet of Things (IoT) devices, which require reliable and sustainable energy supply strategies [3,4]. Although techniques such as data aggregation and sleep scheduling have enhanced operational efficiency, there remains an increasing demand for wireless energy harvesting (WEH) solutions that can harness far-field radio frequency (RF) energy [4–7]. Several specific applications in IoT can benefit from RF energy harvesting. In smart homes, RF energy can power wireless sensors and devices, enabling continuous communication and monitoring without the need for frequent battery replacements. Similarly, wearable health monitoring systems can leverage ambient RF energy to operate autonomously for extended periods, reducing maintenance and improving patient care. Additionally, RF energy harvesting is pivotal in smart agriculture, where IoT-based sensors monitor environmental conditions across large, remote areas. Finally, logistics and supply chain systems that rely on RFID and IoT-based tracking networks benefit from the extended lifespan provided by RF energy harvesting.

Recently, research has been conducted in the field of RF energy harvesting. However, the majority of surveys predominantly center on specific aspects of rectenna circuit design. To comprehensively comprehend recent advancements in RF technology, including antenna arrays, artificial intelligence-assisted antenna design, and metamaterials, one

needs to broaden the scope of reviews. Surveys [8,9] have investigated present patterns and forthcoming paths for RF energy-gathering gadgets and circuits. These assessments underscore methods and approaches to improve the RF-to-DC conversion efficiency of rectenna systems, with a specific concentration on antenna arrays, impedance networks, and rectifiers. However, the incorporation of metamaterials and artificial intelligence in rectenna design remains largely unexplored in these surveys and approaches to enhance the RF-to-DC conversion efficiency of rectenna systems, with a specific concentration on antenna arrays, impedance matching networks, and rectifiers. However, the incorporation of metamaterials and artificial intelligence in rectenna design remains widely unexplored in these surveys. Contrarily, a review by Mohammad et al. [10] and Bashar et al. [11] thoroughly examined current developments in metamaterial applications in antenna design. It studied planar antenna loading and composite right/left transmission in the literature. The focus is not on impedance matching and rectifier design but rather is restricted to antenna design. Musa et al. [12] reviewed the design of reconfigurable antennas using metamaterials. However, their work did not explore essential topics such as artificial intelligence, rectifiers, and the crucial synergy between the antenna, impedance matching network, and rectifiers. These areas require further exploration to improve the design of reconfigurable antennas. A previous review [13] focused on employing CMOS RF-DC rectifiers for a wide power dynamic range, but it did not cover the broader concept of RF energy scavenging. Despite the abundance of literature on RF energy harvesting and its technology, only a few surveys have comprehensively reviewed all the key recent technologies, such as metamaterial-inspired antenna designs, Schottky diode, rectenna, and power generated in RFEH design. While these reviews provide valuable insights, they tend to focus on specific components, overlooking the broader integration of related advancements such as artificial intelligence (AI), antenna arrays, and Schottky diode RF-DC rectifiers. Moreover, previous reviews have not comprehensively addressed the challenges of efficiency, miniaturization, and fabrication in ambient energy harvesting systems.

This review aims to fill these gaps by providing a comprehensive examination of radio frequency energy harvesting (RFEH) systems, including their structures, features, and applications. It discusses key challenges in rectenna design, bandwidth enhancement, and miniaturization, while also exploring the role of AI-assisted antenna design and metamaterials in enhancing performance. Furthermore, the review considers the integration of CMOS and Schottky diode rectifiers, offering a holistic perspective on RFEH for future electronic devices and sensors.

The rest of this paper is organized as follows: Section 2 covers energy harvesting techniques, focusing on the history and evolution of wireless power transfer (WPT) and RF transmission. Section 3 examines critical parameters in antenna technology, with an emphasis on improving bandwidth, gain, and radiation patterns. Section 4 discusses impedance matching networks and their associated challenges. Section 5 reviews advancements in CMOS and Schottky diode rectifiers, Section 6 focuses on power consumption of sensors and energy harvested from rectenna, and Section 7 concludes with future prospects and challenges for RFEH technology.

2. Energy Harvesting System

Ambient energy harvesting extracts power from surrounding sources, providing a critical energy solution for portable electronics and autonomous sensors [14]. Various energy sources each offer unique advantages and limitations. Figure 1 presents an overview of several energy harvesting methods, including solar, thermal, mechanical, and RF-based approaches, highlighting their respective operating principles and applications.

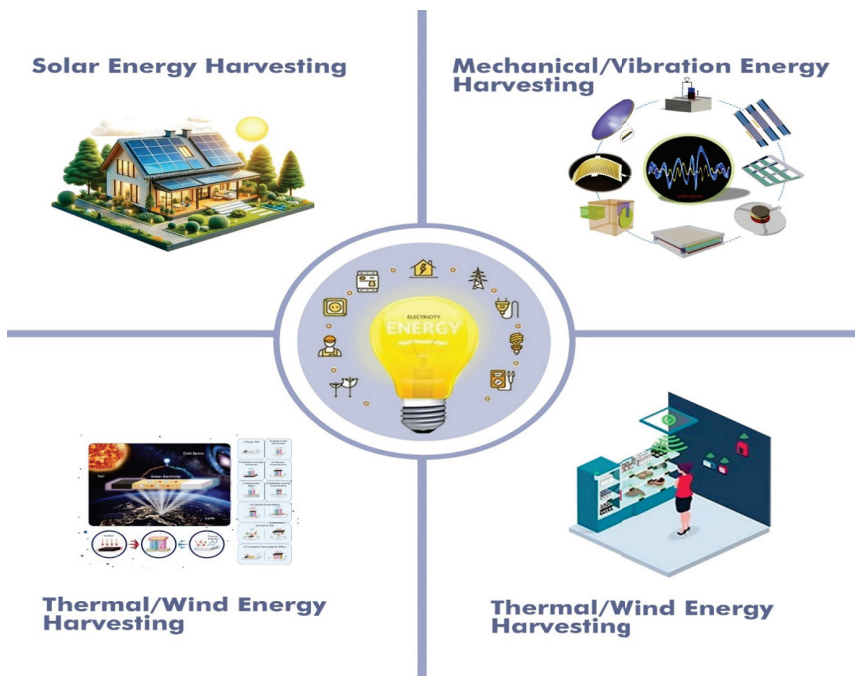


Figure 1. Various energy harvesting techniques.

Solar energy converts sunlight into electricity via photovoltaic cells, making it a sustainable option for outdoor applications. However, its efficiency depends on sunlight intensity and duration, with typical conversion rates around 8% [15]. Thermal energy harvesters exploit temperature differences using the thermoelectric effect. These systems power devices such as health monitors and smartwatches, though they face lower conversion efficiencies [16].

Wind energy harvesters convert wind into electricity using turbines, providing a clean and renewable power source. However, the intermittency of wind flow poses significant challenges to its efficiency [17].

Mechanical energy harvesters capture energy from motion and vibrations through electrostatic, piezoelectric, and electromagnetic mechanisms. These systems harvest energy from activities like walking or from industrial vibrations [18].

RF energy harvesting has gained prominence due to the rise of wireless communication technologies, including IoT and 5G networks. Near-field RF harvesters use specialised sources to achieve high energy transfer efficiencies, often exceeding 80%. Far-field RF harvesters capture signals from distant sources such as cellular towers, converting them into usable power through rectifier circuits. The power density and efficiency of this method depend heavily on the signal propagation distance and source output power [19].

Table ?? compares these energy harvesting methods, evaluating their availability, power density, characteristics, efficiency, applications, and associated benefits and limitations. This comprehensive comparison helps identify the most suitable energy source for specific applications.

Table 1. Characteristics and performance of different types of energy harvesting (EH) technologies.

Type of EH	Solar [15]	Thermal [16]	Wind [17]	Piezoelectric [18]	RF [19]
Power Source	Sun	Solar, equipment malfunctions, and physical attrition	Airspeed	Fluctuations in strength and oscillations	Broadcasting channels, cellular networks, and infrastructure
Access/Availability	Sunlight hours (4–8)	Ongoing system operations	Weather-dependent	Based on activity	Daily
Scavenging process	Photovoltaic/solar cell	Temperature, photoelectric effect	Motor drive, wind turbine	Piezoelectric devices with power electronics	Rectenna
Avg. Power density	100 $\mu\text{W}/\text{cm}^2$	60 $\mu\text{W}/\text{cm}^2$	177 $\mu\text{W}/\text{cm}^2$	250 $\mu\text{W}/\text{cm}^2$	40 $\mu\text{W}/\text{cm}^2$
Features	Hard to manage	Unmanageable, hard to predict	Unmanageable, unpredictable	Manageable	Somewhat manageable
Efficiency	11.7–26.7%	5–15%	-	5–30%	0.4–50%
Uses	External IoT devices, hubs	Body sensors	IoT sensors, base stations	Wearables, sensors	RFID, wearables
Merits	Abundant energy, tech progress	Small-scale harvesters	Energy from light wind	High efficiency, stable voltage output	Compact, available circuits
Demerits	Weather-dependent, large area needed	Thermal compatibility, high power need	Availability varies, bulky systems	Expensive, material-dependent	Interference affects power, signal loss

RF energy harvesting suits modern applications like Industry 5.0, IoT, biomedical devices, and wearables. It delivers continuous, reliable power to sensors and communication devices in smart factories, reducing maintenance and increasing flexibility [20]. IoT devices maintain performance with minimal battery replacements [21]. Biomedical implants use RF energy harvesting to improve patient comfort and device reliability [22]. Wearables benefit from compact, lightweight power sources by utilizing available RF signals [22,23]. RF energy harvesting also applies to smart homes, environmental monitoring, and agricultural sensors, expanding its range of uses [24].

2.1. History of Wireless Power Transfer

Hans Christian Oersted discovered the relationship between electric currents and magnetic fields in 1819, revealing that electric currents generate magnetic fields. This discovery laid the foundation for future developments in electromagnetism and modern technologies [25]. Oersted's findings contributed to key theoretical advancements, including Ampere's Law and Faraday's Law.

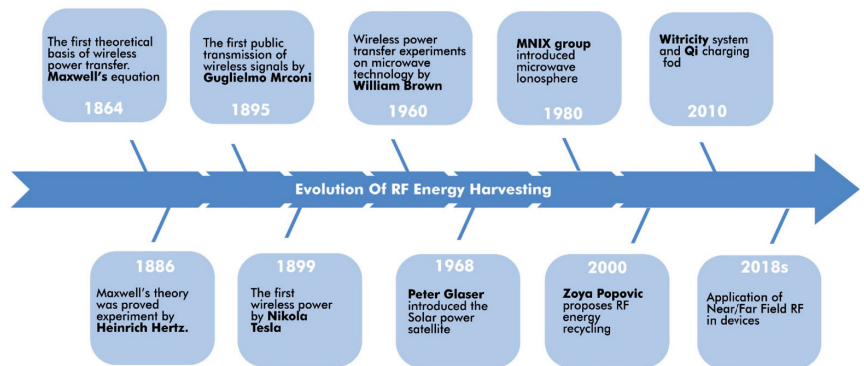
Building on these principles, James Clerk Maxwell introduced Maxwell's Equations in 1864, greatly enhancing the understanding of the interaction between electric and magnetic fields [26]. His 1873 book highlighted the interconnected nature of these forces, setting the stage for further technological developments, including wireless power transfer (WPT).

In 1888, Heinrich Hertz provided the first empirical proof of electromagnetic waves, using advanced instruments to transmit electricity over short distances. This marked a significant milestone in electromagnetic wave research [27]. Inspired by Hertz, Nikola Tesla developed alternating current (AC) systems that revolutionised electricity distribution. Tesla's work, including his solutions to coil overheating, laid the groundwork for modern WPT technology [28]. His famous 1899 Tesla coil experiment demonstrated the feasibility of wireless energy transmission [29].

Tesla's subsequent experiments, conducted between 1899 and 1901, aimed to transmit electrical energy wirelessly over long distances. However, the limitations of available technology constrained these efforts. A major breakthrough in WPT occurred in 1964 when W.C. Brown successfully powered a helicopter using microwaves. Later, in 1975, the JPL Goldstone Facility transmitted 450 kW of power through a 26-meter antenna, converting it to 30 kW of DC power using a rectenna. Innovations in microwave technology and magnetron development during World War II significantly contributed to these advancements [30].

The 1970s and 1980s witnessed further progress in microwave-powered systems, with notable contributions from researchers in Japan and Canada. NASA's 2000 SERT program and the 2007 demonstration of near-field power transfer by Marin Soljacic at MIT were further milestones in WPT development [31]. The establishment of the Wireless Power Consortium in 2008 and the creation of the "Qi" standard in 2010 marked significant progress in the standardisation of wireless charging technologies, as demonstrated by commercial products like the Mophie 3-in-1 charger [32].

Figure 2 illustrates key milestones in the evolution of wireless power transfer (WPT), categorizing it into two primary approaches: non-radiative (near-field) and radiative (far-field), as outlined in Table 2. Non-radiative methods, such as inductive and capacitive coupling, rely on electromagnetic field coupling to transfer power over short distances. Inductive coupling is widely used in modern wireless charging systems, such as those based on the Qi standard, while capacitive coupling is employed in specific low-power applications. In contrast, radiative methods use radio frequency (RF) principles, transmitting power over longer distances through RF waves or laser beams.

**Figure 2.** Milestones of WPT.

Radiative (far-field) methods are particularly important for long-distance power transmission, such as space-based solar power or remote sensing applications, where energy needs to be transferred over significant distances with minimal infrastructure. RF waves and microwave technologies play a critical role in enabling these systems, as they can transmit power efficiently over large distances.

Despite the potential of far-field WPT, several practical challenges remain. Energy losses due to atmospheric interference, scattering, and absorption reduce the efficiency of RF and microwave power transmission over long distances. Safety concerns related to high-power RF waves and lasers pose additional challenges, particularly in ensuring that the transmission of power does not interfere with populated areas or sensitive equipment. Regulatory issues surrounding the allocation of frequencies for RF-based WPT further complicate large-scale implementations.

Nevertheless, far-field WPT holds significant potential for advanced applications such as wireless sensors, other IoT devices, where energy harvested in space can be transmitted back to Earth. Addressing efficiency losses, safety concerns, and regulatory hurdles will be critical to unlocking the full potential of far-field WPT for the future of energy transmission.

Table 2. Types of wireless power transfer.

Types of Wireless Power Transfer	Field Region	Design Method	Effective Distance	Efficiency	Uses	Merits	Di-Merits
RF Harvesting [8]	Far-Field	Antennas	Depends on frequency, works over meters to kilometers.	1% to 85%	Low-power devices, body wireless sensors, wearables	Low radiative effect due to small RF density	High RF can be hazardous, low efficiency
Inductive Coupling [33]	Near-field, non-radiative	Coils	Ranges from mm to cm	10–60% at 15–500 KHz	Mobiles, cards, recharge stations	Easy to implement and safe	Limited range, heating, alignment issues
Magnetic Resonance Coupling [34]	Near-Field	Resonators	Several millimeters to several meters	20% to 90% at 50 cm to 3 m	Wireless charging, electric cars, mid-range applications	Charges multiple devices efficiently, even with misalignment	Limited range and complexity hinder mobile use

2.2. Technical Advancements and Challenges in Far-Field RF Energy Harvesting and Wireless Power Transfer

In RF wireless power transmission (WPT), electrical energy is converted to RF energy, transmitted through free space, and reconverted into electrical energy at the receiver. The transmission distance determines whether the signal operates in near-field or far-field scenarios, defined by the Fraunhofer distance. Far-field WPT involves radiative energy transfer using electromagnetic waves, enabling energy transmission over long distances. Wireless energy harvesting (WEH) in far-field applications captures RF energy from ambient or dedicated RF transmitters [35].

Far-field RF energy harvesting systems use antennas to capture RF signals from ambient sources such as television and radio broadcasts, mobile phones, base stations, and wireless networks, as well as dedicated RF sources. The system architecture, shown in Figure 3, consists of a receiving antenna, an impedance matching network to optimize power transfer, and an RF-DC rectifier that converts RF energy into DC power. This energy powers low-power devices like wearables, medical implants, and sensors. Antennas can be single-band, multiband, or broadband, allowing reception from multiple frequency bands. ISM bands, often used for dedicated RF energy transfer, are regulated by the FCC to ensure safe transmission levels [36]. The Friis transmission equation estimates the received power in a far-field WPT system, considering transmitted and received power, antenna gains, wavelength, and distance. However, it provides only an approximation, as real-world factors like environmental attenuation and signal variability are not accounted for [37].

$$M_r = M_t F_t F_r \left(\frac{\lambda}{4\pi R} \right)^2 \quad (1)$$

where M_r represents received power, M_t is transmitted power, F_t and F_r are transmitting and receiving antenna gains, λ is wavelength, and R is the distance from the transmitting antenna. RF sources are classified as either dedicated or ambient. Dedicated RF sources transmit energy using ISM bands and regulated frequencies, ensuring safe power limits. Ambient RF sources, such as TV and radio towers, offer free energy, but their variability can make energy harvesting less predictable [36,38].

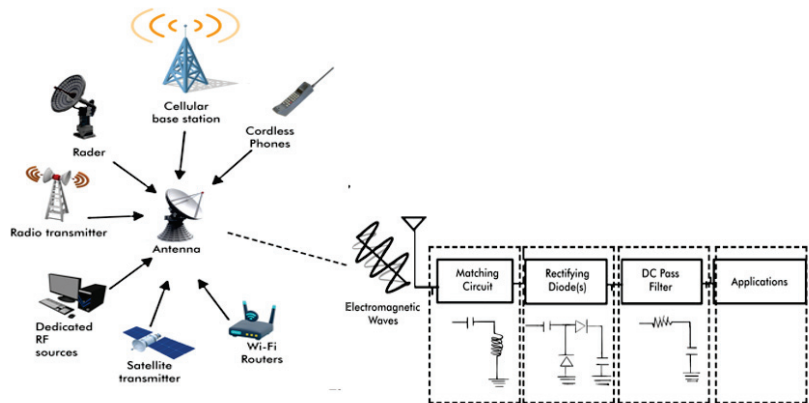


Figure 3. RF energy harvesting architecture.

Certain frequency bands are commonly used for far-field RF energy harvesting, including microwave frequency, UHF (300 MHz to 3 GHz), L Band (1 GHz to 2 GHz), and S-Band (2 GHz to 4 GHz). The efficiency of RF energy harvesting systems depends heavily on the design of key components like impedance matching circuits and RF-DC rectifiers, which maximize power transfer and conversion efficiency.

Long-distance RF energy harvesting is constrained by the inverse-square law, which reduces power density as the distance from the source increases. High-gain antennas are necessary for capturing sufficient energy over long distances. Wideband antennas can collect energy across multiple frequencies, while multiband antennas reduce transmission losses in specific bands. Antenna performance is influenced by gain, bandwidth, and polarization. Omnidirectional antennas are useful for capturing signals from various directions, while unidirectional antennas focus on long-range transmission. Circularly polarized antennas capture signals with varying polarization, but optimizing bandwidth remains key to improving RF power recovery, as ultra-wideband antennas can sometimes reduce efficiency.

Environmental factors, such as atmospheric interference, obstacles, and urban settings, further complicate long-distance RF energy transmission. For example, in dense urban areas, multipath interference can degrade signals due to reflections from buildings. Additionally, atmospheric conditions like humidity and temperature fluctuations attenuate signals, reducing the energy that can be harvested. Developing adaptive antennas and systems that adjust to these conditions will be crucial for improving far-field WPT efficiency.

Despite these challenges, advances in high-gain antenna designs and impedance matching circuits are pushing the boundaries of far-field WPT. These innovations show promise for applications like sensors; space-based solar power, where energy captured in space could be transmitted back to Earth; or for powering IoT networks in remote areas where traditional power infrastructure is unavailable. Continued research to address efficiency losses, safety concerns, and regulatory constraints will be essential to unlocking the full potential of far-field WPT.

Far-field RF energy harvesting also relies on various antenna designs, including linear wire antennas [39], loop antennas [40], array antennas [41,42], microstrip antennas [43], and aperture antennas [44], each contributing to optimizing power transfer over long distances.

3. Antennas Design for RF Energy Harvesting System

Radio frequency (RF) energy harvesting relies on antennas to convert electrical signals into electromagnetic waves and vice versa. Devices like TVs, radios, cell phones, and satellite systems depend on antennas, which vary in design based on frequency, application, and signal characteristics. Impedance matching is a key challenge in rectenna design to maximize power transfer and minimize signal reflections. Antenna gain, bandwidth, and polarization are critical for optimal performance in wireless power transfer (WPT) and RF energy harvesting (RFEH). While high-gain antennas are useful for RF energy harvesting, increasing directivity does not always improve energy capture. The right balance of gain and bandwidth is essential for efficient power recovery from multiple sources. Wideband antennas capture power across multiple frequencies, and multiband antennas generate power more efficiently, avoiding route loss [45].

Antenna gain measures efficiency in transmitting or receiving power in a specific direction. High-gain antennas are essential for RF energy harvesting but are most effective when the energy source is well-known. In some cases, moderate gain suffices if the antenna is well designed [46]. The effectiveness of antennas depends on their pattern, shape, beamwidth, and polarization. Omnidirectional antennas are ideal when the direction of incoming waves is uncertain, while unidirectional antennas suit long-distance transmission. Circularly polarized antennas capture energy from multiple polarizations, while dual linearly polarized antennas reduce polarization mismatch for improved reception [45].

In RF energy harvesting, dipole antennas are widely used for basic rectenna applications, providing broad frequency response [47,48]. Microstrip patch antennas are popular for their low profile and easy fabrication, achieving circular polarization for enhanced energy conversion [49,50]. Monopole antennas, often used in mobile communications and RFID systems, are adaptable for circular polarization [51,52].

For broadband coverage and circular polarization, spiral antennas are effective in radar and wideband communications [53,54]. Yagi-Uda antennas provide high gain and

directionality, making them suitable for point-to-point communications and targeted energy harvesting [55,56]. Horn antennas, common in microwave and satellite communications, support circular polarization and are efficient for high-frequency energy harvesting [54,57]. Slot antennas are compact and suitable for RFID and integrated circuits [58,59]. Parabolic reflector antennas, paired with circularly polarized feed horns, offer extremely high gain for long-range wireless power transfer and satellite communications [60].

Recent advancements include a multiband microstrip patch antenna optimized for LoRa WAN and cellular frequencies, developed using the Coyote Optimization Algorithm, achieving a peak gain of 3.94 dBi [49]. A dual-band receiver antenna developed for energy harvesting at 2.4 GHz and 5.8 GHz reached RF-DC conversion efficiencies of 63% and 54.8% [61].

For compact devices, a small antenna utilizing GSM-900, UTMS2100, and TD-LTE bands was developed to address miniaturization challenges [62]. Multiband and broadband antennas, such as self-complementary slot and patch designs, have been developed to improve RF energy harvesting efficiency by matching rectifier impedance at 2.45 GHz [63]. A triple-band differential antenna targeting frequencies from 2.1 GHz to 3.8 GHz reached maximum efficiencies of 53% and over 59% efficiency at -10 dBm in RF-DC conversion [64,65]. Fractal-based antennas have shown up to 78% RF-to-DC conversion efficiency, making them ideal for compact energy harvesting systems [66].

Miniaturization remains a key challenge for mobile and wearable devices, where small form factors are critical. While high-gain antennas are effective for RF energy harvesting, their size can limit their use in portable systems. Environmental factors such as signal interference and atmospheric conditions also impact energy harvesting efficiency, especially in dense urban environments where multipath interference is common. Designing antennas to adapt to these conditions is crucial for improving long-distance power transmission. Additionally, manufacturing cost is a concern for scaling high-performance antennas for larger applications like IoT networks and wireless sensor systems. Table 3 contains a detailed summary of various multiband and broadband antenna designs for rectenna applications. These antenna designs target different frequency bands and provide high RF-to-DC conversion efficiencies for specific applications, contributing to more efficient energy harvesting systems.

Table 3. Various multiband and broadband antennas for rectenna application.

Antenna	Methodology/ Substrate	Frequency	Size	Gain (dBi)	RF-DC Efficiency	Ref.
Slot	Star antenna on F4B	2.45 GHz 5.8 GHz	133 × 93 mm ²	1.48 dBi @2.4 GHz 3.83 dBi @5.8 GHz	63% @2.4 GHz 54.8% @5.8 GHz	[61]
Monopole	Corrugated mi- crostrip on 0.508 mm R04350, $\epsilon_r = 3.48$	0.9 GHz 2.1 GHz 2.36 GHz	70 × 66 mm ²	1 dBi @0.9 GHz 2.64 dBi @2.1 GHz −0.19 dBi @2.36 GHz	42.2% @0.9 GHz 72.6% @2.1 GHz 32.8% @2.36 GHz	[62]
Meandered	Spiral antenna on FR4	(2.45–2.5 GHz)	32.8 × 9.7 × 0.8 mm ³	2.83 dBi @2.45 GHz	50%	[63]
Circular	Layered circular slot on 1.6 mm FR4, $\epsilon_r = 4.4$	0.908–0.922 GHz 2.35–2.50 GHz	120 × 120 mm ²	5.41 dBi @918MHz 7.9 dBi @2.48 GHz	19%@0.9 GHz 17%@2.45 GHz	[67]

Table 3. Cont.

Antenna	Methodology/ Substrate	Frequency	Size	Gain (dBi)	RF-DC Efficiency	Ref.
Slot	Slot antenna on copper, 1.6 mm FR4, $\epsilon_r = 4.4$	2.1 GHz 2.4–2.48 GHz 3.3–3.8 GHz	120 × 120 × 30 mm ³	7 dBi@2 GHz 5.5 dBi@2.5 GHz 9.2 dBi@3.5 GHz	85%@2 GHz 75%@2.49 GHz 72%@3.4 GHz	[64]
Mono-pole	On 1.6 mm FR4, $\epsilon_r = 4.4$	0.9 GHz 1.8 GHz 2.1 GHz 2.45 GHz	130 × 80 mm ²	2.6 dBi@0.9 GHz 3.6 dBi@1.8 GHz 3.8 dBi@2.1 GHz 4.7 dBi@2.45 GHz	25%@1.8 GHz 27%@2.15 GHz	[65]
Fed square patch	Fractal patch on 1.6 mm FR4	0.8–1.2 GHz 1.6–2.1 GHz 2.2–2.8 GHz 3.1–4.0 GHz 5.3–6.4 GHz 7.0–7.8 GHz	60 × 60 × 1.6 mm ³	1 dBi@900MHz 3 dBi@2 GHz 5 dBi@5.5 GHz 4 dBi@7 GHz	28%@900MHz 24%@2.5 GHz 9%@1.8 GHz 17%@3.5 GHz 13%@5.5 GHz 36%@7.5 GHz	[66]

3.1. Antennas Arrays for Rectenna Design

In RF energy harvesting (RFEH) and wireless power transfer (WPT), antenna arrays outperform single rectennas for higher power needs by improving gain, beam steering, and interference suppression. Their performance depends on element spacing, excitation phase, and amplitude, with larger arrays boosting DC combiner efficiency [47]. Recent designs like printed Yagi [55], square patch [68], and dielectric resonator arrays [69] aim to maximize RF capture. Arrays reduce coupling effects and widen beamwidths, improving efficiency [70]. Some arrays direct RF power to a single rectifier, while others use separate rectifiers for each antenna. Despite advancements, rectifier integration remains a challenge [71]. Ferrite cores and multi-element designs mitigate coupling and maintain multiband performance. Arrays with baffles and reflectors cover 2G, 3G, and 4G bands, optimizing gain and cross-polarization [72].

A Quasi-Yagi array, designed on a Rogers 5880 substrate (0.762 mm thick, relative permittivity 2.2), operates at 2.3–2.63 GHz and is optimized for RFEH. Its compact size (26 mm by 190.5 mm) achieves a peak gain of 8.7 dBi and 25% RF-to-DC conversion efficiency at 2.45 GHz [55]. A stacked microstrip patch array, designed on a 1.6 mm FR4 substrate (relative permittivity 4.4), operates between 3.3 and 3.9 GHz, with a peak gain of 7.8 dBi at 3.5 GHz [68].

The MIMO rectangular patch array, designed on a 1.6 mm FR4 substrate, operates at 2.32 GHz and 2.8 GHz. Despite its relatively low gain (−10.13 dBi), the MIMO configuration improves signal reception and diversity [70]. A dipole antenna array on a Rogers 4350 substrate (0.8 mm thick, permittivity 3.48) operates over 0.76–0.88 GHz, 1.9–2.7 GHz, and 3.3–3.9 GHz. With gains of 6.9 dBi at 0.76 GHz and up to 10.6 dBi at 3.6 GHz, it achieves efficiencies of 57%, 49.5%, and 60.44%, respectively [72].

An antenna system with reflectors and subarrays, designed on a ferrite-loaded substrate (1.0 mm thick, permittivity 15, permeability 1000), operates from 1.7 to 2.7 GHz. It covers 380 mm by 350 mm, with a peak gain of 8.9 dBi [73]. A unidirectional four-patch array, designed on a Rogers 4350 substrate (0.8 mm thick, permittivity 3.48), operates at 2.45 GHz, achieving a peak gain of 12.7 dBi and 81.5% efficiency [74].

A two-element lower band and five-element upper band array on an FR4 substrate operates at 0.69–0.96 GHz and 1.7–2.7 GHz. This array measures 43 mm by 43 mm and provides a peak gain of 14.65 dBi with 35% and 45% efficiency across the bands [75]. A square patch array, providing omnidirectional coverage between 1.65 and 2.76 GHz, achieves a peak gain of 8.5 dBi and 22% efficiency at 2.45 GHz [76]. A twelve-element Vivaldi array, built on a Rogers RT6002 substrate (0.5 mm thick, permittivity 6.15), operates

at 1.7–1.8 GHz and 2.1–2.7 GHz, achieving peak gains of up to 4.33 dBi and efficiency above 60% [77].

Table 4 compares various antenna arrays designed for rectenna applications, detailing their substrates, frequency ranges, dimensions, gains, and efficiencies.

Table 4. Antenna arrays for rectenna applications.

Antenna Array	Methodology/ Substrate	Frequency	Size	Gain (dB)	RF-DC Efficiency	Ref.
Quasi-Yagi	Quasi-Yagi on 0.762 mm Rogers 5880, $\epsilon_r = 2.2$	2.3–2.63 GHz	26 × 190.5 mm ²	8.7 dBi	25% @2.45 GHz	[55]
Stacked Patch	Short pin omni on 1.6 mm FR4, $\epsilon_r = 4.4$	3.3–3.9 GHz	25.7 × 25.7 mm ²	7.8 dBi @3.5 GHz	-	[68]
MIMO Array	Rectangular patch array on 1.6 mm FR4	2.32 GHz 2.8 GHz	100 × 190 mm ²	−10.13 dBi	-	[70]
Dipole	Rogers 4350, 0.8 mm, $\epsilon_r = 3.48$	0.76–0.88 GHz 1.9–2.7 GHz 3.3–3.9 GHz	86 × 125 mm ²	6.9 dBi @0.76 GHz 1.3 dBi @2.3 GHz 10.6 dBi @3.6 GHz	57% 49.5% 60.44%	[72]
Reflector	Ferrite-loaded, 1.0 mm, $\epsilon_r = 15$, $\mu = 1000$	1.7–2.7 GHz	380 × 350 mm ²	8.9 dBi	-	[73]
Four-Patch Array	Unidirectional on 0.8 mm Rogers 4350, $\epsilon_r = 3.48$	2.45 GHz	160 × 160 × 7 mm ³	12.7 dBi	81.5%	[74]
Two-element Array	Unidirectional array on FR4	(0.69–0.96) GHz Lower band (1.7–2.7 GHz) Upper band	43 × 43 mm ²	14.65 dBi	35% Lower band 45% Upper band	[75]
Four Square Patches	Omni antenna on FR4	1.65–2.76 GHz	135 × 135 mm ²	8.5 dBi	22% @2.45 GHz	[76]
Twelve-element Vivaldi Array	Omni antenna on 0.5 mm RT6002, $\epsilon_r = 6.15$	1.7–1.8 GHz 2.1–2.7 GHz	145 × 145 × 1.52 mm ³	4.33 dBi @1.8 GHz 4.22 dBi @2.15 GHz 3.88 dBi @2.45 GHz	>60%	[77]

3.2. Enhancing Rectenna Antenna Performance with Metamaterials Design

Metamaterials, characterized by their engineered electromagnetic properties such as electric permittivity (ϵ) and magnetic permeability (μ), significantly improve antenna functionality. Substrates with negative permeability and permittivity are classified as double-negative (DNG) materials, while those with positive values for both properties are double-positive (DPG). Mu-negative (MNG) materials exhibit negative permeability, and epsilon-positive (EPG) materials show positive permittivity. Single-negative (SNG) materials exhibit negative permittivity or permeability, depending on the specific electromagnetic property [78]. Integrating metamaterials into antenna design enhances performance in RF energy harvesting systems. These materials improve antenna gain and efficiency, facilitating better capture of ambient RF energy. Metamaterials also enable the development of compact antennas with optimized radiation patterns, making them ideal for energy harvesting from specific directions. Their adaptability to varying RF environments enhances antenna effectiveness.

Maxwell's first-order differential equations form the foundation of electromagnetism [79]. The conservation law is written as a continuity equation:

$$I = \oint_A \mathbf{J} \cdot d\mathbf{s} = \frac{\partial}{\partial t} \int_V \rho d\tau \quad (2)$$

In this equation, ω represents angular frequency, \mathbf{H} is the magnetic field, \mathbf{E} is the electric field, \mathbf{B} denotes magnetic flux density, \mathbf{J} is current density, and ρ is charge density. Applying the divergence theorem leads to the differential form of the continuity equation:

$$\nabla \cdot \mathbf{S} = -\frac{d\rho}{dt} \quad (3)$$

Starting from Ampere's law in differential form:

$$\nabla \times \mathbf{B} = \mu_0 \mathbf{J} \quad (4)$$

Taking the divergence of both sides:

$$\nabla \cdot (\nabla \times \mathbf{B}) = \mu_0 \nabla \cdot \mathbf{J} = 0 \quad (5)$$

If there are time-varying charge densities, $\nabla \cdot \mathbf{J} = 0$ is not compatible with the continuity equation. Only in the electrostatic limit is Ampere's law accurate. The addition of displacement current to the RHS provides a more complete solution.

$$\nabla \times \mathbf{B} = \mu_0 (\mathbf{J}_D + \mathbf{J}), \quad \nabla \cdot \mathbf{J}_D = \frac{d\rho}{dt} \quad (6)$$

In the formula for the displacement current, we may apply Gauss' Law to change from ρ to $\nabla \cdot \mathbf{E}$:

$$\nabla \cdot \mathbf{J}_D = \epsilon_0 \frac{d(\nabla \cdot \mathbf{E})}{dt} \quad (7)$$

Eliminating the divergencies:

$$\mathbf{J}_D = \epsilon_0 \frac{d\mathbf{E}}{dt} \quad (8)$$

The displacement current is the electric field's time derivative. Ampere's law, modified with displacement current:

$$\nabla \times \mathbf{B} = \mu_0 \left(\epsilon_0 \frac{d\mathbf{E}}{dt} + \mathbf{J} \right) \quad (9)$$

Therefore, the four differential equations below, sometimes referred to as Maxwell's equations, provide an overview of the rules of electromagnetism:

$$\nabla \cdot \mathbf{E} = -\frac{\rho}{\epsilon_0} \quad \text{Gauss' law to determine } \mathbf{E} \quad (10)$$

$$\nabla \cdot \mathbf{B} = 0 \quad \text{Gauss' law to determine } \mathbf{B} \quad (11)$$

$$\nabla \times \mathbf{E} = -\frac{d\mathbf{B}}{dt} \quad \text{Faraday's law of Induction} \quad (12)$$

$$\nabla \times \mathbf{B} = \mu_0 \left(\epsilon_0 \frac{d\mathbf{E}}{dt} + \mathbf{J} \right) \quad \text{Modified Ampere's law} \quad (13)$$

The electric and magnetic fields for plane waves are determined by:

$$\mathbf{E} = \mathbf{E}_0 e^{-(i\mathbf{k} \cdot \mathbf{r} \mp i\omega t)} \quad (14)$$

$$\mathbf{H} = \mathbf{H}_0 e^{-(i\mathbf{k} \cdot \mathbf{r} \mp i\omega t)} \quad (15)$$

where \mathbf{r} is the distance, and \mathbf{k} is a wave vector that may be represented in terms of the orthogonal system's electric and magnetic fields. The flow of energy is determined by the real portion of the Poynting vector:

$$\mathbf{S}_1 = 0.5\mathbf{E} \times \mathbf{H} \quad (16)$$

Changing the sign of μ_0 and ϵ_0 has no effect on the direction of energy flow. As a result, the group velocity is positive for both left- and right-handed orthogonal systems, and it is given as:

$$n = \pm \sqrt{\epsilon_0 \mu_0} \quad (17)$$

The phase velocity (V_m) is expressed as:

$$V_m = \frac{C}{n} \quad (18)$$

In this equation, V_m represents the phase velocity, n is the refractive index, and C is the speed of light. Forward wave motion results from the fact that energy and waves propagate in the same direction in a right-handed system. Conversely, a left-handed system exhibits a negative value of n , resulting in a corresponding negative phase velocity (V_p) and retrograde propagation of the waves. This reverse propagation increases the reflected wave's intensity.

By virtue of their distinct characteristics, substances possessing negative electric permittivity (ϵ) and positive permeability (μ) are classified as electric plasmas. Surface plasmon generation necessitates the combination of a structured metallic strip, a dielectric coupler, and surface irregularity. Thin metallic filaments that are arranged periodically in a dielectric medium are capable of exhibiting low-frequency stopband characteristics. Rotman investigated diverse wire network configurations capable of producing a controlled negative electric permittivity by resonating with the polarized electric field at frequencies below the plasma frequency. The utilization of a designated formula enables the computation of the effective plasma frequency in this manner [80]:

$$\omega^2 = \frac{2\pi c_0^2}{a^2 \left[\ln \left(\frac{a^2}{4r(a-r)} \right) \right]} \quad (19)$$

Essentially magnetic plasmas, negative materials have positive permittivity (ϵ) and negative permeability (μ). Their magnetic response at optical frequencies is low due to a weak interaction with light's magnetic field, similar to the Bohr magneton. Metallic staples, split-ring resonators (SRRs), nanorods, nanoplates, and strips exhibit negative permeability magnetic responses at high frequencies. The SRR, an inductor–capacitor design, is the most common negative permeability structure. Pendry's sub-wavelength structures have opposing concentric split-ring resonators. Capacitive metal rings collect charges, although circular current cannot travel through their voids.

Analytical formulas can calculate inductance, capacitance, and resonant frequency for complementary split-ring resonators (CSRRs), loop gaps, and SRRs. Spirals, Swiss rolls, squares, and hexagons can also cause negative permeability. Adjusting the geometric characteristics of single and double split-ring resonators can shift SRR resonant frequencies across a wide range. Compactness and tight packing make rectangular SRRs better than circular ones.

The overall capacitance of an SRR circuit is the sum of its upper and lower capacitances divided by the ring gap line. The circuit's resonance frequency can be calculated using the following equation [81]:

$$\omega_{pf} = \sqrt{\frac{2}{\pi r_1 L C_p}} \quad (20)$$

where C_p is the per-unit-length capacitance between the rings, L is the total inductance of the SRR under consideration, and r_1 is the average radius of the SRR under consideration.

Left-handed materials (LHMs), exhibiting both left-handed and right-handed characteristics, are implemented through transmission lines and resonators, specifically as composite right/left-hand metamaterials (CRLHs). The CRLH Transmission Line (CRLH-TL) method uses circuit models to analyze these materials, including three transmission line types: right-handed (RH), left-handed (LH), and CRLH lossless lines. Figure 4a depicts the right-handed transmission line (RH-TL) circuit model, consisting of a series inductor L_R and a shunt capacitor C_R . In this configuration, the right-handed behavior is characterized by positive phase velocity, where energy propagates in the same direction as the wave vector, corresponding to traditional forward-wave transmission. The RH-TL model effectively represents conventional wave propagation and is typically employed in higher-frequency applications. However, it does not support backward-wave propagation, as it is limited to right-handed properties.

Figure 4b shows the left-handed transmission line (LH-TL) circuit model, which is the dual of the RH-TL. It features a shunt inductor L_L and a series capacitor C_L , enabling backward-wave propagation, where the phase velocity is negative. In this model, energy flows in the opposite direction to the wave vector, a phenomenon specific to left-handed materials. Despite its theoretical potential, the practical implementation of purely left-handed structures is hindered by parasitic effects, which cause deviations from ideal performance, particularly at higher frequencies. Figure 4c illustrates the circuit model of a composite right/left-handed transmission line (CRLH-TL), which integrates both right-handed elements (series inductor L_R and shunt capacitor C_R) and left-handed elements (shunt inductor L_L and series capacitor C_L). The CRLH-TL structure offers a solution to the limitations of traditional LH-TL designs by supporting dual-band operation, with backward-wave propagation at lower frequencies due to the LH components and forward-wave propagation at higher frequencies due to the RH components. This model represents a generalized CRLH-TL, where the continuous transition between left-handed and right-handed behavior occurs at the transition frequency, where the phase velocity crosses zero. By mitigating the parasitic effects that affect LH-TLs, the CRLH-TL model enhances the practicality and applicability of transmission line metamaterials in modern technology.

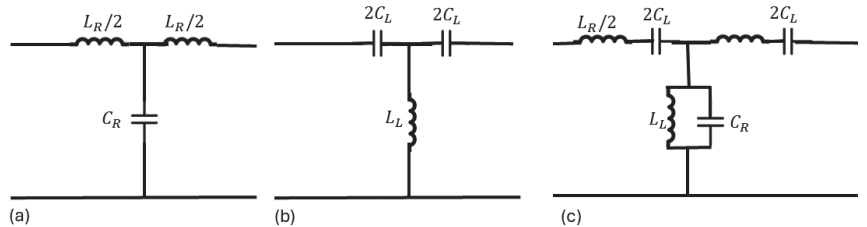


Figure 4. Circuit models for transmission lines in composite right/left-hand metamaterials.

A transmission line's (TL) propagation constant (ρ) is calculated as follows:

$$\rho = \alpha + j\gamma = \sqrt{YZ} \quad (21)$$

where Y and Z denote admittance and impedance, respectively. Using the CRLH-TL, Z and Y can be calculated as follows [82]:

$$Z(\omega) = j \left(\omega L_{R1} - \frac{1}{\omega C_{L1}} \right) \quad (22)$$

$$Y(\omega) = j \left(\omega C_{R1} - \frac{1}{\omega L_{L1}} \right) \quad (23)$$

Therefore, a homogeneous CRLH will exhibit the dispersion relation shown below:

$$\gamma(\omega) = k(\omega) \sqrt{\omega^2 L_{R1} C_{R1} + \frac{1}{\omega^2 L_{L1} C_{L1}} - \left(\frac{L_{R1}}{L_{L1}} + \frac{C_{R1}}{C_{L1}} \right)} \quad (24)$$

where the wavenumber $k(\omega)$ can be determined by:

$$k(\omega) = \begin{cases} -1 & \text{if } \omega < \omega_{l1} = \min\left(\frac{1}{\sqrt{L_{R1} C_{L1}}}, \frac{1}{\sqrt{L_{L1} C_{R1}}}\right) \\ +1 & \text{if } \omega > \omega_{l2} = \max\left(\frac{1}{\sqrt{L_{R1} C_{L1}}}, \frac{1}{\sqrt{L_{L1} C_{R1}}}\right) \end{cases} \quad (25)$$

The phase constant can be real or imaginary, depending on the sign of the radicand. An imaginary phase constant corresponds to a passband where wave propagation occurs, while a real phase constant indicates a stopband where propagation is blocked. CRLH-TL exhibits this stopband behavior, unlike RH-TL and LH-TL. Analyzing LC networks might use SMT chip components or discrete components, but SMT-based CRLHs are limited to lower frequencies and are not suitable for radiating applications. CRLH designs can be applied using CPW, stripline, or microstrip transmission lines [80].

Metamaterial antenna design methods include metamaterial loading, which uses negative ϵ/μ materials and high permeability shells; metamaterial-inspired antennas, such as SRRs and CSRRs; metasurface loading with EBG, RIS, HIS, and FSS technologies; and composite right/left-hand materials, featuring zeroth-order (ZOR) and first resonators [83].

3.2.1. Miniaturization of Antennas Using Metamaterial-Inspired Design

Researchers have made significant strides in miniaturizing antennas by integrating metamaterials such as mu-negative (MNG), epsilon-negative (ENG), and double-negative (DNG) materials into their designs. These materials, known for their engineered electromagnetic properties, allow antennas to maintain or improve performance while reducing size. Metamaterials achieve this by inducing resonant behaviors and generating in-phase currents, which improve radiation efficiency and enable compact designs. Additionally, RLC resonant structures and split-ring resonator (SRR/CSRR) cells help fine-tune antenna characteristics, further optimizing size and performance. The use of metasurfaces and Frequency Selective Surfaces (FSSs) with composite right/left-hand (CRLH) unit cells enhances antenna performance by modifying the electromagnetic field distribution around the antenna, thus reducing physical dimensions without sacrificing gain or bandwidth [81].

The mechanics of miniaturization using metamaterials are primarily based on their ability to alter the effective wavelength of the electromagnetic waves interacting with the antenna. In a conventional antenna, the size is typically related to the wavelength of operation, with longer wavelengths requiring larger antennas. Metamaterials, by introducing negative permittivity (ϵ) or permeability (μ), effectively compress the wavelength within the material, allowing antennas to operate at the same frequency while being physically smaller. This is particularly advantageous for consumer electronics, where space is limited, and compact, efficient antennas are critical.

For instance, a compact, dual-band metamaterial antenna designed for body-centric wireless communication achieves miniaturization through the use of a zeroth-order loop for omnidirectional radiation and a circular patch for unidirectional patterns, allowing it to support both on- and off-body communications. The use of metamaterials to increase substrate permeability allows for the combination of a quarter-wave shorted patch antenna with a T-shaped probe dipole, significantly reducing the antenna's size without compromising performance. This design, which includes a modified split-ring resonator (MSRR) on a Rogers 5870 substrate (0.762 mm thick with a permittivity of 2.33), operates within the 1.7–2.67 GHz frequency range. The antenna measures $0.55\lambda_0 \times 0.363\lambda_0$, delivering a peak gain of 8.51 dBi and an efficiency of 45% [84,85].

Another example involves a complementary split-ring resonator (CSRR) antenna designed on a Rogers RT5800 substrate sourced from Rogers Corporation, located in

Chandler, AZ, USA (1.0 mm thick, permittivity of 2.2). Operating at 1.8 GHz, this antenna has a footprint of $63.8 \times 83.8 \text{ mm}^2$ and achieves a peak gain of 3.1 dBi [86]. The inclusion of SRR/CSRR structures in the antenna design allows for a concentrated electric field in a small area, thereby reducing the physical size of the antenna while maintaining effective radiation characteristics.

Another design incorporates a metasurface with capacitive loading, built on a Rogers 4003C substrate (0.81 mm thick, permittivity of 3.55). This metasurface operates across the 3.02–3.63 GHz frequency range. It achieves a peak gain of 6.57 dBi and has compact dimensions of $0.58\lambda_0 \times 0.58\lambda_0 \times 0.043\lambda_0$. The metamaterial-based design enables the antenna to miniaturize while maintaining high performance, with efficient radiation patterns suitable for various wireless applications [87].

Metamaterials are particularly useful in dual-band antennas, as demonstrated in a GPS antenna array with broadside coupled split-ring resonators (BC-SRRs) and mu-negative (MNG) metamaterials. This design reduces mutual coupling in the L band, which enhances performance and reduces the antenna footprint. The use of metamaterials in this context not only improves the radiation efficiency but also significantly shrinks the overall size of the antenna, making it more suitable for compact systems [88].

In summary, the integration of metamaterials into antenna design enables significant size reduction by altering the propagation characteristics of electromagnetic waves. By compressing the effective wavelength within the metamaterial, antennas can be miniaturized without losing efficiency or performance. This innovation is crucial for developing compact antennas for wireless energy harvesting, wearable devices, and IoT applications, where space constraints and performance demands are high.

Table 5 provides a summary of the various metamaterial-inspired miniaturization methods, detailing the designs, materials used, frequency ranges, gains, and the corresponding size reductions achieved through these techniques.

Table 5. Metamaterial-inspired miniaturization methods.

Methodology/ Substrate	Frequency	S ₁₁ width (%)	Band- width (%)	Maximum Effi- ciency (%)	Gain (dB)	Size	Ref.
CRLH materials on 1.0 mm RT5800, $\epsilon_r = 2.2$.	2.45 GHz 5.8 GHz	-		65	1.5 dBi @2.4 GHz 5.2 dBi @5.8 GHz	30 mm radius	[84]
MSRR on 0.762 mm Rogers 5870, $\epsilon_r = 2.33$.	1.7–2.67 GHz	44.1		45	8.51 dBi	$0.55\lambda_0 \times 0.36\lambda_0$	[85]
CSRR on 1.0 mm RT5800, $\epsilon_r = 2.2$.	1.8 GHz	16		-	3.1 dBi	$63.8 \times 83.8 \text{ mm}^2$	[86]
Capacitive metasurface on 0.8 mm Rogers 4003C, $\epsilon_r = 3.55$.	3.02–3.63 GHz	8.5		-	6.57 dBi	$0.58\lambda_0 \times 0.58\lambda_0 \times 0.043\lambda_0$	[87]
SRRs on 1.0 mm Rogers 3010, $\epsilon_r = 10.2$.	3.02–3.63 GHz	8.5		-	6.57 dBi	$4.3\lambda_0 \times 4.3\lambda_0$	[88]

3.2.2. Bandwidth and Gain Enhancement Antenna Using Metamaterial-Inspired Designs

Metamaterials significantly improve antenna performance by enhancing both bandwidth and gain. Bandwidth enhancement is achieved through techniques such as using thick, low-permittivity substrates, multi-layer designs, and advanced geometries. A thicker substrate increases the storage and radiation of electromagnetic energy, thereby widening the bandwidth. For example, a thick substrate provided a bandwidth of 58.8% (2.11–3.87 GHz) while maintaining omnidirectional radiation and low cross-polarization [89]. Multi-layer structures and innovative geometries, such as fractal designs, allow the antenna to operate across a wider frequency spectrum by supporting multiple resonances.

Gain enhancement is achieved by employing metamaterial-based designs, such as stacked microstrip patches, fractal geometries, and gap-coupling techniques. These innovations focus more electromagnetic energy in a specific direction, increasing efficiency and reducing back radiation. Stacked microstrip patches expand the effective radiating area of the antenna without increasing its physical size, while fractal geometries enable multi-frequency resonance by exploiting their self-similar structure. Gap-coupling improves impedance matching between the antenna and the transmission line, minimizing reflection losses and further boosting gain. Additionally, metamaterial lenses and artificial magnetic conductors (AMCs) enhance gain by shaping and focusing the electromagnetic field, which is particularly valuable for low-frequency antennas.

In low-frequency applications, unidirectional loop antennas integrated with mu-negative (MNG) metamaterials and symmetric split-ring resonators (SSRRs) deliver consistent gain and wide bandwidth by carefully controlling the electromagnetic field distribution, thereby minimizing energy losses. Slotless ground planes and near-zero index metamaterial structures (NZIMSs) further improve performance by optimizing directivity and reducing the antenna's physical footprint. NZIMSs work by altering the wave's phase velocity, which makes it easier to achieve high-gain, narrow-beamwidth characteristics in a compact design [68].

Recent advancements in metamaterial-based antenna designs have demonstrated significant improvements in key performance metrics. A prime example is the zeroth-order resonator (ZOR) antenna, which employs a Rogers RO4003C substrate (0.81 mm thick, permittivity 3.55). Operating between 348 and 772 MHz, the ZOR antenna achieves a bandwidth of 78% and a gain of 9.2 dBi. Its compact dimensions of $0.46\lambda_0 \times 0.46\lambda_0$ make it highly effective for low-frequency applications, where large antenna sizes are typically required [90]. The ZOR design takes advantage of metamaterial properties to reduce the effective wavelength within the structure, enabling resonance with a much smaller physical size.

Another design incorporates split-ring resonators (SRRs) on an FR4 substrate (1.6 mm thick, permittivity 4.4). Covering a wide frequency range from 0.865–1.06 GHz to 4.9–6.5 GHz, this multiband antenna achieves a gain of 6.74 dBi, with compact dimensions of $78.6 \times 42.5 \text{ mm}^2$. This versatility makes it well-suited for various energy harvesting applications [91]. The SRR structures enable efficient operation over multiple frequency bands by creating strong localized resonances, improving the antenna's multiband performance.

A metamaterial-loaded antenna, constructed on a Rogers 6010 substrate (0.635 mm thick, permittivity 6.15), operates at 0.915 GHz and 2.45 GHz, offering bandwidths of 17.8% and 35.8%, respectively. With gains of 17.8 dBi and 9.81 dBi, the compact dimensions of $7 \times 6 \times 0.254 \text{ mm}^3$ highlight the effectiveness of metamaterials in boosting both bandwidth and gain [92]. The metamaterial loading improves energy concentration, ensuring high gain despite the compact antenna size.

Lastly, an antenna employing near-zero-index metamaterials on an FR4 substrate (1.6 mm thick, permittivity 4.6) operates at 0.534 GHz, offering a bandwidth of 2.11% and an efficiency of 74.1%, with a gain of 7.27 dBi and dimensions of $170 \times 170 \text{ mm}^2$. NZIMSs enhance the effective aperture size without increasing the physical footprint, making this design particularly effective for low-frequency applications, where large antenna sizes typically limit performance [93].

Table 6 summarizes the various bandwidth and gain enhancements achieved through metamaterial-inspired designs, demonstrating the effectiveness of these technologies in improving antenna performance across different frequency ranges and applications.

Table 6. Antenna gain and bandwidth enhancement methods.

Methodology/ Substrate	Frequency	S_{11}	Band- width (%)	Maximum Efficiency (%)	Gain (dBi)	Size	Ref.
ZOR on 0.81 mm RO4003C, $\epsilon_r = 3.55$	348–772 MHz	78	NA	9.2 dBi	$0.46\lambda_0 \times 0.46\lambda_0$	[90]	
SRRs on 1.6 mm FR4, $\epsilon_r = 4.4$	0.865–1.06 GHz 2.240–2.52 GHz 3.25–4.31 GHz 4.9–6.5 GHz	28	NA	6.74 dBi	$78.6 \times 42.5 \text{ mm}^2$	[91]	
Metamaterial on 0.635 mm Rogers 6010, $\epsilon_r = 6.15$	0.915 GHz 2.45 GHz	17.8% 35.8%	NA	17.8 dBi@0.915 GHz 9.81 dBi@2.45 GHz	$7 \times 6 \times 0.254 \text{ mm}^3$	[92]	
Near-zero-index on 1.6 mm FR4, $\epsilon_r = 4.6$	0.534 GHz	2.11%	74.1%	7.27 dBi	$170 \times 170 \text{ mm}^2$	[93]	

3.2.3. Circular Polarization of Antenna Using Metamaterial-Inspired Design

The effectiveness of RF energy harvesting systems is closely tied to antenna polarization, which can be either linear or circular, depending on the orientation of the electric field. Circular polarization is particularly beneficial in RF systems, as it allows antennas to capture signals from multiple orientations and mitigate polarization mismatches that commonly occur in dynamic environments. This results in more stable signal reception, especially in systems prone to multipath interference or rapidly changing signal directions. Proper alignment between the transmitter and receiver antennas minimizes cross-polarization losses, which occur when the electric fields of the antennas are misaligned.

Metamaterial structures play a crucial role in enhancing circular polarization by enabling compact antenna designs with improved performance. Metamaterials allow antennas to maintain or even increase gain while reducing size and broadening bandwidth. Additionally, metamaterials help address polarization issues by mitigating Faraday rotation, which can distort the polarization of signals as they propagate through the atmosphere. By incorporating metamaterials, antennas can achieve circular polarization with improved signal strength, often increasing gain by 3 dB.

For instance, a metamaterial-loaded cavity antenna using Rogers RT6010 and Rogers 5880 substrates with thicknesses of 0.635 mm and 0.762 mm, respectively, and permittivities of 6.15 and 2.2, operates across the frequency range of 9.7 GHz to 10.27 GHz. This design achieves an efficiency of 6.0% and a bandwidth of 74.1%, with a peak gain of 14.1 dBi. The metamaterials in this configuration significantly enhance the antenna's circular polarization performance, allowing for higher efficiency and gain [75].

An electromagnetic bandgap (EBG) structure, fabricated on an FR4 substrate with a thickness of 1.0 mm and a permittivity of 3.5, operates at two distinct frequencies: 12.5 GHz and 14.2 GHz. This structure achieves gains of 6.0 dBi and 4.3 dBi, respectively, with an overall efficiency of 47.7%. The total gain at these frequencies reaches 23.1 dBi and 24.4 dBi. The use of an EBG structure helps control electromagnetic wave propagation, improving circular polarization and making the design suitable for high-frequency applications [79]. Metamaterial elements in the EBG structure, such as split-ring resonators (SRRs), contribute to the effective manipulation of electromagnetic fields, facilitating improved polarization control.

Another design, a frequency-agile near-field resonator antenna, incorporates parasitic elements on a Rogers 5880 substrate with a thickness of 0.762 mm and a permittivity of 2.2. Operating at 1.39 GHz, this antenna achieves an efficiency of 3.92% and a gain of 5.92 dBi. The parasitic elements enable the antenna to dynamically adapt to different operational frequencies while maintaining stable circular polarization. This design underscores the

effectiveness of metamaterials in creating adaptable, high-performance antennas for RF energy harvesting systems [94].

In summary, metamaterials enable significant advancements in the deployment of circularly polarized antennas by improving gain, enhancing bandwidth, and reducing size. Through the use of engineered electromagnetic properties, such as negative permittivity and negative permeability, metamaterial-based designs offer superior control over the electromagnetic field, allowing antennas to operate more efficiently in challenging RF environments. These improvements are essential for applications in wireless energy harvesting, satellite communications, and IoT systems, where polarization stability and compact designs are critical. Table 7 provides a summary of the operating frequency, bandwidth, maximum efficiency, and gain for circularly polarized metamaterial-enhanced designs, highlighting the key performance metrics achieved through these innovations.

Table 7. Circular polarization antenna for rectenna.

Methodology/Substrate	Frequency	S ₁₁ Bandwidth (%)	Maximum Efficiency (%)	Gain (dB)	Size	Ref.
Metamaterial cavity on 0.635mm RT6010, 0.762 mm Rogers 5880, $\epsilon_r = 6.15/2.2$.	9.7–10.27 GHz	6.0	74.1	14.1 dBi	NA	[75]
EBG on 1.0 mm F4B, $\epsilon_r = 3.5$.	12.5 GHz 14.2 GHz	6.0 4.3	47.7	23.1 dBi 24.4 dBi	150 × 150 mm ²	[79]
Agile resonator with parasitics on 0.762 mm Rogers 5880, $\epsilon_r = 2.2$.	1.39 GHz	3.92	NA	5.92 dBi	NA	[94]

3.2.4. Metamaterial Enhancement of Isolation and Mutual Coupling Reduction in Antenna for Multi-Port Rectenna

Maintaining proper separation between components is crucial for minimizing mutual coupling in multi-port rectenna systems. Mutual coupling occurs when energy radiated from one antenna element interferes with another, leading to performance degradation through reduced efficiency, increased signal interference, and lower data rates. Metamaterials, such as Electrically Neutral Material (ENG), Magnetically Neutral Material (MNG), and Dielectrically Neutral Material (DNG), provide effective decoupling elements when integrated into antenna designs to address these issues.

For example, a Metastrip antenna, fabricated on a Rogers 5880 substrate with a thickness of 0.762 mm and a permittivity of 2.2, operates at 28 GHz. This design achieves a gain of 20.12 dBi and provides a peak gain of 8 dBi, with a bandwidth of 22%, and an efficiency of 24%. This setup demonstrates the effectiveness of Metastrip technology in high-frequency applications [60].

Other strategies to mitigate mutual coupling include using metasurface structures to reduce surface wave propagation and enhance isolation. Near-field resonator structures, such as split-ring resonators (SRRs) and complementary split-ring resonators (CSRRs), also prevent antenna coupling. Additionally, composite right/left-handed (CRLH) structures generate reverse currents, effectively reducing mutual coupling between antennas [95].

In beamforming applications, a printed antenna array with CSRRs operating at 25 GHz effectively reduces mutual coupling while preserving the array's radiation pattern without altering the antenna profile. This design was developed using simulation tools like Ansys HFSS version 2022 R and MATLAB Version R2023a. Furthermore, integrating a metamaterial superstrate with modified CSRRs significantly suppresses coupling between microstrip phased array elements, providing a compact and easily applicable solution for performance enhancement in various high-frequency applications [96].

A CSRR with a slot, constructed on a Rogers 6010 substrate with a thickness of 0.635 mm and a permittivity of 6.15, operates at 3.6 GHz. This design achieves a gain of

27 dBi and an efficiency of 3.59%, with a bandwidth of 35% and a peak gain of 52 dBi. This configuration highlights the use of CSRRs with slot technology to enhance antenna performance characteristics, especially in terms of gain and efficiency [97].

In summary, metamaterials provide a robust solution for reducing mutual coupling in multi-port rectenna systems, improving isolation and preserving antenna performance. By integrating elements such as SRRs, CSRRs, and CRLH structures, metamaterial-enhanced designs offer improved efficiency, higher gain, and greater bandwidth, making them ideal for advanced MIMO systems in high-frequency applications. Table 8 provides a summary of mutual coupling reduction methods and how they improve multi-port rectenna performance, detailing the key metrics like gain, bandwidth, efficiency, and isolation.

Table 8. Isolation and mutual coupling method to improve the multi-port rectenna.

Methodology/Substrate	Frequency	S ₁₁ Bandwidth (%)	Maximum Efficiency (%)	Gain (dBi)	In Band Iso-lation (dB)	Peak Isolation (dB)	Ref.
Metastrip on 0.762 mm Rogers 5880, $\epsilon_r = 2.2$.	28 GHz	20.12	NA	8 dBi	22	24	[60]
EBG/DGS on 0.76 mm TLY-5 ($\epsilon_r = 2.2$) and 1.6 mm FR4 ($\epsilon_r = 4.4$).	28 GHz	47.7	81.9%	9 dBi	32.7	71.9	[95]
CSRR on 0.762 mm Rogers 5880, $\epsilon_r = 2.2$.	25 GHz	31.8	NA	NA	32	55	[96]
CSRR with slot on 0.635 mm Rogers 6010, $\epsilon_r = 6.15$.	3.6 GHz	27	3.59	NA	35	52	[97]

4. Impedance Matching Network (IMN) of Antenna and Rectifier

Impedance matching is a critical area of study in virtually all fields of electronics. Effective termination is crucial for minimizing reflections and maintaining signal integrity, particularly for communication and energy harvesting applications where signal transmission is essential [98]. In an RF network, impedance mismatch causes power to be reflected back to the source from the boundary. This reflection creates a standing wave instead of transferring energy to the load [99].

Achieving optimal performance for antennas, such as improving return loss, efficiency, and gain, involves addressing impedance matching, a challenging phase in the design process. Moreover, impedance matching simplifies tuning the antenna's frequencies faster than altering its design. The additional resonances introduced by impedance matching circuits also improve the antenna's bandwidth [100].

In rectifiers that incorporate diodes and transistors, the impedance fluctuates with frequency due to their nonlinear nature. This variation makes it difficult to match a standard 50-ohm antenna to an RF-DC rectifier [101]. The reflection coefficient equation, described in [102], is used to represent the electrical signal reflection resulting from this impedance mismatch:

$$Y = S_{11} = S_{22} = \frac{Z_{\text{rect}} - Z_{\text{ant}}^*}{Z_{\text{rect}} + Z_{\text{ant}}^*} \quad (26)$$

It is commonly referred to as the S_{11} parameter or reflection coefficient. Here, Z_{rect} denotes the rectifier's impedance, which is represented as $R_1 + X_1$, and Z_{ant} represents the antenna impedance, expressed as $R_2 + X_2$. Additionally, Z_{ant}^* is the complex conjugate of the antenna impedance. The reflection coefficient Y is always less than or equal to 1.

In radio frequency energy harvesting (RFEH) systems, L, T, and π -matching networks [103] are commonly used impedance matching circuits. These circuits consist of inductors and capacitors arranged in L, T, and π shapes to match the load impedance at a desired frequency.

Impedance matching for antennas can also be achieved using the distributed impedance matching technique [104]. This technique involves making structural adjustments to the antenna using stubs, single- and multi-section quarter-wave transformers, tapered lines, baluns, and active components. A key advantage of the distributed impedance matching

technique is that it does not require altering the geometry of the radiating structure. As a result, the radiation efficiency of the antenna remains unaffected by the matching network, thereby simplifying the design process. However, this method increases the antenna's size, making it less ideal for practical array systems. Additionally, the extra circuitry added to the matching network may increase spurious radiation losses, reducing system efficiency.

The impedance matching network (IMN) has unique challenges due to the very low and changing levels of input power. The input to the IMN is the rectifier's nonlinear load impedance, which varies with the power received by the antenna. Meanwhile, the antenna provides the IMN's source impedance, which is not necessarily 50 ohms. Therefore, the IMN must be designed for a specific level of received power and may not be optimal at varying power levels [105].

5. Rectifier Design for Wireless Energy Scavenging/Wireless Power Transfer System

Radio frequency energy harvesting (RFEH) devices use rectifiers to convert RF signals into direct current (DC) signals. The main obstacles in RFEH technology are the low power density of RF waves and inefficient harvesting circuits. To enhance the output DC power, multiband and broadband rectifiers (BBRs) have been developed [106]. However, the performance of rectifiers can be impacted by variations in ambient electromagnetic (EM) radiation.

Rectifier design employs various strategies to reduce the influence of input power variations. Rectifiers are categorized based on several factors, including topology, operating frequency (broadband, single band, multiband), impedance matching, type of combiner, feeding antenna, and power level (low, medium/high power, or wide input power dynamic range). As shown in Figure 5, rectifier designs vary according to their intended operational requirements.

A rectifier's performance can be assessed using factors like sensitivity, power conversion efficiency, and power dynamic range. Sensitivity refers to the amount of input power needed to produce a 1 V DC output at the expected load. The rectifier's effectiveness can decline as these factors change, primarily due to the nonlinearity of the Schottky diode or CMOS in the circuit. Variations in RF input power and frequency can affect the rectifier's input impedance, causing mismatches that reduce power conversion efficiency. Ensuring consistent activation and performance of the RFEH system in practical applications depends on addressing these issues [21].

The formula for estimating the sensitivity of the rectifier is given below [107]:

$$S_{\text{dBm}} = 10 \times \log_{10}(P_s) \quad (27)$$

Rectifier sensitivity (S_{dBm}) is in dBm, and power received (P_s) is in milliwatts (mW).

The power conversion efficiency (PCE) of a rectifier is the ratio of the DC output power to the RF input power [108]:

$$P_{\text{eff}} = \frac{P_{\text{DC1}}}{P_{\text{re}}} = \frac{\left(\frac{V_1^2}{R_L}\right)}{100 \times \mu W} \quad (28)$$

where P_{eff} denotes the rectifier's power conversion efficiency (PCE), P_{DC1} the output DC power, R_L the load resistance, V_1 the rectifier's output DC voltage, and P_{re} the RF power received by the rectifier.

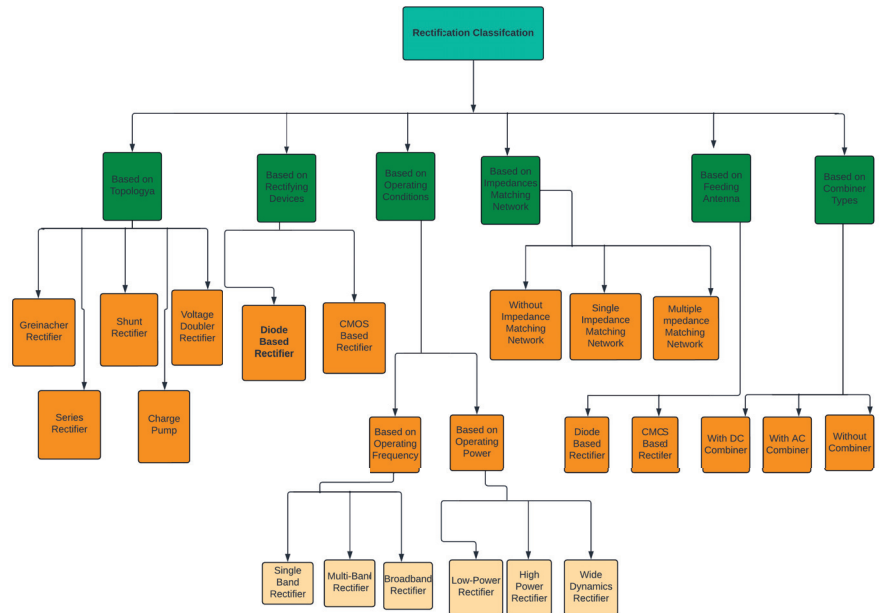


Figure 5. Classification of rectifiers.

The power dynamic range (PDR) of a rectifier is the input power range in which the rectifier maintains a PCE greater than 20%. This is significant because, in an RF environment with changing power densities, the greater the range, the more dependable the rectifier will be [109]:

$$P_{DR} = \{100\% \geq P_{eff} \geq 20\%\} \quad (29)$$

A PDR in the rectifier is critical for ensuring the RFEH system's dependability in an RF environment. The voltage produced from rectification is usually too low to power electronics. In RFEH systems, rectifiers are often used alongside DC–DC voltage conversion technologies like voltage multipliers, charge pumps, or voltage boosters to raise output DC voltage for electronic devices.

5.1. Circuit Design of CMOS Rectifier

RF rectifying transistors operate as three-terminal switches or diodes to correct signals, needing extra gate voltage. In recent CMOS rectifier designs, significant improvements have been made in performance and efficiency. A CMOS differential rectifier, operating at 2.4 GHz on a 0.508 mm thick Rogers substrate, occupies an area of 1.5×0.47 mm² and achieves a dynamic range of 25.5 dB with an efficiency of 46% [90]. The CMOS Villard multiplier rectifier operates at both 400 MHz and 2.4 GHz, achieving an efficiency of 75% [106].

In comparison, a CMOS passive rectifier working at 0.2 GHz takes up 0.88 mm² of space, offering a dynamic range from –4 to 7 dB and reaching an efficiency of 70.3% [110], while a 434 MHz differential CMOS bootstrap rectifier achieves 71% PCE [111]. RF energy harvesting technology has advanced with a cross-coupled differential-drive (CCDD) rectifier with PCE > 40%, automated design optimization using Deep Neural Networks, and a co-design approach for RF harvester matching networks and rectifiers to maximize PCE [112].

The CMOS bootstrap rectifier, operating at 0.433 GHz with a 0.30 mm² area, features a dynamic range of –6 to 6 dB and achieves 71% efficiency at 3 dBm [111]. Another notable design, the cross-coupled CMOS rectifier, functions at 2.45 GHz with an area of 0.90 mm²

and has a dynamic range of -5 to 7 dB, achieving efficiencies of 73% at -6 dBm and 70.4% at -5.5 dBm [113].

The CMOS-CCDD rectifier, with a frequency of 0.9 GHz and unspecified area, covers a dynamic range of -21 to 13 dB and offers efficiencies of 83.7% at -18.4 dBm and 80.3% at -17 dBm [114]. The double-sided CMOS rectifier, also at 0.9 GHz, features a compact area of 0.088 mm 2 and achieves 66% efficiency [115]. The CMOS reconfigurable rectifier operates at 0.9 GHz with a 25% efficiency [116]. Meanwhile, a CMOS rectifier functioning at 6.78 MHz covers an area of 8 mm 2 and achieves a high efficiency of 92.2% [117].

These advancements in CMOS rectifier technology highlight a range of designs, each offering different balances of frequency, area, efficiency, and dynamic range to meet various application needs in modern electronics, as shown in Table 9.

Table 9. Overview of CMOS rectifier designs for wireless energy scavenging.

Design	Frequency	Efficiency (%)	Dynamic Range (dB)	Area (mm 2)	Ref.
CMOS Differential Rectifier	2.4 GHz	46%	25.5	1.5×0.47	[90]
CMOS Villard Multiplier Rectifier	400 MHz/ 2.4 GHz	75%	NA	NA	[106]
CMOS Passive Rectifier	0.2 GHz	70.3%	-4 to 7	0.88	[110]
CMOS Bootstrap Rectifier	434 MHz	71%	-6 to 6	0.30	[111]
Cross-Coupled CMOS Rectifier	2.45 GHz	73% (-6 dBm) 70.4% (-5.5 dBm)	-5 to 7	0.90	[113]
CMOS-CCDD Rectifier	0.9 GHz	83.7% (-18.4 dBm) 80.3% (-17 dBm)	-21 to 13	NA	[114]
Double-Sided CMOS Rectifier	0.9 GHz	66%	NA	0.088	[115]
CMOS Reconfigurable Rectifier	0.9 GHz	25%	NA	NA	[116]
CMOS Rectifier	6.78 MHz	92.2%	NA	8.0	[117]

5.2. Circuit Design of Schottky Diode Rectifier

A nonlinear Schottky diode is used in the rectifying circuit for RF-to-DC conversion. Understanding the impedance characteristics of this diode is crucial for designing an appropriate matching circuit. The goal is to determine the diode's equivalent circuit model and, using small-signal analysis, understand its impedance behavior. The process for creating an effective rectifier involves selecting a suitable Schottky diode based on the available power level, and then analyzing its impedance behavior.

The design steps for an efficient rectifier are illustrated in Figure 6a. The primary determinant in choosing a diode is the available power level. The maximum diode efficiency versus input power is shown in Figure 6b. The breakdown voltage and threshold voltage of the diode limit the power handling capacity of the rectifier.

Once a suitable Schottky diode is selected, its impedance behavior is analyzed. Figure 7 shows the small-signal model of the diode, highlighting the junction resistance (R_j) and junction capacitor (C_j), which contribute to the diode's nonlinearity. The parasitic series resistance (R_s) and inductance (L_p) are also considered.

The series resistance R_s of the Schottky diode is given by:

$$R_s = \frac{nkT}{q(I_{s1} + I_b)} \quad (30)$$

where n is the ideality factor, k is the Boltzmann constant, T is the temperature, q is the electronic charge, I_{s1} is the saturation current, and I_b is the bias current.

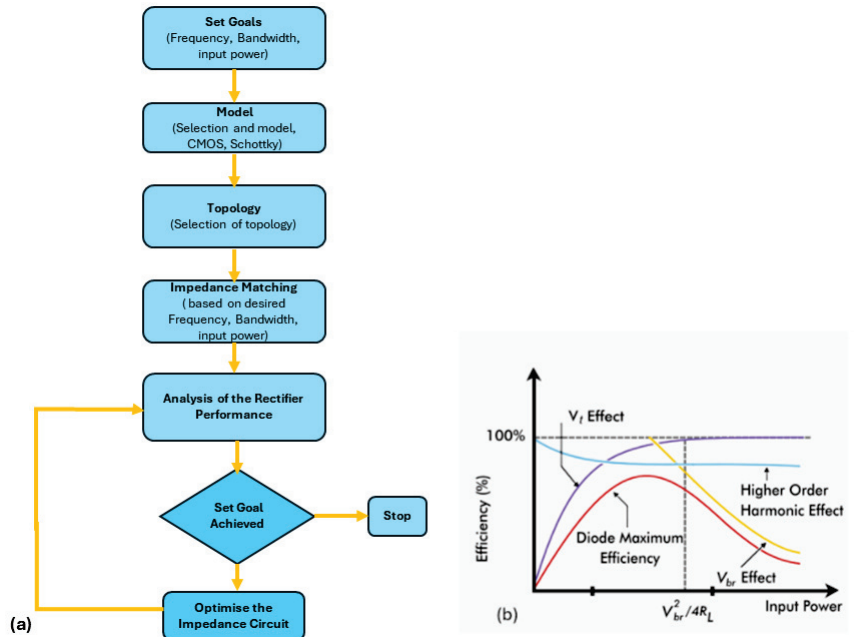


Figure 6. (a) Flowchart of rectifier design (b) Input power and efficiency analysis.

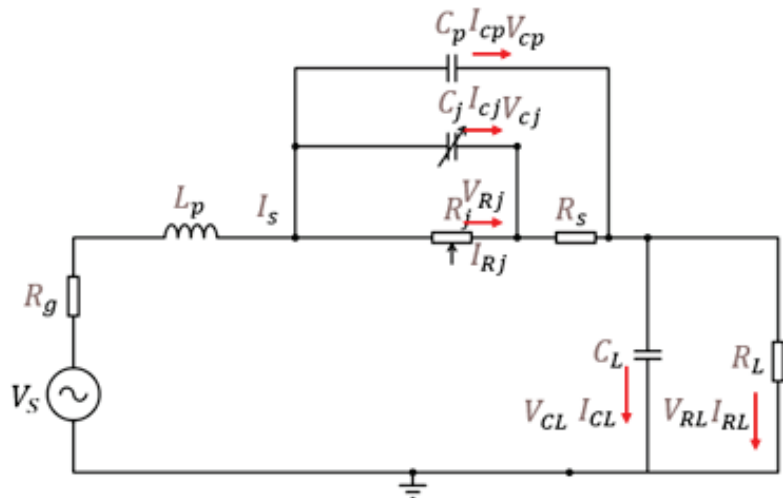


Figure 7. Equivalent circuit for single-diode model.

The junction capacitance C_j is defined as:

$$C_j = \begin{cases} \frac{C_{j0}}{\sqrt{1 + \frac{V_{cj}}{V_{Rj}}}} + C_{d1} & \text{when } V_{cj} > 0 \\ \frac{C_{j0}}{\sqrt{1 + \frac{V_{cj}}{V_{Rj}}}} & \text{for the second case when } -V_{on} \leq V_{cj} \leq 0 \end{cases} \quad (31)$$

where C_{j0} is the zero-bias junction capacitance, V_{cj} is the junction voltage, V_{Rj} is the reverse breakdown voltage, and C_{d1} is the diffusion capacitance.

Schottky diodes, with metal–semiconductor junctions, offer lower threshold voltages than semiconductor–semiconductor junctions, outperforming p–n junction diodes in I–V characteristics with a 4:1 reverse bias breakdown voltage and a forward bias turn-on voltage around 0.2 V. Engineering challenges in rectifiers involve generating usable output voltage from low input power, with Schottky diodes preferred for their low-voltage application suitability and high-speed operation due to their unipolar nature, avoiding charge storage issues of bipolar diodes [76].

Schottky diodes, characterized by their lower metal–semiconductor (MS) barrier height compared to PN diodes, are the go-to choice for low-voltage applications due to their unipolar nature. This feature enables high-speed operations free from the charge storage issues seen in bipolar PN junction and PIN diodes, with capacitive loading being the primary factor affecting switching speed. The operational efficiency of Schottky diodes, determined by conduction resistance, junction capacitance, and saturation current, benefits significantly from their low turn-on voltage. However, elevated voltages can induce nonlinearity, leading to the generation of significant harmonic signals that detract from RF-to-DC conversion efficiency.

Owing to their fast-switching capabilities and minimal voltage drop in comparison to traditional p–n diodes, various microwave Schottky diode models such as HSMS-2852, HSMS-2822, HSMS-285C, HSMS-2860, and SMS7630 have been tailored to meet specific application needs across different sectors [66]. The HSMS-286C double diode, built on a Rogers4350B substrate, operates within a frequency range of 2 to 3.05 GHz. It has dimensions of $25 \times 13 \text{ mm}^2$ and achieves 60% efficiency at 17 dBm, with load values ranging from 620 to 2700 ohms [60].

Another notable design is the HSMS-2820 full-wave voltage doubler, built on an FR4 substrate. This device supports multiple frequencies: 0.9 GHz, 1.8 GHz, 3.5 GHz, 5.5 GHz, and 7.3 GHz, and provides efficiencies greater than 78% over a power range of –10 to 30 dBm, with a load of 5 kΩ [66].

The HSMS-286 half-wave rectifier, also using a Rogers4350 substrate, operates between 2 and 3 GHz, with dimensions of $36 \times 35 \text{ mm}^2$. It delivers efficiencies exceeding 40% at 10 dBm and handles power levels from 0 to 10 dBm, with a load of 400 ohms [75].

The SMS7630 voltage doubler, constructed on an RT6002 substrate, operates within the frequency ranges of 1.7–1.8 GHz and 2.1–2.7 GHz. It achieves efficiencies between 55% and 65% and has dimensions of $145 \times 145 \times 1.52 \text{ mm}^3$, with a load of 2 kΩ [77]. For higher-frequency applications, the HSMS-2860 shunt series diode, using a RO4003C substrate, functions at 2.38 GHz and 2.45 GHz. It handles power levels from –20 to 10 dBm and achieves an efficiency of 75.3% [118]. The SMS7630-079 single-series diode, featuring a Rogers5880 substrate, operates at 1.8 GHz, with efficiencies of 21.1% at –20 dBm and 6.9% at –30 dBm, and has a load of 6 kΩ [119].

The HSMS-285C rectifier, available as both a 1-stage and 3-stage Dickson rectifier and built on an FR4 substrate, operates at 1 GHz, achieving a high efficiency of 77% with a load of 14.61 kΩ [120]. For frequencies up to 26.5 GHz, the MA4E-1319 full-wave voltage doubler, using a textile substrate, provides 12% efficiency at 10 dBm, with dimensions of $32.6 \times 16 \text{ mm}^2$ and a load of 630 ohms [121].

A self-tunable artificial transmission line combining the HSMS-2820 and HSMS-2850 diodes on a Taconic RF-35 substrate operates at 0.9 GHz, achieving 70% efficiency with an impedance of 390 ohms [122]. The HSMS-2860 branch two voltage doubler, employing

a Rogers5880 substrate, functions at 0.866 GHz, 0.915 GHz, and 2.45 GHz, delivering efficiencies of 65%, 62%, and 60%, respectively, with a load of 10 kΩ [123].

The SMS7630 multiple diode configuration on a Rogers5880 substrate covers frequencies from 1.84 GHz to 5.8 GHz, offering efficiencies ranging from 28.3% to 65%, depending on the frequency [124]. The HSMS-285C Greinacher full-wave rectifier, with an FR4 substrate, operates at 1.85 GHz and provides 40% efficiency with a load of 4.7 kΩ [125].

The HSMS-2862-TRI diode, a voltage doubler using a RogersRO3003 substrate, functions across a broad frequency range from 0.06 GHz to 3.8 GHz, achieving an efficiency of 77.3% [126]. The combined HSMS-2862 and SMS7630 voltage doubler on an FR4 substrate operates at 0.915 GHz, 1.8 GHz, and 2.4 GHz, delivering efficiencies of 74.9%, 71.2%, and 60%, respectively, with dimensions of $24 \times 8.8 \text{ cm}^2$ and a load of 1500 ohms [127].

Summary of Schottky Rectifier Radio Frequency Energy Harvesters

Table 10 highlights several performance metrics for Schottky rectifiers used in RF energy harvesting systems. The significant findings include high power conversion efficiency (PCE) at specific frequencies and high input power levels. Schottky rectifiers have a low turn-on voltage, making them highly efficient for harvesting low-power RF signals. Additionally, some have compact sizes, making them ideal for integration into small and portable devices.

Table 10. Schottky diode rectifier performance.

Diodes	Methodology/Substrate	Frequency	Size	Input (dBm)	Power	RF-DC Efficiency (%)	Load (Ω)	Ref.
HSMS 286C	Double diode on Rogers 4350B	2–3.05 GHz	$25 \times 13 \text{ mm}^2$	0 to 25	60%@17 dBm	620 to 2700	[60]	
HSMS 2820	Full-wave doubler on FR4	0.9 GHz, 1.8 GHz, 3.5 GHz, 5.5 GHz, 7.3 GHz	-	-10 to 30	>78%	5 K	[66]	
HSMS 286	Half-wave rectifier on Rogers 4350	2–3 GHz	$36 \times 35 \text{ mm}^2$	0–10	>40%@10 dBm	400	[75]	
SMS 7630	Voltage doubler on RT6002	1.7–1.8 GHz, 2.1–2.7 GHz	$145 \times 145 \times 1.52 \text{ mm}^3$	3	55–65%	2 K	[77]	
HSMS 2860	Shunt diode on RO4003C	2.38 GHz, 2.45 GHz	-	-20 to 10	75.3%@dBm	4.47 K	[118]	
SMS 7630-079	Single diode on Rogers 5880	1.8 GHz	$32 \times 32 \text{ mm}^2$	-40 to 20	21.1%@–20 dBm, 6.9%@–30 dBm	6 K	[119]	
HSMS 285C	1-stage/3-stage rectifier on FR4	Dickson 1 GHz	-	20	77%	14.61 K	[120]	
MA4E-1319	Full-wave doubler on textile	20–26.5 GHz	$32.6 \times 16 \text{ mm}^2$	10	12%	630	[121]	
HSMS 2820 and 2850	HSMS- Self-tunable line on Taconic RF-35	0.9 GHz	$0.195 \times 0.073 \lambda^2$	13	70%	390	[122]	
HSMS 2860	Branch doubler on Rogers 5880	0.866 GHz, 0.915 GHz, 2.45 GHz	$3.5 \times 2.6 \text{ cm}^2$	-30 to 0	65%@0.866 GHz, 62%@0.915 GHz, 60%@2.45 GHz	10 K	[123]	
SMS 7630	Multiple diodes on Rogers 5880	1.84 GHz, 2.04 GHz, 2.36 GHz, 2.54 GHz, 3.3 GHz, 4.76 GHz, 5.8 GHz	$54 \times 42 \text{ mm}^2$	-20 to 4	65%@4 dBm, 28.3–65% across frequencies	1300	[124]	
HSMS 285C	Greinacher rectifier on FR4	1.85 GHz	$70 \times 70 \times 1.6 \text{ mm}^3$	20	40%	4.7 K	[125]	
HSMS-2862-TRI	Voltage doubler with virtual battery on Rogers RO3003	0.06–3.8 GHz	$20 \times 7.4 \text{ mm}^2$	23	77.3%	1.3 K	[126]	
HSMS 2862 SMS 7630	Voltage doubler with dual-band transmission on FR4	0.915 GHz, 1.8 GHz, 2.4 GHz	$24 \times 8.8 \text{ cm}^2$	17	74.9%, 71.2%, 2.45 GHz	1500	[127]	

Despite these advantages, several deficiencies are evident. Schottky rectifiers are often optimized for specific frequency ranges, limiting their effectiveness across broader frequency spectrums. Their performance can degrade significantly with variations in load and input power, leading to inefficiencies in fluctuating RF environments. Parasitic series resistance and inductance can cause substantial power losses, reducing overall efficiency. Moreover, manufacturing errors can affect performance, particularly at microwave frequencies where the wavelength is close to the dimension of the microstrip line.

The identified deficiencies suggest several areas for improvement in Schottky rectifier designs. Future designs should aim to increase the operational bandwidth of Schottky rectifiers to enhance their versatility across different RF applications. Developing rectifiers that maintain high efficiency across varying input power levels and loads can help mitigate performance degradation in dynamic RF environments. Additionally, exploring advanced materials, design techniques, and models to minimize parasitic losses can enhance overall power conversion efficiency.

5.3. Research Challenges on Rectifier

An effective RF energy harvesting (RFEH) system should capture energy across various frequencies and power levels, deliver high output voltage with minimal power, and maintain a compact form. Current advancements in RFEH are focused on identifying research directions and addressing existing challenges [128].

The challenge lies in accurately determining parasitic and conduction losses, harmonic losses, and manufacturing errors, which can lead to low efficiency and impedance mismatches.

5.3.1. Broadband Design Challenges

RFEH systems require rectifiers capable of functioning within designated frequency ranges to harvest energy from any accessible band. However, many rectifiers face challenges in efficiently covering the full spectrum. Since many frequency bands are closely spaced, a broadband rectifier is anticipated to deliver effective performance across broad or multiple bands.

5.3.2. Rectifiers with Wide Power Range Challenges

The received power in wireless power transfer (WPT) systems is inversely proportional to the square of the transmitter-to-receiver distance. Thus, variations in the receiver's position have an impact on the rectenna's input power level. The fluctuating ambient RF power level in a WEH system affects rectifier performance. The relationship between the load resistance and the maximum power handling capability of the rectifier, or critical input power (P_c), is inverse. Changes in load have an impact on the rectifier's capacity to handle power and may result in impedance mismatches, which lower PCE. Rectifiers must therefore minimize impedance fluctuations and sustain PCE by becoming less sensitive to input RF power and load variations.

5.3.3. Improving Power Conversion Efficiency (PCE)

Enhancing PCE in RFEH systems involves reducing energy usage and losses. Innovations such as Schottky diodes and CMOS technology help minimize power consumption. Additional components like TFTs and SC-Schottky diodes further reduce energy use. Efficiency can also be improved by optimizing model performance, such as reconfigurable and distributed matching networks for operation across diverse frequency bands. Co-designing antennas and rectifiers to eliminate matching networks and developing new rectifier topologies for better PCE are crucial strategies. To achieve broader bandwidth and input power range, RFEH circuits should support a wide dynamic range. Multiband and array antennas cater to systems requiring extensive bandwidth and broad input ranges. Unique matching network topologies can address the nonlinear input impedance issues of rectifiers, expanding bandwidth and power range capabilities. Machine learning can sim-

plify adjusting transmission line dimensions for improved matching, while reconfigurable rectifiers can adapt to various dynamic ranges and bandwidth requirements.

5.3.4. Advanced Techniques and Tools

Fast and precise Maximum Power Point Tracking (MPPT) algorithms and artificial intelligence (AI) tools are essential for maintaining high PCE across a wide dynamic range, with simplified control circuits for power-aware Power Management Units (PMUs) ensuring consistent performance and system efficiency. Optimizing the electromagnetic field of the substrate through iterative simulations and integrating artificial intelligence for antenna design can maximize RFEH system performance. Co-designing antennas, matching networks, and rectifiers can enhance sensitivity and PCE while reducing system size, offering a comprehensive approach to improving RFEH systems' efficiency and functionality.

6. Far-Field Rectenna: Power Harvesting and Conversion Efficiency

Rectennas are critical components in far-field radio frequency energy harvesting (RFEH) systems, converting ambient RF energy into DC power and allowing low-power devices to operate when conventional power sources are unavailable or unfeasible [8]. While previous parts addressed the design and functionality of antennas and rectifiers in RFEH systems, this section focuses on the power harvested by rectennas and the issues associated with optimizing power usage [19]. Far-field rectennas must efficiently capture energy delivered over long distances, and their performance is vital in applications such as distant sensors, medical implants, and satellite communications, where reducing power loss is essential for prolonged operation [129].

Table 11 outlines the power consumption of common electronic devices and sensors, ranging from GPS receiver chips at 15 mW to RF transmission at sub- μ W levels. In far-field RF energy harvesting (RFEH) systems, rectennas must supply adequate power to support these devices. High-demand components like GPS chips and cell phones in standby mode present a challenge for RF harvesting [130], while lower-power sensors like accelerometers, pressure, humidity, and temperature sensors, which require between 0.32 mW and 27 μ W, are more suitable for energy harvesting applications. This demonstrates the potential of RFEH systems to power low-energy devices, particularly in IoT and sensor networks.

Table 11. Average power consumption of typical electronic devices and sensors [130].

Device	Power Consumption (mW)
GPS Module	15
Mobile Device (Sleep Mode)	8.1
Optical Heart Rate Sensor	1.47
Air Moisture Sensor	1
Pressure Sensing Device	0.5
3D Accelerometer	0.32
Temperature Sensor	0.027
A/D Conversion	0.001
RF Transmission	Sub- μ W

Multiband rectennas [64] are designed for certain frequencies, such as the ISM bands at 915 MHz and 2.45 GHz, and are extremely efficient within these regions. Broadband rectennas, on the other hand, capture energy across a broader frequency range. Rectennas use power combiners such as DC, RF, and hybrid to improve energy harvesting. DC combiners combine the rectified DC output, whereas RF combiners blend RF signals before rectification, decreasing energy loss. Hybrid combiners combine both technologies, allowing for harvesting at several frequencies and power levels. This paper [64] presents a triple-band

differential rectenna designed for RF energy harvesting. It operates in the 2.1 GHz (UMTS), 2.4–2.48 GHz (WLAN/Wi-Fi), and 3.3–3.8 GHz (WiMAX) frequency bands. The rectenna consists of a differentially fed multiband slot antenna with peak gains of 7 dBi at 2 GHz, 5.5 dBi at 2.5 GHz, and 9.2 dBi at 3.5 GHz. A triple-band rectifier using a Villard voltage doubler and interdigital capacitors is implemented, achieving a peak RF-to-DC conversion efficiency of 68%. When integrated, the rectenna shows maximum conversion efficiencies of 53% at 2 GHz, 31% at 2.5 GHz, and 15.56% at 3.5 GHz. Conventional antennas [131] are constrained by narrow beamwidths, but high-gain antennas improve power collection. To reduce the requirement for sophisticated beamforming networks, we present a traveling-wave grid-array antenna (GAA) with two isolated ports and symmetrically inclined beams. A prototype was created and tested, displaying increased sensitivity and wide-angle coverage. With a power density of $1 \mu\text{W}/\text{cm}^2$, the dual-beam system produced more than $100 \mu\text{W}$ of DC power, expanding the harvesting range beyond 70° . At 2.45 GHz, the rectenna produced a DC output of $3.6\text{--}203.8 \mu\text{W}$ and achieved a maximum RF-to-DC conversion efficiency of 16.3–45.3%. Power densities ranged from 0.052 to $1 \mu\text{W}/\text{cm}^2$. This article [132] introduces a six-beam antenna design that removes the need for a complex feeding system. Integrating a surface waveguide layer and a triangular patch array, it achieves a peak gain of 8.3 dBi and 3 dB beamwidths of 62° in the H-plane and 56° in the E-plane, providing full azimuthal coverage. The energy harvester effectively gathers electromagnetic energy from various horizontal directions and substantially boosts DC power output in the presence of multiple EM transmitters.

The receiving array is optimized for power transmission using quadratic programming, offering adjustable angular coverage. The SMS 7630 diode improves rectification at low incident power. A six-element patch array and 5.8 GHz rectifier were tested, showing stable DC output as the energy source moves between -45° and $+45^\circ$ in the H-plane [133]. The hybrid power combining array has a beam-forming matrix and a DC power management network (PMN), and its normalized DC output is compared to traditional approaches using incident wave angles and received DC power. Four patch antennas were designed using a 4×4 Butler matrix with quadrature hybrids. A reconfigurable voltage doubler rectifier and DC PMN convert RF energy into DC and provide the necessary voltage to the load [134]. Table 12 summarizes various rectenna designs, highlighting their performance metrics and the types of combiners used, illustrating the efficiency and power generated by the rectennas.

Table 12. Performance of far-field rectenna system and power combining method.

Rectenna Design	Frequency	Load	Size	Gain (dBi)	Rectifier	RF-DC Efficiency (%) Power	Ref.
Multiband Differentially fed	2 GHz 2.5 GHz 3.5 GHz	$2\text{--}1.5 \text{k}\Omega$	$2.94 \times 0.027 \lambda^3$	2.94 × 7@2 GHz 5.5@2.5 GHz 9.2 @ 3.5 GHz	Villard Voltage Doubler	53%@2 GHz for $P_{in} = -13 \text{ dBm}$, 30.7% at 2.5 GHz for $P_{in} = 12 \text{ dBm}$, max power is $26.58 \mu\text{W}$.	[64]
Grid-Array DC combiner	2.45 GHz	$6 \text{k}\Omega$	$3.87 \times 0.274 \lambda^3$	5.77 × 15.5	Voltage Doubler	58%@2.45 GHz for $P_{in} = -13.2 \text{ dBm}$, max power is $83.3 \mu\text{W}$.	[131]
Patch Array DC combiner	5.2 GHz	$1 \text{k}\Omega$	$2.39 \times 0.073 \lambda^3$	2.06 × 8.3	Single series	57.7%@5.2 GHz for $P_{in} = 7 \text{ dBm}$, max power is 0.69 mW .	[132]
Square Patch RF combiner	5.8 GHz	$1.18 \text{k}\Omega$	$2.76 \times 0.02 \lambda^3$	0.76 × 6.5	Single shunts	60.1%@5.8 GHz for $P_{in} = 0 \text{ dBm}$, max power is $382 \mu\text{W}$.	[133]
Suspended Patch Hybrid combiner	2.45 GHz	$6.2 \text{k}\Omega$	$1.7 \times 0.085 \lambda^3$	4.11 × 5.9	Voltage Doubler	55.3%@2.45 GHz for $P_{in} = -4 \text{ dBm}$, max power is $250 \mu\text{W}$.	[134]

7. Conclusions

In conclusion, this review emphasizes the critical role of rectenna technology in advancing IoT and 5G systems, which demand sustainable and low-maintenance solutions. RF energy harvesting is pivotal for enabling real-time data acquisition and contributing to a carbon-free future.

The key challenges are as follows:

Rectifier Performance: Existing rectifiers are typically optimized for narrow frequency bands, leading to inefficiencies when handling a broad range of frequencies. Performance can also degrade with variations in input power and load.

Antenna Miniaturization: Although miniaturization is essential for compact devices, it often compromises performance and efficiency. Achieving effective circular polarization in reduced form factors presents additional challenges.

Impedance Matching: Efficient impedance matching across varying frequencies and power levels remains difficult, impacting overall system effectiveness.

Our recommendations are as follows:

Develop Versatile Rectifiers: Design rectifiers that perform efficiently across a wide frequency range and are less sensitive to variations in input power and load. Explore innovations such as adaptive topologies and advanced materials.

Advance Miniaturization Techniques: Research should focus on enhancing miniaturization while maintaining performance, including developing new materials and designs that improve efficiency.

Optimize Impedance Matching: Create advanced impedance matching networks capable of dynamically adjusting to changes in frequency and power levels. Implementing machine learning algorithms for real-time optimization could be advantageous.

Explore Innovative Materials: Investigate new materials, such as advanced metamaterials and emerging semiconductor technologies, to enhance the performance of rectifiers and antennas.

Integrate Machine Learning: Utilize machine learning techniques to optimize design parameters, such as antenna dimensions and rectifier topologies, to improve adaptability and performance under various operating conditions.

Addressing these challenges and implementing these recommendations will be crucial for advancing RF energy harvesting technologies, enhancing the efficiency and sustainability of IoT, 5G systems, and Industrial 5.0 in the future.

Funding: This research received no external funding.

Conflicts of Interest: The authors declare no conflict of interest.

List of Acronyms

Acronyms	Full Form
RF, WEH	Radio Frequency, Wireless Energy Harvesting
RFEH, WPT	RF Energy Harvesting, Wireless Power Transfer
PCE, DC	Power Conversion Efficiency, Direct Current
CMOS	Complementary Metal-Oxide-Semiconductor
AC, Qi	Alternating Current, Charging Flow
EM, RFID	Electromagnetic, RF Identification
GSM, UMTS	Global System for Mobile, Universal Mobile Telecommunications System
LoRaWAN	Long Range Wide Area Network
TSOP, WLAN	Tapered Slot Patch, Wireless Local Area Network
LTE, WiMAX	Long-Term Evolution, Wireless Microwave Access
FR4, MIMO	Flame-Retardant Material, Multiple Input Multiple Output
ISM, TD-LTE	Industrial, Scientific, Medical, Time Division LTE
DNG, MNG	Double-Negative, Magnetic-Negative

SNG, EPG	Single-Negative, Epsilon-Negative
CRLH-TL, RH-TL	Composite Right/Left-Hand Transmission Line, Right-Handed
FSS, CSRR	Frequency Selective Surface, Complementary Split-Ring Resonator
IMN, CMOS-CCDD	Impedance Matching Network, CMOS Capacitive Coupled Device

References

1. Karthick Raghunath, K.; Koti, M.; Sivakami, R.; Vinoth Kumar, V.; NagaJyothi, G.; Muthukumaran, V. Utilization of IoT-assisted computational strategies in wireless sensor networks for smart infrastructure management. *Int. J. Syst. Assur. Eng. Manag.* **2022**, *15*, 123–130. [CrossRef]
2. Khan, S.; Lee, W.-K.; Hwang, S.O. AEchain: A Lightweight Blockchain for IoT Applications. *IEEE Consum. Electron. Mag.* **2022**, *11*, 64–76. [CrossRef]
3. Dash, D. Geometric Algorithm for Finding Time-Sensitive Data Gathering Path in Energy Harvesting Sensor Networks. *IEEE Trans. Intell. Transp. Syst.* **2022**, *23*, 7547–7556. [CrossRef]
4. Kim, S.; Kim, B.; Shah, B.; Ullah, S.; Kim, K.I. Survey on communication for mobile sinks in wireless sensor networks: Mobility pattern perspective. *J. Internet Technol.* **2021**, *22*, 3. [CrossRef]
5. Bhaskarwar, R.V.; Pete, D. Cross-Layer Design Approaches in Underwater Wireless Sensor Networks: A Survey. *SN Comput. Sci.* **2021**, *2*, 362. [CrossRef]
6. Gupta, S.; Jana, P. Energy Efficient Clustering and Routing Algorithms for Wireless Sensor Networks: GA Based Approach. *Wirel. Pers. Commun.* **2015**, *83*, 2403–2423. [CrossRef]
7. Rajagopalan, R.; Varshney, P. Data-aggregation techniques in sensor networks: A survey. *IEEE Commun. Surv. Tutor.* **2006**. [CrossRef]
8. Chen, D.; Li, R.; Xu, J.; Li, D.; Fei, C.; Yang, Y. Recent progress and development of radio frequency energy harvesting devices and circuits. *Nano Energy* **2023**, *117*, 108845. [CrossRef]
9. Sharma, P.; Singh, A. A survey on RF energy harvesting techniques for lifetime enhancement of wireless sensor networks. *Sustain. Comput. Inform. Syst.* **2023**, *37*, 100836. [CrossRef]
10. Alibakhshikani, M.; Virdee, B.; Azpilicueta, L.; Naser-Moghadasi, M.; Akinsolu, M.; See, C.; Liu, B.; Abd-Alhameed, R.A.; Falcone, F. A Comprehensive Survey of ‘Metamaterial Transmission-Line Based Antennas: Design, Challenges, and Applications’. *IEEE Access* **2020**, *8*, 144778–144808. [CrossRef]
11. Esmail, B.; Koziel, S.; Szczepanski, S. Overview of Planar Antenna Loading Metamaterials for Gain Performance Enhancement: The Two Decades of Progress. *IEEE Access* **2022**, *10*, 27381–27403. [CrossRef]
12. Hussain, M.; Awan, W.; Alzaidi, M.; Hussain, N.; Ali, E.; Falcone, F. Metamaterials and Their Application in the Performance Enhancement of Reconfigurable Antennas: A Review. *Micromachines* **2023**, *14*, 349. [CrossRef]
13. Chun, A.; Ramiah, H.; Mekhilef, S. Wide Power Dynamic Range CMOS RF-DC Rectifier for RF Energy Harvesting System: A Review. *IEEE Access* **2022**, *10*, 23948–23963. [CrossRef]
14. Yıldız, F. Potential Ambient Energy-Harvesting Sources and Techniques. *J. Technol. Stud.* **2009**, *35*, 40–48. [CrossRef]
15. Green, M.; Dunlop, E.; Hohl-Ebinger, J.; Yoshita, M.; Kopidakis, N.; Hao, X. Solar cell efficiency tables (version 56). *Prog. Photovoltaics Res. Appl.* **2020**, *28*, 629–638. [CrossRef]
16. Stevens, J. Optimized Thermal Design of Small ΔT Thermoelectric Generators; SAE Technical Paper; SAE: Warrendale, PA, USA, 1999. [CrossRef]
17. Mitchenson, P.; Green, T.; Yeatman, E.; Holmes, A. Architectures for Vibration-Driven Micropower Generators. *J. Microelectromech. Syst.* **2004**, *13*, 429–440. [CrossRef]
18. Roundy, S.; Wright, P.; Pister, K. Micro-Electrostatic Vibration-to-Electricity Converters. In Proceedings of the Microelectromechanical Systems, ASME 2002 International Mechanical Engineering Congress and Exposition, New Orleans, LA, USA, 17–22 November 2002; pp. 487–496. [CrossRef]
19. Piñuela, M.; Mitchenson, P.; Lucyszyn, S. Ambient RF energy harvesting in urban and semi-urban environments. *IEEE Trans. Microw. Theory Tech.* **2013**, *61*, 2715–2726. [CrossRef]
20. Srivastava, V.; Sharma, A. A Coil Rectenna Array Design to Harvest All H-Field Components for Lateral Misalignment Tolerant Wireless Powering of Bio-Medical Implant Devices. *IEEE J. Electromagn. RF Microwaves Med. Biol.* **2024**, *8*, 59–67. [CrossRef]
21. Kumar, M.; Kumar, S.; Jain, S.; Sharma, A. A Plug-in Type Integrated Rectenna Cell for Scalable RF Battery Using Wireless Energy Harvesting System. *IEEE Microw. Wirel. Technol. Lett.* **2023**, *33*, 98–101. [CrossRef]
22. Samal, P.; Chen, S.; Fumeaux, C. Wearable Textile Multiband Antenna for WBAN Applications. *IEEE Trans. Antennas Propag.* **2023**, *71*, 1391–1402. [CrossRef]
23. Kiourti, A.; Nikita, K. A review of implantable patch antennas for biomedical telemetry: Challenges and solutions. *IEEE Antennas Propag. Mag.* **2012**, *54*, 210–228. [CrossRef]
24. Zada, M.; Shah, I.; Nasir, J.; Basir, A.; Yoo, H. Empowering Remote Patient Monitoring with a Dual-Band Implantable Rectenna System for Wireless Power and Data Transfer. *IEEE Trans. Antennas Propag.* **2023**, *71*, 9509–9522. [CrossRef]
25. Dibner, B. Oersted and the discovery of electromagnetism. *Electr. Eng.* **2013**, *80*. [CrossRef]
26. Levin, M.; Miller, M. Maxwell’s ‘Treatise On Electricity and Magnetism’. *Sov. Phys.-Uspekhi* **1981**, *24*, 904. [CrossRef]

27. Janik, A. Heinrich hertz: Classical Physicist, Modern Philosopher. Davis Baird, R. I. G. Hughes, Alfred Nordmann. *Isis* **2000**, *91*. [CrossRef]
28. Carlson, W.; Wenaas, E. Tesla: Inventor of the electrical age. *IEEE Technol. Soc. Mag.* **2014**, *33*, 12–15. [CrossRef]
29. Shinohara, N. History and Innovation of Wireless Power Transfer via Microwaves. *IEEE J. Microw.* **2021**, *1*, 218–228. [CrossRef]
30. Surender, D.; Khan, T.; Talukdar, F.; Antar, Y. Rectenna Design and Development Strategies for Wireless Applications: A review. *IEEE Antennas Propag. Mag.* **2022**, *64*, 16–29. [CrossRef]
31. Zhou, X.; Zhao, J.; Liang, N.; Wu, S.; Wang, J. Analysis of WiTricity corporation’s wireless charging patents. *Gaojishu Tongxin/Chinese High Technol. Lett.* **2016**, *26*. [CrossRef]
32. Theodoridis, M. Effective capacitive power transfer. *IEEE Trans. Power Electron.* **2012**, *27*, 4906–4913. [CrossRef]
33. Sanislav, T.; Mois, G.; Zeadaully, S.; Folea, S. Energy Harvesting Techniques for Internet of Things (IoT). *IEEE Access* **2021**, *9*, 39530–39549. [CrossRef]
34. Asiful Huda, S.; Arafat, M.; Moh, S. Wireless Power Transfer in Wirelessly Powered Sensor Networks: A Review of Recent Progress. *Sensors* **2022**, *22*, 2952. [CrossRef]
35. Cho, Y.; Lee, S.; Kim, D.H.; Kim, H.; Song, C.; Kong, S.; Park, J.; Seo, C.; Kim, J. Thin Hybrid Metamaterial Slab with Negative and Zero Permeability for High Efficiency and Low Electromagnetic Field in Wireless Power Transfer Systems. *IEEE Trans. Electromagn. Compat.* **2018**, *60*, 1001–1009. [CrossRef]
36. FCC Rules for Unlicensed Wireless Equipment Operating in the ISM Bands. 2021. Available online: <Https://Afar.Net/Tutorials/Fcc-Rules/> (accessed on 20 July 2024).
37. Soyata, T.; Copeland, L.; Heinzelman, W. RF Energy Harvesting for Embedded Systems: A Survey of Tradeoffs and Methodology. *IEEE Circuits Syst. Mag.* **2016**, *16*, 22–57. [CrossRef]
38. Liu, C.; Zhang, Y.; Liu, X. Circularly Polarized Implantable Antenna for 915 MHz ISM-Band Far-Field Wireless Power Transmission. *IEEE Antennas Wirel. Propag. Lett.* **2018**, *17*, 373–376. [CrossRef]
39. Kim, J.; Cho, S.; Kim, H.J.; Choi, J.W.; Jang, J.; Choi, J. Exploiting the Mutual Coupling Effect on Dipole Antennas for RF Energy Harvesting. *IEEE Antennas Wirel. Propag. Lett.* **2016**, *15*, 1301–1304. [CrossRef]
40. Zeng, M.; Andrenko, A.; Liu, X.; Li, Z.; Tan, H. A Compact Fractal Loop Rectenna for RF Energy Harvesting. *IEEE Antennas Wirel. Propag. Lett.* **2017**, *16*, 2424–2427. [CrossRef]
41. Kamoda, H.; Kitazawa, S.; Kukutsu, N.; Kobayashi, K. Loop antenna over artificial magnetic conductor surface and its application to dual-band RF energy harvesting. *IEEE Trans. Antennas Propag.* **2015**, *63*, 4408–4417. [CrossRef]
42. Schaubert, D.; Kasturi, S.; Borysenko, A.; Elsallal, W. Vivaldi antenna arrays for wide bandwidth and electronic scanning. In Proceedings of the IET Seminar Digest, Scotland, UK, 11–16 November 2007; Volume 2007. [CrossRef]
43. Yadav, H.; Ray, K.; Gupta, M. Differential multiresonator stacked microstrip antenna for wireless energy harvesting. *Int. J. RF Microw. Comput.-Aided Eng.* **2021**, *31*, e22828. [CrossRef]
44. Anandkumar, D.; Sangeetha, R. Design and analysis of aperture coupled micro strip patch antenna for radar applications. *Int. J. Intell. Netw.* **2020**, *1*, 141–147. [CrossRef]
45. Amer, A.; Sapuan, S.; Nasimuddin, N.; Alphones, A.; Zinal, N. A Comprehensive Review of Metasurface Structures Suitable for RF Energy Harvesting. *IEEE Access* **2020**, *8*, 76433–76452. [CrossRef]
46. Shen, S.; Zhang, Y.; Chiu, C.Y.; Murch, R. An Ambient RF Energy Harvesting System Where the Number of Antenna Ports is Dependent on Frequency. *IEEE Trans. Microw. Theory Tech.* **2019**, *67*, 3821–3832. [CrossRef]
47. Balanis, C. *Antenna Theory: Analysis and Design*, 4th ed.; John Wiley & Sons, Inc.: Hoboken, NJ, USA, 2016.
48. Mugitani, A.; Sakai, N.; Hirono, A.; Noguchi, K.; Itoh, K. Harmonic Reaction Inductive Folded Dipole Antenna for Direct Connection with Rectifier Diodes. *IEEE Access* **2022**, *10*, 53433–53442. [CrossRef]
49. Boursianis, A.; Papadopoulou, M.; Piererezan, J.; Mariani, V.; Coelho, L.; Sarigiannidis, P.; Koulouridis, S.; Goudos, S.K. Multiband Patch Antenna Design Using Nature-Inspired Optimization Method. *IEEE Open J. Antennas Propag.* **2021**, *2*, 151–162. [CrossRef]
50. Liu, P.; Jiang, W.; Hu, W.; Sun, S.; Gong, S. Wideband Multimode Filtering Circular Patch Antenna. *IEEE Trans. Antennas Propag.* **2021**, *69*, 7249–7259. [CrossRef]
51. Biswas, B.; Ghatak, R.; Poddar, D. UWB monopole antenna with multiple fractal slots for band-notch characteristic and integrated Bluetooth functionality. *J. Electromagn. Waves Appl.* **2015**, *29*, 1593–1609. [CrossRef]
52. Midya, M.; Bhattacharjee, S.; Mitra, M. Broadband Circularly Polarized Planar Monopole Antenna with G-Shaped Parasitic Strip. *IEEE Antennas Wirel. Propag. Lett.* **2019**, *18*, 581–585. [CrossRef]
53. Sabhan, D.; Nesamoni, V.; Thangappan, J. An Efficient 2.45 GHz Spiral Rectenna without a Matching Circuit for RF Energy Harvesting. *Wirel. Pers. Commun.* **2021**, *119*, 713–726. [CrossRef]
54. Song, M.; Zhang, X.; Wang, Z.; Xu, D.; Loh, T.; Gao, S. 3D-printed Spiral Inverted Ridge Circularly Polarized Horn Antenna with One Octave Bandwidth. *IEEE Antennas Wirel. Propag. Lett.* **2024**, *23*, 3018–3022. [CrossRef]
55. Hu, Y.; Sun, S.; Xu, H. Compact Collinear Quasi-Yagi Antenna Array for Wireless Energy Harvesting. *IEEE Access* **2020**, *8*, 35308–35317. [CrossRef]
56. Soboll, P.; Wienstroer, V.; Kronberger, R. Stacked Yagi-Uda Array for 2.45-GHz Wireless Energy Harvesting. *IEEE Microw. Mag.* **2015**, *16*, 67–73. [CrossRef]
57. Nasimuddin; Esselle, K.; Verma, A. Wideband high-gain circularly polarized stacked microstrip antennas with an optimized C-type feed and a short horn. *IEEE Trans. Antennas Propag.* **2008**, *56*, 578–581. [CrossRef]

58. Pereira, E.; Paz, H.; Silva, V.; Cambero, E.; Casella, I.; Capovilla, C. An Antipodal Vivaldi Antenna with Elliptical Slots for Low-Cost Rectenna Applications. *J. Circuits Syst. Comput.* **2021**, *30*, 2150248. [CrossRef]
59. Shi, Y.; Fan, Y.; Li, Y.; Yang, L.; Wang, M. An efficient broadband slotted rectenna for wireless power transfer at LTE band. *IEEE Trans. Antennas Propag.* **2019**, *67*, 814–822. [CrossRef]
60. Zhang, Y.; Deng, J.; Li, M.; Sun, D.; Guo, L. A MIMO Dielectric Resonator Antenna with Improved Isolation for 5G mm-Wave Applications. *IEEE Antennas Wirel. Propag. Lett.* **2019**, *18*, 747–751. [CrossRef]
61. Bhatt, K.; Kumar, S.; Kumar, P.; Tripathi, C. Highly Efficient 2.4 and 5.8 GHz Dual-Band Rectenna for Energy Harvesting Applications. *IEEE Antennas Wirel. Propag. Lett.* **2019**, *18*, 2637–2641. [CrossRef]
62. Yang, L.; Zhou, Y.; Zhang, C.; Yang, X.; Yang, X.X.; Tan, C. Compact Multiband Wireless Energy Harvesting Based Battery-Free Body Area Networks Sensor for Mobile Healthcare. *IEEE J. Electromagn. RF Microwaves Med. Biol.* **2018**, *2*, 109–115. [CrossRef]
63. Yaseen, R.; Naji, D.; Shakir, A. Optimization Design Methodology of Broadband or Multiband Antenna for RF Energy Harvesting Applications. *Prog. Electromagn. Res. B* **2021**, *93*, 169–194. [CrossRef]
64. Chandravanshi, S.; Sarma, S.S.; Akhtar, M. Design of Triple Band Differential Rectenna for RF Energy Harvesting. *IEEE Trans. Antennas Propag.* **2018**, *66*, 2716–2726. [CrossRef]
65. Khemar, A.; Kacha, A.; Takhedmit, H.; Abib, G. Design and experiments of a dual-band rectenna for ambient RF energy harvesting in urban environments. *IET Microwaves Antennas Propag.* **2018**, *12*, 49–55. [CrossRef]
66. Singh, N.; Kanaujia, B.; Beg, M.; Mainuddin; Kumar, S.; Choi, H.; Kim, K. Low profile multiband rectenna for efficient energy harvesting at microwave frequencies. *Int. J. Electron.* **2019**, *106*, 2057–2071. [CrossRef]
67. Jie, A.; Nasimuddin, N.; Karim, M.; Chandrasekaran, K. A dual-band efficient circularly polarized rectenna for RF energy harvesting systems. *Int. J. RF Microw. Comput.-Aided Eng.* **2019**, *29*, e21665. [CrossRef]
68. Fang, Y.; Wu, L.; Qiu, L.; Zhang, Y. A Method of Introducing Coupling Null by Shorting Pins for Stacked Microstrip Patch Antenna Array. *IEEE Trans. Antennas Propag.* **2022**, *70*, 6030–6035. [CrossRef]
69. Engheta, N. An idea for thin subwavelength cavity resonators using metamaterials with negative permittivity and permeability. *IEEE Antennas Wirel. Propag. Lett.* **2002**, *1*, 10–13. [CrossRef]
70. Li, M.; Zhong, B.; Cheung, S. Isolation enhancement for MIMO patch antennas using near-field resonators as coupling-mode transducers. *IEEE Trans. Antennas Propag.* **2019**, *67*, 755–764. [CrossRef]
71. He, Y.; Huang, W.; He, Z.; Zhang, L.; Gao, X.; Zeng, Z. A Novel Cross-Band Decoupled Shared-Aperture Base Station Antenna Array Unit for 5G Mobile Communications. *IEEE Open J. Antennas Propag.* **2022**, *3*, 583–593. [CrossRef]
72. Lu, X.; Chen, Y.; Guo, S.; Yang, S. An Electromagnetic-Transparent Cascade Comb Dipole Antenna for Multi-Band Shared-Aperture Base Station Antenna Array. *IEEE Trans. Antennas Propag.* **2022**, *70*, 2750–2759. [CrossRef]
73. Chang, Y.; Chu, Q. Ferrite-Loaded Dual-Polarized Antenna for Decoupling of Multiband Multiarray Antennas. *IEEE Trans. Antennas Propag.* **2021**, *69*, 7419–7426. [CrossRef]
74. Qi, X.; Xu, Z.; Li, H. High efficiency 2-D Multi-Beam Rectenna Based on Gain Enhanced Patch Array. *IEEE Antennas Wirel. Propag. Lett.* **2022**, *21*, 2537–2541. [CrossRef]
75. Wu, F.; Luk, K. Circular Polarization and Reconfigurability of Fabry-Pérot Resonator Antenna Through Metamaterial-Loaded Cavity. *IEEE Trans. Antennas Propag.* **2019**, *67*, 2196–2208. [CrossRef]
76. Fakharian, M. A high gain wideband circularly polarized rectenna with wide ranges of input power and output load. *Int. J. Electron.* **2022**, *109*, 83–99. [CrossRef]
77. Song, C.; Lu, P.; Shen, S. Highly Efficient Omnidirectional Integrated Multiband Wireless Energy Harvesters for Compact Sensor Nodes of Internet-of-Things. *IEEE Trans. Ind. Electron.* **2021**, *68*, 8128–8140. [CrossRef]
78. Ali, T.; Pathan, S.; Biradar, R. Multiband, frequency reconfigurable, and metamaterial antennas design techniques: Present and future research directions. *Internet Technol. Lett.* **2018**, *1*, e19. [CrossRef]
79. Yang, P.; Dang, R.; Li, L. Dual-Linear-to-Circular Polarization Converter Based Polarization-Twisting Metasurface Antenna for Generating Dual Band Dual Circularly Polarized Radiation in Ku-Band. *IEEE Trans. Antennas Propag.* **2022**, *70*, 9877–9881. [CrossRef]
80. Maslovski, S.; Tretyakov, S.; Belov, P. Wire media with negative effective permittivity: A quasi-static model. *Microw. Opt. Technol. Lett.* **2002**, *35*, 47–51. [CrossRef]
81. Marques, R.; Mesa, F.; Martel, J.; Medina, F. Comparative analysis of edge- and broadside-coupled split ring resonators for metamaterial design—Theory and experiments. *IEEE Trans. Antennas Propag.* **2003**, *51*, 2572–2581. [CrossRef]
82. Caloz, C.; Itoh, T. *Electromagnetic Metamaterials: Transmission Line Theory and Microwave Applications: The Engineering Approach*; John Wiley & Sons: Hoboken, NJ, USA, 2005. [CrossRef]
83. Kumar, P.; Ali, T.; Pai, M. Electromagnetic metamaterials: A new paradigm of antenna design. *IEEE Access* **2021**, *9*, 18722–18751. [CrossRef]
84. Liu, Z.; Guo, Y. Compact Low-Profile Dual Band Metamaterial Antenna for Body Centric Communications. *IEEE Antennas Wirel. Propag. Lett.* **2015**, *14*, 863–866. [CrossRef]
85. Li, M.; Luk, K.; Ge, L.; Zhang, K. Miniaturization of Magnetoelectric Dipole Antenna by Using Metamaterial Loading. *IEEE Trans. Antennas Propag.* **2016**, *64*, 4914–4918. [CrossRef]
86. Abdalla, M.; Fouad, M.; Elregeily, H.; Mitkees, A. Wideband negative permittivity metamaterial for size reduction of stopband filter in antenna applications. *Prog. Electromagn. Res. C* **2012**, *25*, 55–66. [CrossRef]

87. Juan, Y.; Yang, W.; Che, W. Miniaturized Low-Profile Circularly Polarized Metasurface Antenna Using Capacitive Loading. *IEEE Trans. Antennas Propag.* **2019**, *67*, 3527–3532. [CrossRef]
88. Gheethan, A.; Herzog, P.; Mumcu, G. Compact 2×2 coupled double loop GPS antenna array loaded with broadside coupled split ring resonators. *IEEE Trans. Antennas Propag.* **2013**, *61*, 3000–3008. [CrossRef]
89. Nahar, T.; Rawat, S. Survey of various bandwidth enhancement techniques used for 5G antennas. *Int. J. Microw. Wirel. Technol.* **2022**, *14*, 204–224. [CrossRef]
90. Li, Y.; Chen, J. Design of Miniaturized High Gain Bow-Tie Antenna. *IEEE Trans. Antennas Propag.* **2022**, *70*, 738–743. [CrossRef]
91. Al-Bawri, S.; Islam, M.; Wong, H.; Jamlos, M.; Narbudowicz, A.; Jusoh, M.; Sabapathy, T.; Islam, M.T. Metamaterial cell-based superstrate towards bandwidth and gain enhancement of quad-band CPW-fed antenna for wireless applications. *Sensors* **2020**, *20*, 457. [CrossRef]
92. Zada, M.; Shah, I.; Yoo, H. Metamaterial-Loaded Compact High-Gain Dual-Band Circularly Polarized Implantable Antenna System for Multiple Biomedical Applications. *IEEE Trans. Antennas Propag.* **2020**, *68*, 1140–1144. [CrossRef]
93. Bakhtiari, A. Investigation of Enhanced Gain Miniaturized Patch Antenna Using Near Zero Index Metamaterial Structure Characteristics. *IETE J. Res.* **2022**, *68*, 1312–1319. [CrossRef]
94. Tang, M.; Ziolkowski, R. Frequency-Agile, Efficient, Circularly Polarized, Near-Field Resonant Antenna: Designs and Measurements. *IEEE Trans. Antennas Propag.* **2015**, *63*, 5203–5209. [CrossRef]
95. Dey, S.; Dey, S.; Koul, S. Isolation Improvement of MIMO Antenna Using Novel EBG and Hair-Pin Shaped DGS at 5G Millimeter Wave Band. *IEEE Access* **2021**, *9*, 162820–162834. [CrossRef]
96. Selvaraju, R.; Jamaluddin, M.; Kamarudin, M.; Nasir, J.; Dahri, M. Mutual coupling reduction and pattern error correction in a 5G beamforming linear array using CSRR. *IEEE Access* **2018**, *6*, 65922–65934. [CrossRef]
97. Qamar, Z.; Naeem, U.; Khan, S.; Chongcheawchamnan, M.; Shafique, M. Mutual Coupling Reduction for High-Performance Densely Packed Patch Antenna Arrays on Finite Substrate. *IEEE Trans. Antennas Propag.* **2016**, *64*, 1653–1660. [CrossRef]
98. Haykin, S. *Communication Systems*, 3rd ed.; John Wiley & Sons: Hoboken, NJ, USA, 2005.
99. Mallik, A.; Kundu, S. Design of a novel dual-band microstrip patch antenna operating at 2.45 GHz and 2.84 GHz with practical implementation. In Proceedings of the 16th Int'l Conf. Computer and Information Technology, Khulna, Bangladesh, 8–10 March 2014; pp. 40–45. [CrossRef]
100. Wyndrum, R. Microwave filters, impedance-matching networks, and coupling structures. *Proc. IEEE* **1965**, *53*, 766. [CrossRef]
101. Keshavarz, R.; Shariati, N. Highly Sensitive and Compact Quad-Band Ambient RF Energy Harvester. *IEEE Trans. Ind. Electron.* **2022**, *69*, 3609–3621. [CrossRef]
102. Eroglu, A. *RF/Microwave Engineering and Applications in Energy Systems*; John Wiley & Sons: Hoboken, NJ, USA, 2022. [CrossRef]
103. Mohan, A.; Mondal, S. An Impedance Matching Strategy for Micro-Scale RF Energy Harvesting Systems. *IEEE Trans. Circuits Syst. II Express Briefs* **2021**, *68*, 1458–1462. [CrossRef]
104. Wang, C.; Yuan, B.; Shi, W.; Mao, J. Low-Profile Broadband Plasma Antenna for Naval Communications in VHF and UHF Bands. *IEEE Trans. Antennas Propag.* **2020**, *68*, 4271–4282. [CrossRef]
105. Lauder, D.; Sun, Y. Design Considerations of Antennas and Adaptive Impedance Matching Networks for RF Energy Harvesting. In Proceedings of the 2020 European Conference on Circuit Theory and Design (ECCTD), Sofia, Bulgaria, 7–10 September 2020; pp. 1–4. [CrossRef]
106. Jabbar, H.; Song, Y.; Jeong, T. RF energy harvesting system and circuits for charging of mobile devices. *IEEE Trans. Consum. Electron.* **2010**, *56*, 247–253. [CrossRef]
107. Chong, G.; Ramiah, H.; Yin, J.; Rajendran, J.; Wong, W.; Mak, P.I.; Martins, R. Ambient RF energy harvesting system: A review on integrated circuit design. *Analog Integr. Circuits Signal Process.* **2018**, *97*, 515–531. [CrossRef]
108. Barton, T.; Gordonson, J.; Perreault, D. Transmission line resistance compression networks for microwave rectifiers. In Proceedings of the IEEE MTT-S International Microwave Symposium Digest, Tampa, FL, USA, 1–6 June 2014. [CrossRef]
109. Khan, D.; Oh, S.; Shehzad, K.; Basim, M.; Verma, D.; Pu, Y.; Lee, M.; Hwang, K.C.; Yang, Y.; Lee, K.-Y. An Efficient Reconfigurable RF-DC Converter with Wide Input Power Range for RF Energy Harvesting. *IEEE Access* **2020**, *8*, 79310–79318. [CrossRef]
110. Li, X.; Lu, Y.; Martins, R. A 200 MHz Passive Rectifier with Active-Static Hybrid V TH Compensation Obtaining 8% PCE Improvement. *IEEE Trans. Power Electron.* **2023**, *38*, 5655–5658. [CrossRef]
111. Akram, M.; Ha, S. A 434-MHz Bootstrap Rectifier with Dynamic V TH Compensation for Wireless Biomedical Implants. *IEEE Trans. Power Electron.* **2023**, *38*, 1423–1428. [CrossRef]
112. Karami, M.; Moez, K. Systematic Co-Design of Matching Networks and Rectifiers for CMOS Radio Frequency Energy Harvesters. *IEEE Trans. Circuits Syst. I Regul. Pap.* **2019**, *66*, 3238–3251. [CrossRef]
113. Lau, W.; Ho, H.; Siek, L. Deep Neural Network (DNN) Optimized Design of 2.45 GHz CMOS Rectifier with 73.6% Peak Efficiency for RF Energy Harvesting. *IEEE Trans. Circuits Syst. I Regul. Pap.* **2020**, *67*, 4322–4333. [CrossRef]
114. Chong, G.; Ramiah, H.; Yin, J.; Rajendran, J.; Mak, P.I.; Martins, R. A Wide-PCE-Dynamic-Range CMOS Cross-Coupled Differential-Drive Rectifier for Ambient RF Energy Harvesting. *IEEE Trans. Circuits Syst. II Express Briefs* **2021**, *68*, 1743–1747. [CrossRef]
115. Almansouri, A.; Ouda, M.; Salama, K. A CMOS RF-to-DC Power Converter with 86% Efficiency and -19.2-dBm Sensitivity. *IEEE Trans. Microw. Theory Tech.* **2018**, *66*, 2409–2415. [CrossRef]

116. Abouzied, M.; Ravichandran, K.; Sanchez-Sinencio, E. A Fully Integrated Reconfigurable Self-Startup RF Energy-Harvesting System with Storage Capability. *IEEE J. Solid-State Circuits* **2017**, *52*, 704–719. [CrossRef]
117. Cheng, L.; Ki, W.; Tsui, C. A 6.78-MHz Single-Stage Wireless Power Receiver Using a 3-Mode Reconfigurable Resonant Regulating Rectifier. *IEEE J. Solid-State Circuits* **2017**, *52*, 1412–1423. [CrossRef]
118. Zhao, F.; Inserra, D.; Gao, G.; Huang, Y.; Li, J.; Wen, G. High-Efficiency Microwave Rectifier with Coupled Transmission Line for Low-Power Energy Harvesting and Wireless Power Transmission. *IEEE Trans. Microw. Theory Tech.* **2021**, *69*, 916–925. [CrossRef]
119. Shen, S.; Chiu, C.; Murch, R. Multiport Pixel Rectenna for Ambient RF Energy Harvesting. *IEEE Trans. Antennas Propag.* **2018**, *66*, 644–656. [CrossRef]
120. Kasar, Ö.; Gözel, M.; Kahriman, M. Analysis of rectifier stage number and load resistance in an RF energy harvesting circuit. *Microw. Opt. Technol. Lett.* **2020**, *62*, 1542–1547. [CrossRef]
121. Wagih, M.; Hilton, G.; Weddell, A.; Beeby, S. Broadband millimeter-wave textile-based flexible rectenna for wearable energy harvesting. *IEEE Trans. Microw. Theory Tech.* **2020**, *68*, 4960–4972. [CrossRef]
122. Oh, T.; Lim, T.; Lee, Y. A Self-Matching Rectifier Based on an Artificial Transmission Line for Enhanced Dynamic Range. *IEEE Trans. Circuits Syst. I Regul. Pap.* **2022**, *69*, 2225–2234. [CrossRef]
123. Quddious, A.; Zahid, S.; Tahir, F.; Antoniades, M.; Vryonides, P.; Nikolaou, S. Dual-Band Compact Rectenna for UHF and ISM Wireless Power Transfer Systems. *IEEE Trans. Antennas Propag.* **2021**, *69*, 2392–2397. [CrossRef]
124. Wang, Y.; Zhang, J.; Su, Y.; Jiang, X.; Zhang, C.; Wang, L.; Cheng, Q. Efficiency Enhanced Seven-Band Omnidirectional Rectenna for RF Energy Harvesting. *IEEE Trans. Antennas Propag.* **2022**, *70*, 8473–8484. [CrossRef]
125. Gozel, M.; Kahriman, M.; Kasar, O. Design of an efficiency-enhanced Greinacher rectifier operating in the GSM 1800 band by using rat-race coupler for RF energy harvesting applications. *Int. J. Microw.-Comput.-Aided Eng.* **2018**, *29*, e21621. [CrossRef]
126. Gyawali, B.; Thapa, S.; Barakat, A.; Yoshitomi, K.; Pokharel, R. Analysis and design of diode physical limit bandwidth efficient rectification circuit for maximum flat efficiency, wide impedance, and efficiency bandwidths. *Sci. Rep.* **2021**, *11*, 19941. [CrossRef]
127. Liu, J.; Zhang, X.; Xue, Q. Dual-Band Transmission-Line Resistance Compression Network and Its Application to Rectifiers. *IEEE Trans. Circuits Syst. I Regul. Pap.* **2019**, *66*, 119–132. [CrossRef]
128. Khan, W.; Raad, R.; Tubbal, F.; Theoharis, P.; Iranmanesh, S. RF Energy Harvesting Using Multidirectional Rectennas: A Review. *IEEE Sens. J.* **2024**, *24*, 18762–18790. [CrossRef]
129. Ding, S.; Koulouridis, S.; Pichon, L. Implantable Wireless Transmission Rectenna System for Biomedical Wireless Applications. *IEEE Access* **2020**, *8*, 195551–195558. [CrossRef]
130. Yang, Y.; Yeo, J.; Priya, S. Harvesting Energy from the Counterbalancing (Weaving) Movement in Bicycle Riding. *Sensors* **2012**, *12*, 10248–10258. [CrossRef]
131. Hu, Y.Y.; Sun, S.; Xu, H.; Sun, H. Grid-Array Rectenna with Wide Angle Coverage for Effectively Harvesting RF Energy of Low Power Density. *IEEE Trans. Microw. Theory Tech.* **2019**, *67*, 402–413. [CrossRef]
132. Deng, W.; Wang, S.; Yang, B.; Zheng, S. A Multibeam Ambient Electromagnetic Energy Harvester with Full Azimuthal Coverage. *IEEE Internet Things J.* **2022**, *9*, 8925–8934. [CrossRef]
133. Cai, X.; Geyi, W.; Guo, Y. A Compact Rectenna with Flat-Top Angular Coverage for RF Energy Harvesting. *IEEE Antennas Wirel. Propag. Lett.* **2021**, *20*, 1307–1311. [CrossRef]
134. Lee, D.J.; Lee, S.J.; Hwang, I.J.; Lee, W.S.; Yu, J.W. Hybrid Power Combining Rectenna Array for Wide Incident Angle Coverage in RF Energy Transfer. *IEEE Trans. Microw. Theory Tech.* **2017**, *65*, 3409–3418. [CrossRef]

Disclaimer/Publisher’s Note: The statements, opinions and data contained in all publications are solely those of the individual author(s) and contributor(s) and not of MDPI and/or the editor(s). MDPI and/or the editor(s) disclaim responsibility for any injury to people or property resulting from any ideas, methods, instructions or products referred to in the content.

MDPI AG
Grosspeteranlage 5
4052 Basel
Switzerland
Tel.: +41 61 683 77 34

Sensors Editorial Office
E-mail: sensors@mdpi.com
www.mdpi.com/journal/sensors



Disclaimer/Publisher's Note: The title and front matter of this reprint are at the discretion of the Guest Editor. The publisher is not responsible for their content or any associated concerns. The statements, opinions and data contained in all individual articles are solely those of the individual Editor and contributors and not of MDPI. MDPI disclaims responsibility for any injury to people or property resulting from any ideas, methods, instructions or products referred to in the content.



Academic Open
Access Publishing
mdpi.com

ISBN 978-3-7258-3642-0